



**US Army Corps
of Engineers**
Waterways Experiment
Station

Technical Report HL-95-14
November 1995

Montgomery Point Lock and Dam Gate Study

Report 2

Montgomery Point Torque-Tube Gate, A Structural Model Study

by Luis A. de Bejar

DTIC QUALITY INSPECTED 1

Approved For Public Release; Distribution Is Unlimited

19960311 153

Prepared for Headquarters, U.S. Army Corps of Engineers
U.S. Army Engineer Division, Southwestern
U.S. Army Engineer District, Little Rock

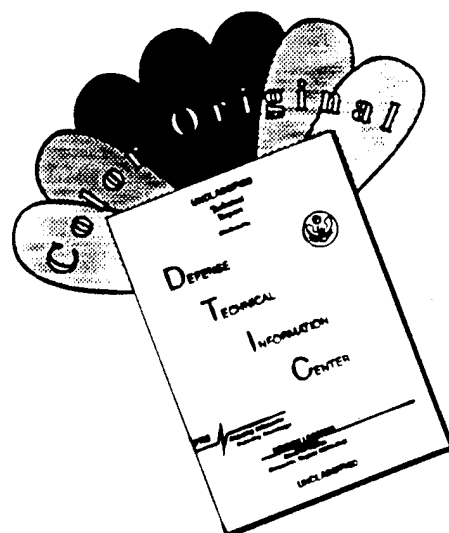
DTIC QUALITY INSPECTED 1

The contents of this report are not to be used for advertising, publication, or promotional purposes. Citation of trade names does not constitute an official endorsement or approval of the use of such commercial products.



PRINTED ON RECYCLED PAPER

DISCLAIMER NOTICE



THIS DOCUMENT IS BEST QUALITY AVAILABLE. THE COPY FURNISHED TO DTIC CONTAINED A SIGNIFICANT NUMBER OF COLOR PAGES WHICH DO NOT REPRODUCE LEGIBLY ON BLACK AND WHITE MICROFICHE.

Montgomery Point Lock and Dam Gate Study

Report 2

Montgomery Point Torque-Tube Gate, A Structural Model Study

by Luis A. de Bejar

U.S. Army Corps of Engineers
Waterways Experiment Station
3909 Halls Ferry Road
Vicksburg, MS 39180-6199

Report 2 of a series

Approved for public release; distribution is unlimited

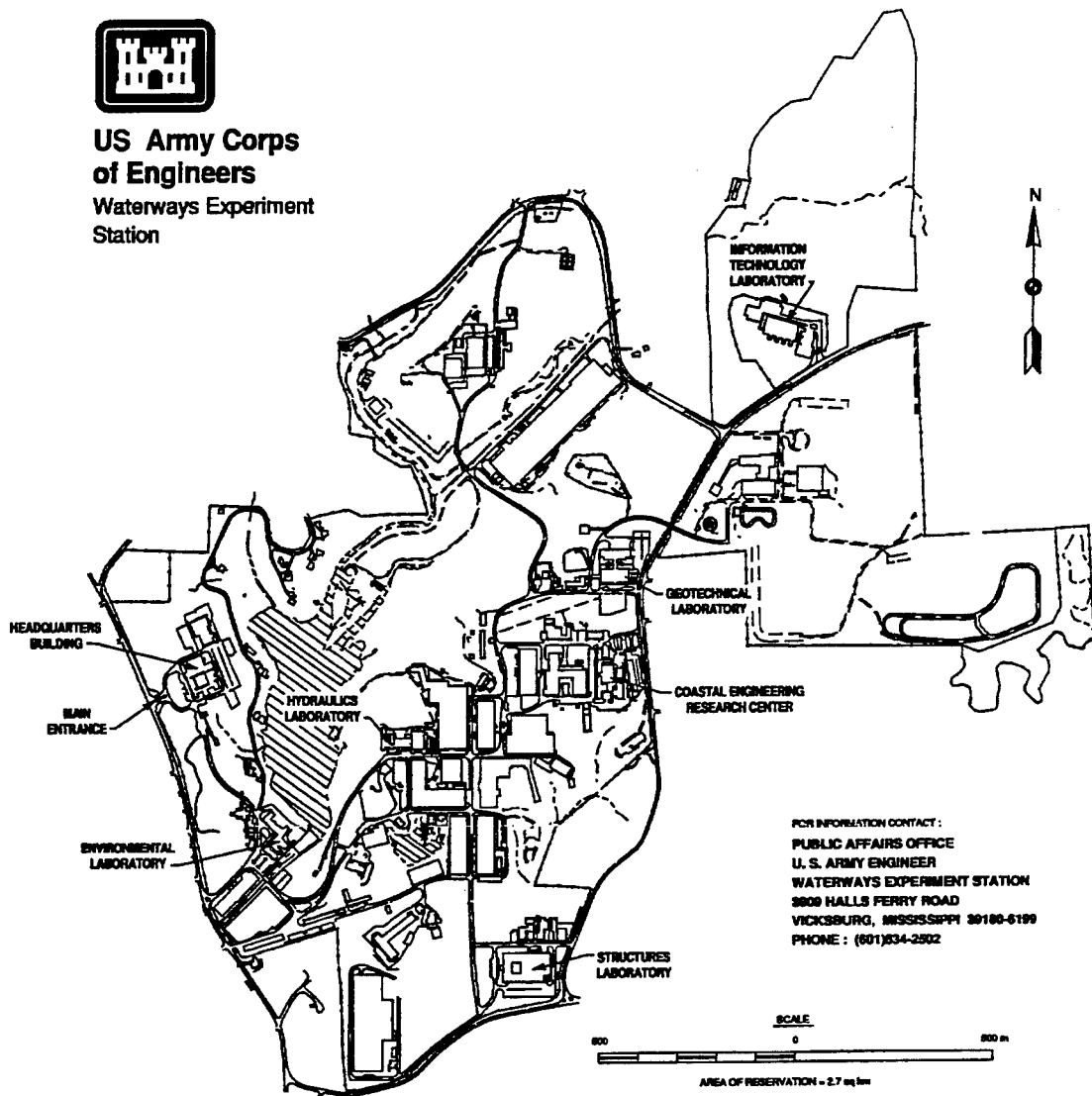
Prepared for U.S. Army Corps of Engineers
Washington, DC 20314-1000

U.S. Army Engineer Division, Southwestern
1114 Commerce Street, Dallas, TX 75242-0216

and U.S. Army Engineer District, Little Rock
P.O. Box 867, Little Rock, AR 72203-0867



**US Army Corps
of Engineers**
Waterways Experiment
Station



Waterways Experiment Station Cataloging-in-Publication Data

Bejar, Luis A. de.

Montgomery Point Lock and Dam Gate Study. Report 2, Montgomery Point Torque-tube Gate : a structural model study / by Luis A. de Bejar ; prepared for U.S. Army Corps of Engineers, U.S. Army Engineer Division, Southwestern, and U.S. Army Engineer District, Little Rock.

186 p. : ill. ; 28 cm. — (Technical report ; HL-95-14 rept.2)

Includes bibliographical references.

Report 2 of a series.

1. Locks (Hydraulic engineering) — Arkansas. 2. Hydraulic gates. 3. Dams — Arkansas. 4. Montgomery Point Lock and Dam (Ark.) I. United States. Army. Corps of Engineers. Southwestern Division. II. United States. Army. Corps of Engineers. Little Rock District. III. U.S. Army Engineer Waterways Experiment Station. IV. Hydraulics Laboratory (U.S. Army Engineer Waterways Experiment Station) V. Title. VI. Title: Montgomery Point Torque-tube Gate, a structural model study. VII. Series: Technical report (U.S. Army Engineer Waterways Experiment Station) ; HL-95-14 rept.2.

TA7 W34 no.HL-95-14 rept.2

Contents

Preface	xii
Conversion Factors, Non-SI to SI Units of Measurement	xiii
1—Introduction	1
Purpose and Scope of the Research Project on the Structure	1
Organization of Report 2	2
2—Mathematical Model for Hydraulic Pressure Field	7
3—Experimental and Finite Element Analyses	39
4—Extreme-Value Analysis of Experimental Pressure Data	67
Probability Distribution for Maxima	67
Probability Distribution for Extreme Values	70
Pressure Envelopes—Phase 2 of the Experimental Project	72
5—Gate Eigenproperties	85
6—Engineering Model	124
Deterministic Mathematical Model	124
Random Vibration Model for Fluctuations	130
7—Conclusions and Recommendations	144
References	146
Appendix A: Spectral Analysis	A1
SF 298	

List of Tables

Table 1.	Theoretical Prediction versus Experimental Measurements	19
Table 2.	Average Experimental Upstream Pressure Field on Gate (100-s test)	41
Table 3.	Montgomery Point Gate 1/15-Scale Model (3 supports): Summary of Finite Element Analysis Bearing Reactions, lb	43
Table 4.	Montgomery Point Gate Prototype (5 supports): Summary of Finite Element Analysis Bearing Reactions, kips	44
Table 5.	Computation of Energy Parameter ϵ for Test T1080 (Sampling Rate: 500 sps; Duration: 100s)	69
Table 6.	Probability that Allowable Stress be Exceeded at Least Once in a Given Time Interval, 50-year Mean Recurrence Interval	71
Table 7.	Montgomery Point Gate Model, Phase 2, New Tests to Replace Some Defective Pressure-Cell Records	73
Table 8.	Natural Frequencies for the Physical Model, Hz	86
Table 9.	Dynamic Equilibrium, Formulation of the Principle of Virtual Displacements	126

List of Photos

Photo 1.	Montgomery Point Torque-Tube Gate Model. Aperture in experimental flume corresponding to central (instrumented) gate in fully open position	4
Photo 2.	Montgomery Point Torque-Tube Gate Model. Central (instrumented) gate in fully closed position. Lateral gates in the experimental flume in fully open position	5
Photo 3.	Montgomery Point Torque-Tube Gate Model. Design controlling condition: the three gates in the experimental flume in fully closed position	6

List of Plates

Plate 1.	Montgomery Point Torque-Tube Gate. Lateral view of physical model in closed position with a ventilated nappe (T1109)	20
Plate 2.	Montgomery Point Lock and Dam. Plan of borings at the site (Design Memorandum No. 1, Plate 31/1)	21
Plate 3.	Montgomery Point Lock and Dam. Boring profile C (Design Memorandum No. 1, Plate 31/3)	22
Plate 4.	Montgomery Point Torque-Tube Gate. Longitudinal cross section of prototype	23
Plate 5.	Montgomery Point Gate. Variation of hydraulic pressure with point elevation	24
Plate 6.	Montgomery Point Gate System. Idealized control volume	25
Plate 7.	Montgomery Point Rigid Gate Model. Sliding the resultant of forces exerted by the gate skin on the fluid	26
Plate 8.	Montgomery Point Gate Model. Shaded area A_s subtended by the gate arc AB	27
Plate 9.	Montgomery Point Gate Model. Free-body diagram of gate	28
Plate 10.	Montgomery Point Gate Model. Free-body diagram of gate differential element	29
Plate 11.	Montgomery Point Gate Model. Comparison of theoretical prediction of hydraulic pressure field with its experimental counterpart (T1080)	30
Plate 12.	Montgomery Point Gate Model. Reference longitudinal arcs on the skin of the physical-model gate	31
Plate 13.	Montgomery Point Rigid Gate Model. Plan view of physical model and location of load cells at blocks 2, 4 and 6 (three supports)	45
Plate 14.	Montgomery Point Rigid Gate Model. Typical load cell and corresponding bridge wiring	46
Plate 15.	Montgomery Point Rigid Gate Model. Accelerometer locations	47
Plate 16.	Montgomery Point Rigid Gate Model. Pressure cell locations on the upstream side of gate	48
Plate 17.	Montgomery Point Rigid Gate Model. Pressure cell locations on the downstream side of gate	49

Plate 18.	Montgomery Point Rigid Gate Model. Curvilinear coordinate (s) along the reference longitudinal arcs (right edge, middle arc, and left edge) on the upstream side of gate	50
Plate 19.	Montgomery Point Rigid Gate Model. Comparison of recommended design pressure field with the theoretical prediction and its 100-s test experimental counterpart	51
Plate 20.	Montgomery Point Rigid Gate Model. Comparison of recommended design pressure field with the maximum net pressure field on the gate in 200-s experiments T1108 (integral nappe) and T1109 (ventilated nappe)	52
Plate 21.	Montgomery Point Rigid Gate 1/15-Scale Model. Isometric view of the upstream side of the finite element grid	53
Plate 22.	Montgomery Point Rigid Gate 1/15-Scale Model. Isometric view of the downstream side of the finite element grid	54
Plate 23.	Montgomery Point Rigid Gate 1/15-Scale Model. Lateral view of the deflected configuration of the finite element model subjected to the recommended design pressure field	55
Plate 24.	Montgomery Point Prototype Gate. Plan view of gate and location of recommended five supports	56
Plate 25.	Montgomery Point Prototype Gate. Envelopes for horizontal (HE) and vertical (VE) components of the resultant reaction at supports 1 and 2 as a function of the gate elevation (X)	57
Plate 26.	Montgomery Point Prototype Gate. Envelopes for horizontal (HC) and vertical (VC) components of the resultant reaction at the central support 3 as a function of the gate elevation (X)	58
Plate 27.	Montgomery Point Prototype Gate. Envelopes for horizontal (HE) and vertical (VE) components of the resultant reaction at supports 4 and 5 as a function of the gate elevation (X)	59
Plate 28.	Montgomery Point Prototype Gate. Envelope for the total hydraulic moment (M) as a function of the gate elevation (X)	60
Plate 29.	Montgomery Point Prototype Gate. Isometric view of upstream side of finite element grid	61

Plate 30.	Montgomery Point Prototype Gate. Iso-principal-stress (tensile) regions on the upstream face of the gate	63
Plate 31.	Montgomery Point Prototype Gate. Iso-principal-stress (compressive) regions on the elements of the downstream face of the gate	65
Plate 32.	Probability density function for the peaks of the non-dimensional random field η ($\eta = \xi/m_0^{1/2}$), for different values of the parameter ϵ	75
Plate 33.	Spectral density for the pressure at cell 4 on the upstream face of the gate model during test T1080	76
Plate 34.	Spectral density for the pressure at cell 4 on the downstream face of the gate model during test T1080	77
Plate 35.	Spectral density for the net pressure on the upstream face of the gate model at the location of cell 4 during test T1080	78
Plate 36.	Probabilistic description of the extreme value of the net pressure on the upstream face of the gate model at the location of cell #1 during test T1108 [in. of H_2O]. (a) Probability density function (Gumbel Type I, of the largest values), and (b) the corresponding probability distribution function	79
Plate 37.	Extreme pressure field as predicted by test T1080 on the three reference longitudinal arcs on the gate skin, i.e., the right edge, the middle arc, and the left edge. Level 1: 68% confidence bound; level 2: 96% confidence bound; and level 3: 99.7% confidence bound	80
Plate 38.	Extreme pressure field as predicted by test T1108 on the three reference longitudinal arcs on the gate skin, i.e., the right edge, the middle arc, and the left edge. Level 1: 68% confidence bound; level 2: 96% confidence bound; and level 3: 99.7% confidence bound	81
Plate 39.	Montgomery Point Prototype Gate. Design pressure line as per tests T1179 and T1180	82
Plate 40.	Montgomery Point Prototype Gate. Design pressure line as per test T1192. Pressure envelope for middle arc	83
Plate 41.	Montgomery Point Prototype Gate. Pressure envelope for left edge. Pressure envelope for right edge	84
Plate 42.	Finite element eigensolution for 1/15-scale model. Relevant mode of vibration 1	87

Plate 43.	Finite element eigensolution for 1/15-scale model. Relevant mode of vibration 2	88
Plate 44.	Finite element eigensolution for 1/15-scale model. Relevant mode of vibration 3	89
Plate 45.	Finite element eigensolution for 1/15-scale model. Relevant mode of vibration 4	90
Plate 46.	Finite element eigensolution for 1/15-scale model. Relevant mode of vibration 5	91
Plate 47.	Finite element eigensolution for 1/15-scale model. Relevant mode of vibration 6	92
Plate 48.	Finite element eigensolution for 1/15-scale model. Relevant mode of vibration 7	93
Plate 49.	Finite element eigensolution for 1/15-scale model. Relevant mode of vibration 8	94
Plate 50.	Finite element eigensolution for 1/15-scale model. Relevant mode of vibration 9	95
Plate 51.	Finite element eigensolution for 1/15-scale model. Relevant mode of vibration 10	96
Plate 52.	Finite element eigensolution for prototype. Relevant mode of vibration 1	97
Plate 53.	Finite element eigensolution for prototype. Relevant mode of vibration 2	98
Plate 54.	Finite element eigensolution for prototype. Relevant mode of vibration 3	99
Plate 55.	Finite element eigensolution for prototype. Relevant mode of vibration 3	100
Plate 56.	Finite element eigensolution for prototype. Relevant mode of vibration 4	101
Plate 57.	Finite element eigensolution for prototype. Relevant mode of vibration 5	102
Plate 58.	Finite element eigensolution for prototype. Relevant mode of vibration 6	103
Plate 59.	Finite element eigensolution for prototype. Relevant mode of vibration 7	104
Plate 60.	Dry Twang test T0137. Free-vibration decay of bending moment at the root of right operating arm	105
Plate 61.	Spectral density function for the time-history of response in Plate 60	106

Plate 62.	Scanning Laser Vibrometry System. (a) Test setup, and (b) Laser position	107
Plate 63.	Scanning Laser Vibrometry System. Frequency-response function for selected nodes on the gate skin	108
Plate 64.	Scanning Laser Vibrometry System. Node definition on the gate skin	109
Plate 65.	Scanning Laser Vibrometry System. Frequency-response function for the velocity of nodes 19 and 21 on the gate skin	110
Plate 66.	Scanning Laser Vibrometry System. Mode-shape 1	111
Plate 67.	Scanning Laser Vibrometry System. Mode-shape 2	112
Plate 68.	Scanning Laser Vibrometry System. Mode-shape 5	113
Plate 69.	Scanning Laser Vibrometry System. Frequency-response function for the acceleration of nodes 9 and 10 on the gate skin when all three gates are raised	114
Plate 70.	Scanning Laser Vibrometry System. Frequency-response function for the acceleration of nodes 3 and 4 on the gate skin when one lateral gate is down and the other two are raised	115
Plate 71.	Scanning Laser Vibrometry System. Frequency-response function for the acceleration of nodes 4 and 6 on the gate skin when both lateral gates are down and the instrumented (central) gate is raised	116
Plate 72.	Scanning Laser Vibrometry System. Comparison between the frequency-response functions for the acceleration of nodes 1 and 2 on the gate skin with and without a leaning trash rack	117
Plate 73.	Free vibration of gate with upstream side submerged in water. Transverse time-history of response for triaxial accelerometer 1 (Twang test T0139)	118
Plate 74.	Free vibration of gate with upstream side submerged in water. Spectral density for transverse time-history of response for triaxial accelerometer 1 (Twang test T0139)	119
Plate 75.	Free vibration of gate with upstream side submerged in water. Transverse time-history of response for triaxial accelerometer 6 (Twang test T0139)	120
Plate 76.	Free vibration of gate with upstream side submerged in water. Spectral density for transverse time-history of response for triaxial accelerometer 6 (Twang test T0139)	121

Plate 77.	Free vibration of gate with upstream side submerged in water. Time-history of response for uniaxial accelerometer 4 (Twang test T0139)	122
Plate 78.	Free vibration of gate with upstream side submerged in water. Spectral density for time-history of response for uniaxial accelerometer 4 (Twang test T0139)	123
Plate 79.	Lateral view of gate components, properties, and external forces	135
Plate 80.	Analytical model. Gate components idealized as lines	136
Plate 81.	Mathematical model. Structural coordinates and single degree of freedom Δ	137
Plate 82.	Dynamic equilibrium of 1-DOF rigid-body gate system. Virtual displacement	138
Plate 83.	Identification of equivalent viscous damping ratio for dry gate. Logarithmic decrement	139
Plate 84.	Identification of equivalent viscous damping ratio of gate with upstream side submerged in water	140
Plate 85.	Rigid-body torque-tube system in horizontal position	141
Plate 86.	Finite element eigensolution for fundamental mode of vibration of the rigid-body torque-tube system.	142
Plate 87.	Spectral density of moment at root of operating arms	143
Plate A1.	Pressure cells in spectral analysis of tests T1080 and T1085	A3
Plate A2.	Spectral densities for the records of pressure cell 4 in tests T1080 and T1085	A4
Plate A3.	Spectral densities for the records of pressure cell 5 in tests T1080 and T1085	A5
Plate A4.	Spectral densities for the records of pressure cell 6 in tests T1080 and T1085	A6
Plate A5.	Spectral densities for the records of pressure cell 7 in tests T1080 and T1085	A7
Plate A6.	Spectral densities for the records of pressure cell 8 in tests T1080 and T1085	A8
Plate A7.	Spectral densities for the records of pressure cell 9 in tests T1080 and T1085	A9
Plate A8.	Pressure cells in spectral analysis of tests T1086 and T1087	A10

Plate A9.	Spectral densities for the records of pressure cell 4 in tests T1086 and T1087	A11
Plate A10.	Spectral densities for the records of pressure cell 5 in tests T1086 and T1087	A12
Plate A11.	Spectral densities for the records of pressure cell 6 in tests T1086 and T1087	A13
Plate A12.	Spectral densities for the records of pressure cell 7 in tests T1086 and T1087	A14
Plate A13.	Spectral densities for the records of pressure cell 8 in tests T1086 and T1087	A15
Plate A14.	Spectral densities for the records of pressure cell 9 in tests T1086 and T1087	A16
Plate A15.	Pressure cells in spectral analysis of tests T1108 and T1109	A17
Plate A16.	Spectral densities for the records of pressure cell 5 in tests T1108 and T1109	A18
Plate A17.	Spectral densities for the records of pressure cell 7 in tests T1108 and T1109	A19
Plate A18.	Spectral densities for the records of pressure cell 4 in tests T1108 and T1109	A20
Plate A19.	Spectral densities for the records of pressure cell 1 in tests T1108 and T1109	A21
Plate A20.	Pressure cells in coherence analysis of test T1080	A22
Plate A21.	Coherence between upstream pressure-cell records in test T1080	A23
Plate A22.	Coherence between downstream pressure-cell records in test T1080	A24
Plate A23.	Coherence between net pressure-cell records in test T1080	A25

List of Programs

Program 1.	Theoretical Estimate of Pressure Field	32
Program 2.	Location of Resultant Hydraulic Load	37

Preface

This structural model investigation on the Montgomery Point torque-tube gates was authorized by Headquarters, U.S. Army Corps of Engineers (HQUSACE), on 15 October 1993 at the joint request of the U.S. Army Engineer Division, Southwestern (USACE-SWD), and the U.S. Army Engineer District, Little Rock (USACE-SWL). The studies were conducted by personnel of the Hydraulics (HL) and Structures Laboratories (SL), U.S. Army Engineer Waterways Experiment Station (WES) during the period November 1993 to February 1995 under the direction of Mr. F. A. Herrmann, Jr., Director, HL; Mr. B. Mather, Director, SL; Mr. R. A. Sager, Assistant Director, HL; Mr. John Ehrgott, Assistant Director, SL; and under the general supervision of Mr. G. A. Pickering, Chief, Hydraulics Structures Division (HSD), HL; Dr. J. P. Balsara, Chief, Geomechanics and Explosion Effects Division (GEED), SL; Dr. R. Mosher, Chief, Structural Mechanics Division (SMD), SL; Mr. N. R. Oswalt, Chief, Spillways and Channels Branch, HSD; and Dr. R. L. Hall, Chief, Structural Analysis Group, SS-A, SL. Project Engineers for the model studies were Mr. B. P. Fletcher, HSD, and Dr. L. A. de Bejar, SS-A. Mrs. S. Garner, SMD, assisted with the finite element analysis of the gate. Instrumentation support was provided by Messrs. H. C. Greer III, T. W. Warren, J. C. Ables, and W. Guy, Instrumentation Services Division, Information Technology Laboratory. This second report of the investigation was written by Dr. de Bejar.

During the structural investigation, Messrs. L. Winters and T. Papageorge (USACE-SWL-ED-DS) and Mr. R. Veselka (USACE-SWD-ED-TS) visited WES to discuss the structural models and provide valuable suggestions.

At the time of publication of this report, Director of WES was Dr. Robert W. Whalin. Commander was COL Bruce K. Howard, EN.

The contents of this report are not to be used for advertising, publication, or promotional purposes. Citation of trade names does not constitute an official endorsement or approval of the use of such commercial products.

Conversion Factors, Non-SI to SI Units of Measurement

Non-SI units of measurement used in this report can be converted to SI units as follows:

Multiply	By	To Obtain
cubic feet per second	0.02831685	cubic metres
degrees (angle)	0.01745329	radians
feet	0.3048	metres
inches	25.4	millimetres
kips	4.448222	kilonewtons
kips per foot	1,355.818	newton-metres
kips per square foot	47.88026	kilopascals
kips per square inch	6.894757	megapascals
pounds	4.448222	newtons
pounds per cubic foot	16.01846	kilogram-force per cubic metre
pounds per foot	14.5939	newtons per metre
pounds per square foot	47.88026	pascals
pounds per square inch	0.006894757	megapascals
slugs	14.5939	kilogram-mass

1 Introduction

Montgomery Point Lock and Dam will be constructed near the mouth of the White River Entrance Channel, which is the passageway from the Mississippi River to the McClellan-Kerr Arkansas River Navigation System. The flow through the navigable pass spillway will be controlled by a parallel array of 10 torque-tube gates. Due to complex hydraulic loading, the gates are subjected to stressing steady-state flow and random vibrations.

This is the second of a two-part report on a research project to assist the engineer in designing the torque-tube gates. The objective of the first report is to provide the designer with experimentally based information on the structural response of the gate system in operation. This second report describes several mathematical models to represent the effect of the hydraulic pressure field on the structure of a typical Montgomery Point torque-tube gate and its experimental verification from tests on a corresponding 1/15-scale physical model at the U.S. Army Engineer Waterways Experiment Station (WES).

Purpose and Scope of the Research Project on the Structure

The research project on the structure satisfies multiple purposes:

- a.* Construct and instrument a rigid 1/15-scale physical model of the gate to experimentally determine (1) reaction forces for prototype design of the support bearings, and (2) time-histories of hydraulic pressure at selected discrete locations on both sides of the gate skin.
- b.* Determine a design representation of the net hydrodynamic pressure field acting on the gate under (1) regular operating conditions, and (2) extreme conditions of discharge and pool elevations, and unusual operation, or both. These semiempirical representations of the pressure field on the gate are based on sound theoretical principles and adjusted to fit the results from numerous automatically controlled tests.

- c. Construct an analytical model of the gate for the finite element analysis of the structure subjected to the design hydraulic pressure field. This analysis renders design reaction forces at the support bearings to be compared with the experimental measurements.
- d. Determine the gate natural frequencies, mode shapes, and parameters of energy-dissipation mechanisms using (1) finite element analyses, and (2) nondestructive experimental techniques. Knowledge of the gate eigenproperties is necessary for effective assessments of structural safety during the useful life of the gate.
- e. Develop a simple structural model for engineering analysis of the dynamic response of the gate under hydraulic flow. A random-vibration model for the stochastic description of the fluctuations of both the hydraulic pressure field and selected parameters of structural response about the respective steady-state mean components follows a simple deterministic representation of the gate system subjected to the hydraulic forces.
- f. Evaluate, by spectral analysis, the safety of a typical torque-tube gate in service against fatigue from flow-induced vibrations over its design life.

Organization of Report 2

Chapters in this report are organized in a prerequisite-development sequence. Thus, the first step is to develop an analytical representation for the hydraulic forces on the gate. In Chapter 2, the steady-state mean pressure field is derived from a semiempirical application of the theorem of moment-of-momentum in fluid dynamics. This theoretical prediction tells the analyst what to expect as input during the tests (Photos 1 through 3 exhibit the series of three gates in the experimental flume at WES) and suggests the general trend for a proposed design pressure envelope from the results of Phase 1 of the experimental program, which involves the regular operating conditions of the gate.

The experimentation follows together with finite element analyses. The results of these experimental analyses (Chapter 3 and the second part of Chapter 4) support the final design of the gate system. Chapter 3 describes the details of the experimental setup and the results of finite element analyses for both the physical model (a brass structure standing on three supports) and the prototype gate system (made of structural steel standing on five supports). Reaction forces for prototype design of the support bearings are obtained through finite element analysis of the prototype subjected to the scaled design pressure field on the physical model. The reaction forces from the finite element analysis provide the input for the final design of bearings.

In Chapter 4, two separate models use the experimental data from Phase 1 of the experimental program to estimate extreme-value wide-band hydrodynamic pressure fluctuations during the useful life of the gates, with excellent agreement between the two results. The chapter ends with a description of Phase 2 of the experimental project, which generally considers very large hydraulic pressure fields on the gate due to extreme conditions of discharge and pool elevations, and unusual operation, or both.

In Chapter 5, natural frequencies and mode shapes obtained from different experimental techniques (Twang tests, forced-vibration tests, and Laser vibrometer tests) applied to the data are successfully compared with the corresponding analytical results from finite element analyses on the grid for the small-scale physical model. Knowledge of these eigenproperties is necessary for effective assessments of structural safety during the useful life of the gate.

Chapter 6 discusses the approximate evaluation of the natural frequency of free vibration of the gate and the identification of the equivalent viscous damping ratio for the physical model (both dry and upstream submerged). Two ramifications of an engineering model for the dynamic response of the torque-tube gate system are presented. The first section describes the structural dynamics model from an entirely deterministic point of view. The governing equation of motion for the gate system is formulated and solutions are derived for the mean of selected parameters of response. The second section describes a random vibration model for the stochastic description of the fluctuations of both the hydraulic pressure field and selected parameters of structural response about their steady-state mean components.

The results of the simulations presented in Chapters 4 through 6 suggest further investigations on extreme-value prediction, gate parameter identification, and practical engineering estimates of structural response.

Chapter 7 outlines the conclusions of the study and formulates recommendations for design.

The report ends with an elemental spectral analysis to assess the fatigue performance of the gate system in service over the long run. A set of selected power spectral density functions for pressure-cell records in the controlling experiments illustrate some of the salient points in the discussion.

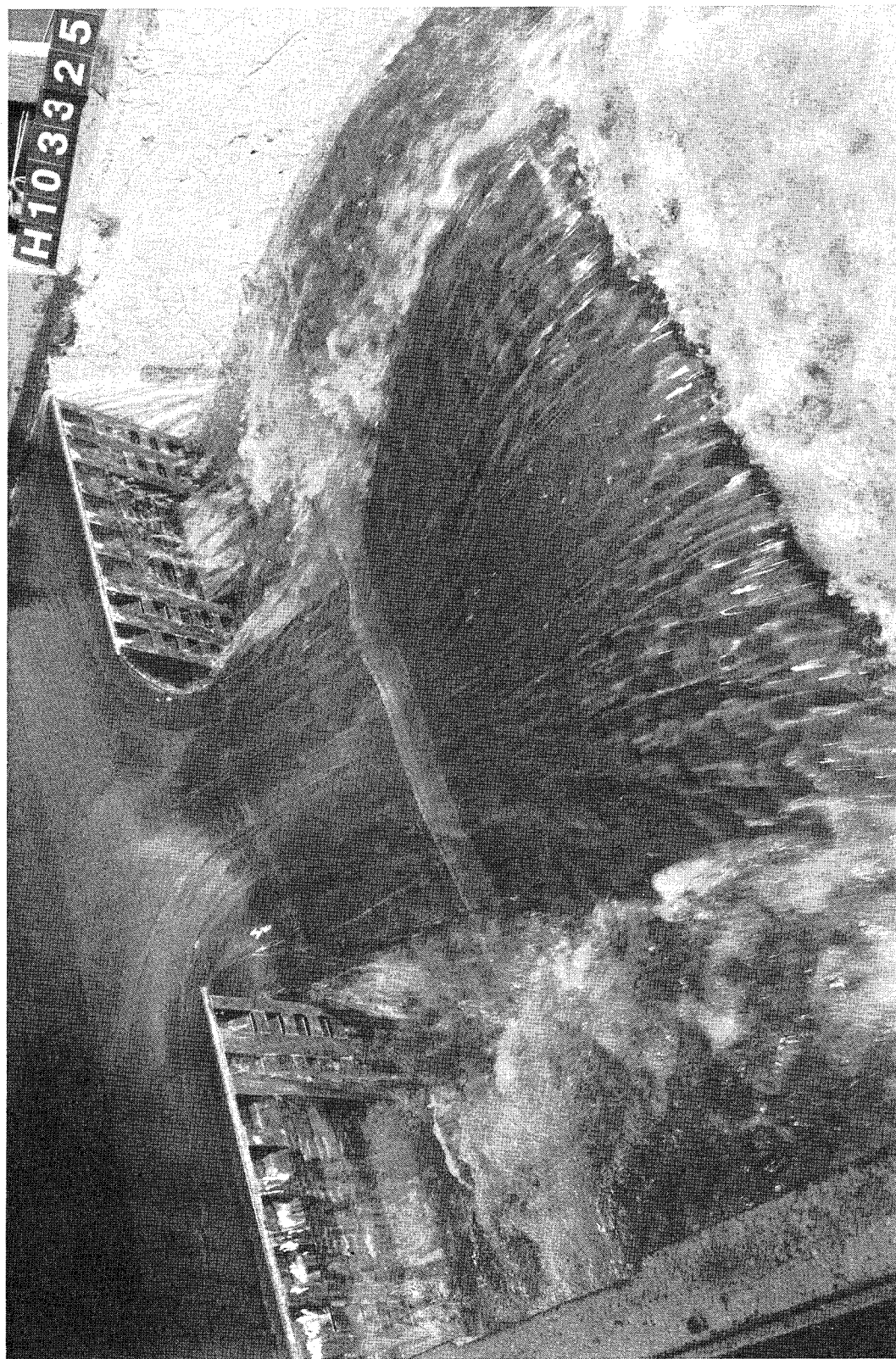


Photo 1. Montgomery Point Torque-Tube Gate Model. Aperture in experimental flume corresponding to central (instrumented) gate in fully open position



Photo 2. . . Montgomery Point Torque-Tube Gate Model. Central (instrumented) gate in fully closed position. Lateral gates in experimental flume in fully open position

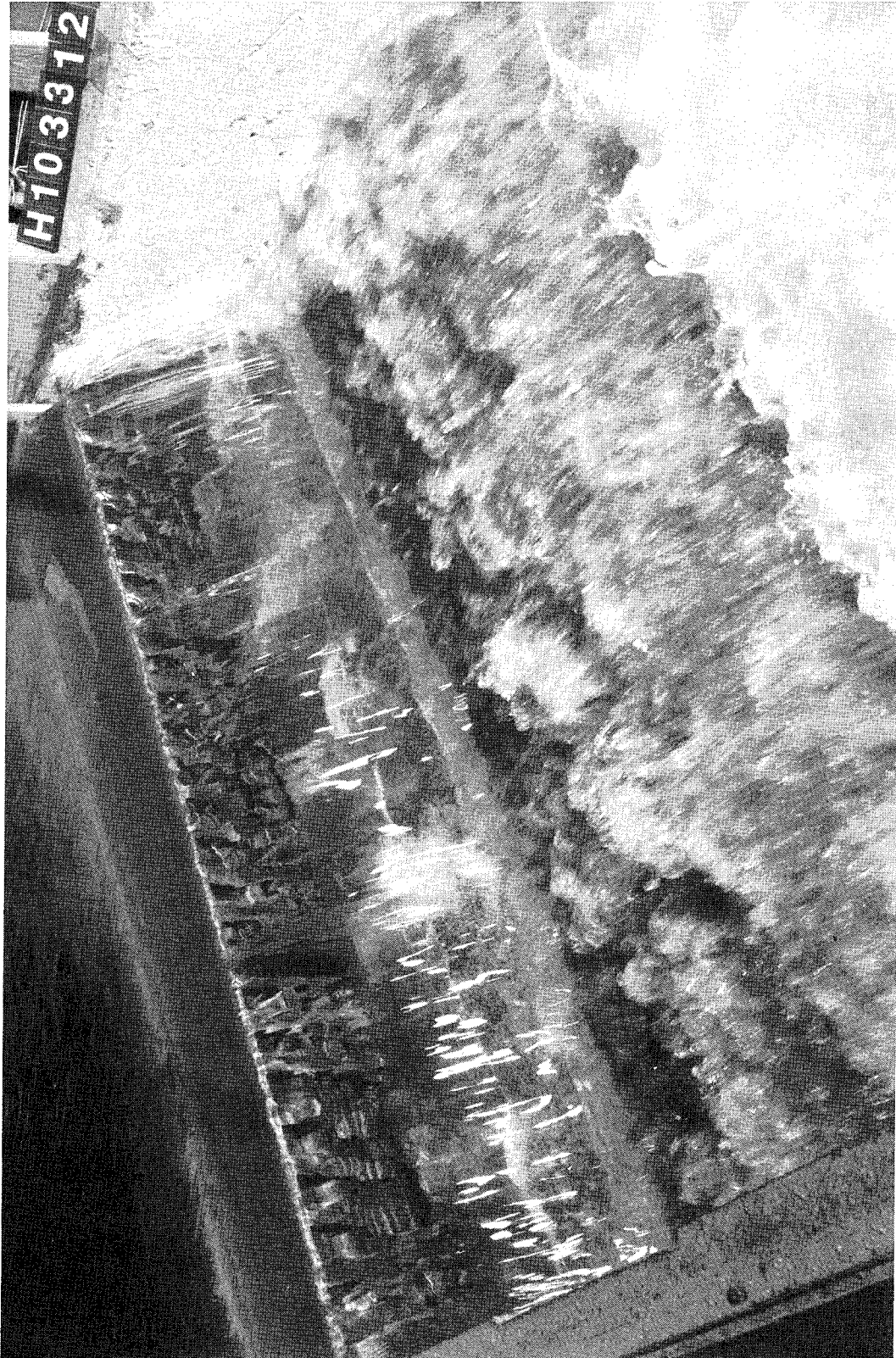


Photo 3. Montgomery Point Torque-Tube Gate Model. Design controlling condition: the three gates in the experiment flume in fully closed position

2 Mathematical Model for Hydraulic Pressure Field

The study begins by introducing a semiempirical model for the hydraulic pressure field on the gate. The objective of this representation is to predict the hydraulic forces on the gate in service. The model will allow expedient estimation of forces on the prototype, for engineering purposes, as well as on other small-scale torque-tube gates in future experimental projects.

Water is assumed an incompressible, inviscid, and homogeneous fluid; and its flow is taken as irrotational. The critical hydraulic effect on the structural model is considered to occur when the upstream flow at the maximum operational headwater pool runs over the torque-tube gate in a fully raised position. This critical condition is simplified in the model by neglecting the effect of the tailwater pressure.

This idealization leans on experimental evidence. During the experiments with the physical model at WES, the maximum reaction response for regular operation was obtained when a unit discharge of water of 50 cfs runs over the system of fully raised gates (70-deg elevation (el)) with the tailwater pool maintained at 95 ft (prototype level) and the headwater pool growing monotonically from about 114 to 119 ft (prototype level).

Plate 1 shows a lateral view of the physical model of the gate in closed position (70-deg el) with a ventilated nappe and prototype-equivalent 95-ft tailwater pool (the model described in this section will be developed in the context of prototype dimensions). The thickness of the nappe root (water depth over the gate ridge) is carefully measured to scale in this picture as $h_f = 2.9$ ft. Similarly, the nappe thickness at the level of the midheight of the approaching flow is (approximately) determined experimentally as $d' = 1.6$ ft.

Plate 2 shows a plan view of the geotechnical borings at the site (U.S. Army Engineer District, Little Rock (USACE-SWL) 1993). The corresponding survey determines the natural elevation of the White River bed at selected locations on the upstream side of the projected navigational pass. Standard Penetration Test boring station No. 83 at 200 ft from the gates is particularly noticed at a level of 88.1 ft in Plate 3. This location is also

schematically located in Plate 4 exhibiting a longitudinal cross section of the prototype system.

Assuming a parabolic upper surface for the nappe, its equation is easily determined from the condition of fitting the thickness of the nappe root, i.e., $h = h_f$ at the location of the gate ridge. The following simple expression is obtained:

$$y = \left(\frac{x}{15.03} \right)^2, \quad (1)$$

where both x and y are in feet.

Using this expression and the geometry of the circle with center at C in Plate 4, the following equation for the general water depth over the gate is derived:

$$h = H - a \sin \theta - 2.346 (1 - 1.0643 \cos \theta)^2, \quad (2)$$

where

$H = 27.4$ ft is the level difference between points O and C

$a = 24.5$ ft is the radius of the circle

$\theta \in (20 \text{ deg}, 72.75 \text{ deg})$ = elevation of a general point K on the gate skin

Recognizing that the streamlines going through the sections at G and G' of the control volume between them in Plate 4 are locally approximately parallel to each other and that the gauge pressure at G' is practically zero, the following Bernoulli equation is formulated for streamline GG' (Prandtl and Tietjens 1957a,b, Shames 1962):

$$\frac{v_G^2}{2g} + \frac{p_G}{\gamma} = \frac{v_{G'}^2}{2g}, \quad (3)$$

where

p_G = gauge pressure at point G

v_G and $v_{G'}$ = assumed uniform flow velocities at points G and G' , respectively

γ = unit weight of water

g = acceleration of gravity

Invoking the principle of continuity between the cross sections at G and G' (Prandtl and Tietjens 1957a,b, Shames 1962), one may solve for the velocity v_G to get

$$v_G = \sqrt{\frac{gd}{\left(\frac{d'}{d}\right)^2 - 1}} \quad , \quad (4a)$$

or, evaluating this expression (using $d = 30.9$ ft, the depth of the approaching flow),

$$v_G = 1.64 \text{ fps} \quad . \quad (4b)$$

This value of the approaching flow velocity compares very well with the value obtained from the design approaching unit flow $q_1 = 50$ cfs, i.e.,

$$v_G = \frac{q_1}{d} = 1.62 \text{ fps} \quad . \quad (4c)$$

The average value $v_G = 1.63$ fps will be used in the development of the model.

Notice that although streamlines at cross section OA at the base of the gate are not strictly parallel to each other, the Bernoulli equation for line GG^{iv} provides an approximate estimate for the total pressure head at G^{iv} (Olson 1961, Vennard and Street 1975), giving

$$\frac{p_{G^{iv}}}{\gamma} = 9.43 \text{ ft} \quad ,$$

which is close to the hydrostatic pressure head at the same location (9.5 ft).

Likewise, since the streamlines are practically parallel to each other at cross sections G' and G'' , respectively, i.e., at the ends of the nappe portion being considered, the Bernoulli equation for line $G'G''$ provides an accurate estimate for the hydrodynamic pressure head at G'' , giving

$$\frac{\bar{p}_{G''}}{\gamma} = -3.573 \text{ ft} .$$

If the total pressure head at a point is envisioned as the summation of hydrostatic and hydrodynamic components (Prandtl and Tietjens 1957a,b), i.e.,

$$\frac{p}{\gamma} = \frac{\bar{p}}{\gamma} + \frac{\tilde{p}}{\gamma} ,$$

and the hydrodynamic pressure head is assumed to vary linearly from G^{iv} to G'' , i.e.,

$$\text{from } \frac{\tilde{p}_{G^{iv}}}{\gamma} = -0.07 \text{ ft to } \frac{\tilde{p}_{G''}}{\gamma} = -3.573 \text{ ft} ,$$

recognizing that the hydrostatic component at a general point G''' is one-half of the corresponding water depth, the following expression for the total pressure head at G''' is obtained, as a function of the point elevation (Plate 5):

$$\frac{p(\theta)}{\gamma} = 14.95816 - 12.25 \sin \theta - 1.173 (1 - 1.0643 \cos \theta)^2 - 0.066408 \theta . \quad (5)$$

Therefore, the general energy-balance equation for line GG''' in Plate 4 provides an approximate means to determine the water depth, h , at any point G''' out directly over the gate AB, i.e.,

$$H - a \sin \theta + \frac{v_G^2}{2g} \left[1 - \left(\frac{d}{h} \right)^2 \right] - \frac{h}{2} - \frac{p(\theta)}{\gamma} = 0 \quad (6)$$

where $p(\theta)$ is given by Equation 5.

Simultaneous solution of Equations 5 and 6 allows the numerical evaluation of h , resulting in a negligible variation from the parabolic profile originally assumed.

Consider now the idealized unit-thickness control volume $D'DA^{iv}ABB'$ $A''A'''D'$ in Plate 6 and its natural partition into two components by the vertical plane $A'''A^{iv}$. The approaching flow may be assumed to enter and exit the volume with uniform velocities U and u , respectively. The forces acting on the boundary surface are schematically represented in the diagram. The weights of water in the various parts of the control volume are designated by

$W_i, i = 1, 2, 3$. The vertical and horizontal components of the hydraulic force exerted by the flow on the gate are designated by R_1 and R_2 , respectively. The plate shows the components of the corresponding reactive force, i.e., the force exerted by the gate on the fluid, after sliding along its line of action from the point of application Q' to point Q on the gate skin surface (Plate 7). These forces have lever arms r_1 and r_2 with respect to the pivoting point A , respectively.

Assuming that the flow through AA'' is approximately horizontal, the vertical equilibrium of control volume $ABB'A''A$ may be expressed as (Prandtl and Tietjens 1957a,b, Shames 1962)

$$R_1 - W_2 - W_3 = 0 \quad (7)$$

In the absence of horizontal body forces, the equation of conservation of linear momentum applied to the whole control volume in Plate 6 may be expressed as

$$P_1 - P_2 - R_2 = -U^2 \rho A_D + u^2 \rho A_B \quad (8)$$

where P_1 and P_2 represent the resultant forces of pressures acting on sides DD' and AA'' of the control volume, respectively; A_D and A_B are the cross-sectional areas of the control volume at locations D and B , respectively; U and u are the corresponding flow velocities, assumed to have a direction approximately normal to the respective cross-sectional areas; and ρ is the mass density of water.

The theorem of moment-of-momentum about point A , applied to the whole control volume, produces the following equation:

$$\begin{aligned} P_1 \left(\frac{H}{3} - a \sin \theta_0 \right) + W_2 \frac{a}{2} (\cos \theta_0 - \cos \theta_f) + W_3 x_3 + P_2 y_2 \\ - R_1 r_1 - R_2 r_2 = - \left(\frac{H}{2} - a \sin \theta_0 \right) U^2 \rho A_D \quad (9) \\ + \left[a (\sin \theta_f - \sin \theta_0) + \frac{h_f}{2} \right] u^2 \rho A_B, \end{aligned}$$

where

H and h_f = water depths at sides DD' and BB' of the same control volume, respectively

θ_0 and θ_f = elevation angles of points A and B, which are the respective ends of the circular gate AB in closed position (70-deg elevation with respect to the horizontal plane)

a = circle radius (Plate 4).

Since point Q is on the circle, the following relationship is satisfied:

$$(a \cos \theta_0 - r_1)^2 + (a \sin \theta_0 + r_2)^2 = a^2 \quad (10)$$

Next consider the generating radius vector with center at C, magnitude a , and argument θ shown in Plate 8. The shaded area A_s is given by

$$\begin{aligned} A_s &= \int_{a \cos \theta_f}^{a \cos \theta_0} \int_{\sqrt{a^2 - x^2}}^{a \sin \theta_f} dy dx \\ &= a^2 \left[\sin \theta_f (\cos \theta_0 - \cos \theta_f) + \frac{1}{4} (\sin 2\theta_f - \sin 2\theta_0) - \left(\frac{\theta_f - \theta_0}{2} \right) \right] \end{aligned} \quad (11a)$$

and its centroidal point has abscissa

$$\begin{aligned} \bar{x} &= \frac{1}{A_s} \int_{a \cos \theta_f}^{a \cos \theta_0} \int_{\sqrt{a^2 - x^2}}^{a \sin \theta_f} x dx dy \\ &= \frac{1}{2A_s} \left[\frac{a^3}{3} (\sin^3 \theta_f - \sin^3 \theta_0) - a^3 \sin^2 \theta_0 (\sin \theta_f - \sin \theta_0) \right] \end{aligned} \quad (11b)$$

Therefore, the weight W_3 is obtained from

$$W_3 = \gamma A_s \quad (11c)$$

where

$\gamma = \rho g$ is the unit weight of water,

and the location of its line of action can be calculated from

$$x_3 = a \cos \theta_0 - \bar{x} \quad (11d)$$

On the other hand, the resultant forces P_i , $i = 1, 2$, can be estimated by the expressions (Prandtl and Tietjens 1957a,b)

$$P_1 = \frac{\gamma H^2}{2} \quad (12a)$$

and

$$P_2 = \frac{\gamma H^2}{2} \left[1 - \left(1 - \frac{a}{H} \sin \theta_0 \right)^2 \right], \quad (12b)$$

corresponding to the hydrostatic pressure distributions on DD' and AA^{iv}, respectively.

Evaluating for the prototype gate dimensions, $a = 24.5$ ft and $H = 27.4$ ft, with $\theta_0 = 20$ deg, $\theta_f = 72.75$ deg and $\gamma = 62.4$ pcf, Equations 11a and 11c render

$$A_s = 80.91 \text{ ft}^2 \quad (13a)$$

and

$$W_3 = 5.049 \text{ k}, \quad (13b)$$

respectively; whereas Equations 11b and 11d render

$$\bar{x} = 18.66 \text{ ft} \quad (13c)$$

and

$$x_3 = 4.36 \text{ ft}, \quad (13d)$$

respectively.

Likewise, Equations 12a and 12b yield

$$P_1 = 23.424 \text{ k} \quad (14a)$$

and

$$P_2 = 12.136 \text{ k} , \quad (14b)$$

respectively.

Now the reactive force R_1 may be computed from Equation 7 as

$$\begin{aligned} R_1 &= W_2 + W_3 \\ &= \gamma ah(\cos\theta_0 - \cos\theta_f) + W_3 \\ &= 2.852 \text{ k} + 5.049 \text{ k} = 7.901 \text{ k} . \end{aligned} \quad (15)$$

The experimental water depth at the root of the nappe was previously obtained as

$$h_f = 2.9 \text{ ft} , \quad (16)$$

and the flow velocities U and u may be estimated from direct application of the equation of continuity, i.e.,

$$\begin{aligned} U &= v_G \left(\frac{H}{d} \right) \\ &= 1.63 \text{ fps} \left(\frac{30.9}{27.4} \right) = 1.84 \text{ fps} \end{aligned} \quad (17a)$$

and

$$\begin{aligned} u &= U \left(\frac{H}{h_f} \right) \\ &= 1.84 \text{ fps} \left(\frac{27.4}{2.9} \right) = 17.39 \text{ fps} \end{aligned} \quad (17b)$$

Putting Equations 14a, 14b, 16, 17a, and 17b into Equation 8, the reactive force R_2 may also be computed as

$$\begin{aligned}
 R_2 &= (P_1 - P_2) + \frac{\gamma}{g} (U^2 H - u^2 h_f) \\
 &= 9.768 k
 \end{aligned}
 \tag{18}$$

Plate 9 shows the free-body diagram of the idealized gate subjected to the hydraulic forces R_1 and R_2 (per unit width of gate) and the corresponding internal reactions at the base of the cantilever, where N_0 , V_0 , and M_0 represent the axial load, shear force, and bending moment per unit width of gate. The equilibrium formulation leads to the following force transformation (Boresi and Sidebottom 1985, Przemieniecki 1985):

$$\begin{Bmatrix} N_0 \\ V_0 \end{Bmatrix} = \begin{bmatrix} \cos\theta_0 & \sin\theta_0 \\ -\sin\theta_0 & \cos\theta_0 \end{bmatrix} \begin{Bmatrix} -R_1 \\ R_2 \end{Bmatrix}
 \tag{19a}$$

Equation 19a allows the direct evaluation of the shear force:

$$\begin{aligned}
 V_0 &= R_1 \sin\theta_0 + R_2 \cos\theta_0 \\
 &= 11.881 k
 \end{aligned}
 \tag{19b}$$

The result in Equation 19b provides one of the boundary conditions for the boundary-value problem to be formulated next. The other boundary condition is given by the fact that the curved cantilever has a free end at B, i.e.,

$$\begin{aligned}
 V(\theta_0) &= V_0 = 11.881 k \\
 V(\theta_f) &= 0
 \end{aligned}
 \tag{20}$$

Now, if the analysis leading to Equations 15 and 18 for the hydraulic forces is generalized for an end elevation θ , instead of θ_f (Plate 4), the following expressions are obtained

$$\begin{aligned}
 R_1(\theta) &= \gamma \left\{ ah(\cos\theta_0 - \cos\theta) + a^2 \left[\cos\theta_0(\sin\theta - \sin\theta_0) \right. \right. \\
 &\quad \left. \left. - \frac{1}{4}(\sin 2\theta - \sin 2\theta_0) - \frac{1}{2}(\theta - \theta_0) \right] \right\}
 \end{aligned}
 \tag{21a}$$

$$R_2(\theta) = \frac{\gamma H^2}{2} \left[\left(1 - \frac{a}{H} \sin \theta_0 \right)^2 - 2 \frac{U^2}{g} \left(\frac{1}{h} - \frac{1}{H} \right) \right], \quad (21b)$$

where

h = water depth of the nappe root at the crest of the generalized cantilever AK.

After some algebraic manipulations, the first two derivatives of each of these expressions may be obtained as

$$\frac{dR_1}{d\theta} = \gamma a^2 \cos \theta \left[\left(\frac{h}{a} \right) \tan \theta + \frac{\eta^2 (\cos \theta_0 - \cos \theta)}{\eta^2 - 1} \right] \quad (22a)$$

$$\begin{aligned} \frac{d^2 R_1}{d\theta^2} = & \gamma a^2 \left\{ \left(\frac{h}{a} \right) \cos \theta + \frac{\sin 2\theta}{2(\eta^2 - 1)} + \frac{\eta^2}{\eta^2 - 1} (\sin 2\theta \right. \\ & \left. - \sin \theta \cos \theta_0) + 3 \left(\frac{a}{h} \right) \left(\frac{1 + \cos 2\theta}{2} \right) (\cos \theta_0 - \cos \theta) \frac{\eta^2}{(\eta^2 - 1)^3} \right\} \end{aligned} \quad (22b)$$

$$\frac{dR_2}{d\theta} = \gamma a h \cos \theta \frac{\eta^2}{\eta^2 - 1} \quad (22c)$$

$$\frac{d^2 R_2}{d\theta^2} = \gamma a^2 \left\{ \frac{\eta^2}{\eta^2 - 1} \left[\frac{\cos^2 \theta}{\eta^2 - 1} - \left(\frac{h}{a} \right) \sin \theta \right] + \frac{3\eta^2 \cos^2 \theta}{(\eta^2 - 1)^3} \right\}, \quad (22d)$$

where

$$\eta^2 = \left(\frac{U^2}{gh} \right) \left(\frac{H}{h} \right)^2. \quad (22e)$$

Next, consider the free-body diagram of the differential element of gate in Plate 10. The equilibrium of forces in the radial and tangential directions, respectively, leads to the following relations:

$$R_1' \sin \theta + R_2' \cos \theta + N = \frac{dV}{d\theta} \quad (23a)$$

and

$$R_2' \sin \theta - R_1' \cos \theta + V + \frac{dN}{d\theta} = 0 \quad , \quad (23b)$$

where the prime symbol represents derivative with respect to θ .

Eliminating $dN/d\theta$ from these equations, one obtains the following governing differential equation:

$$2R_1' \cos \theta - 2R_2' \sin \theta + R_1'' \sin \theta + R_2'' \cos \theta = \frac{d^2 V}{d\theta^2} + V \quad , \quad (23c)$$

which together with the boundary conditions (Equation 20) constitute a boundary-value problem for the shear force function $V(\theta)$ (Kreyszig 1988).

To facilitate the numerical solution of Equation 23c, the boundary-value problem will be transformed into an initial-condition problem (MATHSOFT 1994). Since $V(0)$ is already known, only $V'(0)$ is missing to complete the formulation. The problem is entirely solved with MATHCAD 5.0 (see Program 1: "Theoretical Estimate of Pressure Field," at the end of this chapter). Initially, a guess value for $V'(0)$ is provided. Subsequently, the program 'sweeps' the θ -domain numerically, evaluating the function $V(\theta)$ until the value $V(\theta_p)$ at the other end of the domain is obtained. If this value coincides with that one stipulated by the original boundary-value problem [$V(\theta_p) = 0$], within a previously established tolerance, then the starting initial condition $V'(0)$ is correct and the initial-condition problem is fully formulated. Otherwise, a new trial value is automatically advanced, and the process is repeated iteratively until convergence is reached.

Once the value of $V'(0)$ is obtained, the governing differential Equation 23c is solved using the Fourth-Order Runge-Kutta method for initial-condition problems (Kreyszig 1988). The solution function $Z^{<1>} = V(\theta)$ and its derivative $Z^{<2>} = dV/d\theta$ are plotted within the hardcopy of the workspace for the submitted task. Notice that the hydraulic pressure field is given by

$$p(\theta) = \frac{1}{a} \frac{dV}{d\theta} \quad (24)$$

and appears plotted and listed both for the prototype gate and for the model at the end of the workspace, with the objective of direct comparison with the experimental pressure field on the small-scale physical model.

Plate 11, generated with the program MATLAB 4.0 (MATHWORKS 1993), shows the minimum and maximum values of the experimental pressure acting on the upstream side of the gate during the controlling 100-s test (T1080). The pressure field is described along three different gate arcs: the left edge, the middle arc, and the right edge (Plate 12). Notice that the curves represent polynomial fits on three data points, which explains the intersection between the upper and the lower bound curves for the middle arc toward the gate base. These minimum and maximum curves delimit narrow bands, suggesting very little fluctuation of the pressure at a given location during the test. The theoretical estimation of the pressure field is an excellent upper bound over most of the domain, except on a small region toward the gate base, where the estimation is slightly unconservative.

The assessment of the hydraulic moment M_0 requires the previous evaluation of the lever arms r_1 and r_2 . These lever arms are obtained from the simultaneous solution of Equations 9 and 10. Notice that evaluation of the segment y_2 is required to define this system of equations. Segment y_2 may be computed from

$$y_2 = a \sin \theta_0 - \bar{y} , \quad (25a)$$

where

$$\bar{y} = \frac{1}{P_2} \frac{\gamma H^3}{6} \left[1 - \left(1 - \frac{a}{H} \sin \theta_0 \right)^3 - 3 \left(\frac{a}{H} \right) \left(1 - \frac{a}{H} \sin \theta_0 \right)^2 \sin \theta_0 \right] . \quad (25b)$$

This system of equations is solved numerically using the program MATHCAD 5.0 (MATHSOFT 1994) (see Program 2: "Location of Resultant Hydraulic Load," at the end of this chapter), yielding the values

$$r_1 = 3.434 \text{ ft} \quad (26a)$$

and

$$r_2 = 6.336 \text{ ft} . \quad (26b)$$

Consequently, the hydraulic moment per unit width of gate, M_0 , may be obtained as

$$\begin{aligned} M_0 &= R_1 r_1 + R_2 r_2 \\ &= 89 \text{ k-ft} . \end{aligned} \quad (27)$$

The theoretical total hydraulic forces on a prototype gate (total width = 30 ft) appear listed in Table 1. The experimental counterpart values (USAEWES 1994a) were obtained from data on ventilated-nappe tests T1087 (sampling rate: 100 sps; duration: 500 s) and T1109 (sampling rate: 500 sps; duration: 200 s). The experimental forces are scaled up from the model by multiplying by a factor $\lambda_L^3 = 15^3$. The hydraulic moment is scaled up by a factor $\lambda_L^4 = 15^4$. In general, there is good agreement because the experimentally measured moment is really bending moment at the root of the operating arms not at the torque-tube center, and the theoretical vertical component of reactive force (R_1) does not include the effect of the hydrostatic pressure due to the tailwater acting on the downstream side of the gate (Plate 1).

Table 1 Theoretical Prediction versus Experimental Measurements			
	Hydraulic Forces on 70 deg gate (Tailwater pool: 95 ft)		
	Vertical Force, k	Horizontal Force, k	Hydraulic Moment, k-ft
T1087	172	313	2,466
T1109	172	312	2,350
Theory	237	293	2,870
Average Difference	+ 38%	-6%	+ 11%

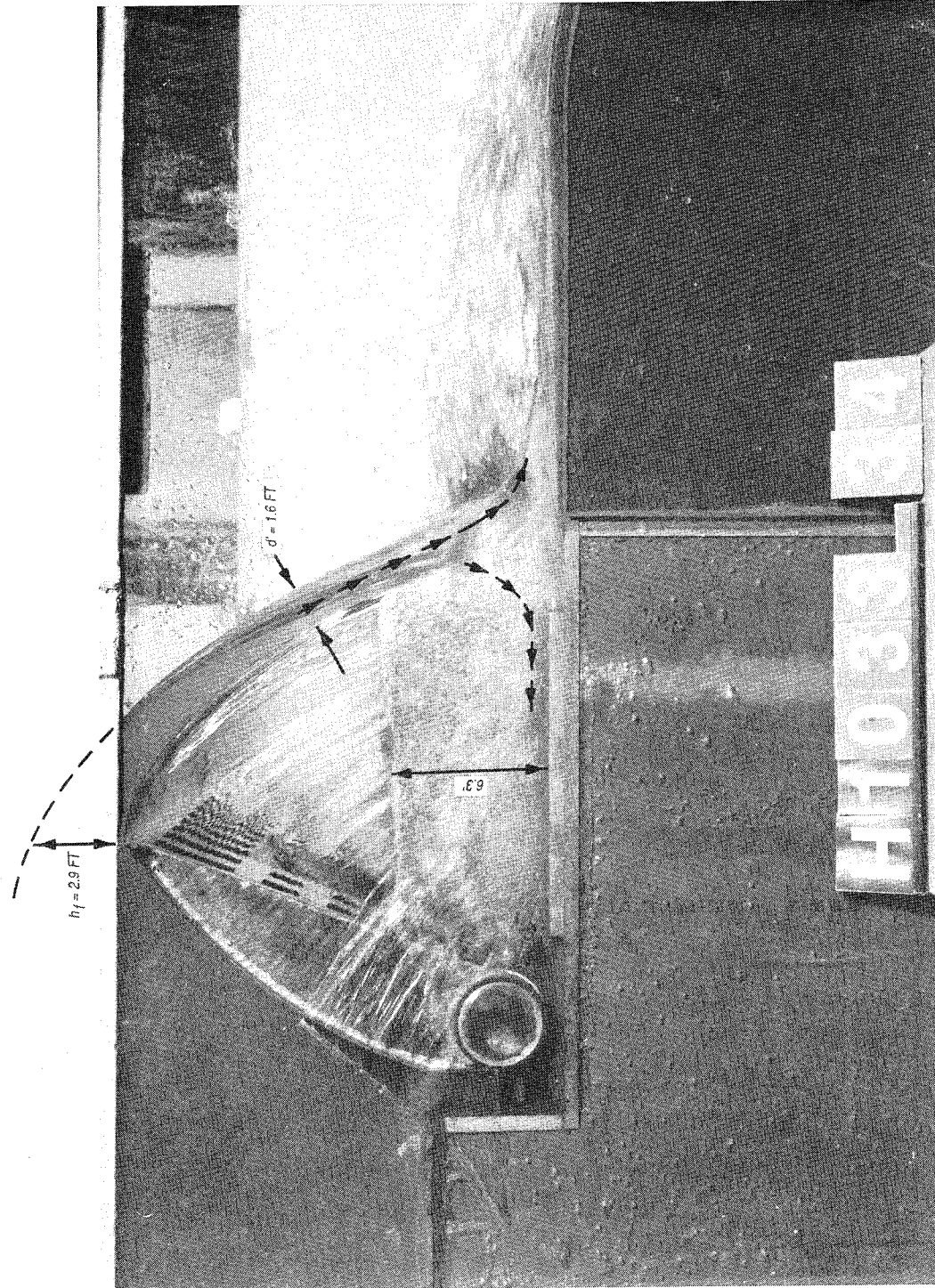


Plate 1. Montgomery Point Torque-Tube Gate. Lateral view of physical model in closed position with a ventilated nappe (T1109)

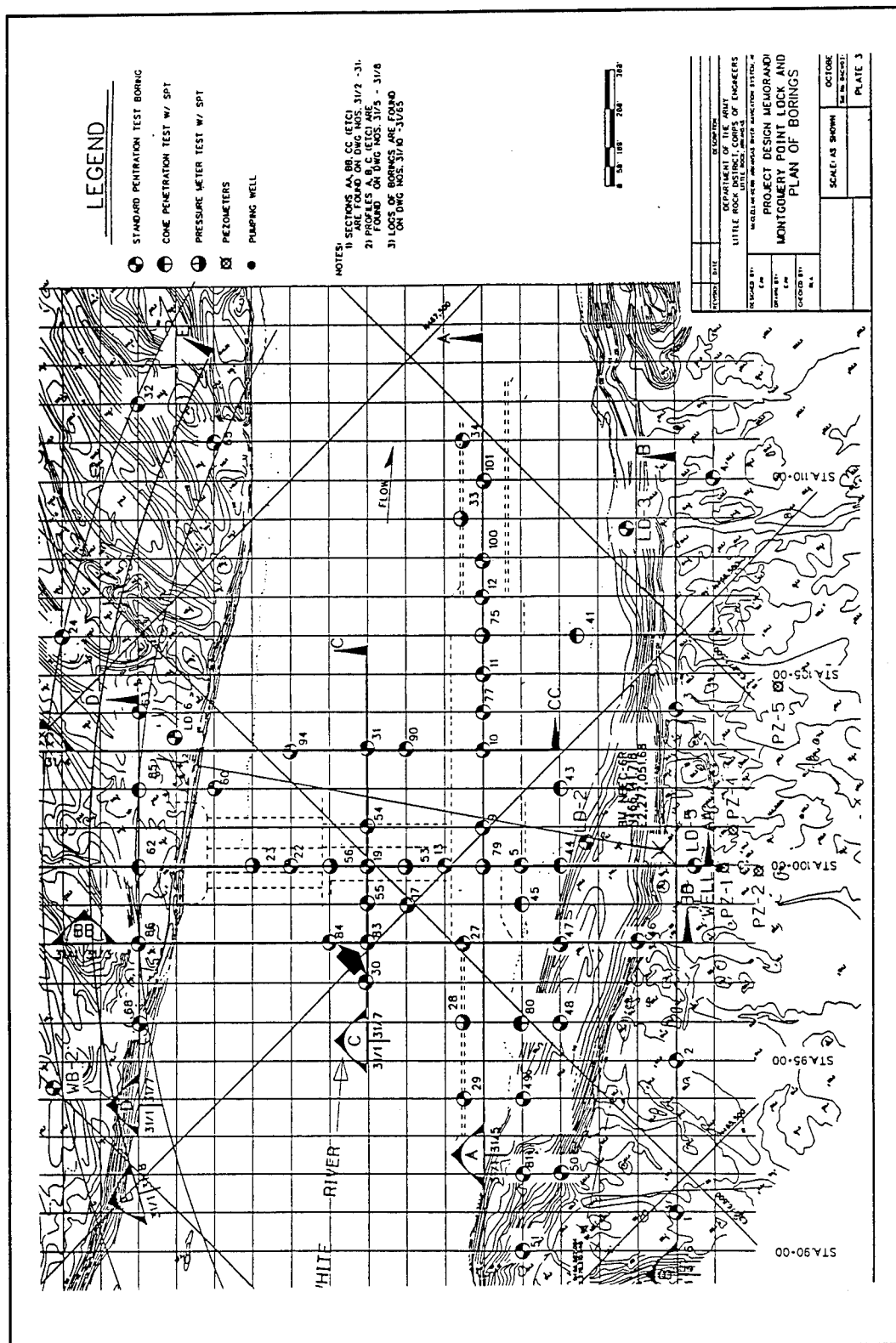


Plate 2. Montgomery Point Lock and Dam. Plan of borings at the site (Design Memorandum No. 1, Plate 31/1)

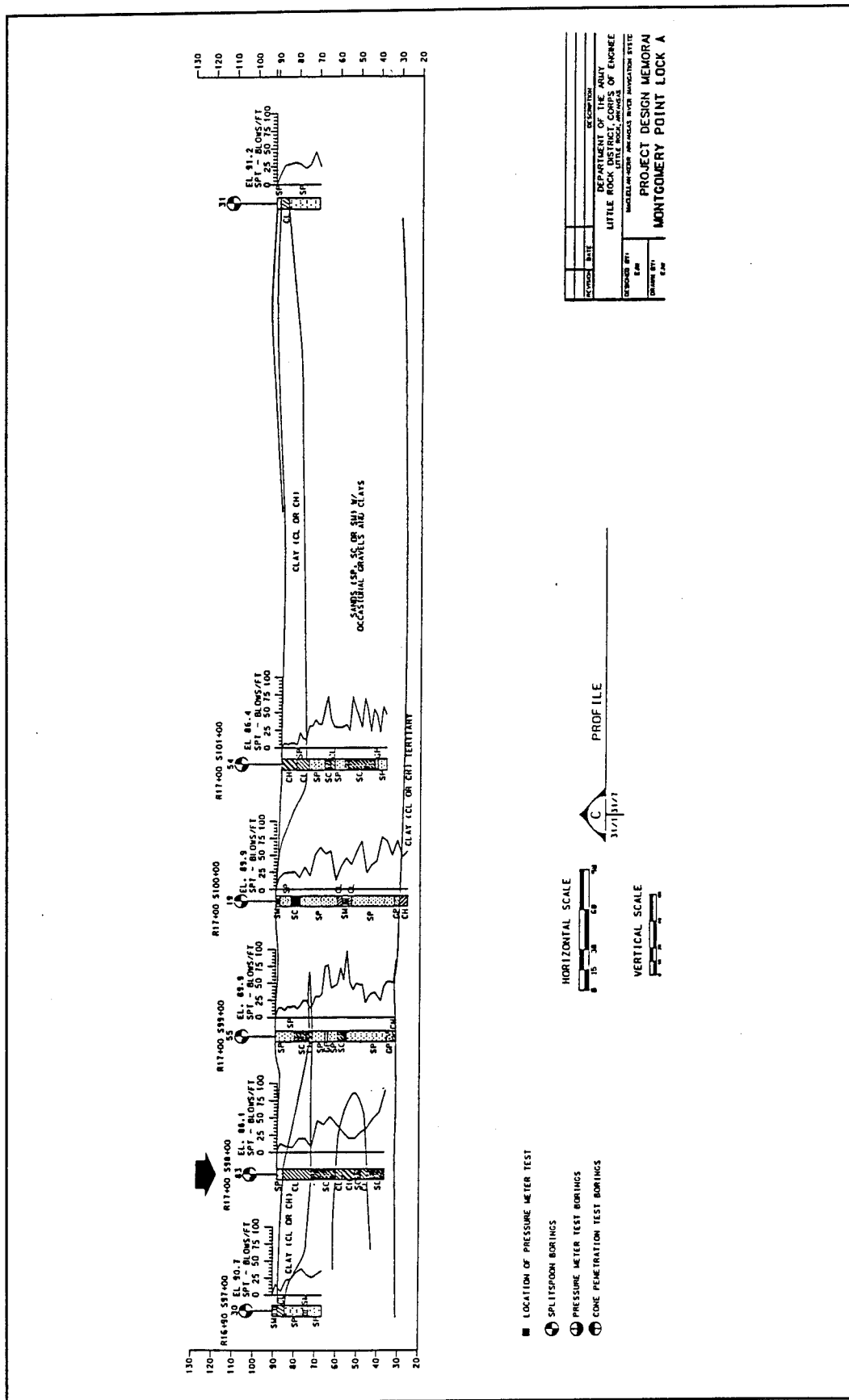


Plate 3. Montgomery Point Lock and Dam. Boring profile C (Design Memorandum No. 1, Plate 31/3)

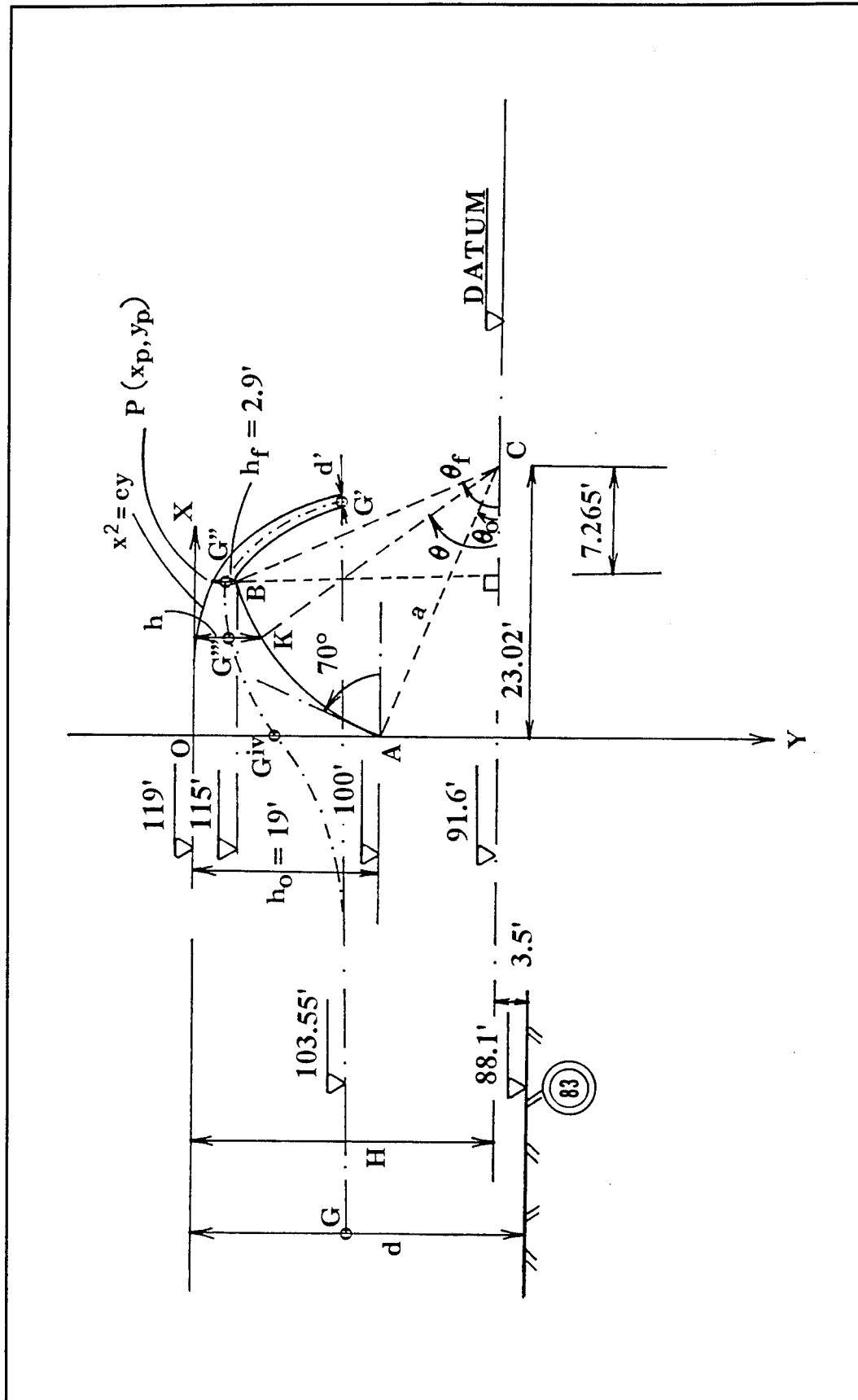


Plate 4. Montgomery Point Torque-Tube Gate. Longitudinal cross section of prototype

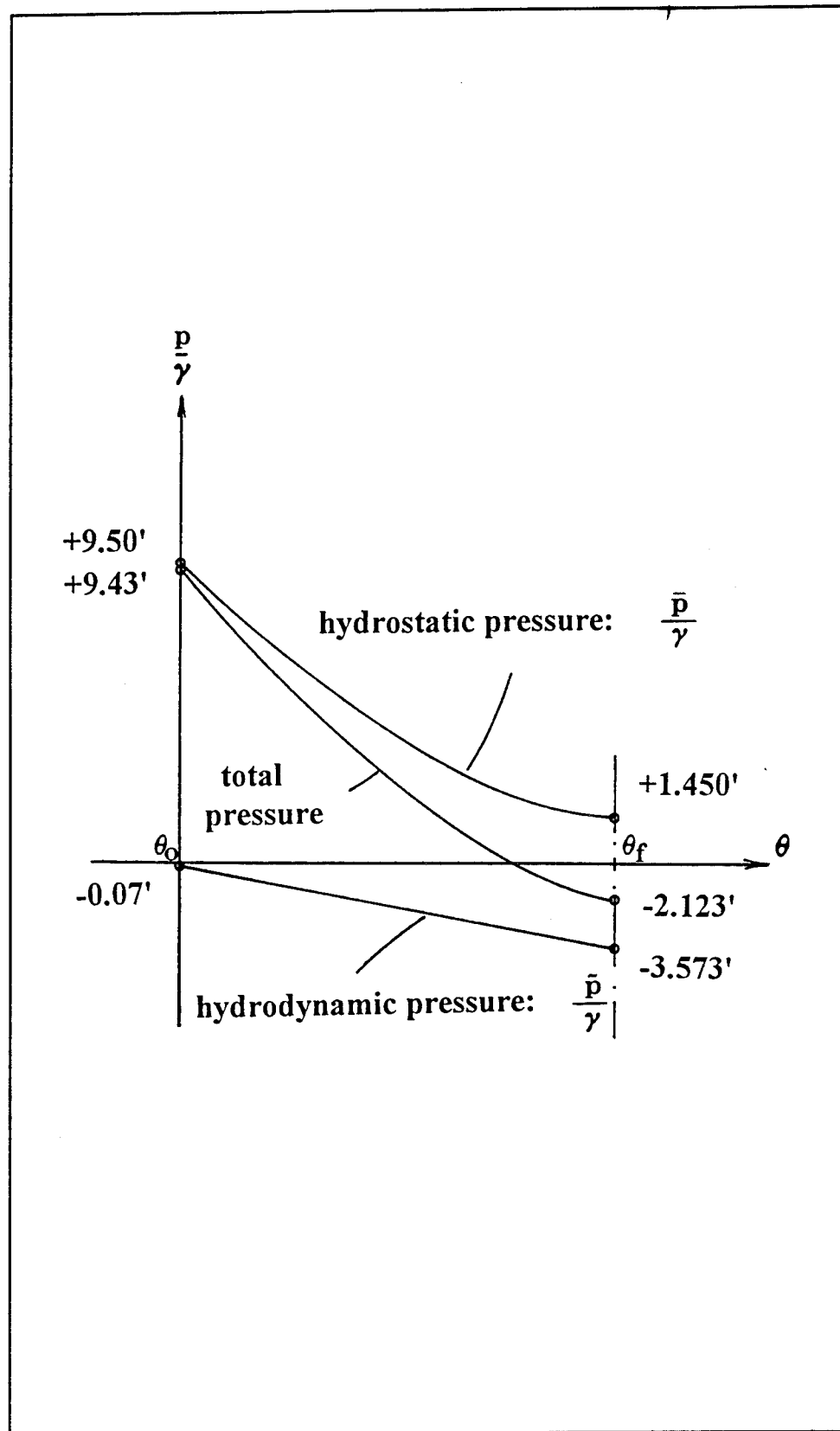


Plate 5. Montgomery Point Gate. Variation of hydraulic pressure with point elevation

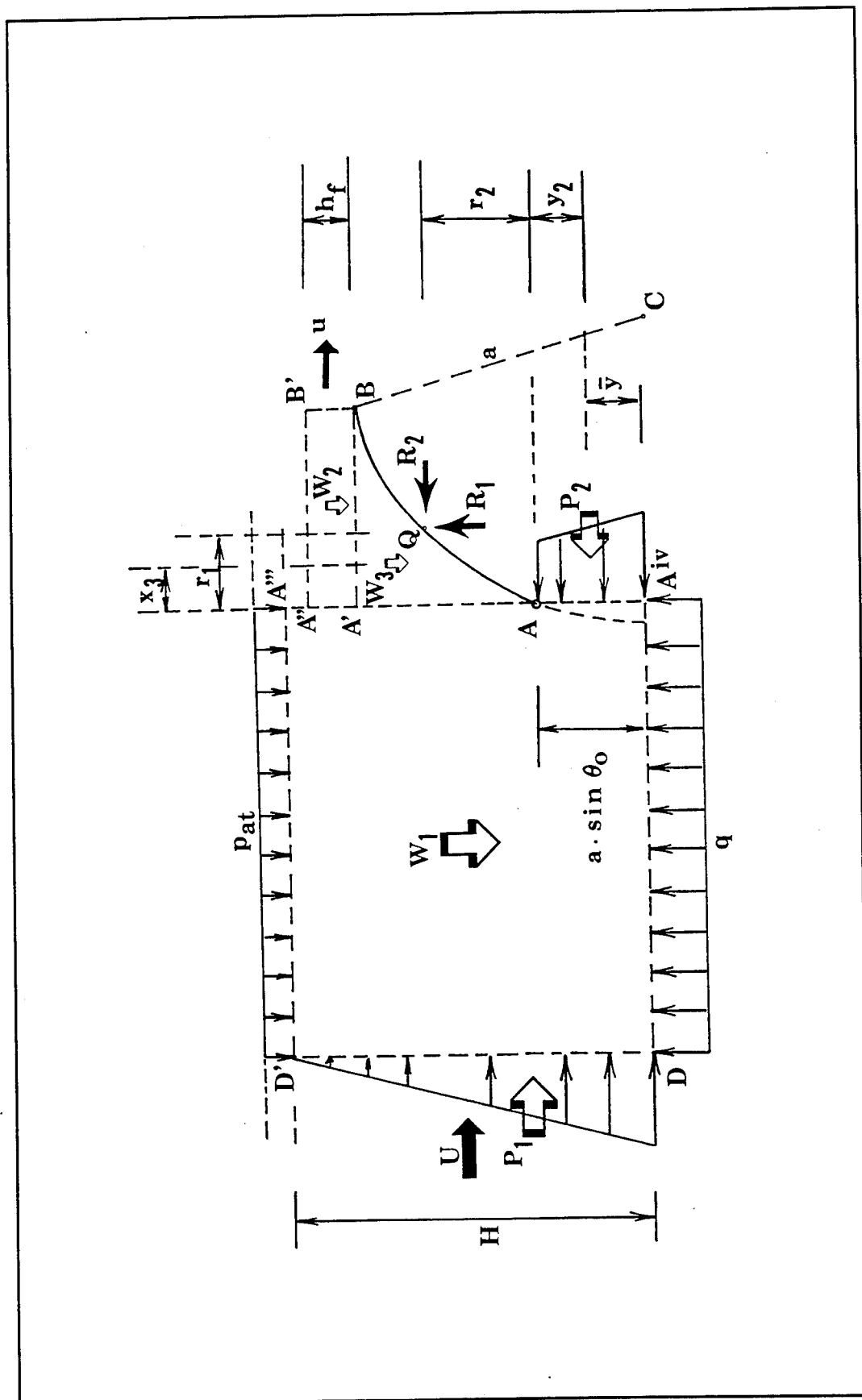


Plate 6. Montgomery Point Gate System. Idealized control volume

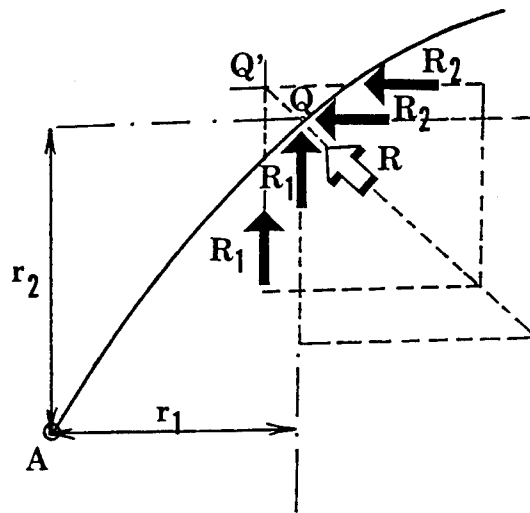


Plate 7. Montgomery Point Rigid Gate Model. Sliding the resultant of forces exerted by the gate skin on the fluid

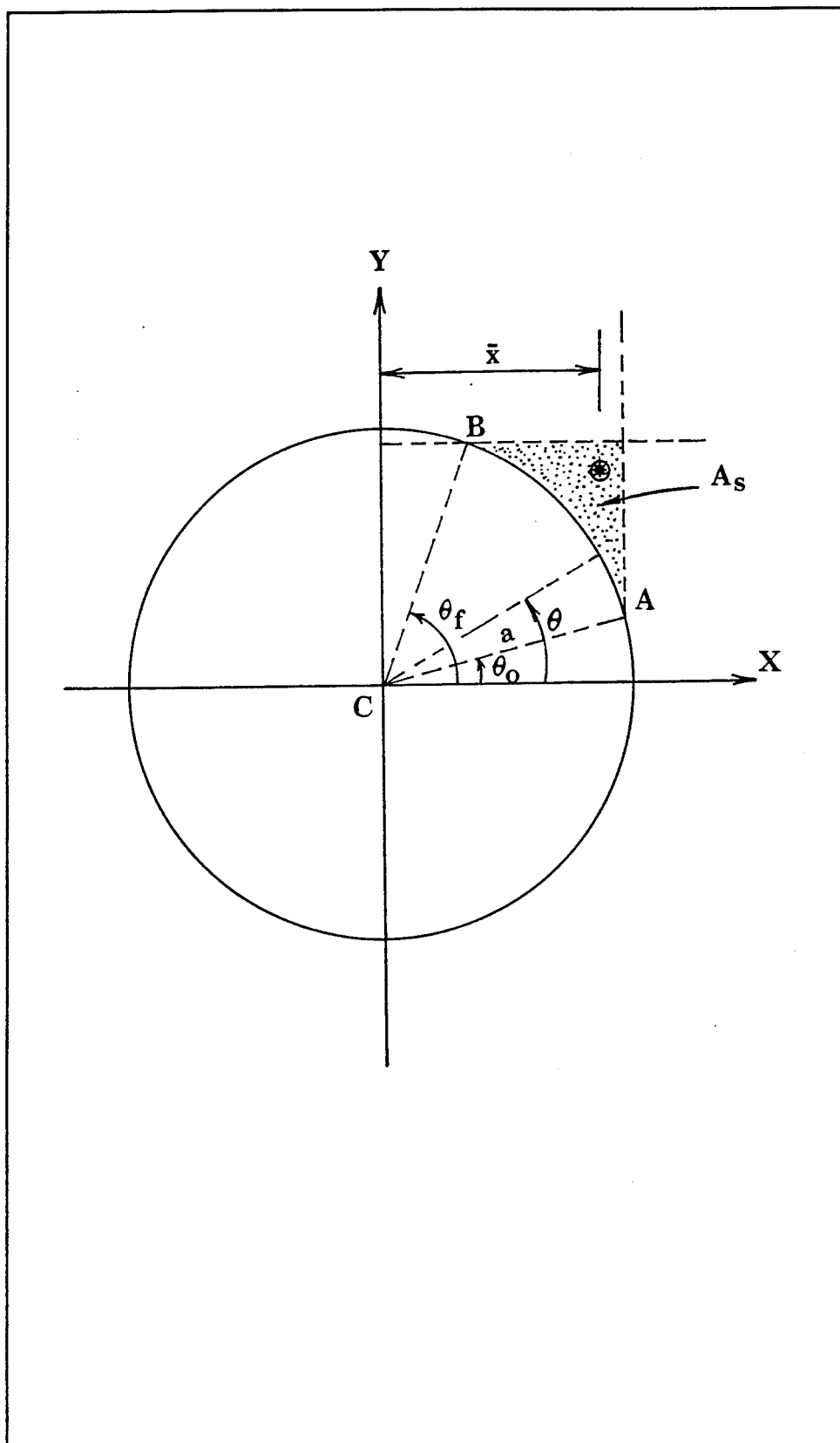


Plate 8. Montgomery Point Gate Model. Shaded area A_s subtended by the gate arc AB

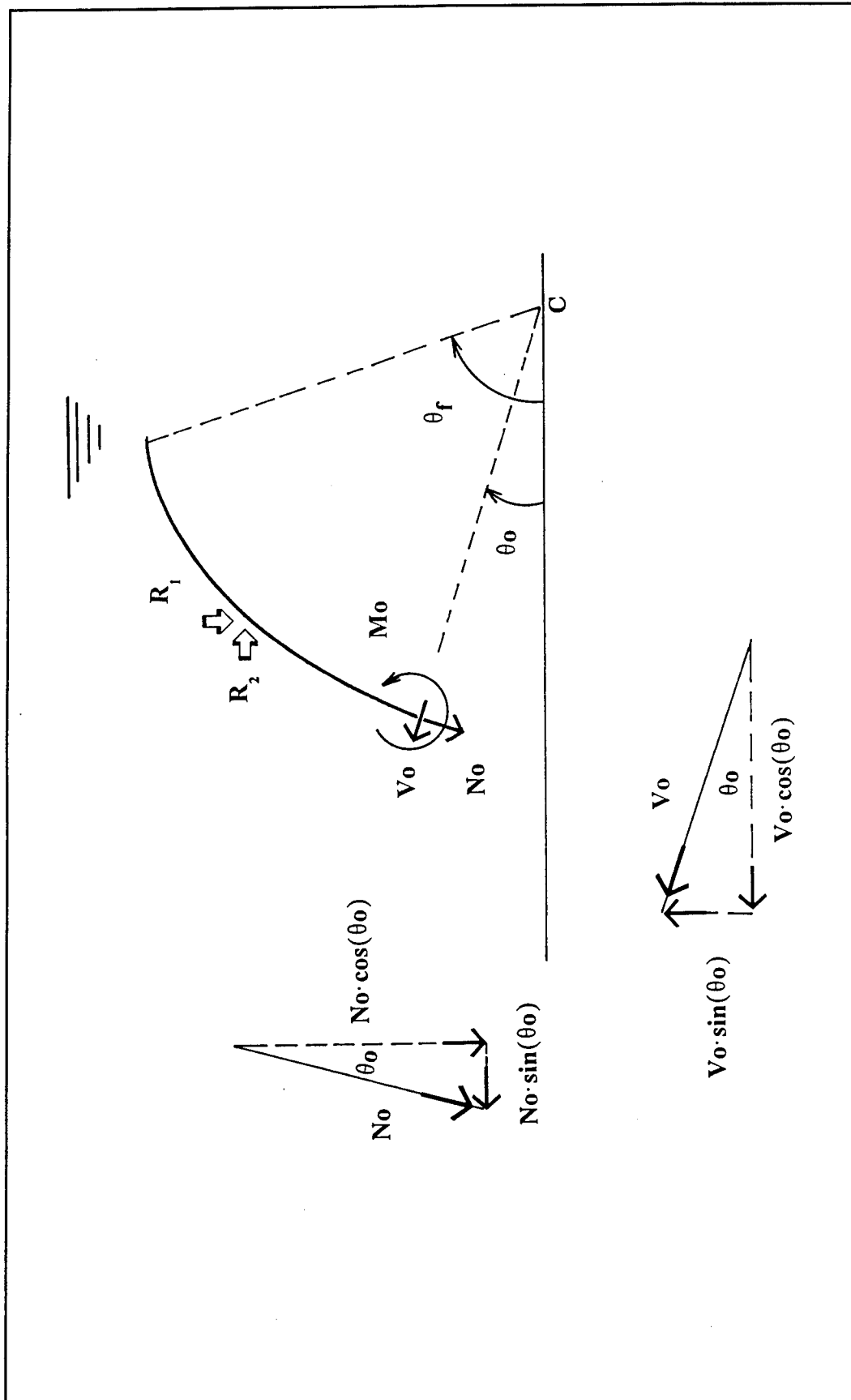


Plate 9. Montgomery Point Gate Model. Free-body diagram of gate

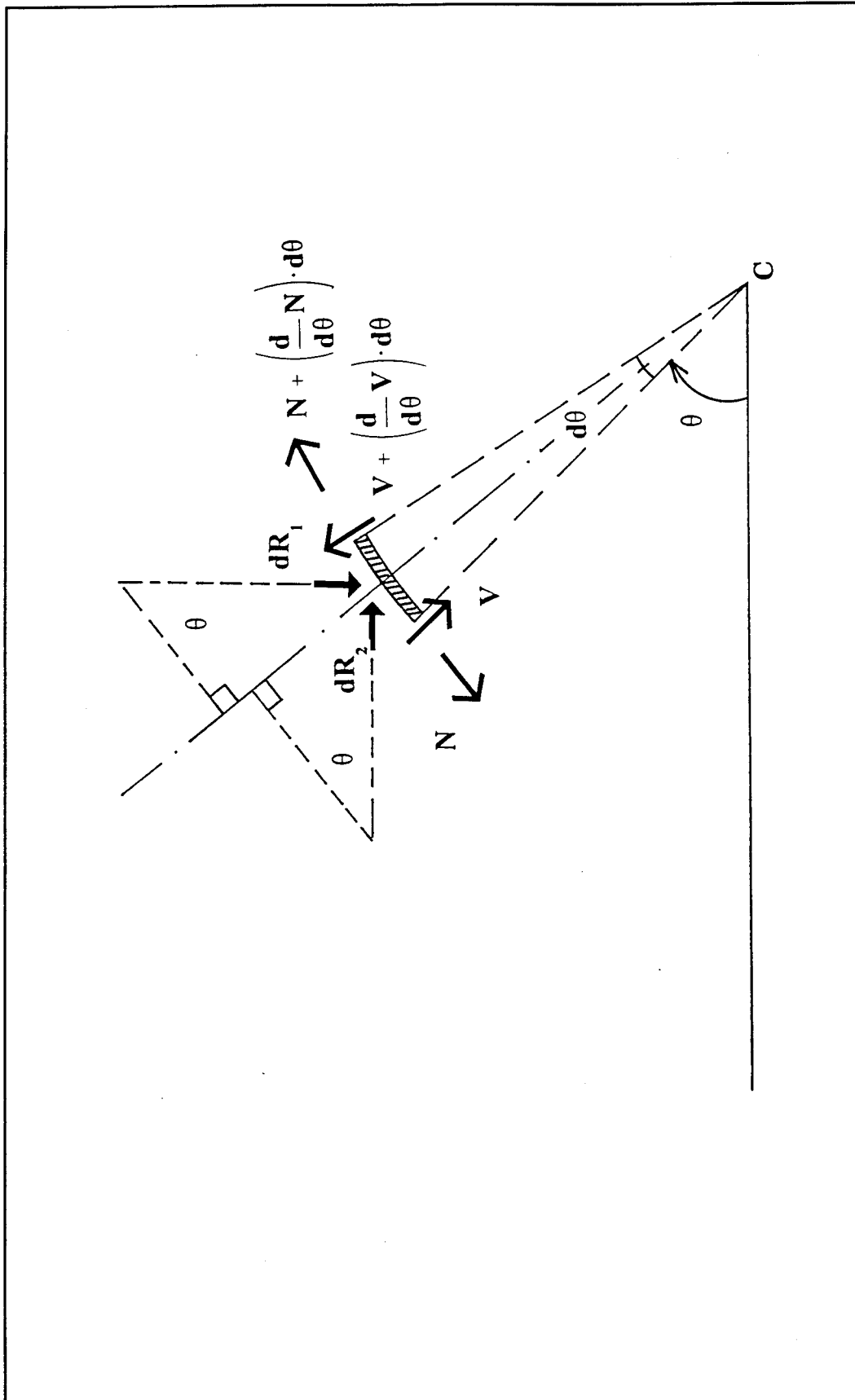


Plate 10. Montgomery Point Gate Model. Free-body diagram of gate differential element

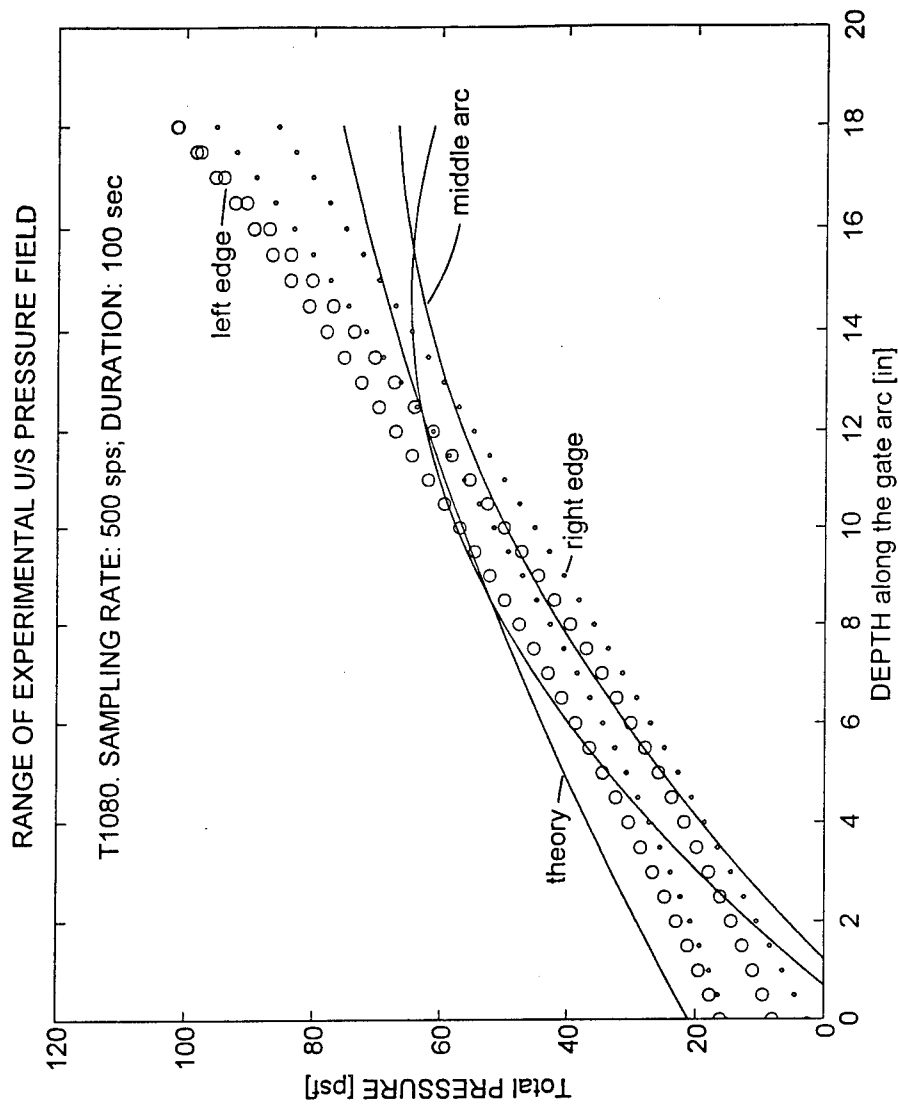


Plate 11. Montgomery Point Gate Model. Comparison of theoretical prediction of hydraulic pressure field with its experimental counterpart (T1080)

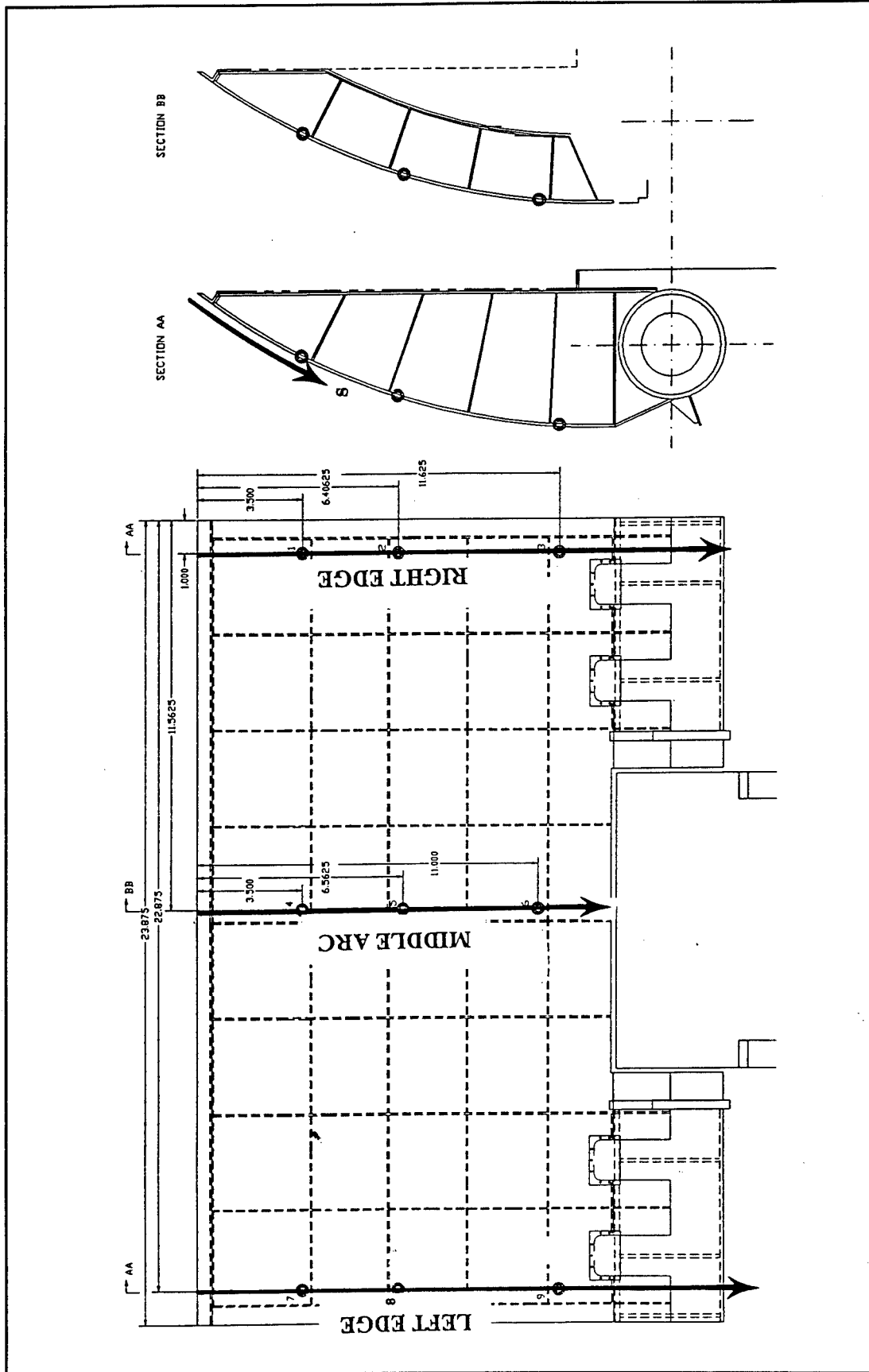


Plate 12. Montgomery Point Gate Model. Reference longitudinal arcs on the skin of the physical-model gate

**USAE-Waterways Experiment Station, Structures Laboratory
Vicksburg, Mississippi**

**Montgomery Point Gate Model
Theoretical Estimate of Pressure Field**

**Dr. Luis A. de Bejar
November 9, 1994**

$\gamma := 62.4$ **Unit weight of water**

$a := 24.5$ **Radius**

$U := 1.84$ **Approach VELOCITY in fps**

$g := 32.2$ **Gravity**

$H := 27.4$ **Channel depth upstream from gate**

$h_0 := 19.021$ **Initial value**

$\theta := 20..73$ **Elevation Range**

$h_{\theta-19} := 27.4 - 24.5 \cdot \sin\left(\frac{\pi}{180} \cdot \theta\right) - 2.346 \cdot \left(1 - 1.0643 \cdot \cos\left(\frac{\pi}{180} \cdot \theta\right)\right)^2$ **Water depth**

$$\eta^2 := \left[\left(\frac{U^2}{g \cdot h} \right) \cdot \left(\frac{H}{h} \right)^2 \right]$$

$$s\theta_0 := \sin\left(20 \cdot \frac{\pi}{180}\right) \quad c\theta_0 := \cos\left(20 \cdot \frac{\pi}{180}\right)$$

$$\text{theta}_{\theta-19} := \theta \cdot \frac{\pi}{180}$$

$$\overrightarrow{s\theta} := \sin(\text{theta}) \quad \overrightarrow{c\theta} := \cos(\text{theta})$$

$$R1pr := \gamma \cdot a^2 \cdot \left[\left(\frac{h}{a} \right) \cdot s\theta + c\theta \cdot \frac{c\theta_0 - c\theta}{1 - \frac{1}{\eta^2}} \right] \quad R2pr := \gamma \cdot a \cdot \left[h \cdot \frac{c\theta}{1 - \frac{1}{\eta^2}} \right]$$

$$\overrightarrow{s2\theta} := 2 \cdot (\overrightarrow{s\theta} \cdot \overrightarrow{c\theta}) \quad \overrightarrow{c2\theta} := (\overrightarrow{c\theta} \cdot \overrightarrow{c\theta} - \overrightarrow{s\theta} \cdot \overrightarrow{s\theta})$$

Program 1. "Theoretical Estimate of Pressure Field" (Sheet 1 of 5)

$$R1prpr := \text{gamma} \cdot a^2 \cdot \left[\left(\frac{h}{a} \right) \cdot c\theta + \frac{s2\theta}{2 \cdot (\eta^2 - 1)} + \frac{\eta^2}{\eta^2 - 1} \cdot (s2\theta - s\theta \cdot c\theta_0) + 3 \cdot \left(\frac{a}{h} \right) \cdot c\theta \cdot c\theta \cdot (c\theta_0 - c\theta) \cdot \frac{\eta^2}{(\eta^2 - 1)^3} \right]$$

$$R2prpr := \text{gamma} \cdot a^2 \cdot \left[\frac{\eta^2}{\eta^2 - 1} \cdot \left[c\theta \cdot \frac{c\theta}{\eta^2 - 1} - \left(\frac{h}{a} \right) \cdot s\theta \right] + 3 \cdot \eta^2 \cdot c\theta \cdot \frac{c\theta}{(\eta^2 - 1)^3} \right]$$

$$r\theta := ((R1prpr - 2 \cdot R2prpr) \cdot s\theta + (R2prpr + 2 \cdot R1prpr) \cdot c\theta)$$

$$v_0 := -31500 \quad \text{Guess value for } V'(0)$$

$$\text{load}(x1, v) := \begin{pmatrix} -11881 \\ v_0 \end{pmatrix}$$

$$D(r\theta, V) := \begin{pmatrix} V_1 \\ -V_0 + r\theta \end{pmatrix}$$

$$\text{score}(x2, V) := V_0$$

$$S := \text{sbval}(v, 1, 54, D, \text{load}, \text{score})$$

$$S = -2.769 \cdot 10^4$$

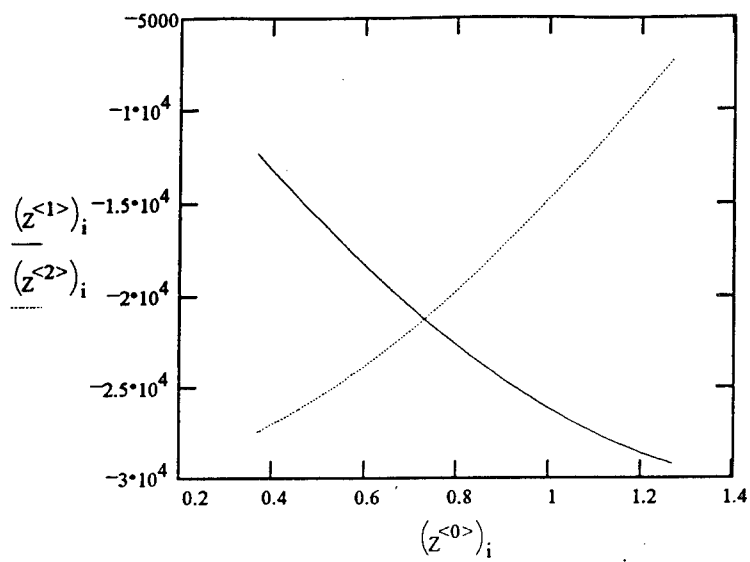
$$y := \begin{pmatrix} -11881 \\ -27690 \end{pmatrix}$$

$$DD(r\theta, y) := \begin{pmatrix} y_1 \\ -y_0 + r\theta \end{pmatrix}$$

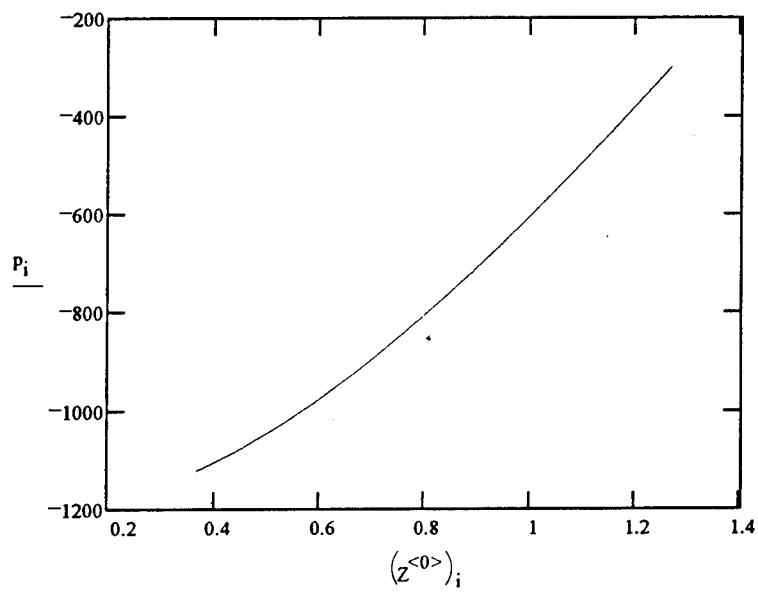
$$Z := \text{rkfixed}(y, 0.3491, 1.26973, 54, DD)$$

$$i := 1..54$$

Program 1. (Sheet 2 of 5)



$$p := \frac{z^{<2>}}{a}$$



$$p_{\text{model}} := \frac{p}{15}$$

-1.13·10 ³	-75.347	<<< θ = 20
-1.122·10 ³	-74.785	
-1.113·10 ³	-74.201	
-1.104·10 ³	-73.596	
-1.095·10 ³	-72.969	
p = -1.085·10 ³	pmodel = -72.321	[psf]
-1.075·10 ³	-71.652	
-1.064·10 ³	-70.962	
-1.054·10 ³	-70.251	
-1.043·10 ³	-69.52	<<< θ = 30
-1.032·10 ³	-68.769	
-1.02·10 ³	-67.998	
-1.008·10 ³	-67.207	
-995.954	-66.397	
-983.509	-65.567	
-970.777	-64.718	
-957.764	-63.851	
-944.472	-62.965	
-930.905	-62.06	
-917.068	-61.138	
-902.964	-60.198	<<< θ = 40
-888.598	-59.24	
-873.974	-58.265	
-859.095	-57.273	
-843.967	-56.264	
-828.594	-55.24	
	-54.199	

Chapter 2 Mathematical Model for Hydraulic Pressure Field

828.594	-53.142	
-812.98	-52.07	
-797.129	-50.982	
-781.047	-49.88	<<< $\theta = 50$
-764.737	-48.764	
-748.206	-47.633	
-731.457	-46.488	
-714.495	-45.33	
-697.326	-44.159	
-679.954	-42.975	
-662.384	-41.778	
-644.622	-40.569	
-626.672	-39.349	<<< $\theta = 60$
-608.54	-38.117	
-590.232	-36.874	
-571.751	-35.62	
-553.105	-34.356	
-534.298	-33.082	
-515.335	-31.798	
-496.223	-30.505	
-476.967	-29.203	
-457.571	-27.893	
-438.043	-26.574	<<< $\theta = 70$
-418.388	-25.248	
-398.611	-23.914	
-378.718	-22.574	
-358.715	-21.227	<<< $\theta = 74$
-338.607	-19.874	
-318.402		
-298.103		

USAE-Waterways Experiment Station, Structures Laboratory
Vicksburg, Mississippi

Montgomery Point Gate Model
Location of Resultant Hydraulic Load

Dr. Luis A. de Bejar
November 9, 1994

$$\begin{aligned}
 \theta_0 &:= 20 \cdot \frac{\pi}{180} & \theta &:= 72.75 \cdot \frac{\pi}{180} \\
 a &:= 24.5 \\
 H &:= 27.4 & h &:= 2.9 \\
 U &:= 1.84 & u &:= 17.39 \\
 \gamma &:= 62.4 \\
 g &:= 32.2 \\
 A &:= 27.4 & aB &:= 2.9 \\
 R1 &:= 7901 & R2 &:= 9768 \\
 W2 &:= 2852 & W3 &:= 5049 \\
 & & x3 &:= 4.36 \\
 P1 &:= 23423.71 & P2 &:= 12136.2 \\
 ybar &:= \gamma a \frac{H^3}{6 \cdot P2} \left[1 - \left(1 - \frac{a}{H} \sin(\theta_0) \right)^3 - 3 \cdot \left(\frac{a}{H} \right) \cdot \left(1 - \frac{a}{H} \sin(\theta_0) \right)^2 \cdot \sin(\theta_0) \right] \\
 y2 &:= a \cdot \sin(\theta_0) - ybar
 \end{aligned}$$

Program 2. "Location of Resultant Hydraulic Load" (Continued)

Solve a system of 2 simultaneous equations:

Guess values:

$$r1 := 15$$

$$r2 := 15$$

Given

$$\left(\cos(\theta_0) - \frac{r1}{a} \right)^2 + \left(\sin(\theta_0) + \frac{r2}{a} \right)^2 = 1$$

$$\left[P1 \cdot \left(\frac{H}{3} - a \sin(\theta_0) \right) + W2 \cdot \frac{a}{2} (\cos(\theta_0) - \cos(\theta_f)) + W3 \cdot x3 + P2 \cdot y2 - R1 \cdot r1 - R2 \cdot r2 \right] + \left(\frac{H}{2} - a \sin(\theta_0) \right) \cdot U^2 \cdot \text{gamma} \cdot \frac{A}{g} - \left[a (\sin(\theta_f) - \sin(\theta_0)) + \frac{h}{2} \right] \cdot \frac{2}{2} \cdot U \cdot \text{gamma} \cdot \frac{aB}{g} = 0$$

$$\begin{pmatrix} r1val \\ r2val \end{pmatrix} := \text{Find}(r1, r2)$$

Results:

$$r1val = 3.434$$

$$r2val = 6.336$$

Test result:

$$\left(\cos(\theta_0) - \frac{r1val}{a} \right)^2 + \left(\sin(\theta_0) + \frac{r2val}{a} \right)^2 = 1$$

$$\left[P1 \cdot \left(\frac{H}{3} - a \sin(\theta_0) \right) + W2 \cdot \frac{a}{2} (\cos(\theta_0) - \cos(\theta_f)) + W3 \cdot x3 + P2 \cdot y2 - R1 \cdot r1val - R2 \cdot r2val \right] + \left(\frac{H}{2} - a \sin(\theta_0) \right) \cdot U^2 \cdot \text{gamma} \cdot \frac{A}{g} - \left[a (\sin(\theta_f) - \sin(\theta_0)) + \frac{h}{2} \right] \cdot \frac{2}{2} \cdot U \cdot \text{gamma} \cdot \frac{aB}{g} = -3.638 \cdot 10^{-12}$$

Program 2. (Concluded)

3 Experimental and Finite Element Analyses

The objective of the experimental program is to provide a realistic assessment of the hydraulic forces on the gate. Complemented by theoretical models, the experimental analysis renders an effective pressure field to be used as input in the finite element analysis of the gate. This finite element analysis provides the designer with the response stress field within components of the gate, the reactions at the support bearings, and the force in the actuator cylinder.

The 1/15-scale physical model of the gate was made of bronze for convenience of construction. Since bronze has roughly one-half the modulus of elasticity of structural steel (American Institute of Steel Construction (AISC) 1986, Flinn and Trojan 1990), plates are easier to cut and assemble, thereby facilitating the overall construction process. Another advantage of bronze as the construction material for the model is to have approximately the same mass density as structural steel, thereby making the rigid gate model close to a true Froude's model in free-fall experiments (Novak and Cabelka 1981).

In the early stages of the experimental program, due to imperfections inherent to the construction process at the shop and due to warping while welding some component plates into the gate, the torque tube turned out to be slightly misaligned, introducing in this way asymmetry in the final configuration of the model at the site of the experiments. To compound the situation, it was not possible to achieve, within a tolerance satisfactory for experimental analysis, horizontal alignment of the seven supports originally planned in the prototype design, thereby introducing further asymmetry in the experimental records for structural parameters, in particular, for support reactions.

The effects of the asymmetric configuration of the model became evident during the preliminary calibrational experiments on the gate, thus becoming a source of concern. Since the hydraulic forces on the gate are expected to be approximately symmetrical, the corresponding experimental response records for selected structural parameters should similarly reflect symmetry. The problem was finally resolved, to engineering satisfaction, by reconstructing the gate with extraordinary attention to the effects of uneven cooling of welded parts and by having it standing on only three supports. The multiple

difficulties found in the construction of a balanced gate model standing on supports aligned on the horizontal plane led to a recommendation from the WES engineering team to reduce the number of supports in the final prototype gate to five (the construction process in larger scale is more controllable). This recommendation was readily accepted by the sponsor (USAEWES 1994a).

Consequently, the experimental program on the gate proceeded on a model standing on three supports, and the finite element analysis was effected on two analytical models: (a) one for the physical model on three supports, and (b) another for the prototype gate standing on five supports. Plate 13 shows a plan view of the physical model and the instrumented bearing blocks 2, 4, and 6, according to the original notation for seven supports.

Plate 14 shows a schematic representation of a typical load cell and the corresponding bridge wiring. The load cells consist of two structural aluminum tubes (Al 6061-T6, std $\phi 3/8"$, $L = 3/4$ in.) per support block (one tube by the upstream face of the model and the other tube by the downstream face), bolted at both ends, i.e., to the bearing housing and to the base, respectively. Each tube was instrumented with four strain gauges, one per quadrant, as indicated in Plate 14. The 0-/180-deg strain gauges were calibrated to sense the normal load on the tube, upon its axial distortion, whereas the 90-/270-deg strain gauges were calibrated to sense the shear force at the ends of the tube, upon its flexural deformation (lateral displacement of the bearing housing with respect to the base). Individual tubes tested satisfactorily against inelastic lateral instability, even after reducing the number of actual support blocks to only three (The Aluminum Association 1981, 1982). The length of the tubes was engineered to fit the expected deformations during the experiments to the sensitivity of the strain gauges. The performance of the load cells during the tests was considered excellent.

The model gate was also instrumented with accelerometers (PCB 302A) to identify its natural structural properties from the forced experimentation (frequencies of natural vibration and corresponding modal shapes). Plate 15 shows the location of the accelerometers on the model. The corner accelerometers 1 and 6 are triaxial in nature to provide information on the lateral-torsional modes. One of the triaxial accelerometer axes is normal to the gate skin, while the other two axes are tangential to it. One of the tangential axes is aligned with the gate ridge. Accelerometers 2 through 5 and 7 through 8 are uniaxial, sensing motion in the direction normal to the gate skin.

One of the most important objectives of the project is the experimental determination of the hydraulic pressure field on the gate in the controlling operational configuration. To this end, the model gate was instrumented with nine pressure cells (thermally insulated Kulite XTM-190-10 psia) on each of its faces, to provide information on the spatial variation of the total (hydrostatic plus hydrodynamic) pressure field on the gate. Plates 16 and 17 show the location of the pressure cells on the upstream and downstream sides of the model, respectively. Notice that the general tributary area for a given

pressure cell number on the upstream face corresponds with the same pressure cell number on the downstream side of the gate. For example, pressure cell 1 on the upstream side of the gate senses hydraulic pressure on a gate area whose back experiences hydraulic pressure sensed by pressure cell 1 on the downstream side of the gate.

The experimental records for each test typically consist of the time-history of response for the parameter sensed by each transducer on the model, as well as the maximum, average, and minimum readings from the record. Table 2 describes the average values of the experimental hydraulic pressure field on the upstream side of the gate for a representative 100-s test and is introduced at this point to illustrate the degree of asymmetry found in the experiments. Compare the values corresponding to the right edge of the gate (pressure cells 1 through 3) with those corresponding to the left edge of the gate (pressure cells 7 through 9). Plate 18 defines the curvilinear coordinate (s) measured along the reference longitudinal arcs.

Table 2			
Average Experimental Upstream Pressure Field on Gate (100-s test)			
Point	X, in.	S, in.	Pressure, psf
1	1.04	3.52	21.78
2	1.04	6.40	32.75
3	1.04	11.60	56.24
4	11.60	3.52	20.32
5	11.60	6.40	38.11
6	11.60	11.60	58.76
7	22.88	3.52	24.25
8	22.88	6.40	36.04
9	22.88	11.60	62.26
Note: Fully closed gate position (70 deg).			

The required sampling rate and record length were determined as follows (Bendat and Piersol 1993, Newland 1984). From preliminary eigenproblem solution for the gate structure, it was estimated that the frequency range of interest goes as far as 70 Hz to include the first five modes of vibration. Therefore, the required sampling interval would be 1/280 s for a Nyquist frequency of 140 Hz. An acceptable accuracy was established by defining the coefficient of variation of the parameter being measured as $C.O.V. = \sigma/m = 0.14$, which corresponds to the coefficient of variation of the random variable χ^2_k with 100 degrees of freedom ($k = 100$). Now, by estimating the frequency resolution as 1 Hz, the effective bandwidth of the spectral window is given by $B_e T = 51$. And, by defining $B_e = 1/2$ Hz, the required record length is $T = 102$ s. It was decided to sample at a rate of 500 sps for $T = 100$ s. Later, during the development of the experimental project, even longer records were obtained: $T = 200$ s.

During the first phase of experiments with the physical model, the maximum reaction response was obtained when a unit discharge of water of 50 cfs runs over the system of fully raised gates with the tailwater pool maintained at 95 ft (prototype level) and the headwater pool growing monotonically from about 114 ft to 119 ft (prototype level). Plate 19 shows the minimum and maximum values of the experimental pressure acting on the upstream side of the gate during the controlling 100-s test (T1080). The pressure field is described along three different gate arcs: the right edge (described by a sequence of dots), the middle arc (described by a solid line), and the left edge (described by a sequence of small circles). Notice that the curves represent parabolic polynomial fits on three data points, which explains the intersection between the upper and the lower bound curves for the middle arc toward the gate base. These minimum and maximum curves delimit narrow bands, suggesting very little fluctuation of the pressure at a given location during the test. Notice also that the theoretical estimation of the pressure field is an excellent upper bound over most of the domain, except on a small region toward the gate base. This observation together with the analyses of tests T1108 and T1109 below, suggest the proposed design pressure line AB in Plate 19, as per phase 1 of the project (USAEWES 1994a).

Next, this pressure line AB is tested against the maximum net total pressure on the upstream side of the gate, obtained as the algebraic summation of the maximum and minimum pressure fields on the upstream and downstream sides of the gate, respectively. Plate 20 shows this maximum net pressure for each reference longitude in the gate (i.e., right edge, middle arc, and left edge), and for the two 200-s controlling tests T1108 (integral nappe) and T1109 (ventilated or broken nappe). In general, the test with the integral nappe controls for the upper half of the gate, whereas the ventilated nappe test controls for the deeper half of the gate. Notice that line AB represents a reasonable envelope for both the theoretical estimations and the maximum readings during the experiments, except for some slightly unconservative points toward the gate ridge. The design total pressure field under normal operating conditions is then recommended as

$$p = 40 + 3.9 s \text{ [psf]} \quad (28)$$

where s is the curvilinear coordinate [in.] along the 1/15-scale gate arc (USAEWES 1994a).

This design pressure field was used as input for separate finite element analyses of the 1/15-scale physical model and the prototype. The structural geometries were constructed analytically using the preprocessor PATRAN-3 (PDA Engineering 1993) (Plates 21 and 22 display isometric views of the upstream and downstream sides of the finite element grid, respectively); the finite element processes were executed by ABAQUS (Hibbitt, Karlsson and Sorensen 1993, Zienkiewicz 1977) on the structure standing on elastic supports (Teflon bearings); and the postprocessing of output information was again effected by PATRAN-3.

Plate 23 shows the displaced shape of the 1/15-scale physical model subjected to the design pressure field, and Table 3 reports the reaction forces acting on the three bearings. Notice that only the results for one edge support are reported in the table since the results for the other edge support are identical, due to symmetry. The total resultant bearing reaction turns out with 50 percent higher magnitude than experimentally measured, as expected, because of the conservatism in the design envelope for pressure. The corresponding force in the actuator was $f_{cyl} = 131.4$ lb (USAEWES 1994a).

Table 3				
Montgomery Point Gate 1/15-Scale Model (3 supports): Summary of Finite Element Analysis Bearing Reactions, lb				
Support type:	Edge		Center	
Load cell:	#1	#2	#1	#2
Vertical component:	25.32	-83.40	46.90	-91.73
Horizontal component:	41.00	41.00	41.90	41.90
Load cell resultant:	48.19	92.93	62.89	100.85
Resultant bearing reaction:				
Vertical component:	-160.99			
Horizontal component:	247.80			
Total reaction magnitude:	295.50			
Note: A minus sign indicates compressive force on the support.				

Plate 24 shows a plan view of the prototype gate standing on five supports. The design reactions at these supports were obtained through finite element analysis of the structural idealization for the prototype gate (made out of structural steel) subjected to the design distribution of the operational hydrodynamic pressure field properly scaled ($\lambda_p = 15$) and acting on the fully raised gate (70-deg elevation).

The fully raised gate condition was recognized to control the design of the bearing supports among all experiments on the physical model. This point is illustrated in Plates 25 through 28. Plate 25 describes the variation of the horizontal (HE) and vertical (VE) components of the resultant reaction at supports 1 and 2 with the gate elevation (X), and the corresponding engineering envelopes for design (notice that the plate was actually recorded for bearing block 2 in the model, for the controlling test T1027). Apparently, the maximum response is obtained at the end of the experiment when the gate is fully raised. Plates 26 and 27 lead to the same conclusion using similar diagrams for the reaction at the central block and for the resultant reaction at supports 4 and 5 in the prototype gate, respectively. Finally, Plate 28 confirms the controlling fully raised gate position in terms of the total hydraulic moment on the torque tube.

Plate 29 displays an isometric view of the upstream side of the finite element grid for the prototype, standing on rigid supports, and Table 4 reports the reactive forces required for the actual design of the bearings. These reactions are for ideal conditions and do not consider any misalignment in the torque-tubes or imperfections in the construction. Correspondingly, the force in the actuator cylinder was $F_{cyl} = 1,699.4$ kips (USAEWES 1994a). Plates 30 and 31 show iso-principal-stress regions on the gate. Plate 30 exhibits tensile-stress regions on the upstream face of the gate, while Plate 31 exhibits compressive-stress regions on the elements of the downstream face of the gate. No indication of local yielding is detected from the analysis.

Table 4 Montgomery Point Gate Prototype (5 supports): Summary of Finite Element Analysis Bearing Reactions, kips			
Support type:	External Edge	Internal Edge	Center
Vertical component:	-200.87	-221.61	-376.19
Horizontal component:	388.00	444.29	1,259.54
Resultant support reaction:	436.91	496.49	1,314.52
Resultant bearing reaction:			
Vertical component:	-1,221.15		
Horizontal component:	2,924.12		
Total reaction magnitude:	3,168.86		
Note: A minus sign indicates compressive force on the support.			

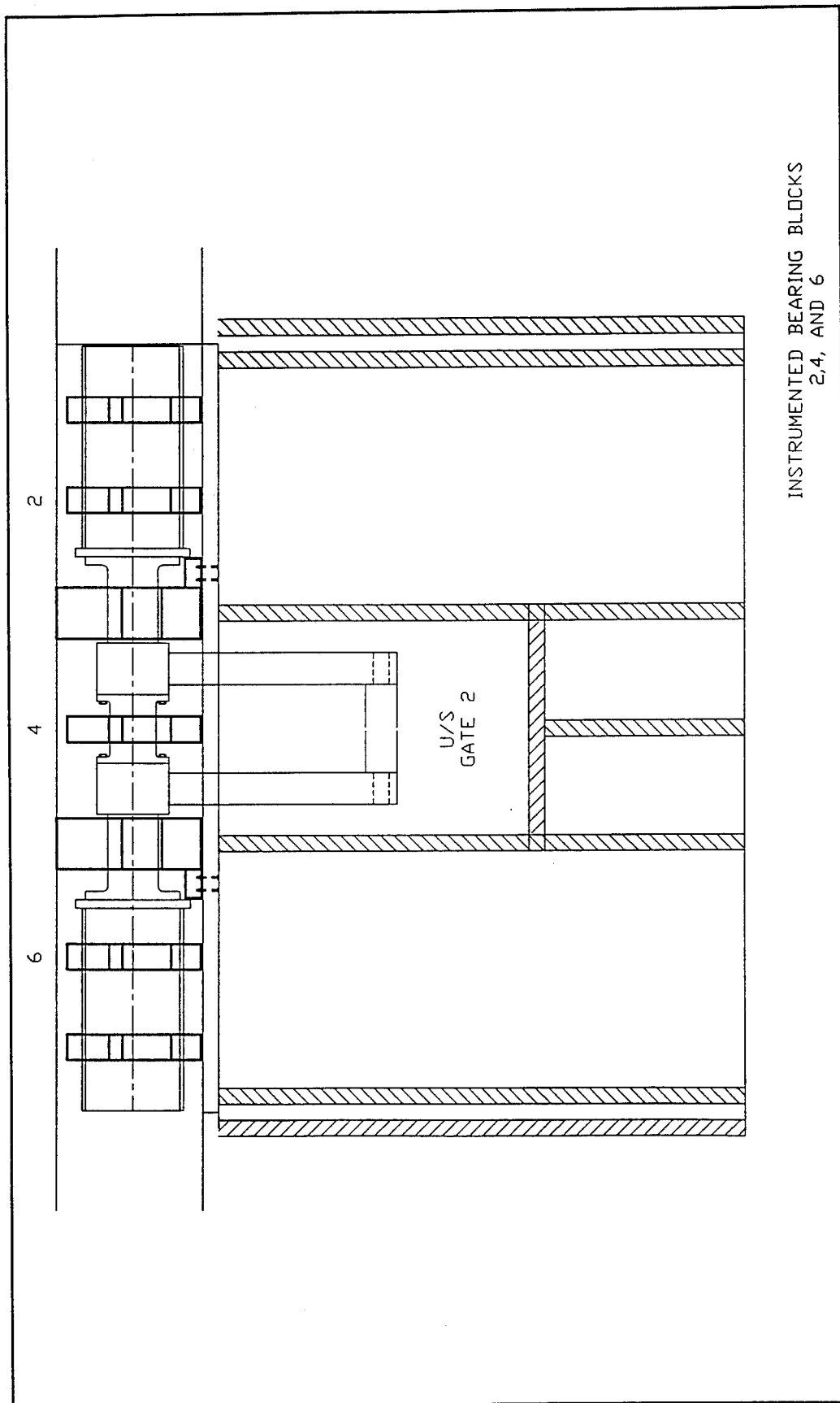


Plate 13. Montgomery Point Rigid Gate Model. Plan view of physical model and location of load cells at blocks 2, 4, and 6 (three supports)

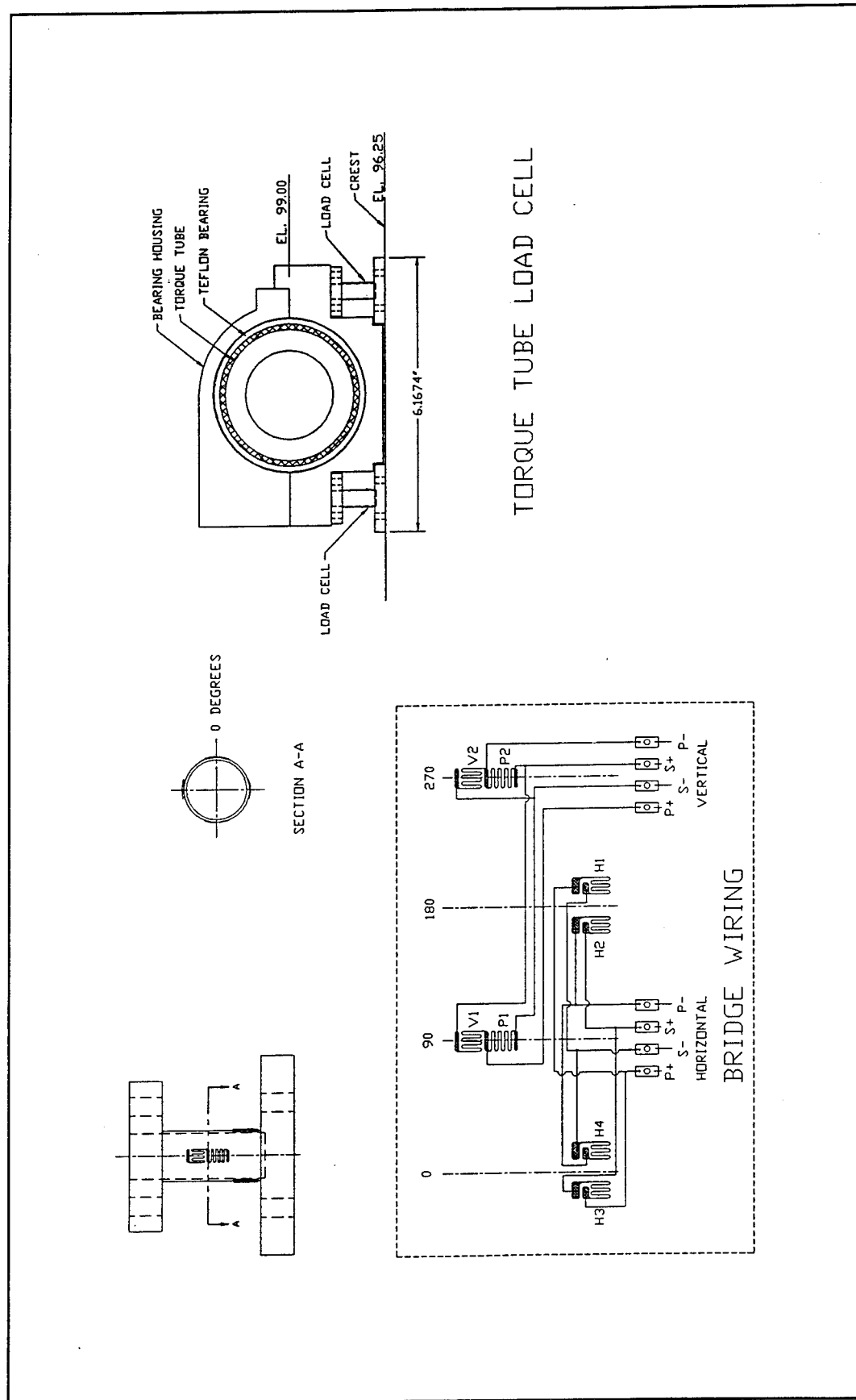


Plate 14. Montgomery Point Rigid Gate Model. Typical load cell and corresponding bridge wiring

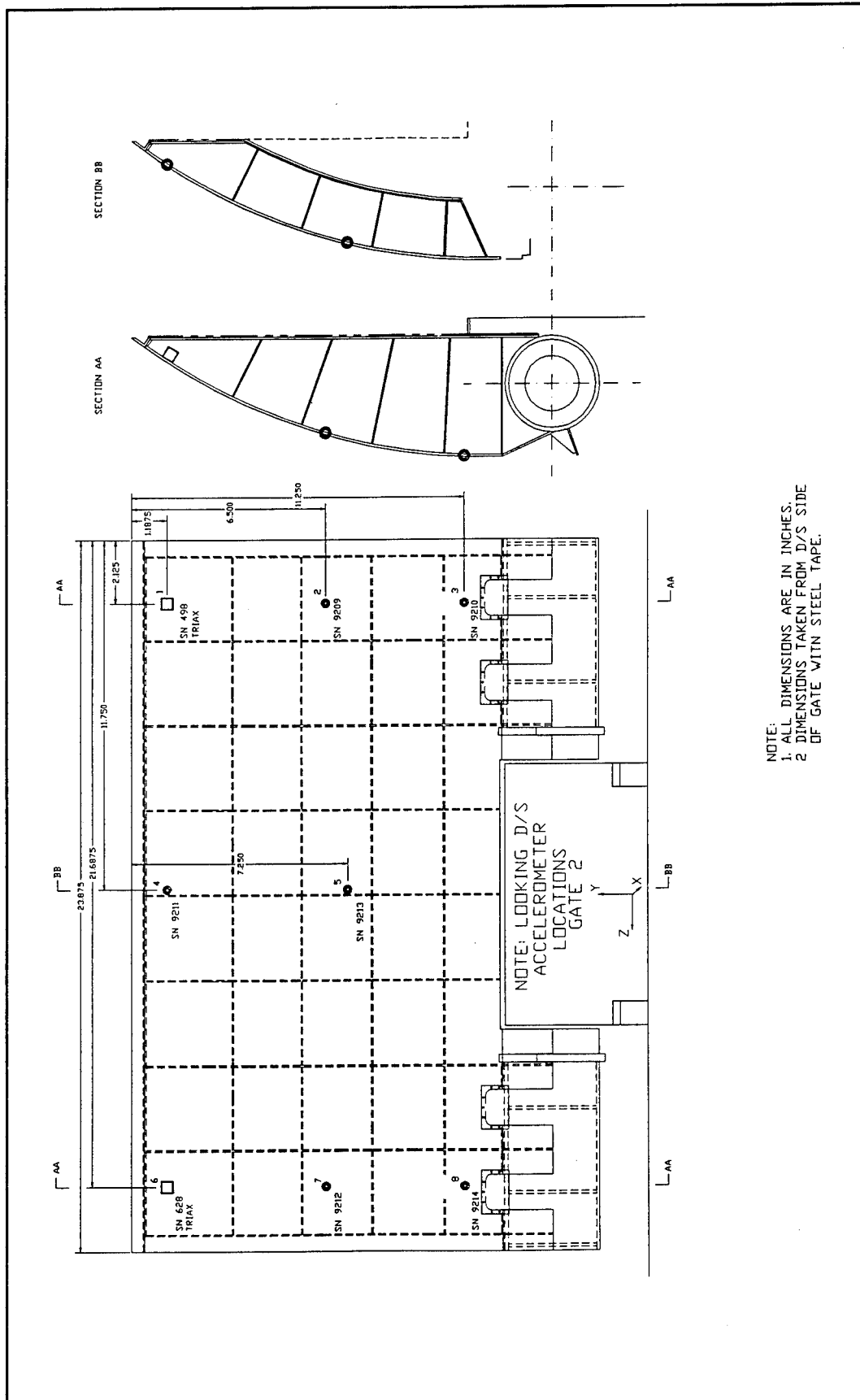


Plate 15. Montgomery Point Rigid Gate Model. Accelerometer locations

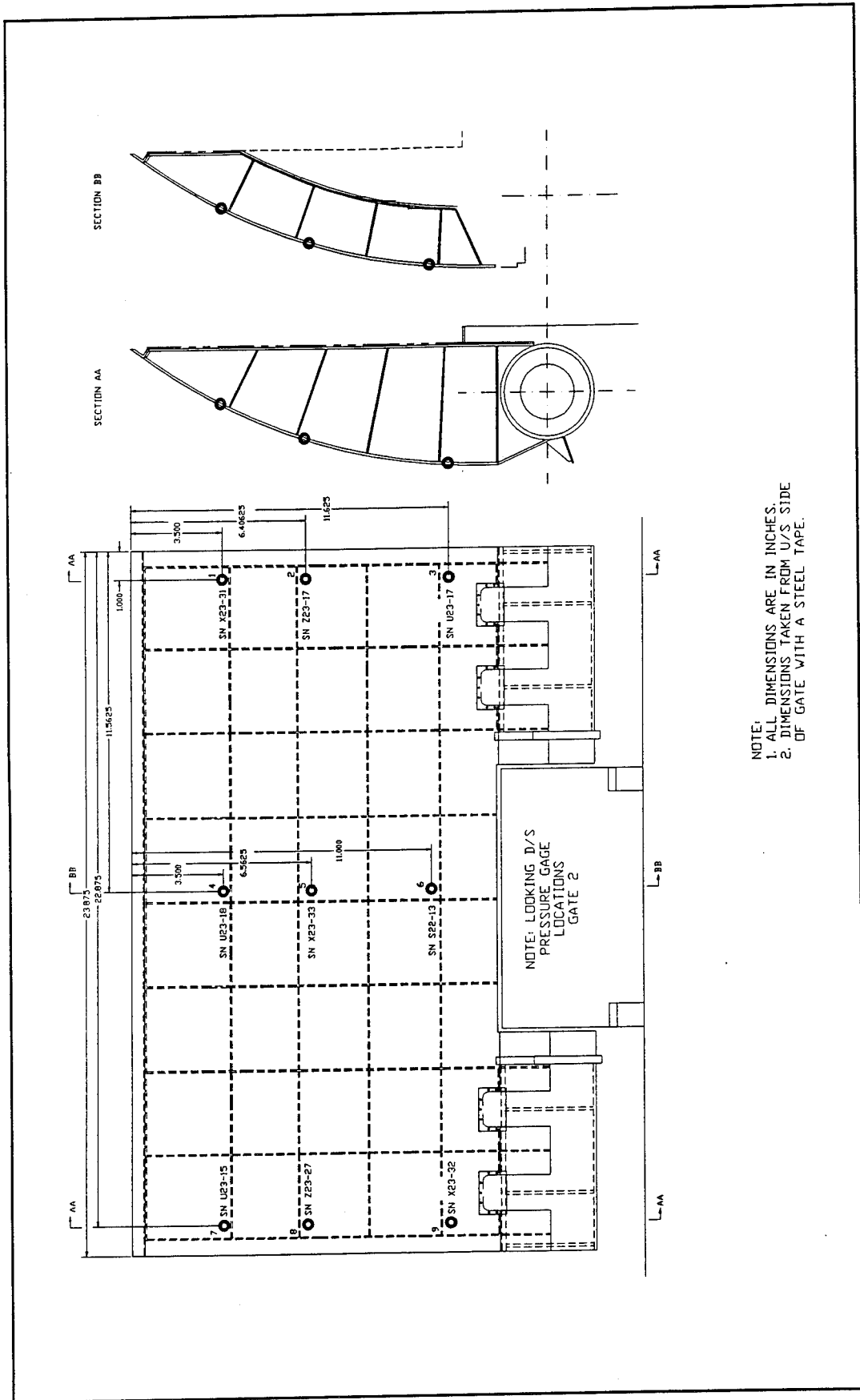


Plate 16. Montgomery Point Rigid Gate Model. Pressure cell locations on the upstream side of gate

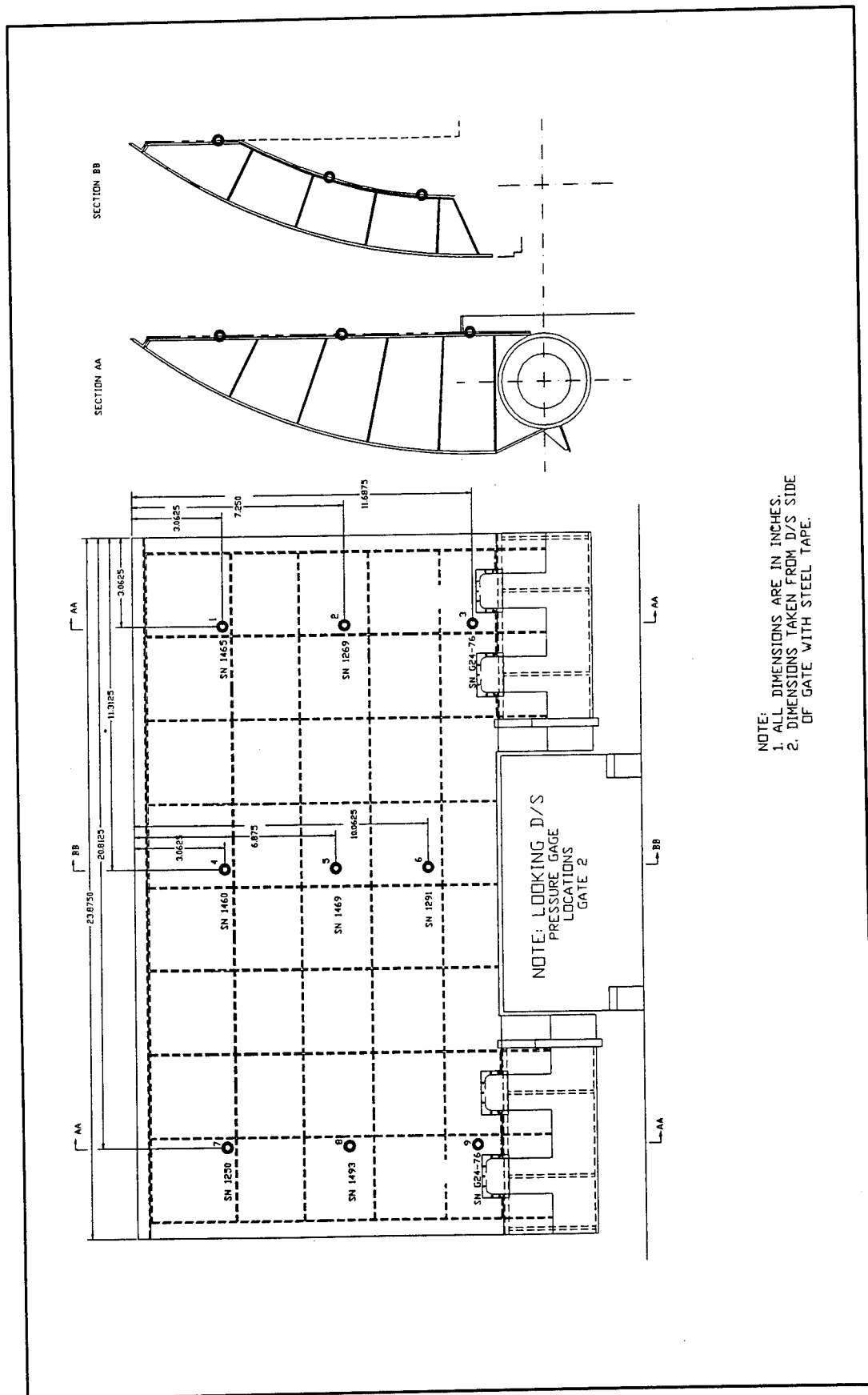


Plate 17. Montgomery Point Rigid Gate Model. Pressure cell locations on the downstream side of gate

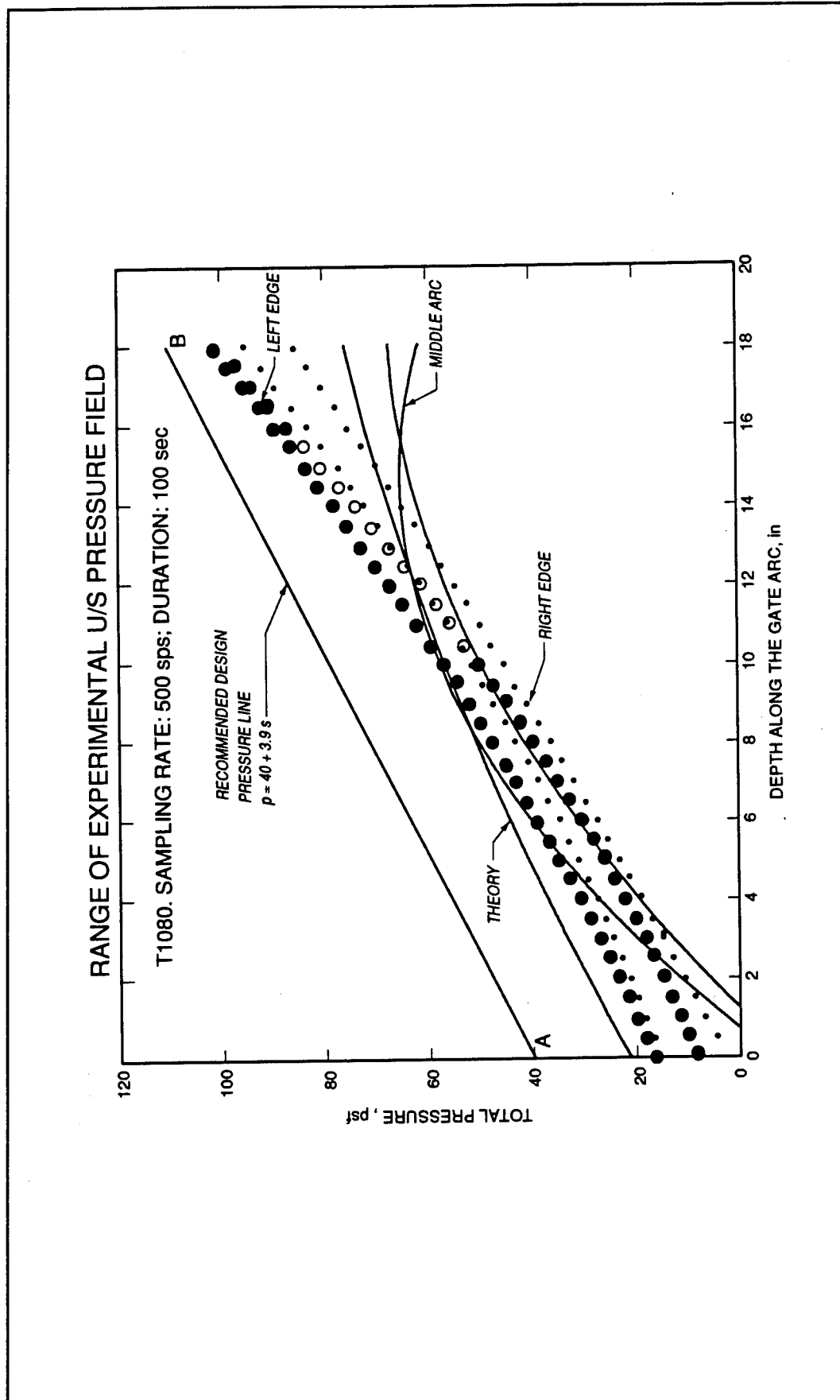


Plate 19. Montgomery Point Rigid Gate Model. Comparison of recommended design pressure field with the theoretical prediction and its 100-s test experimental counterpart

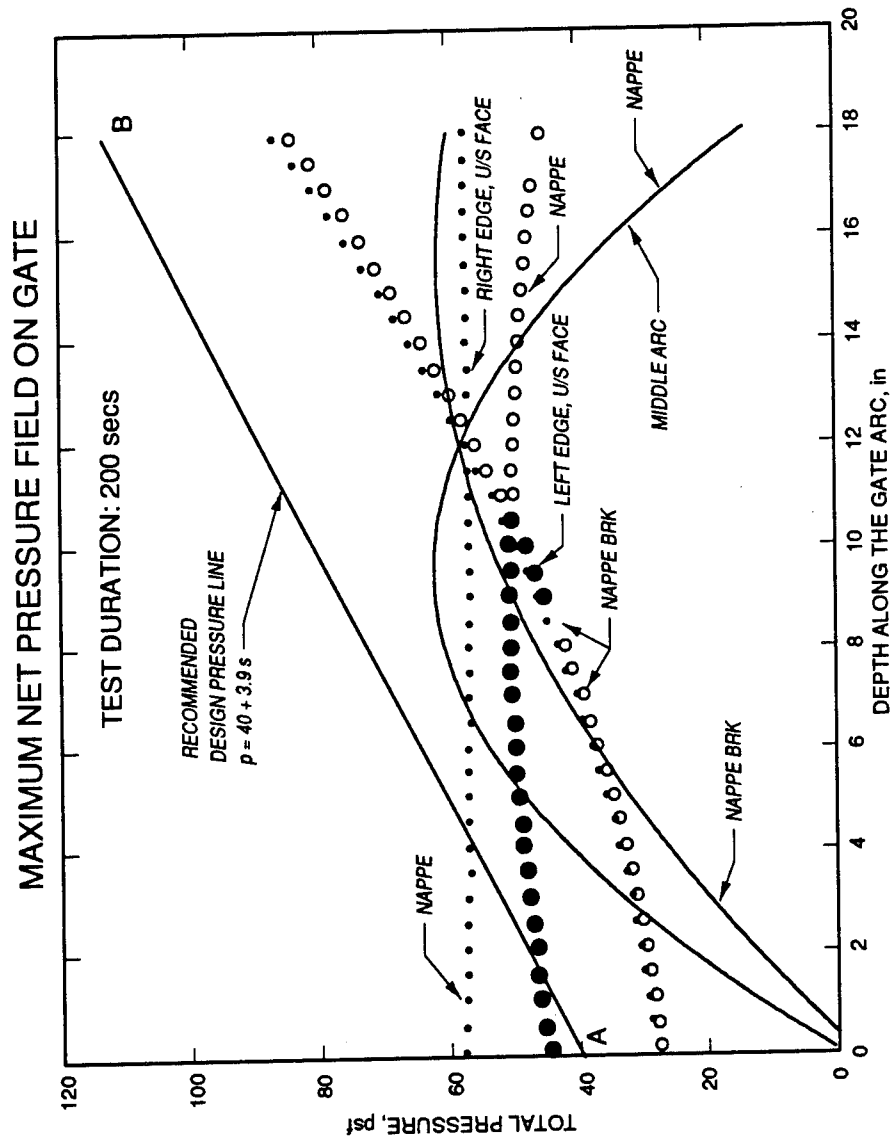


Plate 20. Montgomery Point Rigid Gate Model. Comparison of recommended design pressure field with the maximum net pressure field on the gate in 200-s experiments T1108 (integral nappe) and T1109 (ventilated nappe)

Scale Model F.E. Grid:

16069 Nodes

5580 Elements

Brass

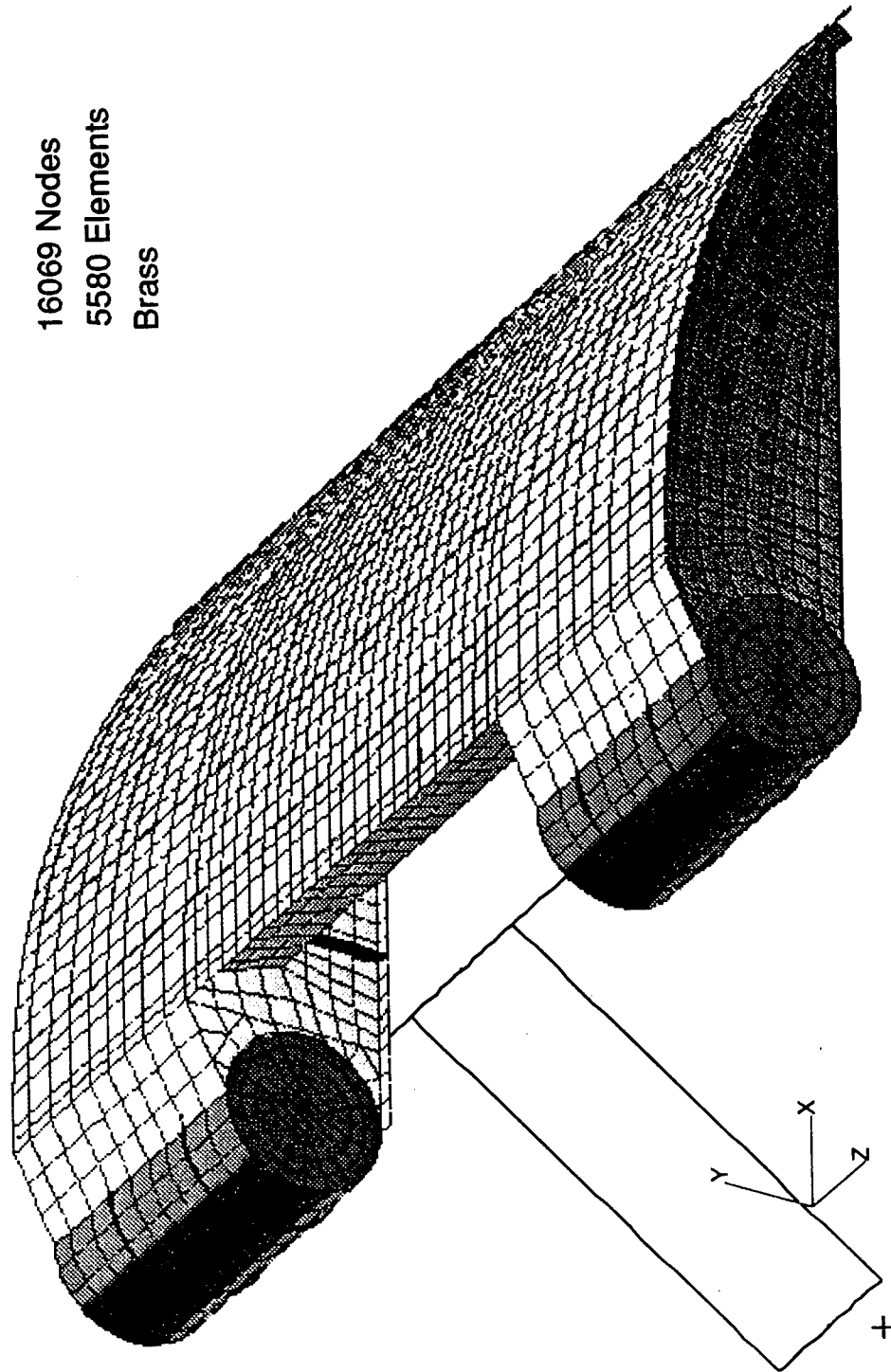


Plate 21. Montgomery Point Rigid Gate 1/15-Scale Model. Isometric view of the upstream side of the finite element grid

Scale Model F.E. Grid:

16069 Nodes
5580 Elements
Brass

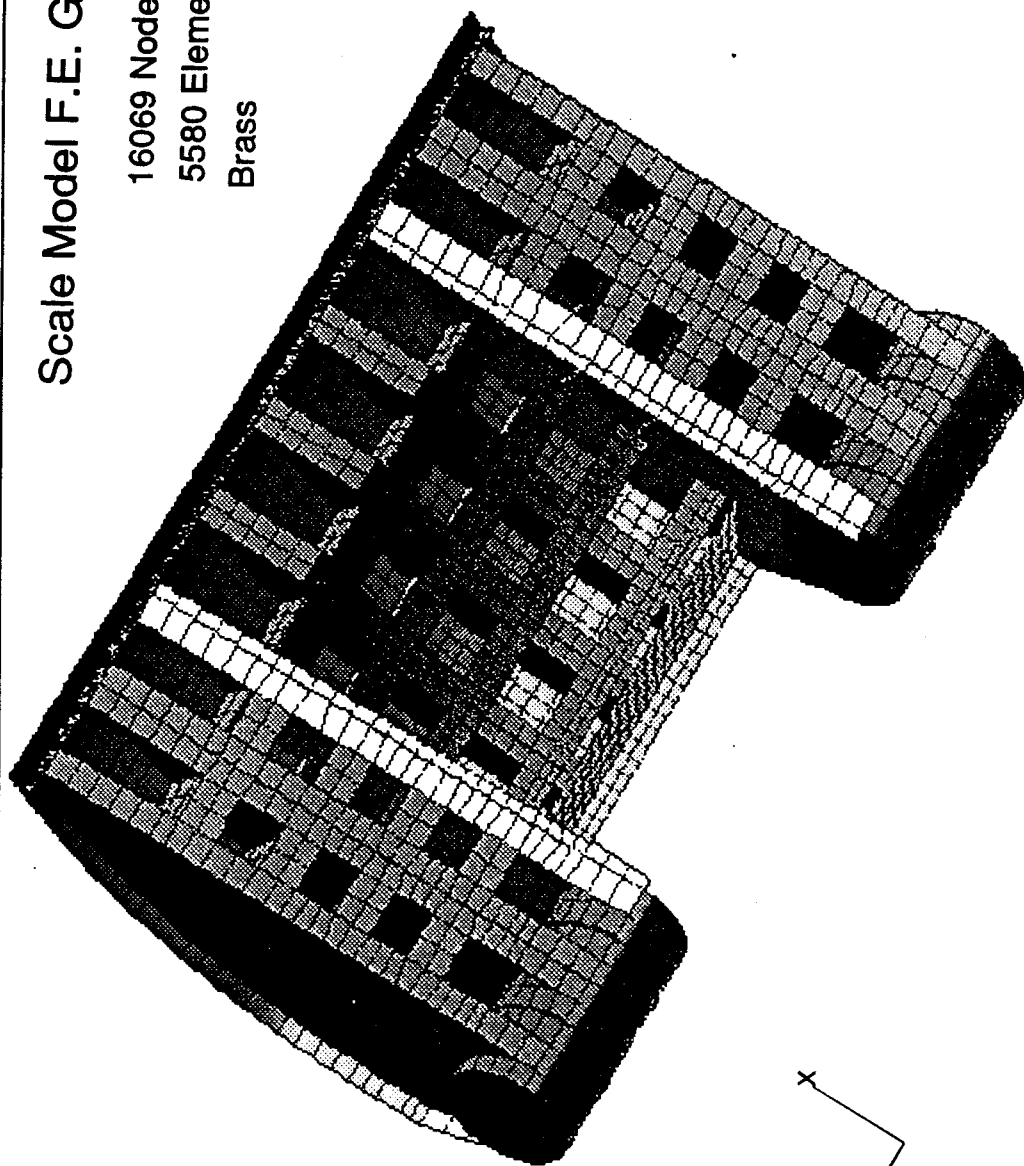


Plate 22. Montgomery Point Rigid Gate 1/15-Scale Model. Isometric view of the downstream side of the finite element grid

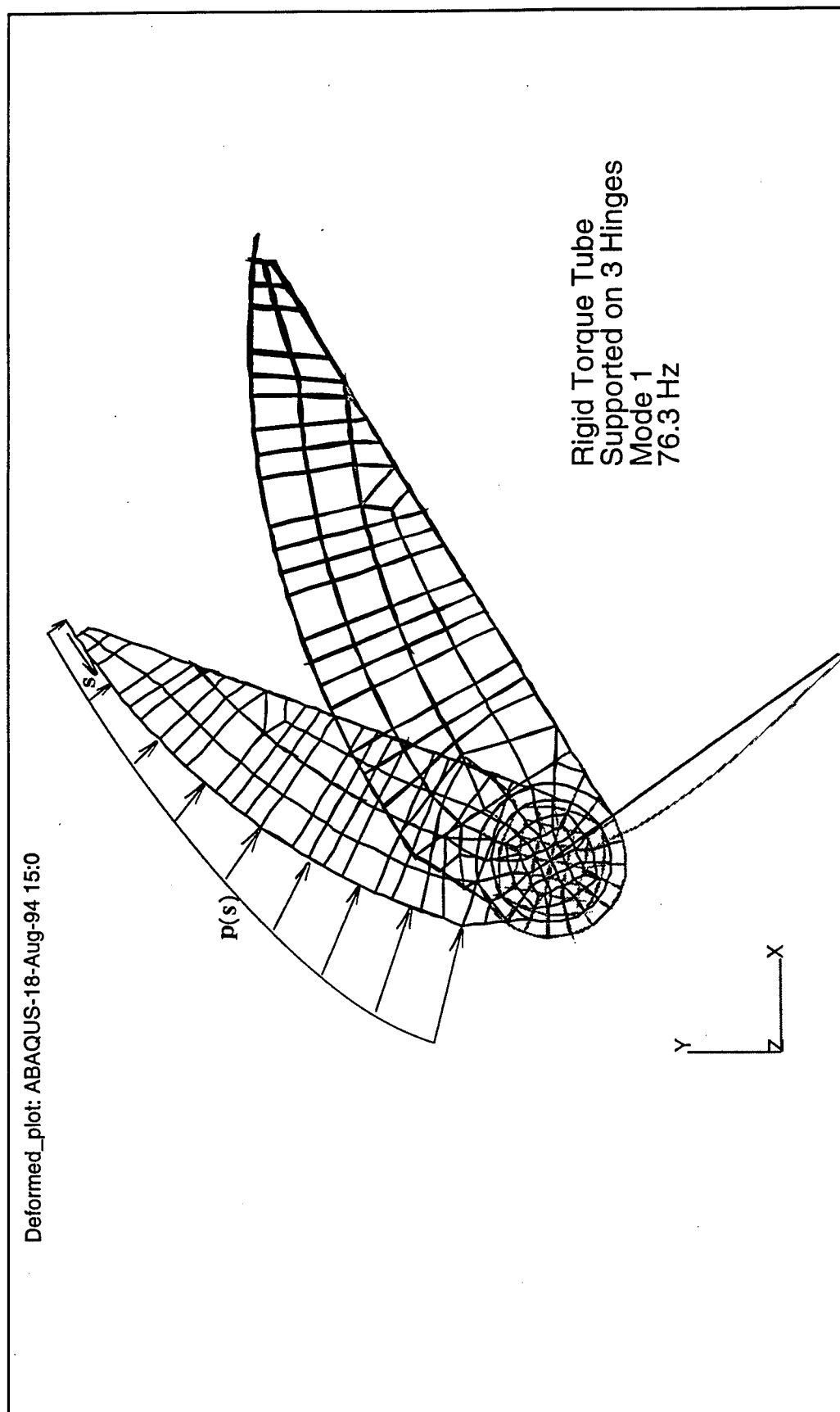


Plate 23. Montgomery Point Rigid Gate 1/15-Scale Model. Lateral view of the deflected configuration of the finite element model subjected to the recommended design pressure field

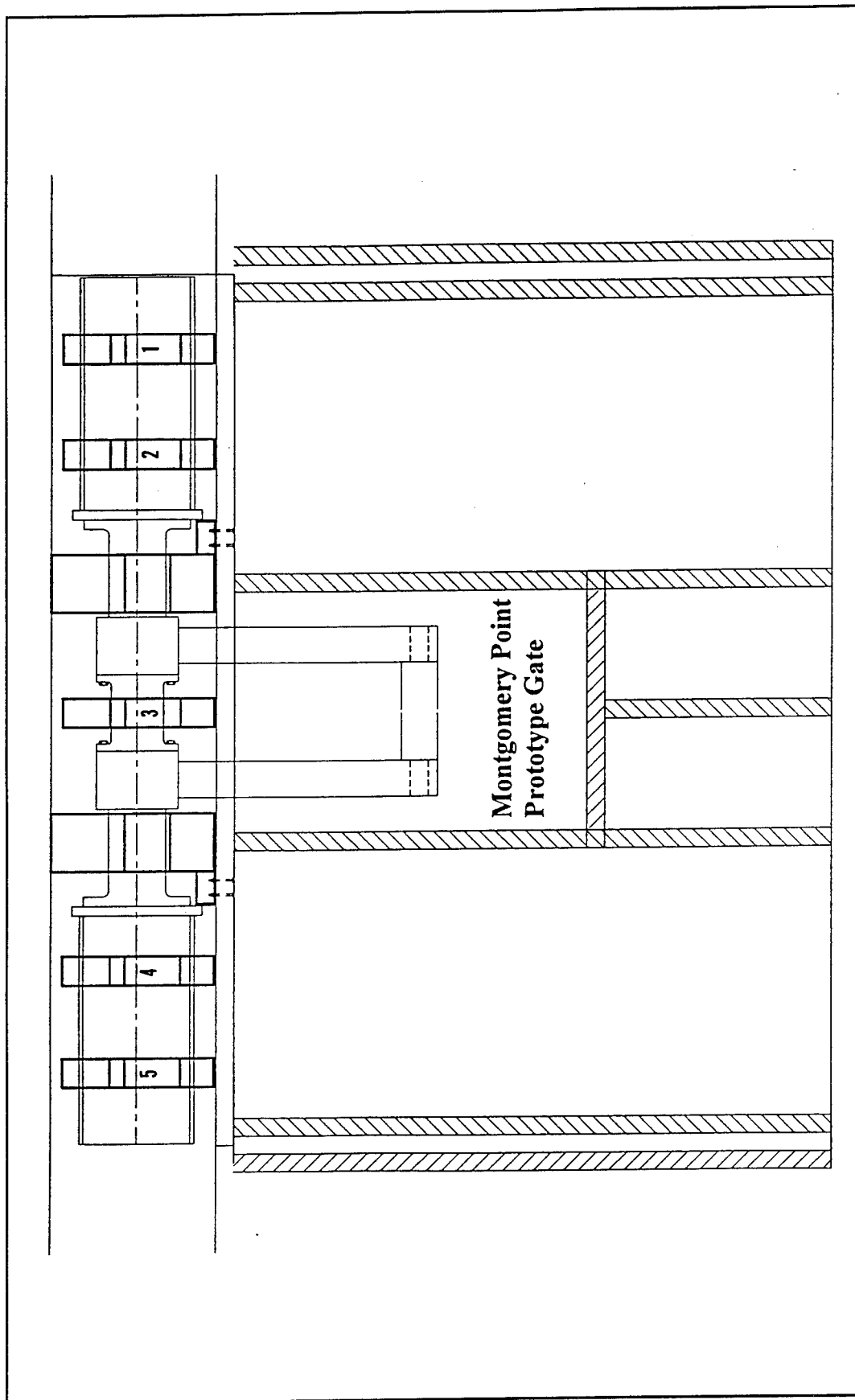


Plate 24. Montgomery Point Prototype Gate. Plan view of gate and location of recommended five supports

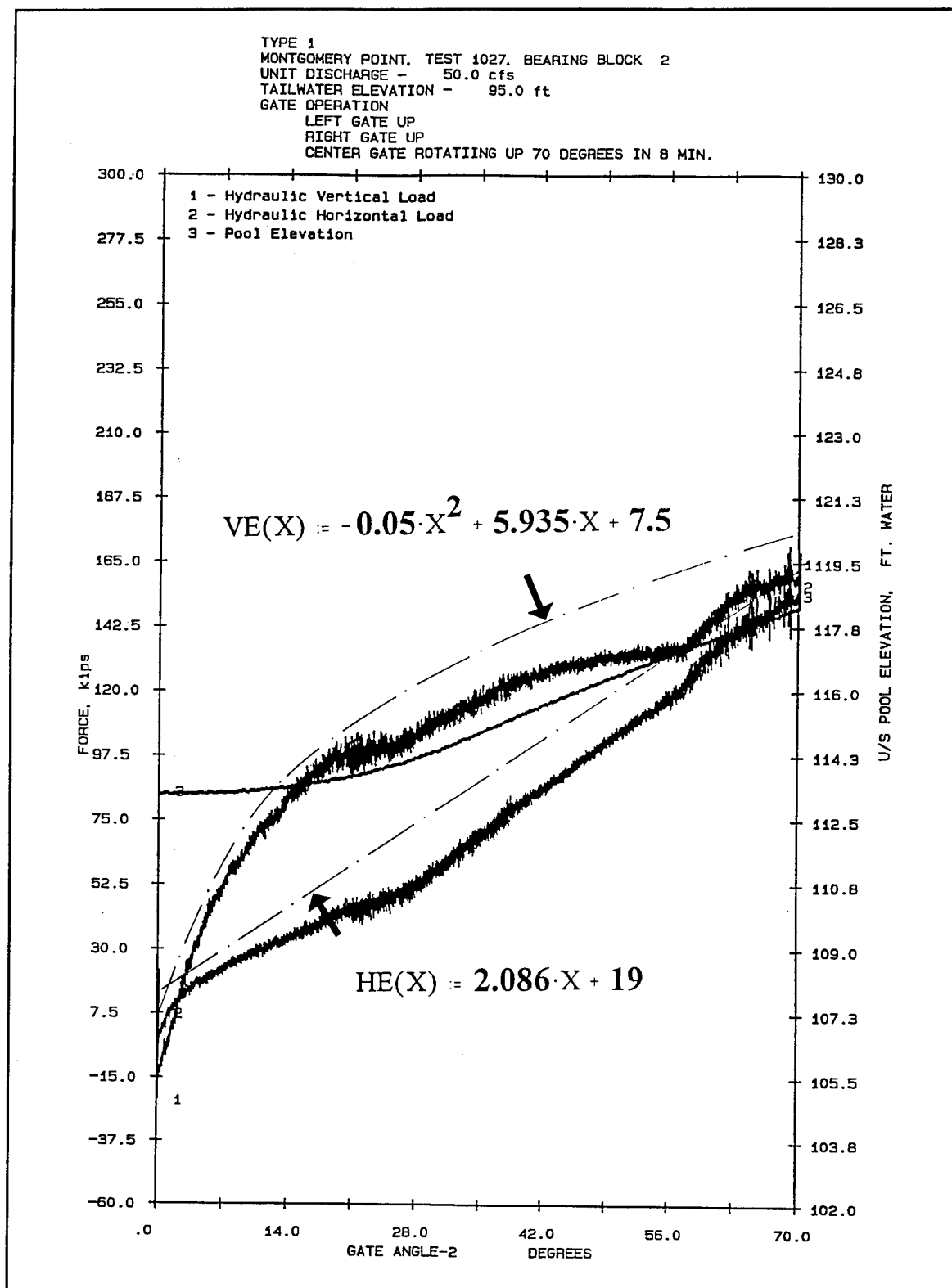


Plate 25. Montgomery Point Prototype Gate. Envelopes for horizontal (HE) and vertical (VE) components of the resultant reaction at supports 1 and 2 as a function of the gate elevation (X). The envelopes are derived from the records for bearing block 2 in the physical model during the controlling test T1027

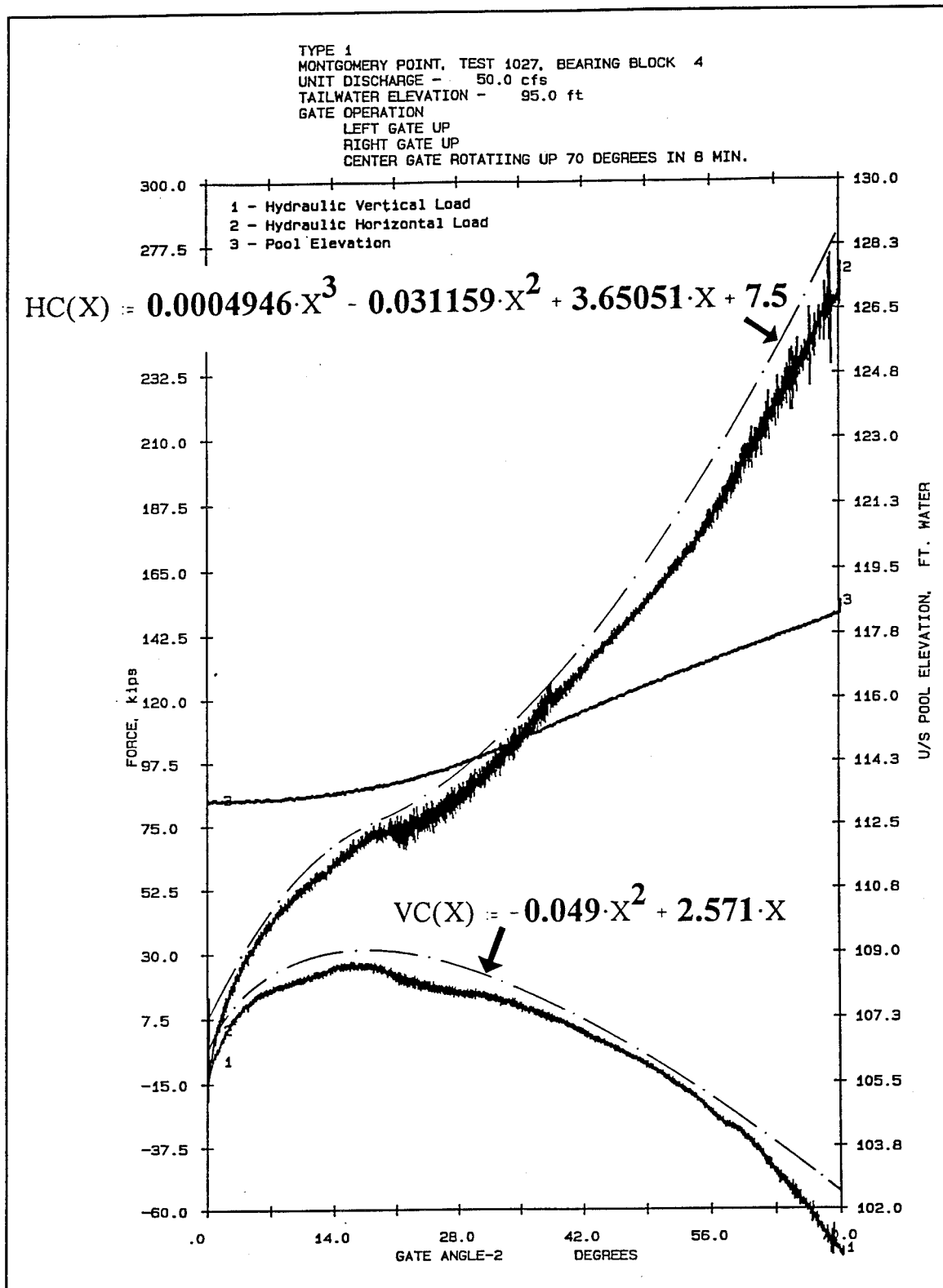


Plate 26. Montgomery Point Prototype Gate. Envelopes for horizontal (HC) and vertical (VC) components of the resultant reaction at the central support 3 as a function of the gate elevation (X). The envelopes are derived from the records for bearing block 4 in the physical model during the controlling test T1027

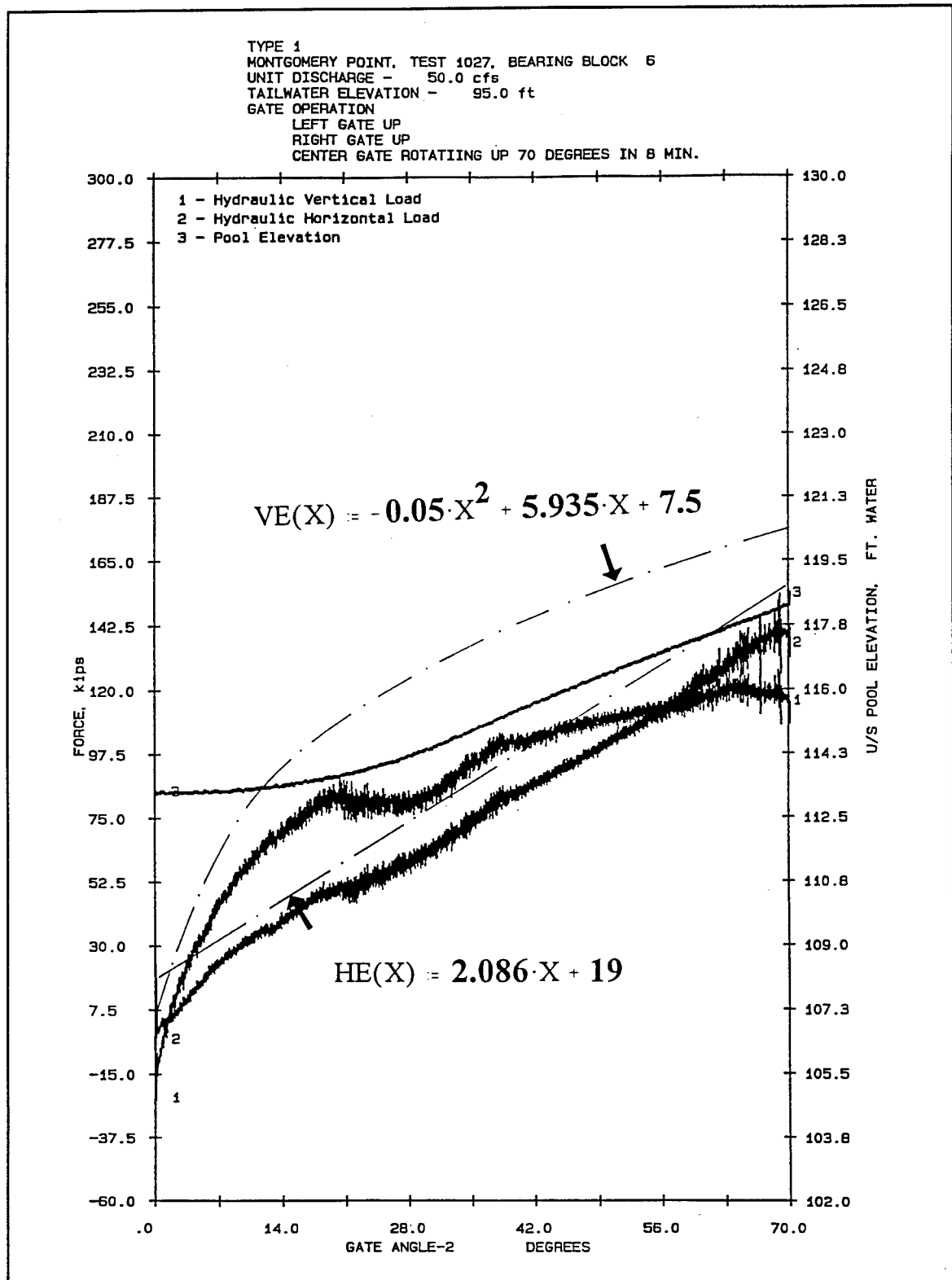


Plate 27. Montgomery Point Prototype Gate. Envelopes for horizontal (HE) and vertical (VE) components of the resultant reaction at supports 4 and 5 as a function of the gate elevation (X). The envelopes are derived from the records for bearing block 6 in the physical model during the controlling test T1027

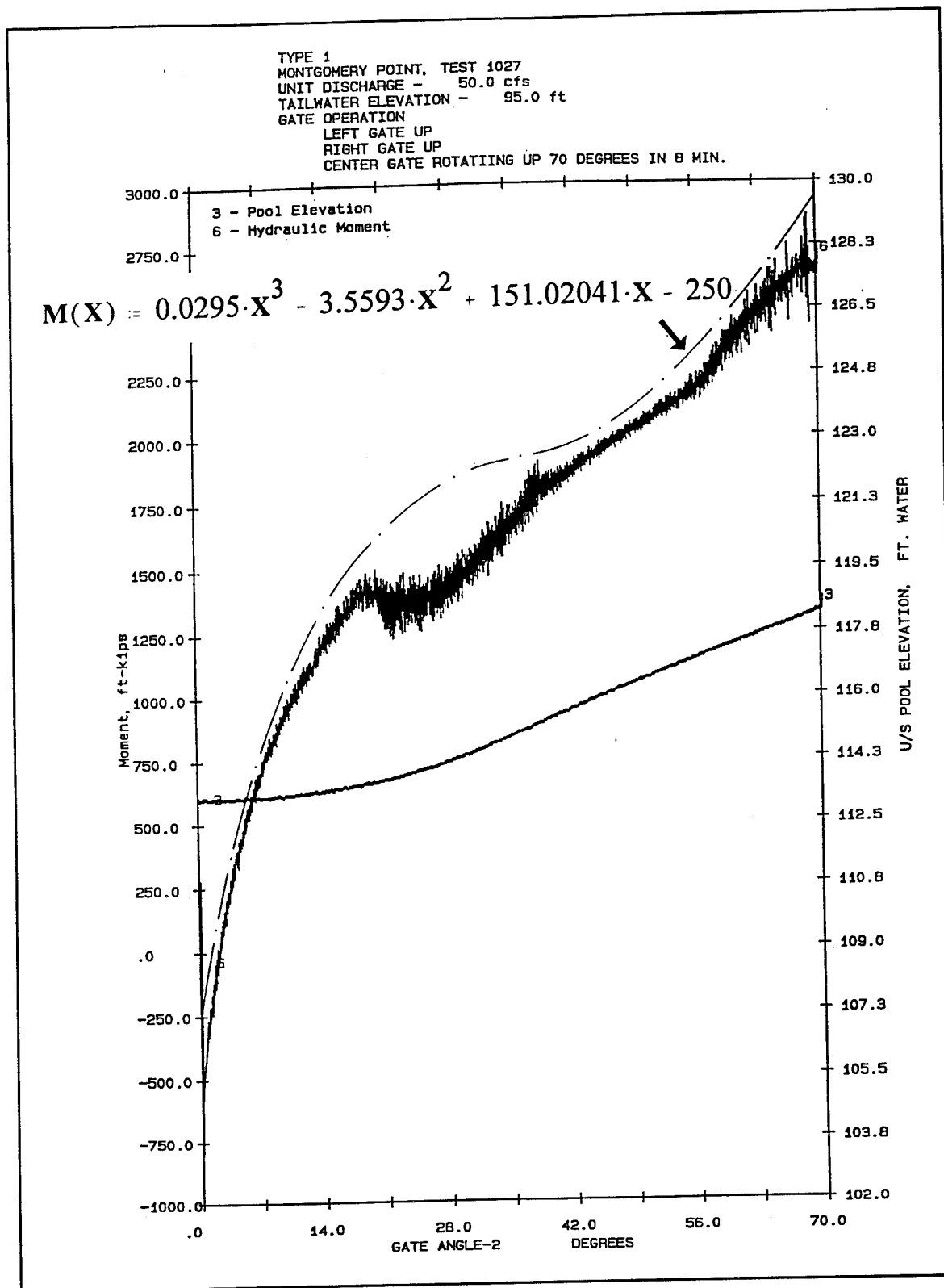


Plate 28. Montgomery Point Prototype Gate. Envelope for the total hydraulic moment (M) as a function of the gate elevation (X). The envelope is derived from the records for the hydraulic moment in the physical model during the controlling test T1027

16889 Nodes
5884 Elements

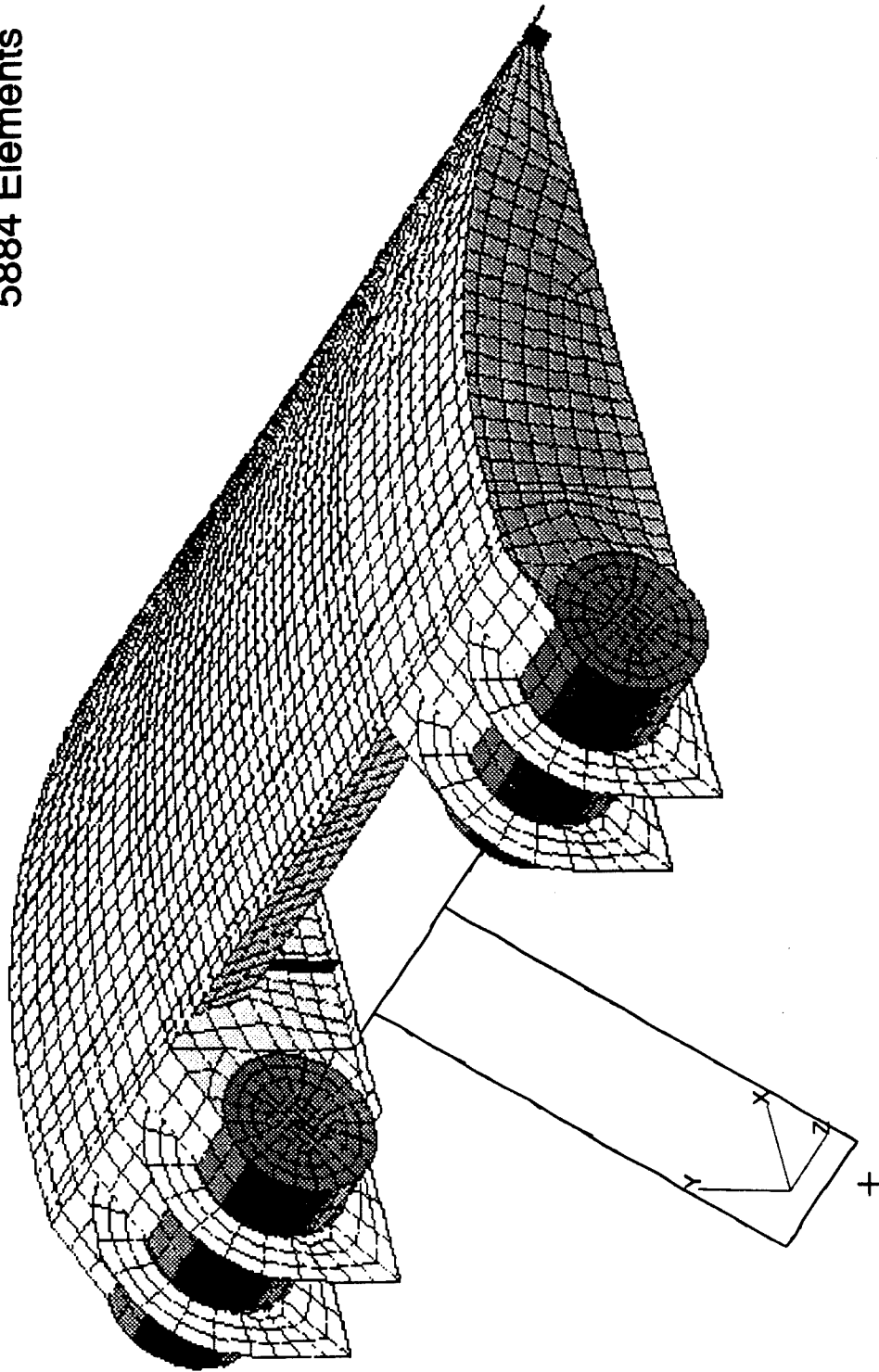
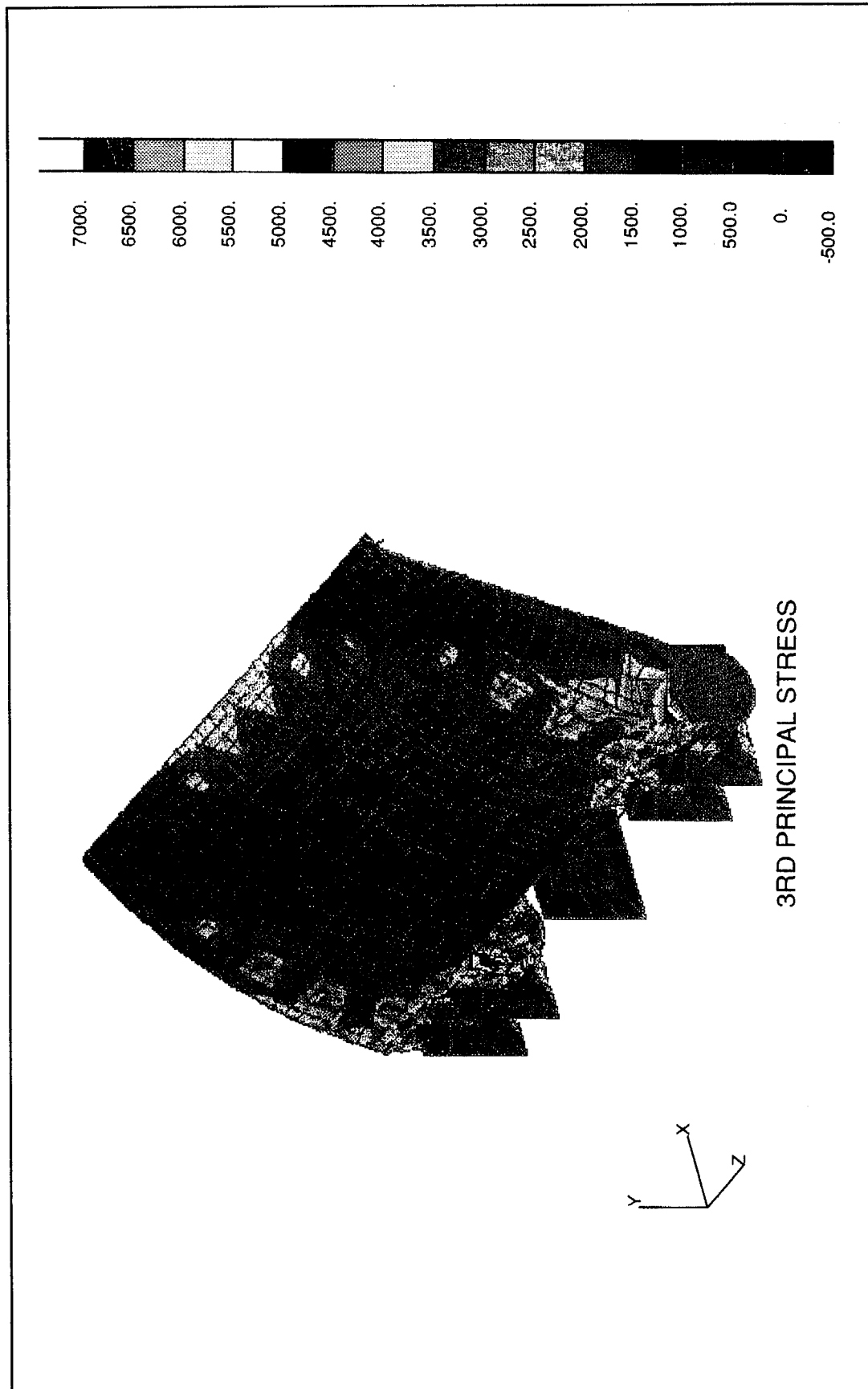


Plate 29. Montgomery Point Prototype Gate. Isometric view of upstream side of finite element grid



63 Plate 30. Montgomery Point Prototype Gate. Iso-principal-stress (tensile) regions on the upstream face of the gate

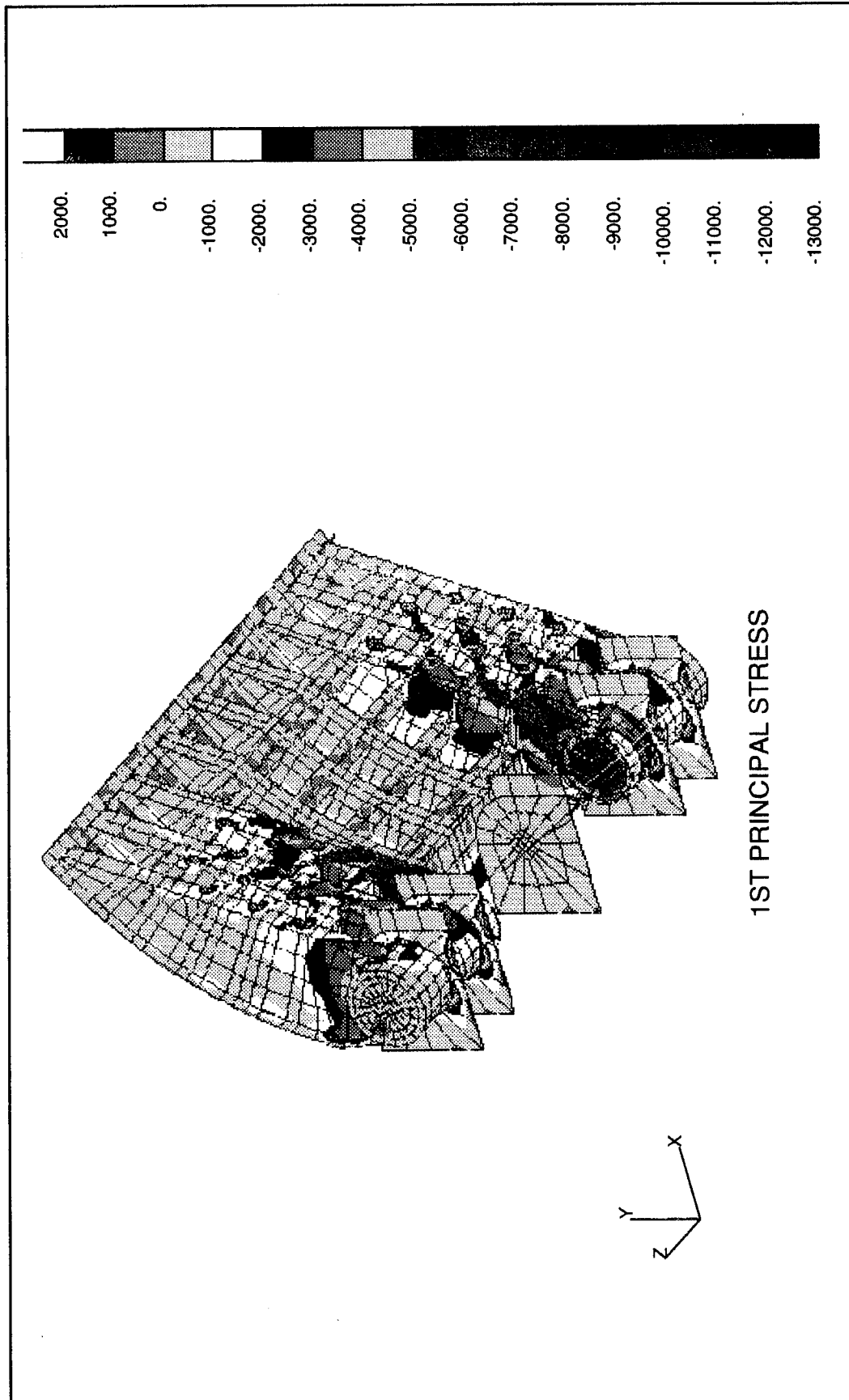


Plate 31. Montgomery Point Prototype Gate. Iso-principal-stress (compressive) regions on the elements of the downstream face of the gate

4 Extreme-Value Analysis of Experimental Pressure Data

The objective of an extreme-value analysis of the experimental pressure data is to provide the designer with a rational estimation of the largest-magnitude hydraulic loads to act on the gate during its useful life. Three models are considered in this study. The first two models are probabilistic in nature and are based on well established extrapolation techniques mostly applied in offshore (Cartwright and Longuet-Higgins 1956, Clough and Penzien 1975) and wind engineering (Davenport 1963, Clough and Penzien 1975, Simiu and Scanlan 1986), respectively. The third model aims at the determination of deterministic design pressure fields involving the results of many tests subjecting the gate physical model to multiple unusual and extreme loading conditions during the second phase of the experimental project.

Probability Distribution for Maxima

Assuming a zero-mean stationary Gaussian process $\xi(t)$ (Benjamin and Cornell 1970, Crandall and Mark 1963, Naudascher 1991) having an arbitrary spectral density $S_\xi(f)$, Cartwright and Longuet-Higgins (1956) have derived the probability density function for maxima in the process as

$$p(\eta) = \frac{1}{(2\pi)^{1/2}} \left[\epsilon e^{-\frac{\eta^2}{2\epsilon^2}} + (1-\epsilon^2)^{1/2} \eta e^{-\frac{\eta^2}{2}} \int_{-\infty}^{\frac{\eta(1-\epsilon^2)^{1/2}}{\epsilon}} e^{-\frac{x^2}{2}} dx \right] \quad (29a)$$

where the nondimensional random field η is defined by

$$\eta = \frac{\xi}{m_0^{1/2}} \quad (29b)$$

the parameter ϵ is given by

$$\epsilon^2 = 1 - \frac{m_2^2}{m_0 m_4} \quad (29c)$$

and m_i , $i = 0, 1, \dots, 4$, are the i^{th} moments of the spectral density function about the origin in the frequency domain.

Plate 32 shows this probability density function for different values of the parameter ϵ . It can be shown that the parameter ϵ lies in the range (0,1). For the limiting case $\epsilon \rightarrow 0$, this density function reduces to the form of a Rayleigh distribution, whereas for the limiting case $\epsilon \rightarrow 1$, the resulting distribution of maxima approaches the form of a Gaussian distribution (Cartwright and Longuet-Higgins 1956, Clough and Penzien 1975).

Test T1080 was selected as a pilot experiment to determine the nature of the parameter ϵ in the context of the experimental project. The process is assumed stationary and ergodic (Yang 1986, Crandall and Mark 1963). The time-average (mean) for each pressure-cell record in the test was first computed and extracted from the data (refer to the third column in Table 5). The power spectral density function was then generated for the upstream, downstream, and net upstream pressure records, respectively, for each cell on the instrumented gate. Plates 33 to 35 show representative spectral densities—in this particular case, for pressure cell 4. The area under each spectral density (m_0), as well as the second and fourth moments (m_2 and m_4), were calculated by means of a computer program under MATLAB (MATHWORKS 1993) (Table 5).

The last column of Table 5 shows the resulting value of the parameter ϵ for each pressure cell recorded during the test. Notice that most results are above 0.9. Thus, for all practical purposes, the energy-content parameter ϵ may be assumed as one ($\epsilon = 1$) for the random field under study (η), and the distribution for the peaks are assumed to be Gaussian. Therefore, the maxima for the pressure field may be predicted using standard tables for the normal distribution, for any confidence level selected by the designer. For example, based on test T1080, the maximum value predicted for the net upstream pressure on cell 1 is its mean value plus $1 \cdot \sqrt{m_0}$, $2 \cdot \sqrt{m_0}$, or $3 \cdot \sqrt{m_0}$, with a confidence level of 68.27, 95.45, or 99.73 percent, respectively (Benjamin and Cornell 1970, Simiu and Scanlan 1986). Assuming a 95.45-percent confidence level, this maximum net upstream pressure is $8.3368 + 2 \cdot \sqrt{4.8196}$ in. of water = 12.73 in. of water, or, approximately, 66.2 psf. The exact 95.45-percent confidence-level extreme-pressure would be given by $8.3368 + \eta^* \sqrt{4.8196}$ in. of water, where η^* is the abscissa in Plate 32 for the curve corresponding to $\epsilon = 0.9122$ such that the area under the curve from $-\infty$ to η^* is 97.75 percent. This technique was verified to give results close to those provided by the second model, and since the second model (described next) is computationally simpler, the present model was not elaborated any further.

Table 5
Computation of Energy Parameter ϵ for Test T1080 (Sampling Rate: 500 sps;
Duration: 100 s)

	Pressure Cell	Mean in. of H ₂ O	Standard in. of H ₂ O	m_0 , in. of H ₂ O ²	m_2 , in. of H ₂ O ² .Hz ² .10 ³	m_4 , in. of H ₂ O ² .Hz ⁴ .10 ⁸	ϵ
Upstream Absolute Pressure	1	6.7416	0.1413	4.2714	9.577	1.3238	0.9153
	2	-	-	-	-	-	-
	3	-	-	-	-	-	-
	4	2.9206	0.1015	2.0862	4.391	0.5029	0.9035
	5	7.7400	0.0965	1.9815	4.538	0.7177	0.9248
	6	9.5441	0.0772	1.1306	4.048	0.9212	0.9180
	7	6.6816	0.0861	1.4237	3.694	0.5590	0.9102
	8	7.0849	0.0758	1.1800	2.664	0.3196	0.9010
	9	11.5024	0.0643	0.7376	2.826	0.7068	0.9202
Upstream Net Pressure	1	8.3368	0.1871	4.8196	16.476	3.3545	0.9122
	2	-	-	-	-	-	-
	3	-	-	-	-	-	-
	4	4.3399	0.1453	1.7876	3.6142	0.5791	0.9348
	5	8.8518	0.1379	1.6158	3.5448	0.7584	0.9473
	6	9.1549	0.1275	2.2399	8.3125	2.7166	0.9415
	7	8.0089	0.1277	1.4084	3.6209	0.7168	0.9328
	8	7.7458	0.1311	1.9458	3.7999	0.8607	0.9559
	9	7.3164	0.1690	3.8893	16.019	6.2200	0.9455
Downstream Absolute Pressure	1	-1.3243	0.1136	0.6609	1.4868	0.1500	0.8880
	2	-0.6609	0.1124	1.0470	2.0179	0.5268	0.9624
	3	4.1859	0.1552	3.0953	12.7070	5.2264	0.9488
	4	-1.4193	0.1168	0.6237	1.481	0.1629	0.8855
	5	-1.1117	0.1248	0.5615	1.2666	0.1241	0.8773
	6	0.3893	0.1113	1.2813	4.7401	1.6991	0.9470
	7	-1.5952	0.1243	1.0473	8.2132	1.9456	0.8179
	8	-	-	-	-	-	-
	9	-	-	-	-	-	-

Probability Distribution for Extreme Values

The second model is the preferred probabilistic extrapolation method for being computationally efficient and, to a certain extent, experimentally verified in the context of wind engineering. The model was originally derived by Davenport (1963) and consists of a modification of the Gumbel Type I extreme-value distribution of the largest values (Benjamin and Cornell 1970, Clough and Penzien 1975). In this method, it is assumed that the parameters of the distribution can be obtained by replacing the mean and the mean square value of the random variable *pressure* (X) by the corresponding statistics of the sample. Specifically,

$$\hat{\sigma} = \frac{\sqrt{6}}{\pi} s \quad (30a)$$

and

$$\hat{\mu} = \bar{X} - 0.5772 \hat{\sigma} \quad (30b)$$

where \bar{X} and s are the sample mean and the sample standard deviation, respectively.

With these estimators, the following estimator can be constructed

$$\hat{G}_X(p) = \bar{X} + s(y - 0.5772) \frac{\sqrt{6}}{\pi} \quad (31a)$$

where

$$y = -\ln(-\ln p) \quad (31b)$$

and p is the probability of exceeding the target pressure level within a predefined subinterval of the mean recurrence interval.

Under the assumption that the random variables \bar{X} and s are asymptotically normally distributed, it can be shown that, for large samples of size n , the standard deviation of the estimator in Equation 31 is given by

$$SD = \left[\frac{\pi^2}{6} + 1.1396(y - 0.5772) \frac{\pi}{\sqrt{6}} + 1.1(y - 0.5772)^2 \right]^{1/2} \frac{\hat{\sigma}}{\sqrt{n}} \quad (32)$$

Then the approximate statement can be made that the interval $\hat{G}_X(p) \pm SD$ corresponds to the 68-percent confidence level, $\hat{G}_X(p) \pm 2 \cdot SD$ corresponds to the 95-percent confidence level, and $\hat{G}_X(p) \pm 3 \cdot SD$ corresponds to the 99.7-percent confidence level.

For example, considering the controlling test T1108 (sampling rate: 500 sps; duration: 200 s), it was decided to envision the records for pressure as composed by series of 2-s lapses. So, the starting objective is to generate a table of two-secondly maximum total hydraulic pressures. Since each record contains 100,000 data points, and each 2-s lapse contains 1,000 points, then the table of two-secondly maxima contains 100 data points from which the sample statistics (mean \bar{X} and standard deviation s) are computed.

If it is decided to design the gate such that the allowable stress under total hydraulic pressure is exceeded with a 50-year mean recurrence period, i.e., $50 \times 365 \times 24 \times 1,800 = 7.884 E+8$ two-s recurrence interval, then the probability of exceedance in any 2-s subinterval is

$$p = \frac{1}{7.884 E+8} = 1.2684 E-9$$

The probability that the allowable stress be attained at least once in a given number of years is given by $1 - (1 - p)^{(1 \times 365 \times 24 \times 1,800)}$ and appears listed in Table 6 (Benjamin and Cornell 1970).

Table 6 Probability that Allowable Stress be Exceeded at Least Once in a Given Time Interval, 50-year Mean Recurrence Interval	
Time Interval, Years	Probability of Exceedance, Percent
1	2.0
5	9.5
10	18.02
20	32.79
25	39.15
50	63.0
100	86.3

A computer program under MATLAB (MATHWORKS 1993) was developed for the automatic execution of Equations 30 through 32. Plate 36 shows the underlying probability distribution for the extreme value of the net pressure field on the upstream face of the physical model at the location of cell 1, as an example. Plates 37 and 38 show the prediction of this extrapolating mathematical model for the same pressure field on the upstream side of the

gate for the pilot test T1080 and for the controlling test T1108, respectively. Each plate presents the extreme-pressure curves for the reference longitudinal arcs of the gate—i.e., the right edge (sequences of dots), the middle arc (solid lines), and the left edge (sequences of circles), looking in the downstream direction into the upstream side of the gate (Plate 18). The curves denoted as 1, 2, and 3 represent parabolic polynomial fits on three data points for the 68, 95, and 99.7-percent confidence levels, respectively.

The plots in Plates 37 and 38 definitely show similar trends.

Pressure Envelopes—Phase 2 of the Experimental Project

A second phase of the experimental project was devised to further examine the response of the gate under extreme conditions of discharge and pool elevations, and unusual operation, or both (USAEWES 1994b). In particular, during the experiments in the second phase, the unit discharge was generally variable and larger than 50 cfs (the unit discharge was maintained fixed during the first phase). Also, in this second phase of the project, conditions involving extensive motion over the whole range of inclinations of the instrumented gate were considered.

For each of 37 experiments in the second phase, a plot presenting the most relevant deterministic information on the pressure field was generated (USAEWES 1994b). However, in reviewing the data from the Phase 2 study, the WES engineering team discovered that a key pressure cell had malfunctioned during the experiments. The controlling tests of the Phase 2 study (Table 7) were repeated and new design pressure fields on the gate were generated.

The information summarized next complements the pressure contours presented in Report 1 of this study (Fletcher and de Bejar 1995). As before, each plot represents the most relevant deterministic information for the individual tests in the series. In general, for each reference longitudinal arc in the gate (i.e., the right edge, the middle arc, and the left edge), a parabolic polynomial has been fitted to the three-point spectral data extracted from the net pressure-cell time-histories of response (duration: 100 s per test). Plates 39 and 40 present the results for the controlling individual tests in the series¹ (analytical expressions for each design pressure line appear at the bottom of each plate). Notice that, although pressure field results are now smaller in magnitude than previously reported (USAEWES 1994b,c), the tests controlling the design remain the same, i.e., test T1192 (before test T1160) for the upper region of the gate and tests T1179 and T1180 (before tests T1139 and T1140) for the intermediate and deep regions of the gate, respectively.

¹ Report 1 of this study describes the results for all tests in Phase 2 of the study.

Table 7
Montgomery Point Gate Model, Phase 2, New Tests to Replace
Some Defective Pressure-Cell Records

Test No.	Previous Test No.	q ¹ cfs/ft	Upper Pool Elev., ft	Lower Pool Elev. ft	Left Gate Position	Initial Center Gate Position	Center Gate Action	Right Gate Position
1179	1139	53.3	119	95	Raised	Raised	Hold	Raised
1180	1140	111.1	119	95	Raised	Raised	Hold	Lowered
1181	1141	144	116.8	95	Lowered	Raised	Hold	Lowered
1183	1143	Varies	119	95	Raised	Raised	Lowering	Raised
1184	1144	Varies	117	95	Raised	Raised	Lowering	Lowered
1187	1145	Varies	116.8	95	Lowered	Raised	Lowering	Lowered
1188	1152	Varies	115	95	Raised	Lowered	Raising	Raised
1189	1153	Varies	115	95	Raised	Lowered	Raising	Lowered
1190	1154	Varies	119	95	Raised	Lowered	Raising	Raised
1191	1155	Varies	117	95	Raised	Lowered	Raising	Lowered
1192	1160	Varies	121	115	Raised	Raised	Lowering	Raised

¹ Unit discharge based on a 90-ft-wide approach channel.

All these tests feature the central and left gates in raised position. In tests 1179 and 1192, the right gate is also held raised; but in the case of test 1179, the central gate (instrumented) is kept stationary, whereas in test 1192, the central gate goes to a lowered position during the test (with the upstream pool maintained above the normal level, simulating improper operation). In test 1180, the right gate is held steadily in lowered position (with the upstream pool maintained at the peak level, simulating extreme normal operation).

The envelopes in Plates 40 and 41 refer to the prototype and are provided as information to the designer. They are expressed algebraically as follows:

For the Right Edge:

$$-80.0 s + 1,000 \text{ [psf]}$$

$$0 \leq s < 5 \text{ ft}$$

$$+18.75 s + 506.25 \text{ [psf]}$$

$$5 \text{ ft} \leq s < 13 \text{ ft}$$

$$+9.649 s^2 - 169.1228 s + 1,317.895 \text{ [psf]}$$

$$13 \text{ ft} \leq s < 20 \text{ ft}$$

For the Middle Arc:

$$\begin{array}{ll} +16.2 s^2 - 348.5 s + 1,996.2 \text{ [psf]} & 0 \leq s < 4.5 \text{ ft} \\ +11.533 s + 704.1 \text{ [psf]} & 4.5 \text{ ft} \leq s < 15 \text{ ft} \\ +10.9 s^2 - 193 s + 1,319.6 \text{ [psf]} & 15 \text{ ft} \leq s < 17.5 \text{ ft} \end{array}$$

For the Left Edge:

$$\begin{array}{ll} -100.0 s + 1,500 \text{ [psf]} & 0 \leq s < 7 \text{ ft} \\ +800 \text{ [psf]} & 7 \text{ ft} \leq s < 14.5 \text{ ft} \\ +127.27 s - 1,045.46 \text{ [psf]} & 14.5 \text{ ft} \leq s < 20 \text{ ft}, \end{array}$$

where s is the depth of the point in question measured along the gate arc.

These input forcing functions should be used in the context of Allowable Stress Design for structural steel, i.e., there is no need for further factoring the loads since sufficient conservatism has already been built into the estimation procedure (AISC 1986).

Notice that the pressure levels as determined in Phase 2 of the project take precedence over all results from Phase 1, even over the results of the extreme-value analysis. Larger unit discharges are considered responsible for this substantial increase in the magnitude of the recommended design pressure field on the gate.

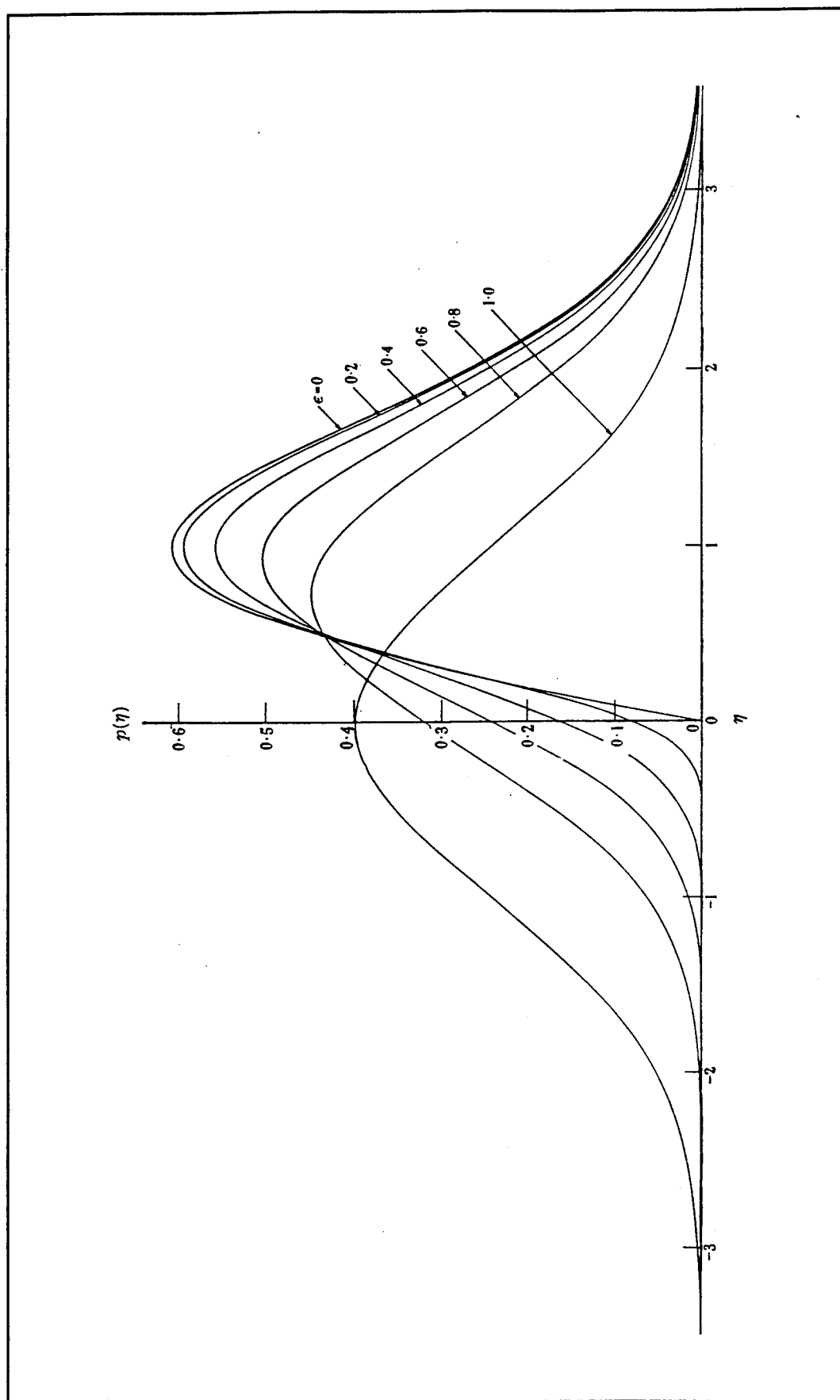


Plate 32. Probability density function for the peaks of the nondimensional random field η ($\eta = \xi/m_0^{1/2}$), for different values of the parameter ϵ

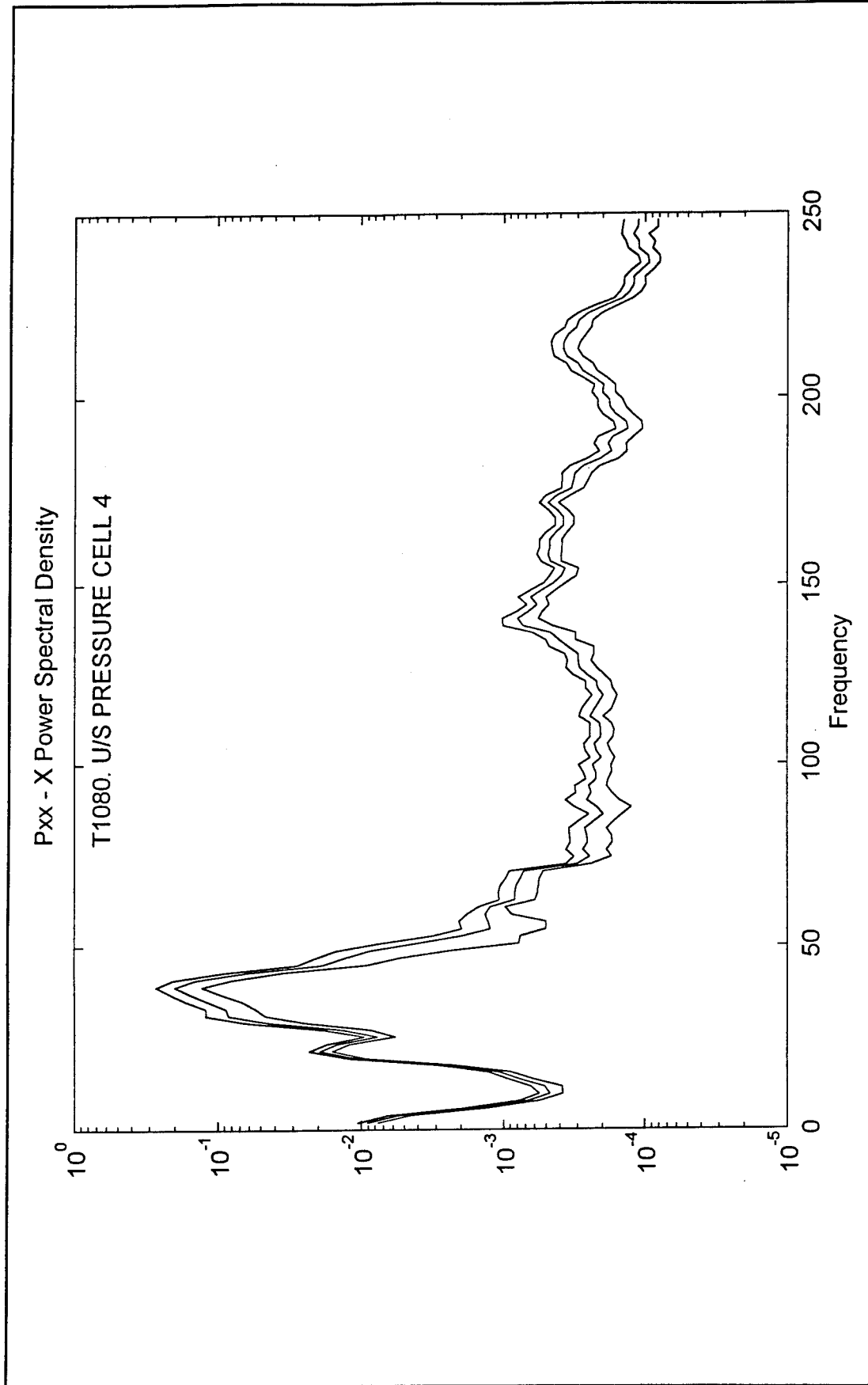


Plate 33. Spectral density for the pressure at cell 4 on the upstream face of the gate model during test T1080

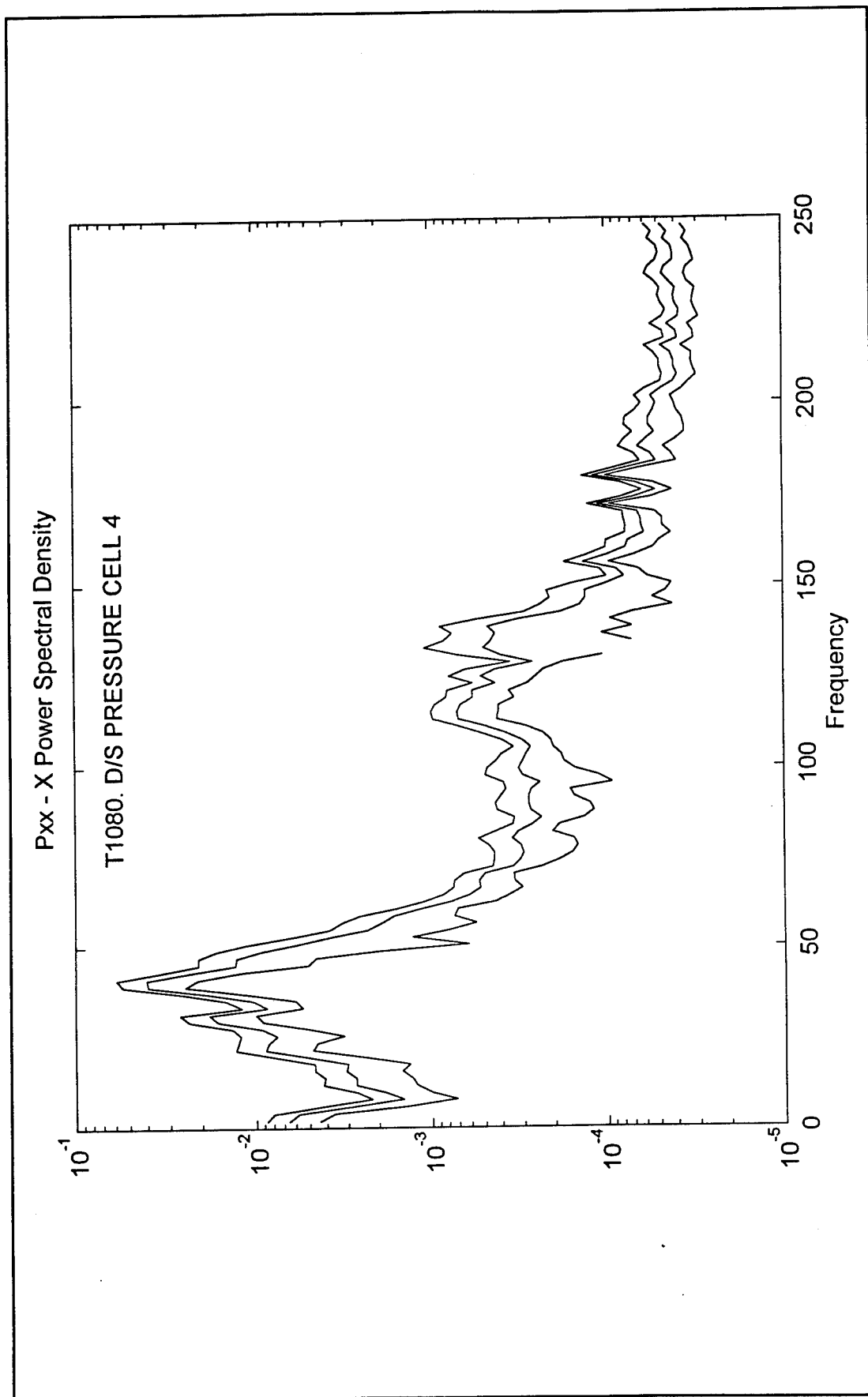


Plate 34. Spectral density for the pressure at cell 4 on the downstream face of the gate model during test T1080

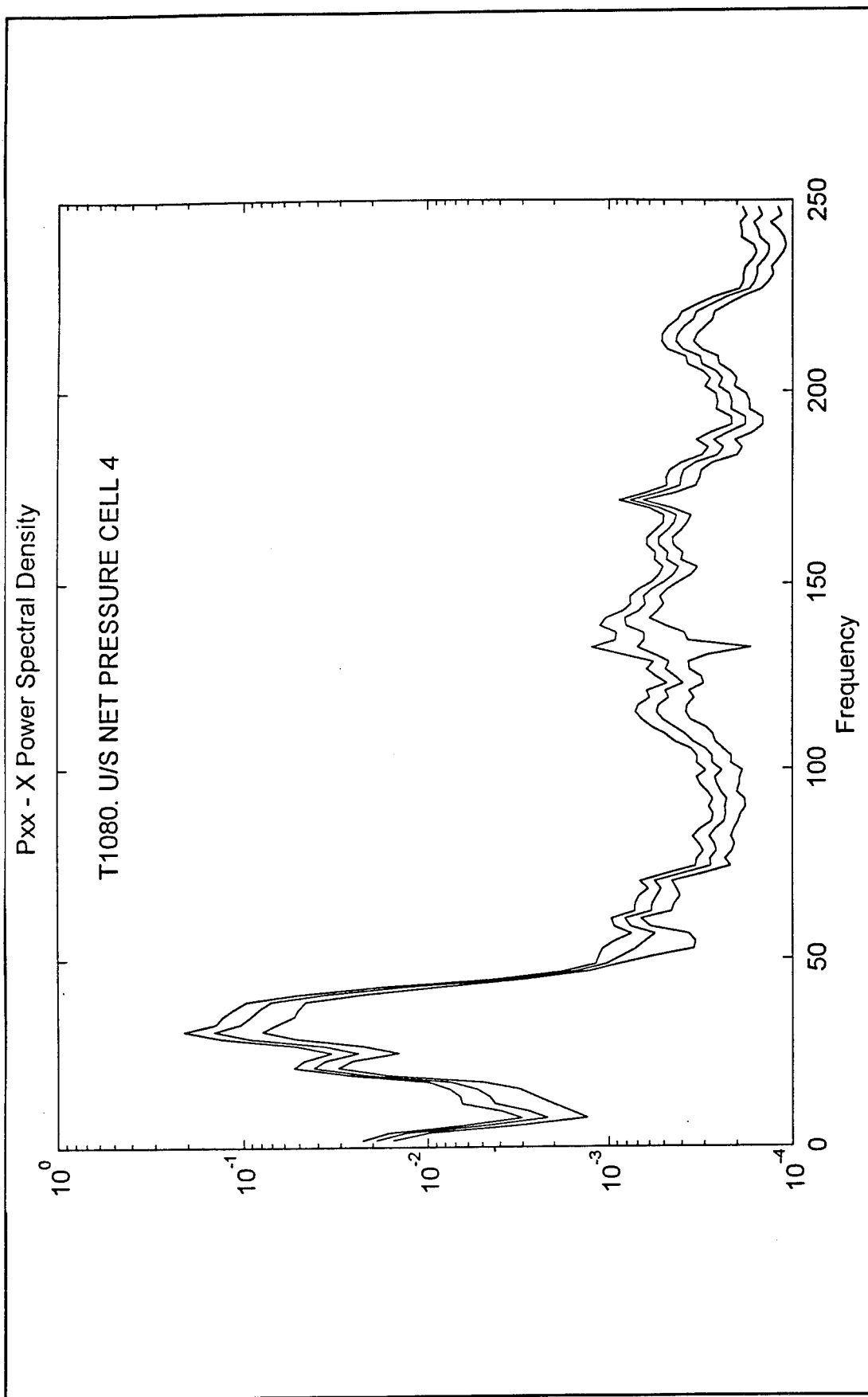


Plate 35. Spectral density for the net pressure on the upstream face of the gate model at the location of cell 4 during test T1080

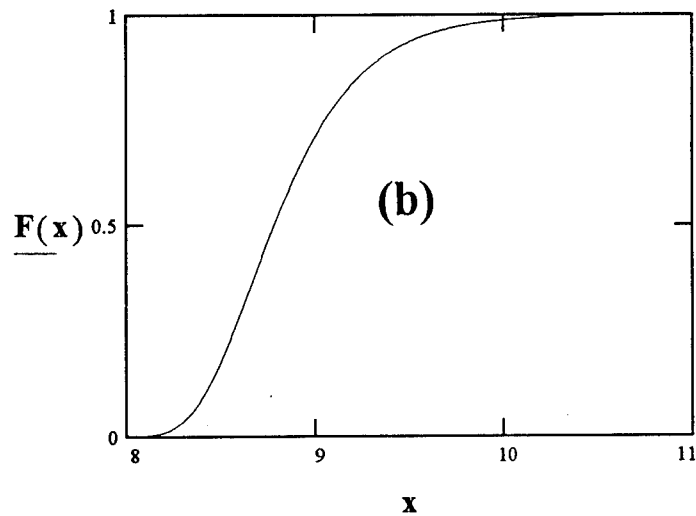
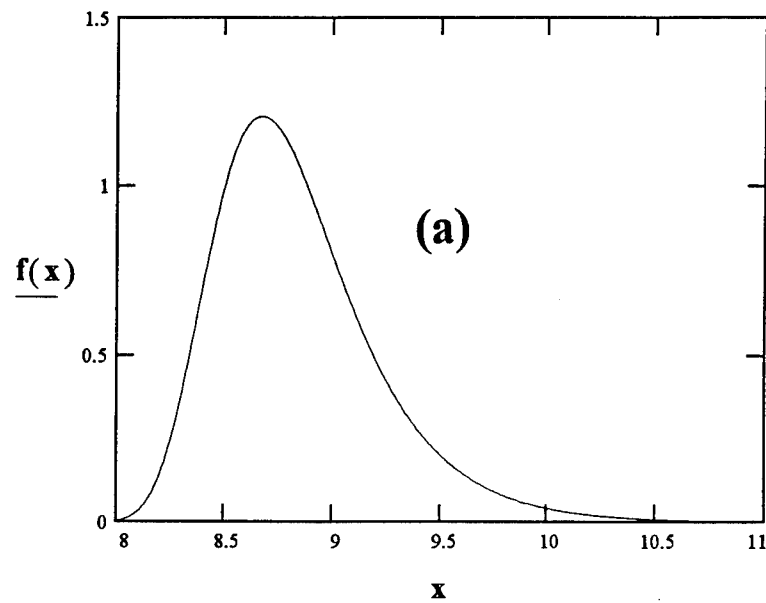


Plate 36. Probabilistic description of the extreme value of the net pressure on the upstream face of the gate model at the location of cell 1 during test T1108 [in. of H_2O]. (a) Probability density function (Gumbel Type I, of the largest values), and (b) the corresponding probability distribution function

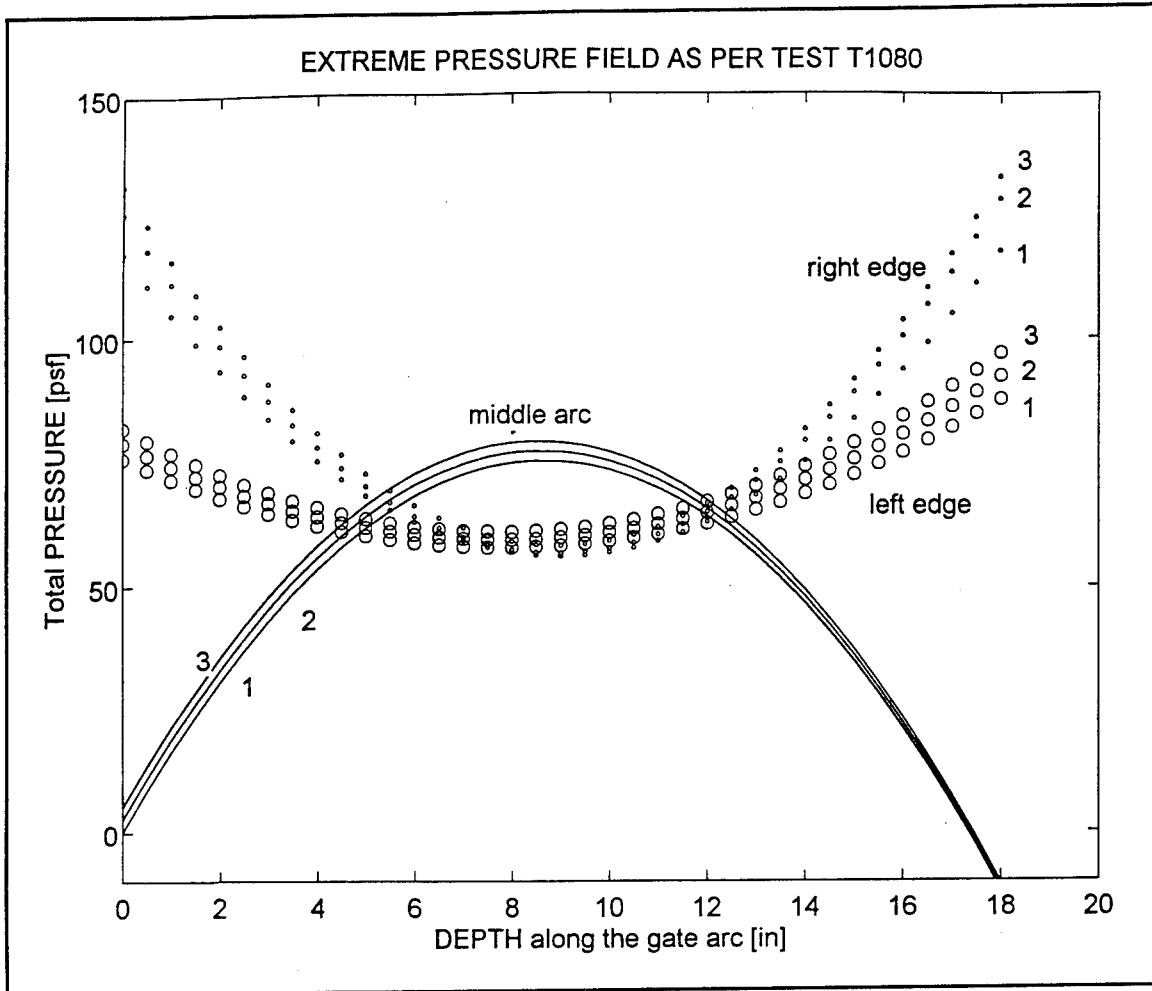


Plate 37. Extreme pressure field as predicted by test T1080 on the three reference longitudinal arcs on the gate skin, i.e., the right edge, the middle arc, and the left edge. Level 1: 68-percent confidence bound; level 2: 96-percent confidence bound; and level 3: 99.7-percent confidence bound

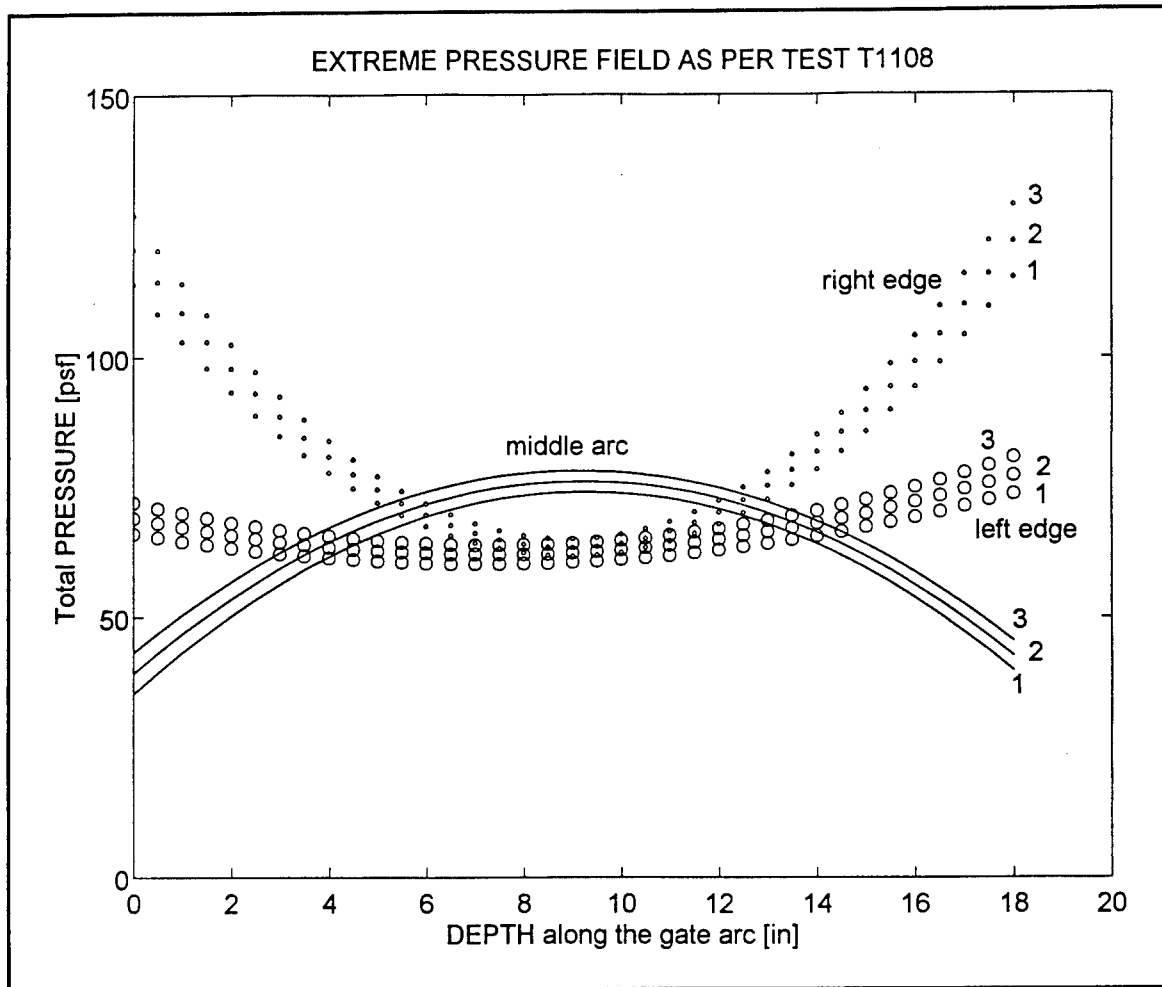


Plate 38. Extreme pressure field as predicted by test T1108 on the three reference longitudinal arcs on the gate skin, i.e., the right edge, the middle arc, and the left edge. Level 1: 68-percent confidence bound; level 2: 96-percent confidence bound; and level 3: 99.7-percent confidence bound

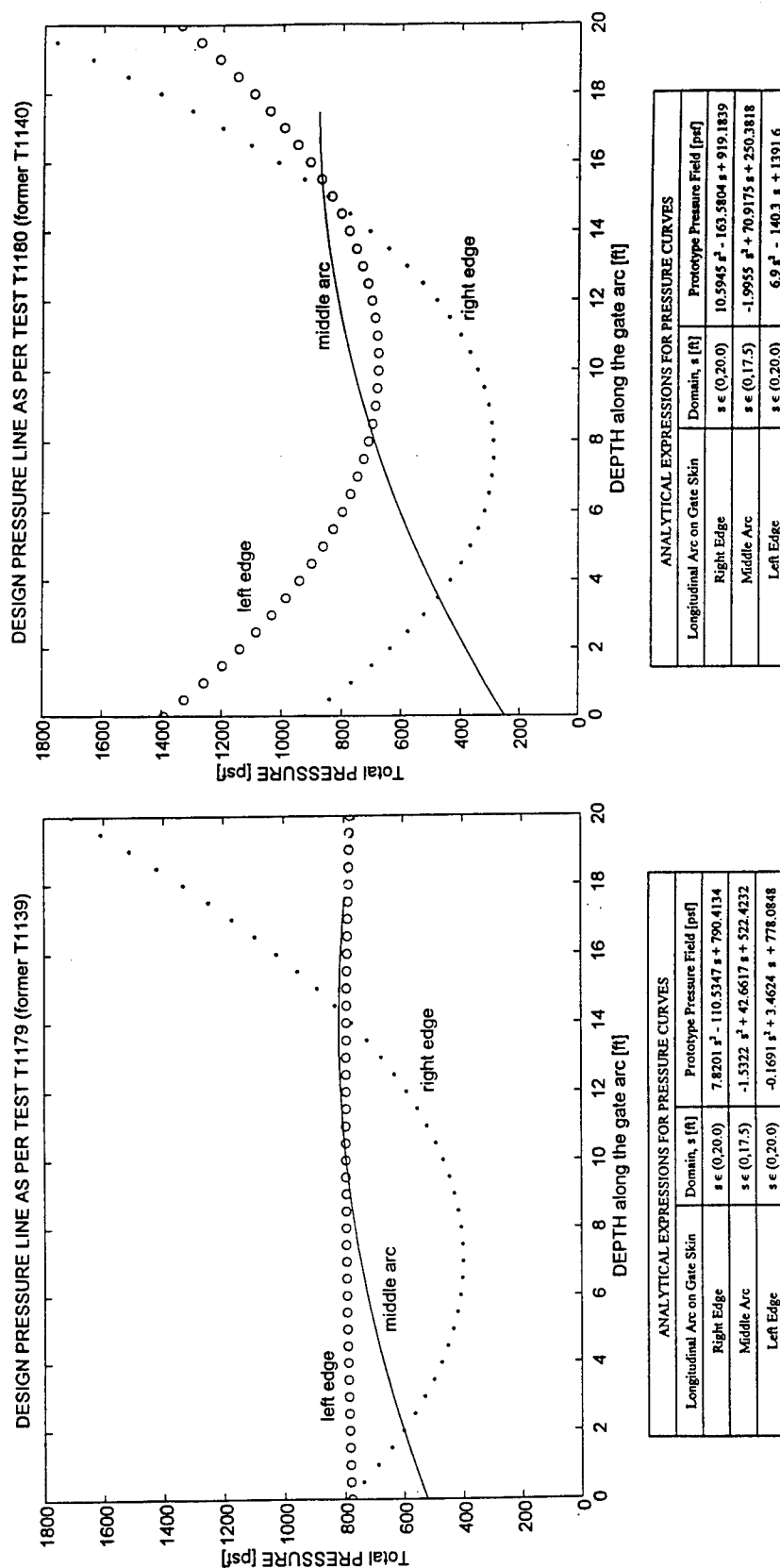


Plate 39. Montgomery Point Prototype Gate. Design pressure line as per tests T1179 and T1180

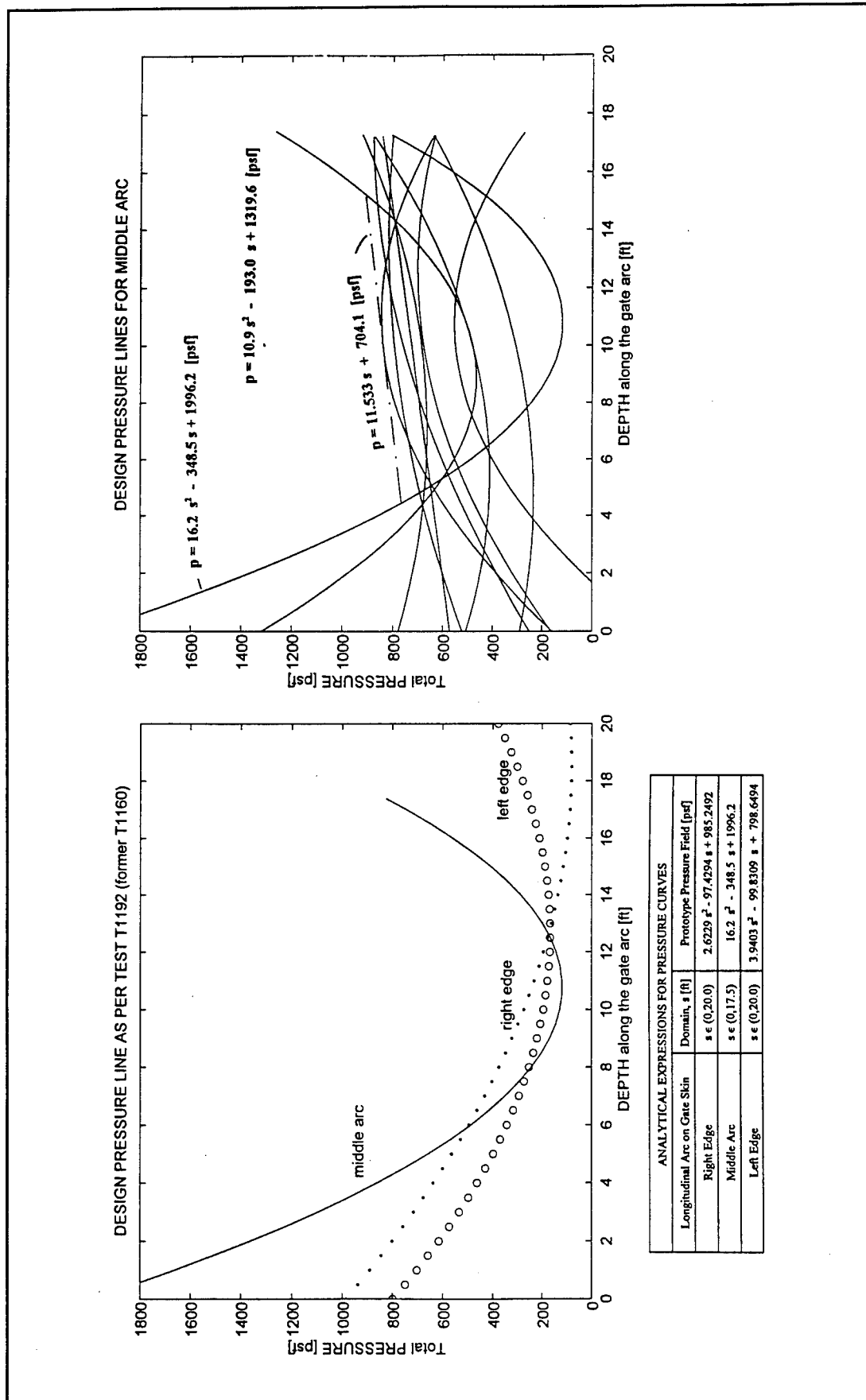


Plate 40. Montgomery Point Prototype Gate. Design pressure line as per test T1192. Pressure envelope for middle arc

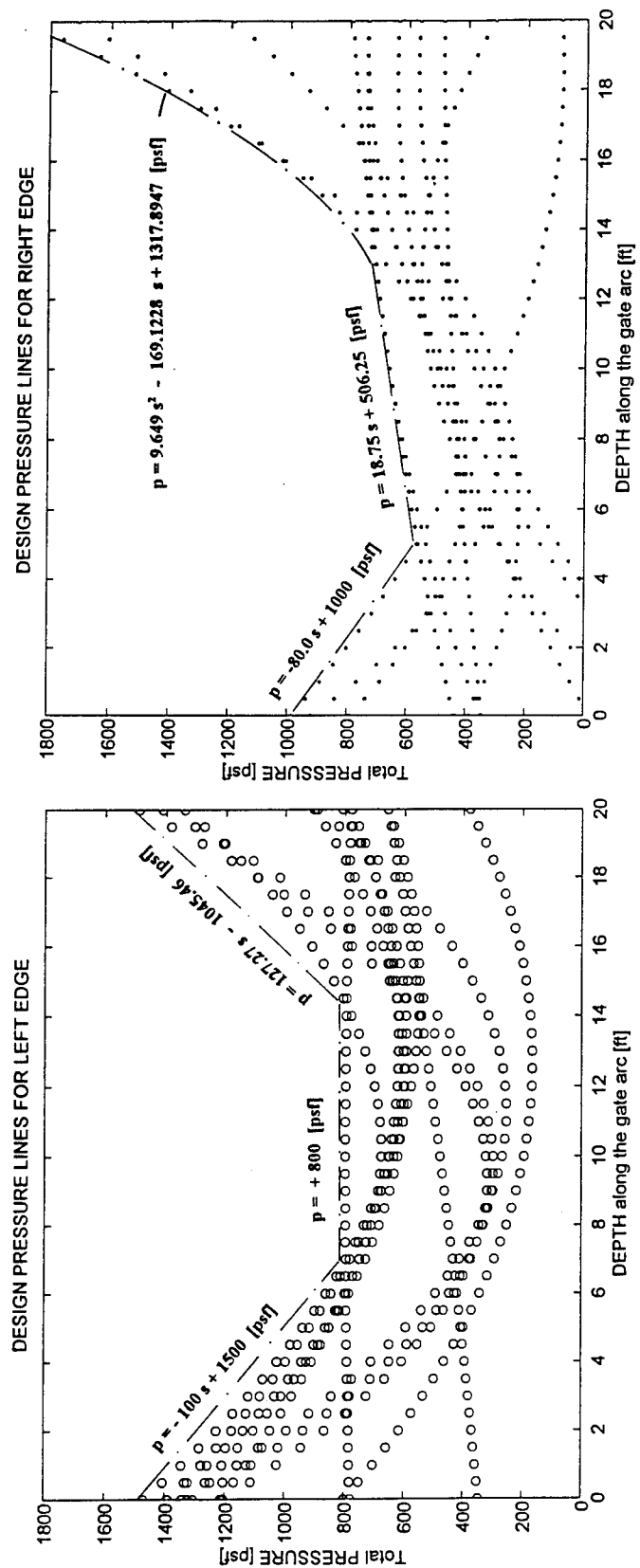


Plate 41. Montgomery Point Prototype Gate. Pressure envelope for left edge. Pressure envelope for right edge

5 Gate Eigenproperties

In this chapter, the experimental identification of natural frequencies of vibration and corresponding mode shapes is described. Knowledge of these structural properties for both the gate model and the prototype system is important to verify parameters entering future modal analyses of the gate; to compare these parameters in relation to the actual prototype gate as it is actually constructed; and to keep track of structural deterioration over the life of the gate in service, due to weathering, corrosion, local fatigue of component elements, or simply due to normal wear (safety assessment) (Crandall and Mark 1963).

A variety of mutually checking methods were implemented in this exercise. A finite element grid for the physical model standing on Teflon bearings on load-cell foundations was first used to identify its first 10 modes of vibration (Zienkiewicz 1977; Clough and Penzien 1975; Hibbitt, Karlsson and Sorensen 1993). Plates 42 through 51 describe the results for each relevant mode in sequence. Plates 52 through 59 similarly describe the eigensolution for the prototype gate (structural steel) standing on a rigid foundation, for the first seven modes in sequence. As expected, the model exhibits much more rigid characteristics than the prototype, but the same general mode-shapes.

A dry Twang test (pull-back test) (Clough and Penzien 1975) was also conducted on the physical model (T0137). Plate 60 shows the time-history of a typical parameter of response, say, the bending moment at the root of the right operating arm (looking in the downstream direction), in its free-vibration decay. Plate 61 shows the spectral density for the signal. The location of the first peak of this function identifies the fundamental frequency of vibration of the model (~ 46.875 Hz).

The natural properties of the physical model were also identified using a scanning Laser vibrometry system (LAZON, by Zonic Co.). Plate 62a shows the test setup (ZONIC + AND 1993). The instrumented (central) gate is excited by a variable-frequency electro-mechanical shaker connected to its downstream face, while its upstream skin is scanned by the Laser beam of a vibrometer during its dynamic response (Plate 62b). Plate 63, for example, shows the frequency-response function for velocity of several previously defined points on the gate skin (nodes 1, 7, 10, and 13 in Plate 64), whereas Plate 65 shows an expansion of the function in the important low-frequency

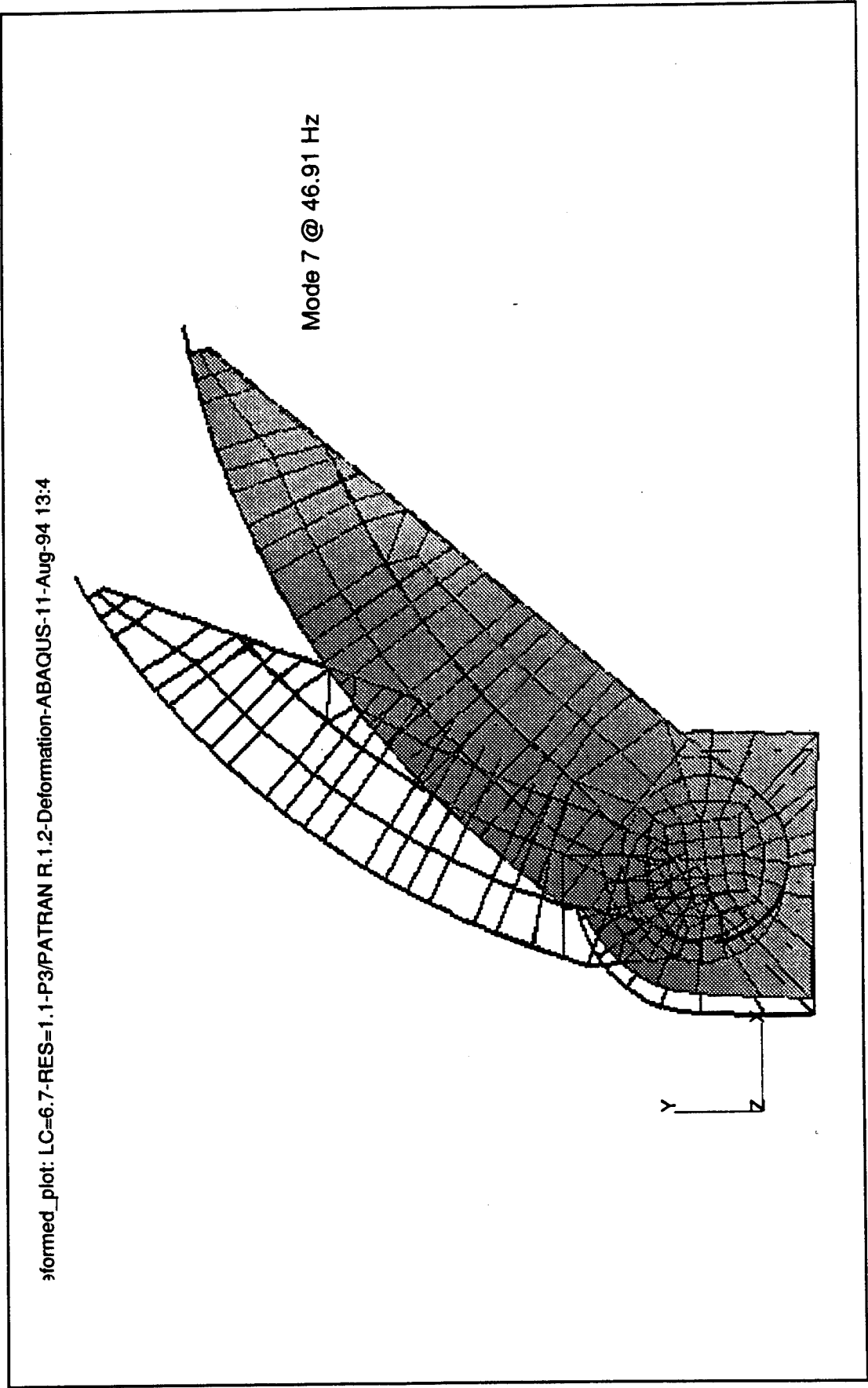
part of the domain (up to 120 Hz), for nodal points 19 and 21. The identified eigenvalues appear listed in Table 8. The first two natural frequencies are in close agreement as predicted by the various techniques. Plates 66 and 67 illustrate the corresponding mode-shapes. Plate 68 is an example of animation of a higher mode.

Table 8 Natural Frequencies for the Physical Model, Hz					
Mode	Finite Element	Twang Test DRY	Accelerometer	LAZON 0-100 Hz	Description
1	46.91	46.875	50.55	49.66	Rigid-Plate Rocking
(1)	-	-	55.5	56.99	Rigid-Plate Rocking
2	74.66	-	79.8	81.07	Rigid-Plate Twist
(2)	-	-	83.96	85.45	Rigid-Plate Twist
3	137.96	-	103.66	102.07	Rigid-Plate Twist
-	-	-	175.3	-	Bending
-	-	-	204.2	-	Torsion

Plates 69 and 70 show very little variation in the frequency-response function from the situation in which all gates are raised to the condition in which only one lateral gate is down. However, Plate 71 shows strong energy-suppression in the region of the frequency-domain beyond about 60 Hz for the condition in which both lateral gates are down and only the instrumented gate is raised. Plate 72 shows the negligible difference in the frequency-response function between the instrumented gate with and without the trash rack.

Plates 73 through 78 illustrate the identification of the fundamental frequency of free vibrations for the gate physical model in the upstream-submerged condition from accelerometer recordings in Twang test T0139 ($f_1 \approx 39$ Hz). The system becomes more flexible (compare with $f_1 \approx 47$ Hz in dry) due to the "added mass" effect of the upstream water.

The identification of the equivalent viscous damping ratio for both the dry and upstream submerged conditions is discussed in Chapter 7 in the context of the engineering model, and the analysis of forced vibrations of the gate in operation is considered in Appendix A (Spectral Analysis).



87 Plate 42. Finite element eigensolution for 1/15-scale model. Relevant mode of vibration 1

formed_plot: LC=6.8-RES=1.1-P3/PATRAN R.1.2-Deformation-ABAQUS-11-Aug-94 09:3

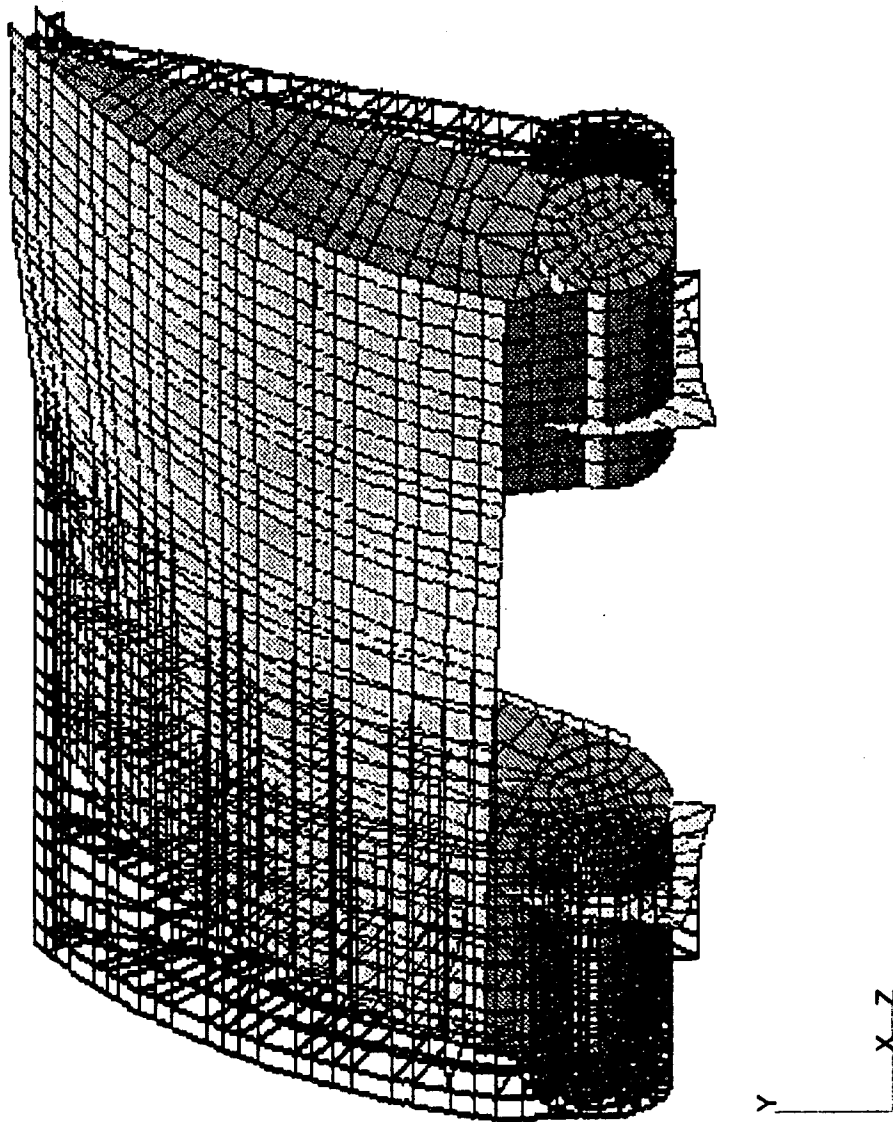


Plate 43. Finite element eigensolution for 1/15-scale model. Relevant mode of vibration 2

formed_plot: LC=6.9-RES=1.1-P3/PATRAN R.1.2-Deformation-ABAQUS-11-Aug-94 10:1

Mode 9 @ 131.17 Hz

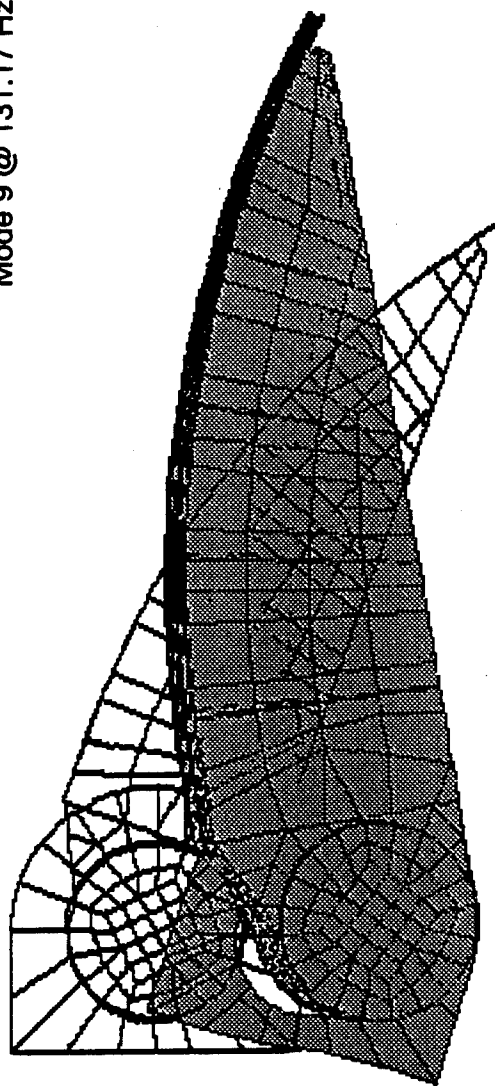


Plate 44. Finite element eigensolution for 1/15-scale model. Relevant mode of vibration 3

formed_plot: LC=6.10-RES=1.1-P3/PATRAN R.1.2-Deformation-ABAQUS-11-Aug-94 09:

Mode 10 @ 137.96

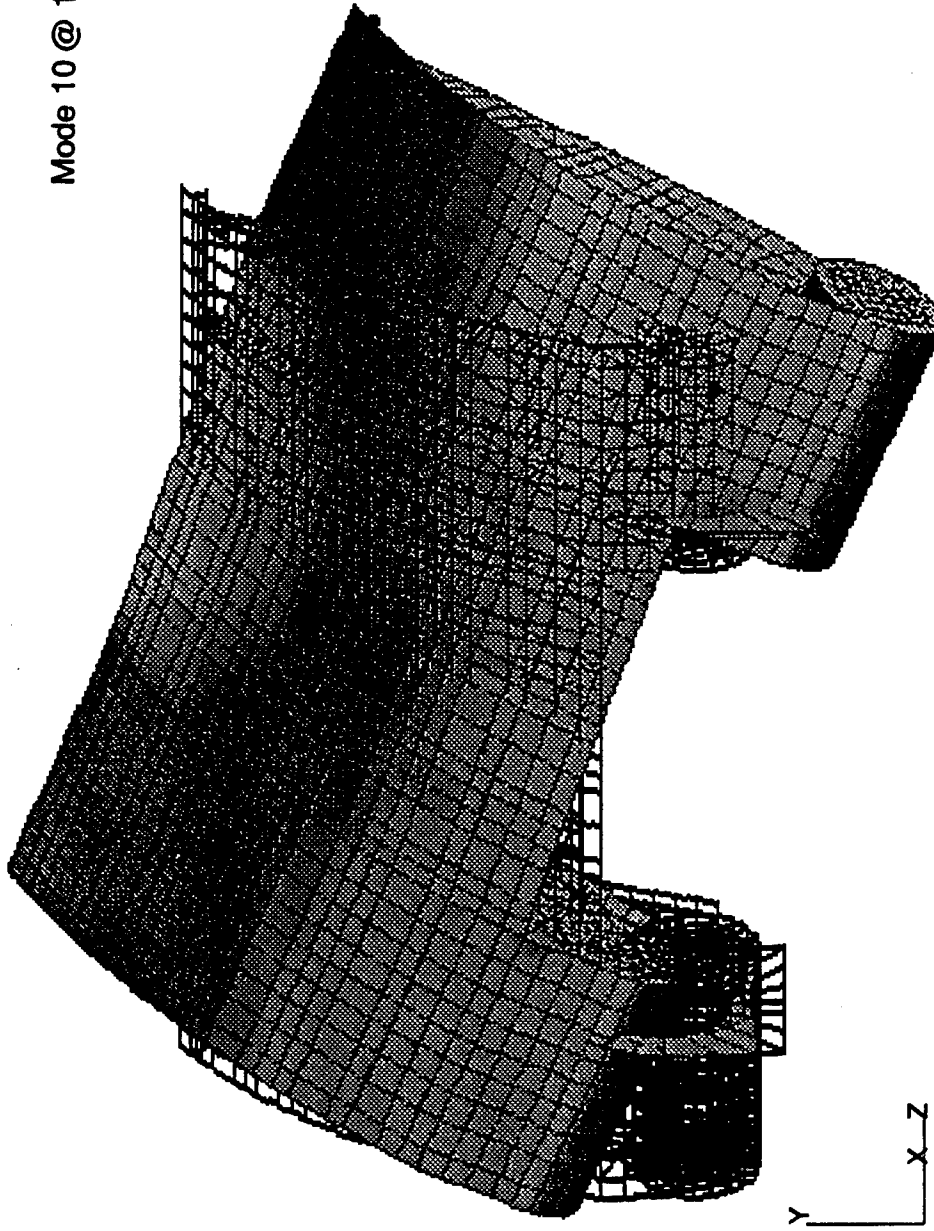
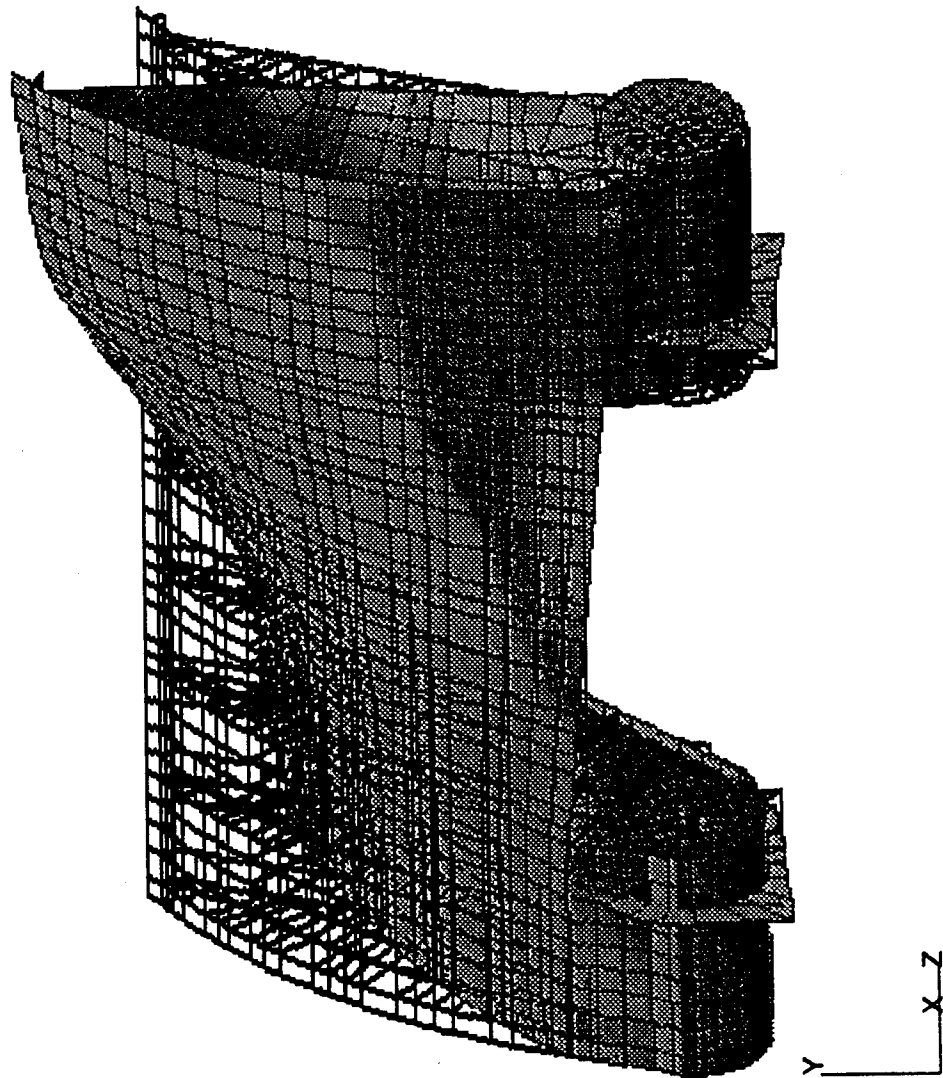


Plate 45. Finite element eigensolution for 1/15-scale model. Relevant mode of vibration 4

formed_plot: LC=6.11-RES=1.1-P3/PATRAN R.1.2-Deformation-ABAQUS-11-Aug-94 10:



Mode 11 @ 194.98

91 Plate 46. Finite element eigensolution for 1/15-scale model. Relevant mode of vibration 5

formed_plot: LC=6.12-RES=1.1-P3/PATRAN R.1.2-Deformation-ABAQUS-11-Aug-94 10:

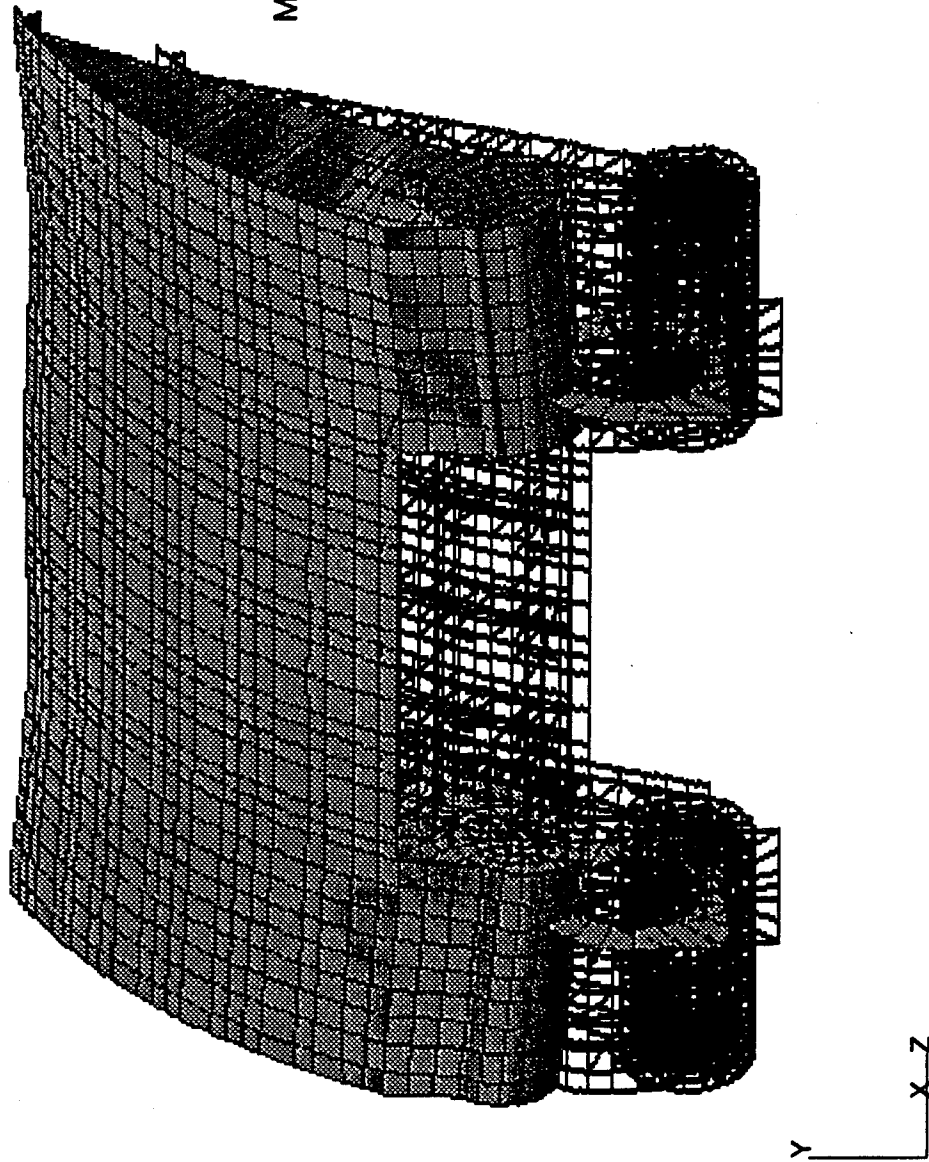


Plate 47. Finite element eigensolution for 1/15-scale model. Relevant mode of vibration 6

formed_plot: LC=6.13-RES=1.1-P3/PATRAN R.1.2-Deformation-ABAQUS-11-Aug-94 11:

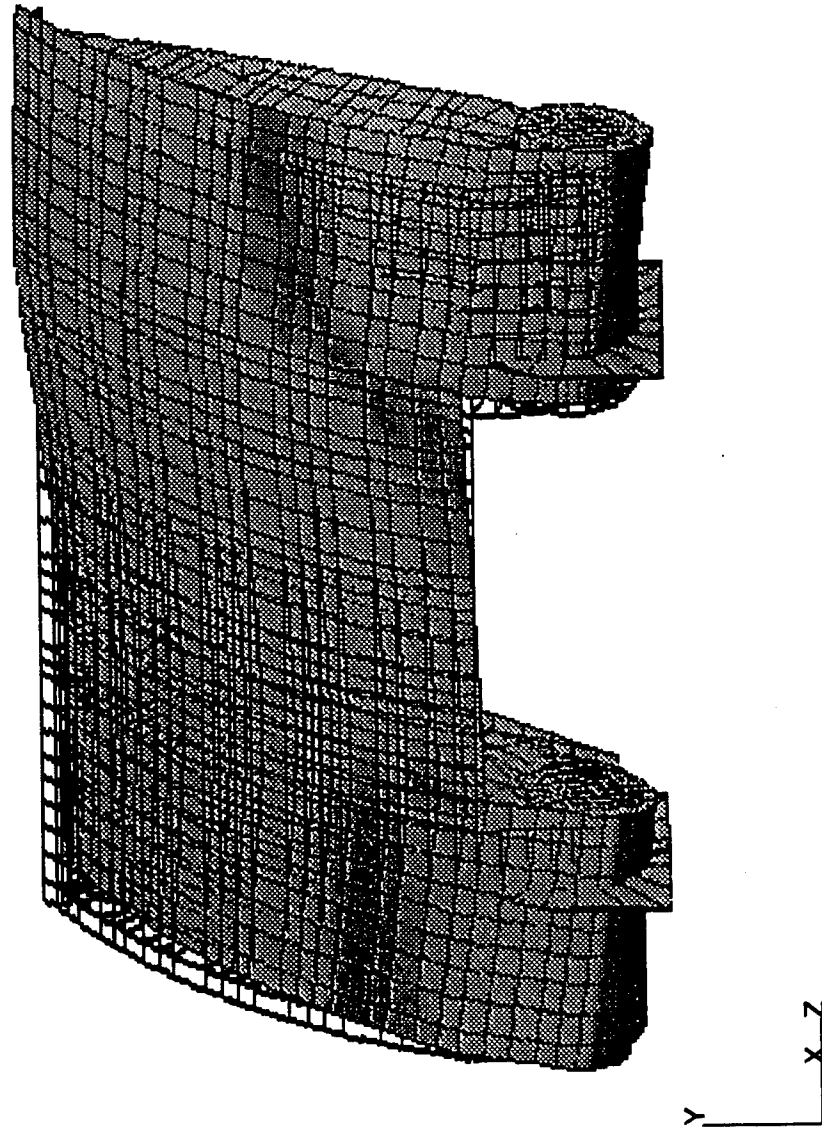


Plate 48. Finite element eigensolution for 1/15-scale model. Relevant mode of vibration 7

formed_plot: LC=6.14-RES=1.1-P3/PATRAN R.1.2-Deformation-ABAQUS-11-Aug-94 11:

Mode 14 @ 399.6 Hz

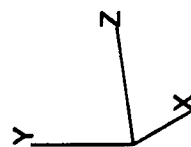
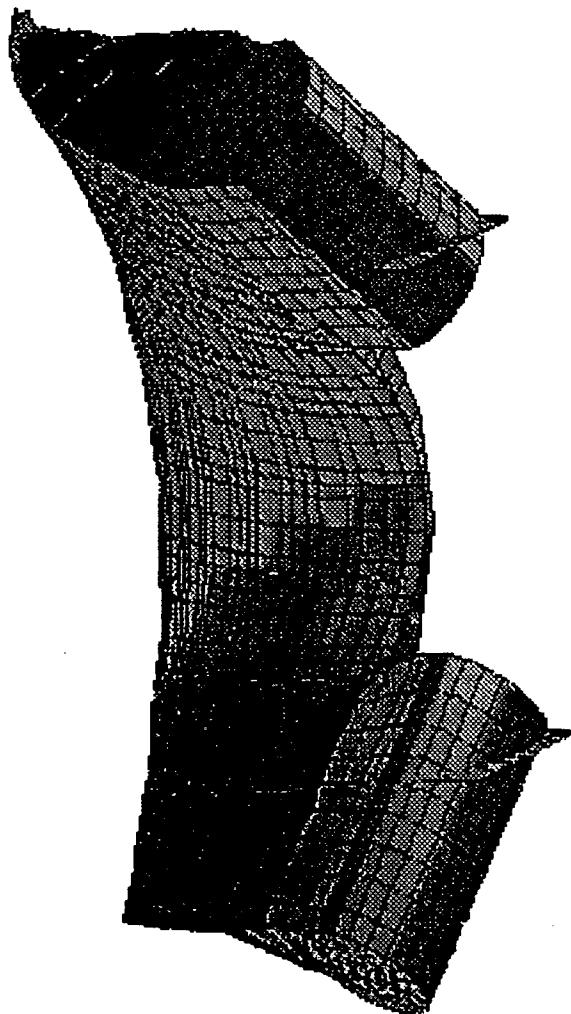
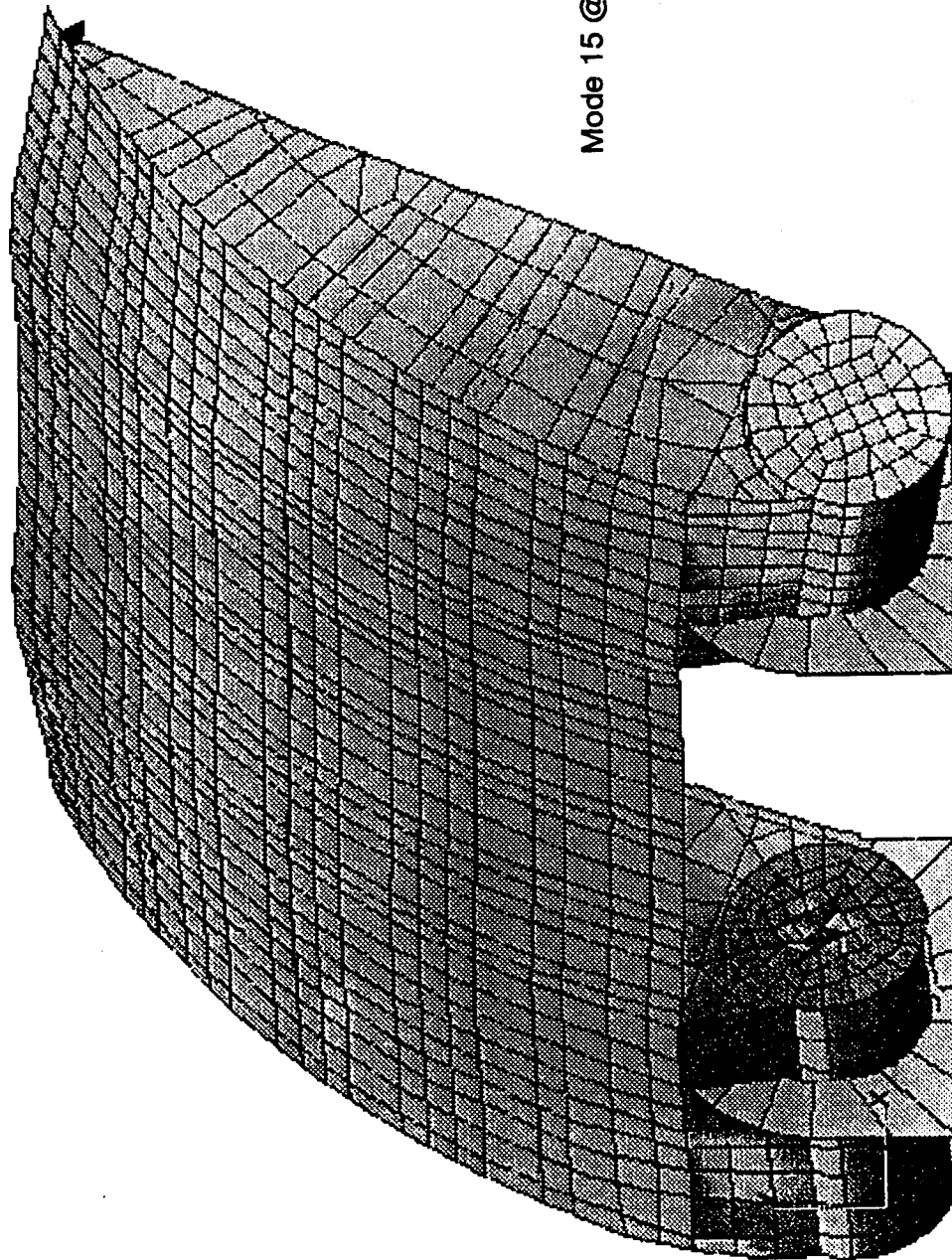


Plate 49. Finite element eigensolution for 1/15-scale model. Relevant mode of vibration 8

formed_plot: LC=6.15-RES=1.1-P3/PATRAN R.1.2-Deformation-ABAQUS-11-Aug-94 11:



Mode 15 @ 456.7 Hz

Plate 50. Finite element eigensolution for 1/15-scale model. Relevant mode of vibration 9

formed_plot: LC=6.16-RES=1.1-P3/PATRAN R.1.2-Deformation-ABAQUS-11-Aug-94 13:

Mode 16 @ 511.92 Hz

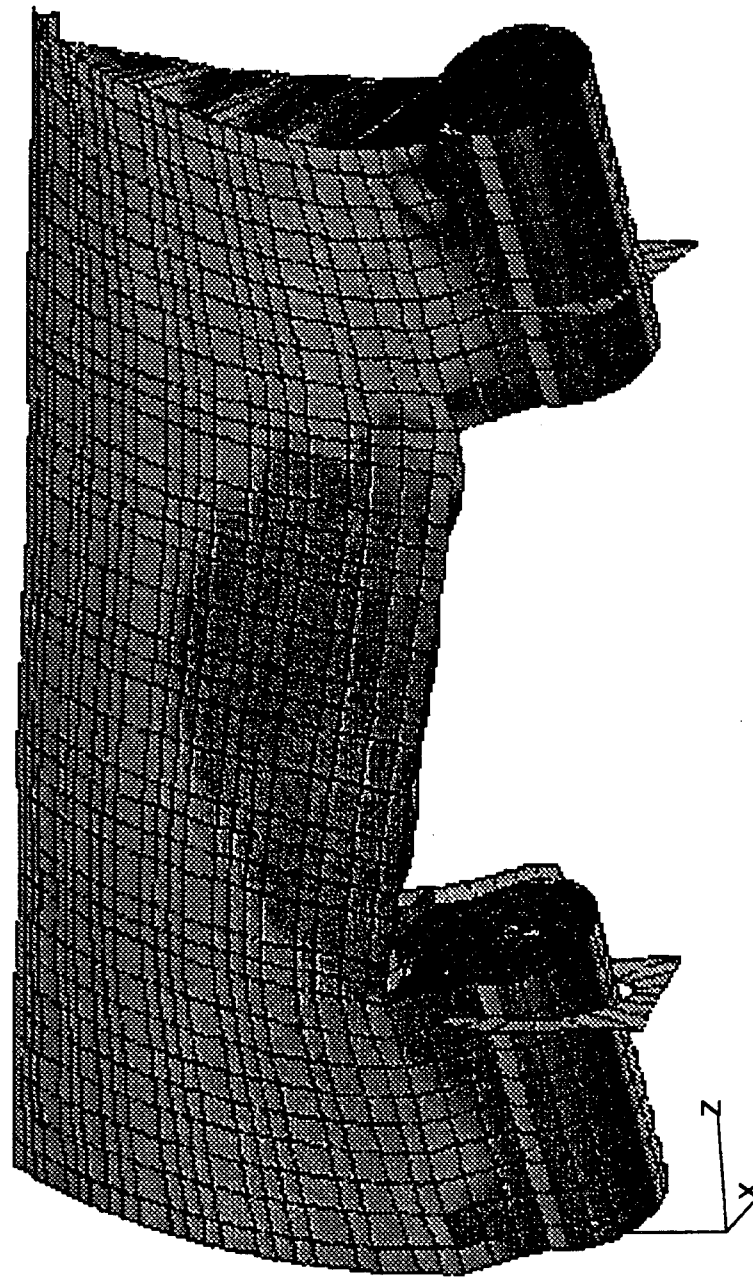
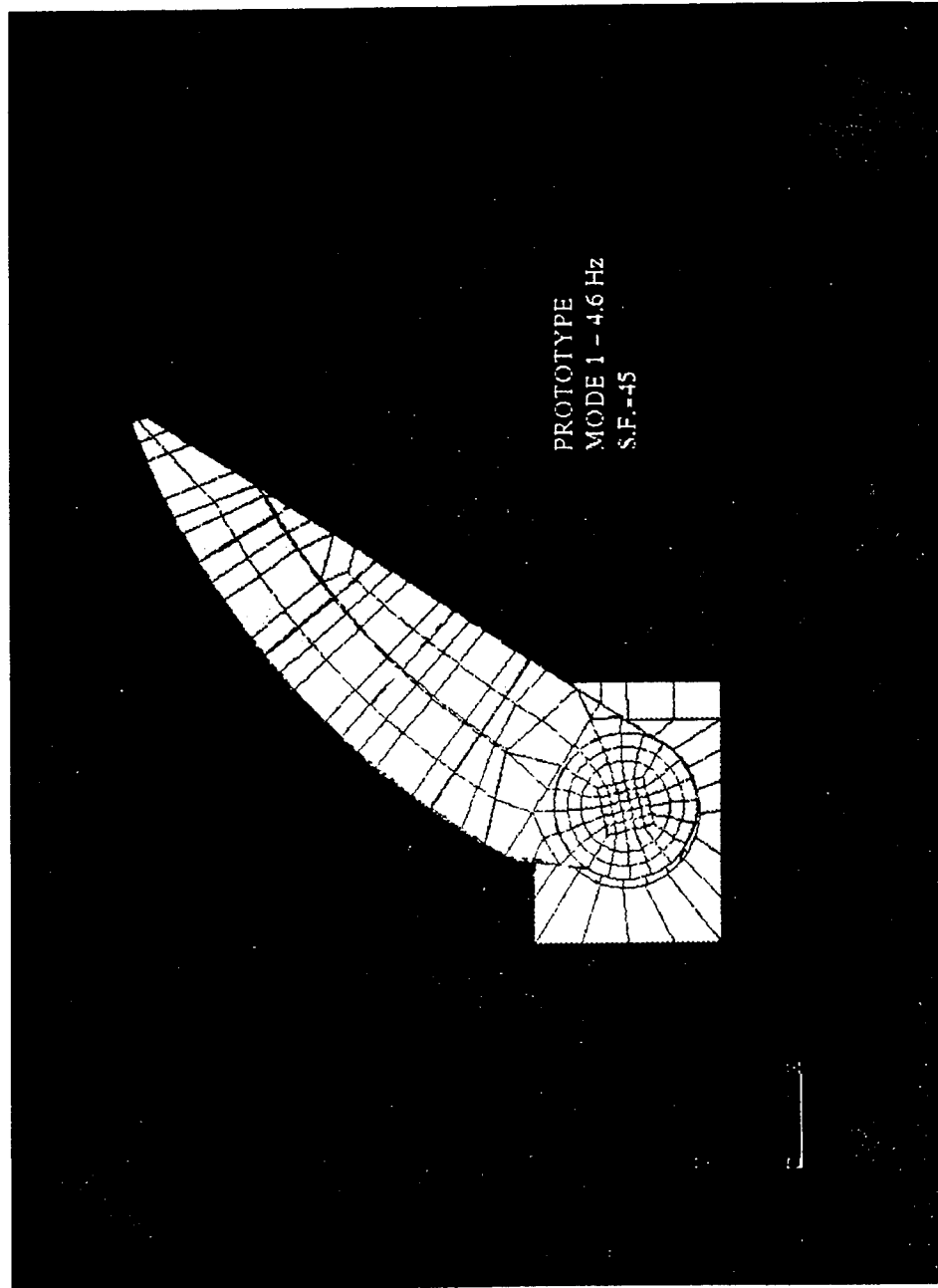


Plate 51. Finite element eigensolution for 1/15-scale model. Relevant mode of vibration 10



97 Plate 52. Finite element eigensolution for prototype. Relevant mode of vibration 1

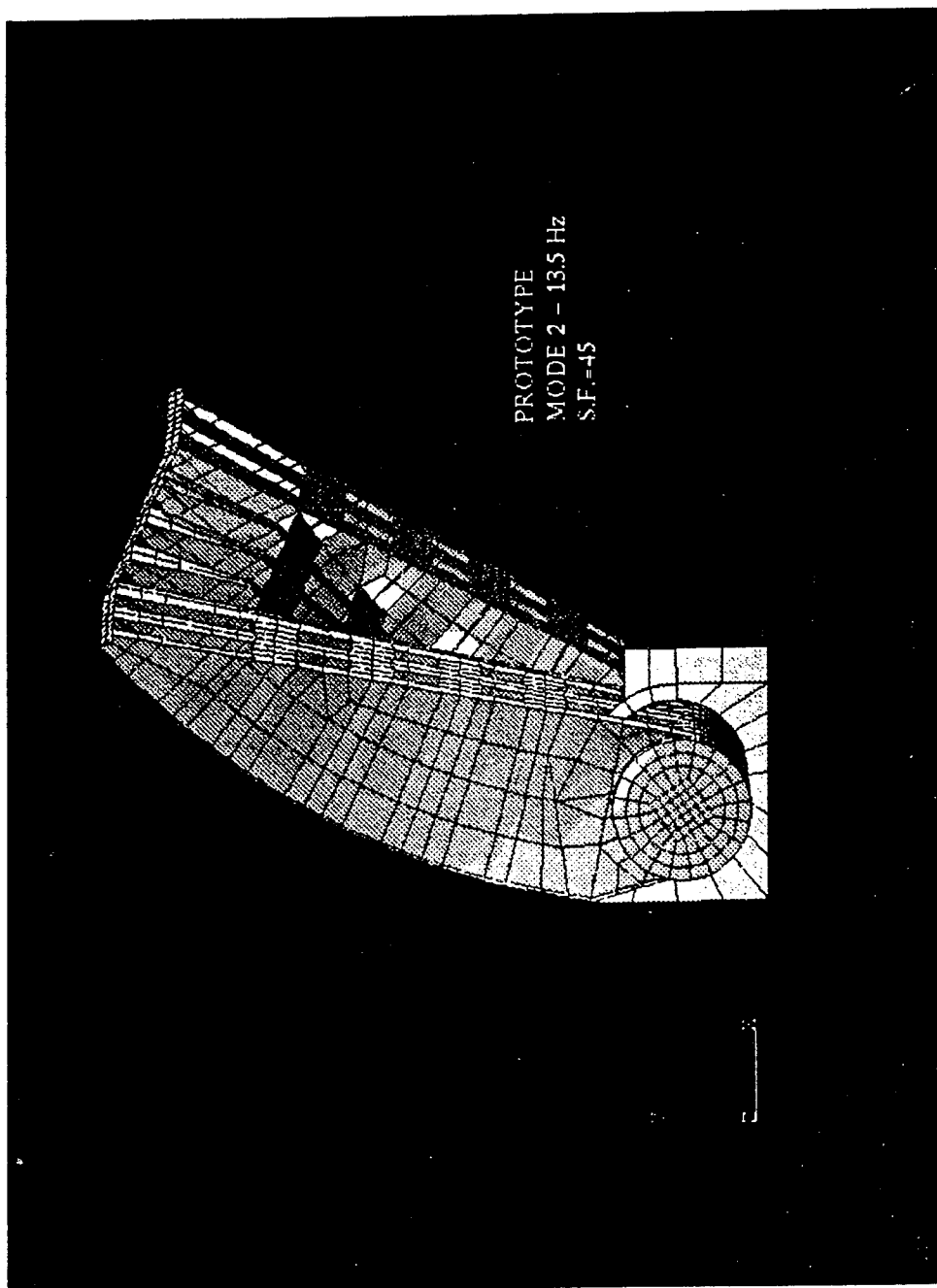
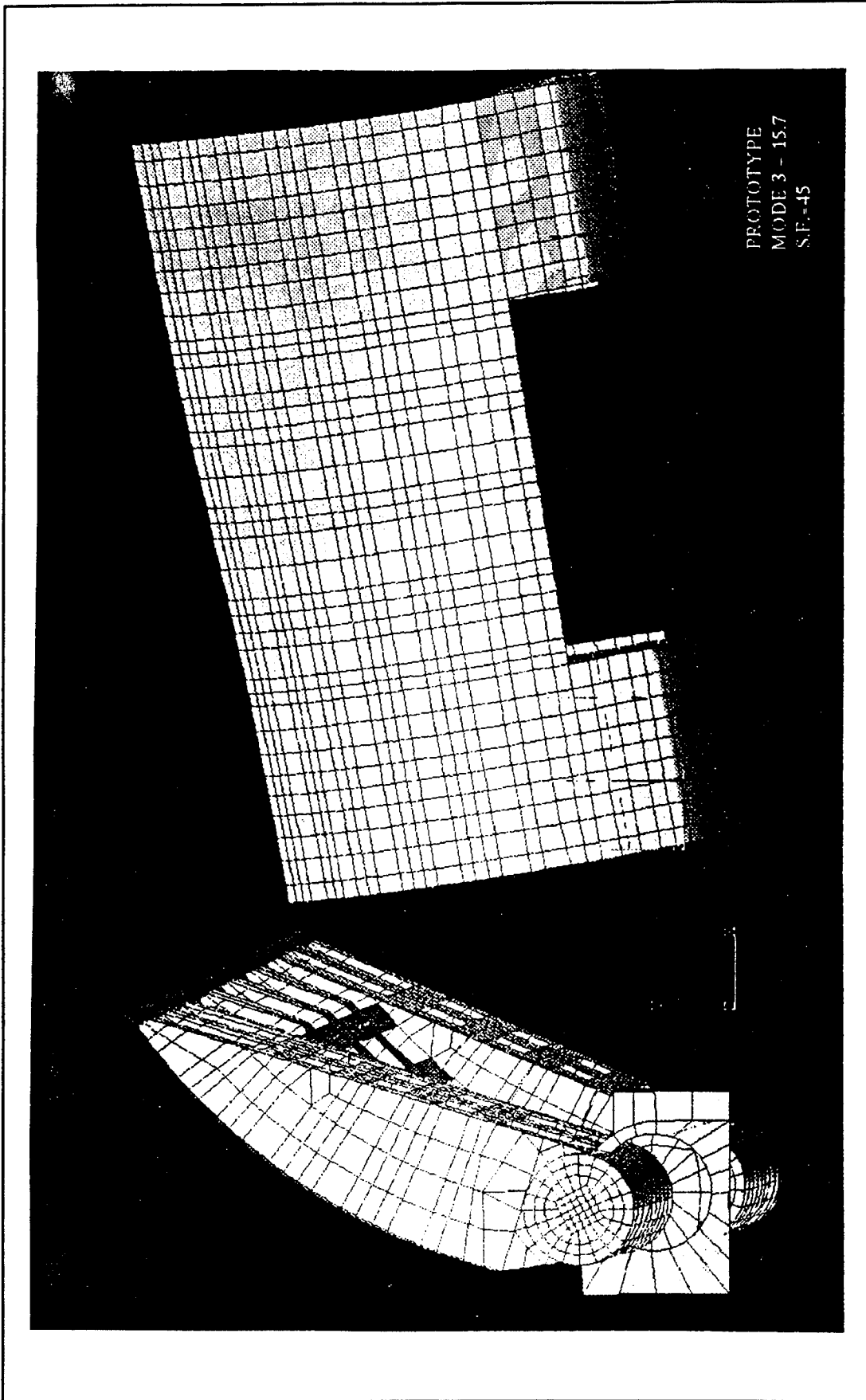


Plate 53. Finite element eigensolution for prototype. Relevant mode of vibration 2



99 Plate 54. Finite element eigensolution for prototype. Relevant mode of vibration 3

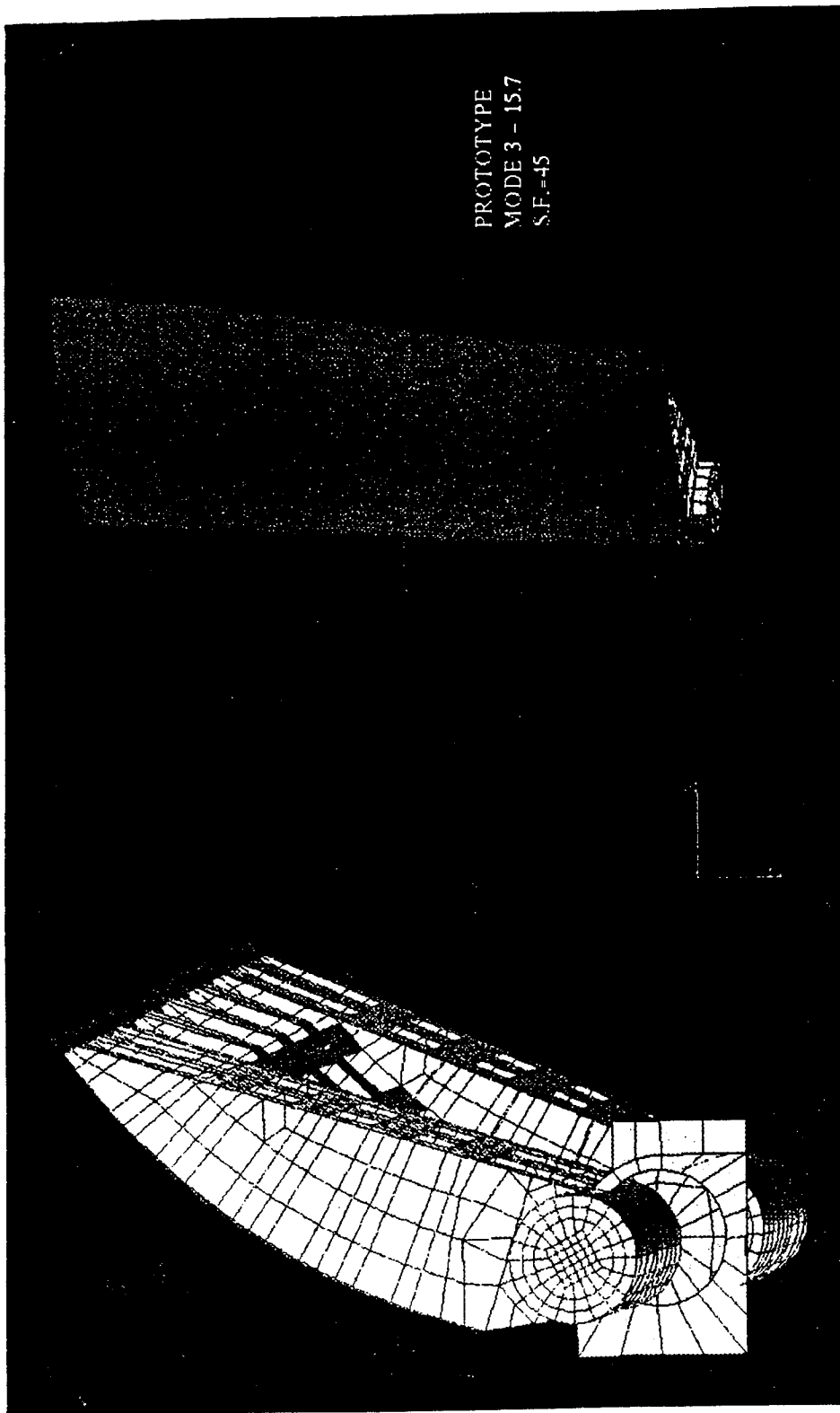


Plate 55. Finite element eigensolution for prototype. Relevant mode of vibration 3

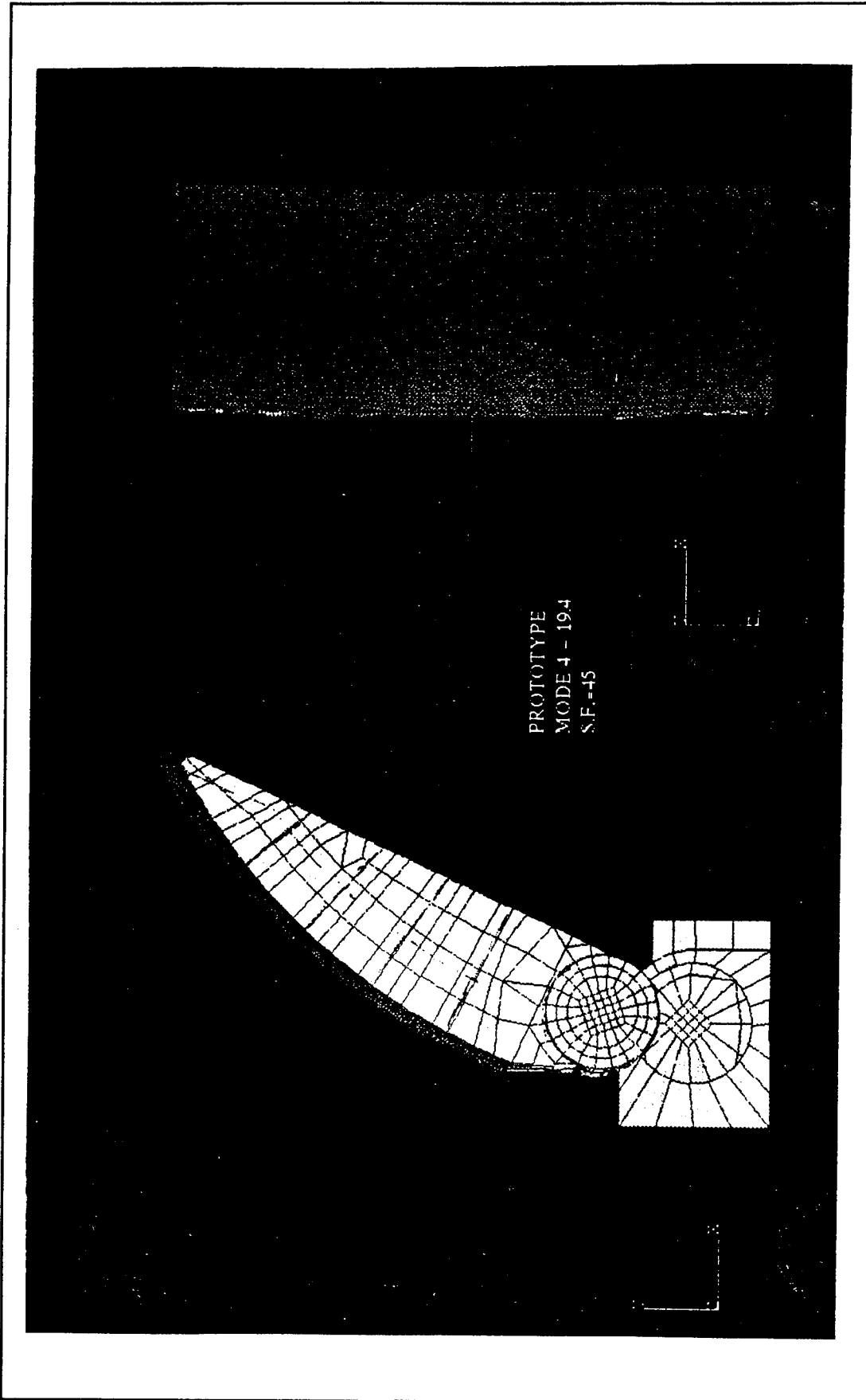


Plate 56. Finite element eigensolution for prototype. Relevant mode of vibration 4

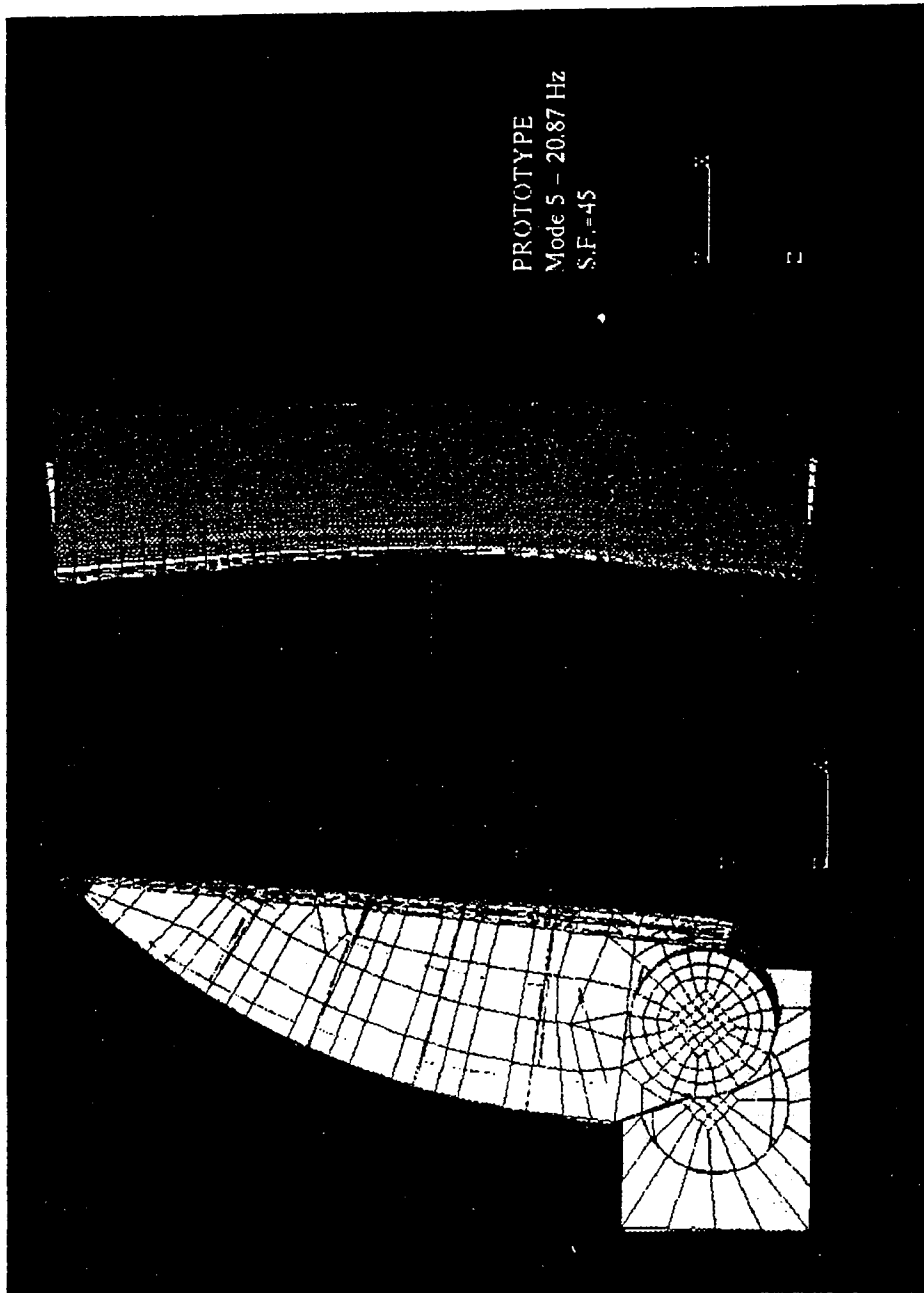


Plate 57. Finite element eigensolution for prototype. Relevant mode of vibration 5

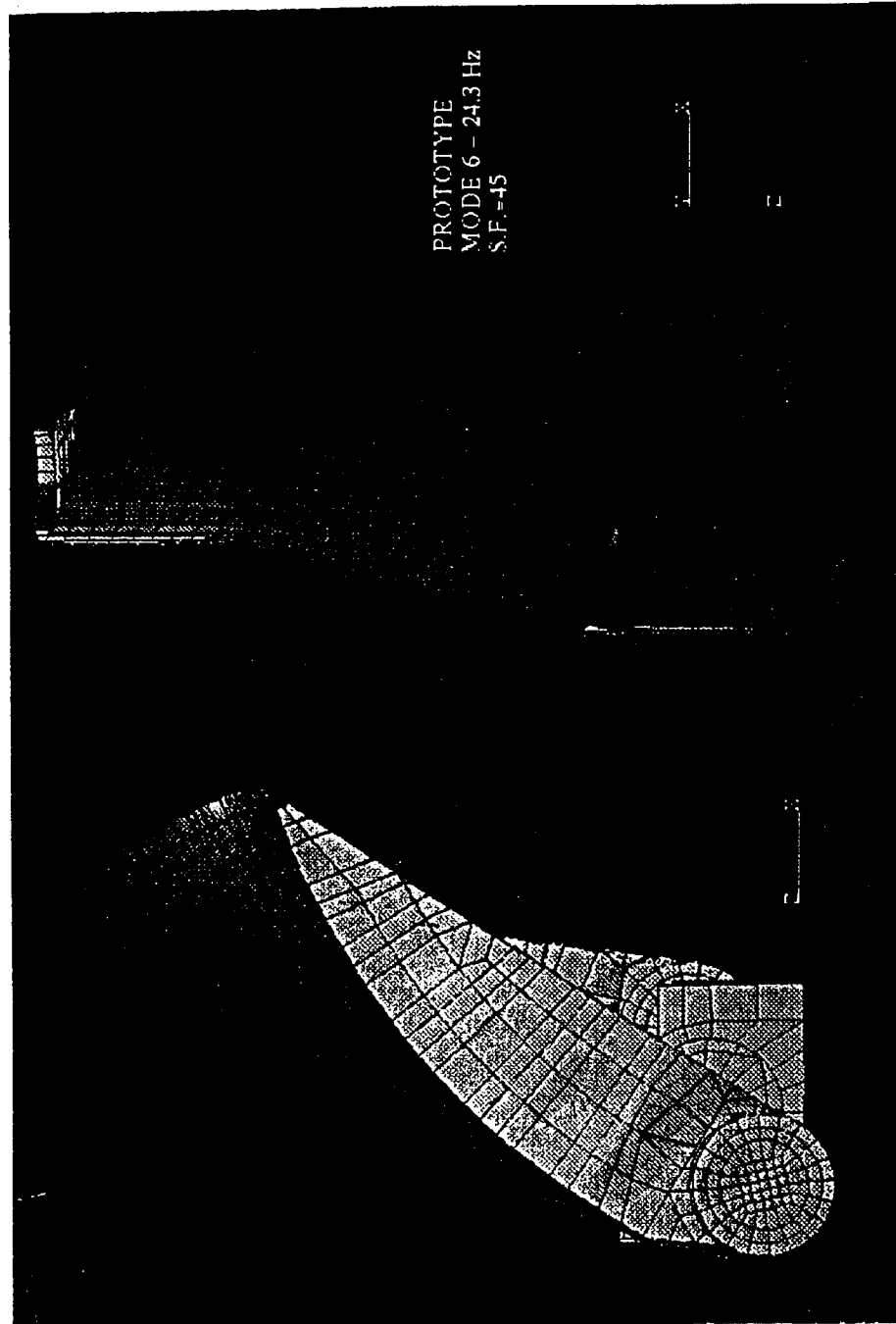


Plate 58. Finite element eigensolution for prototype. Relevant mode of vibration 6

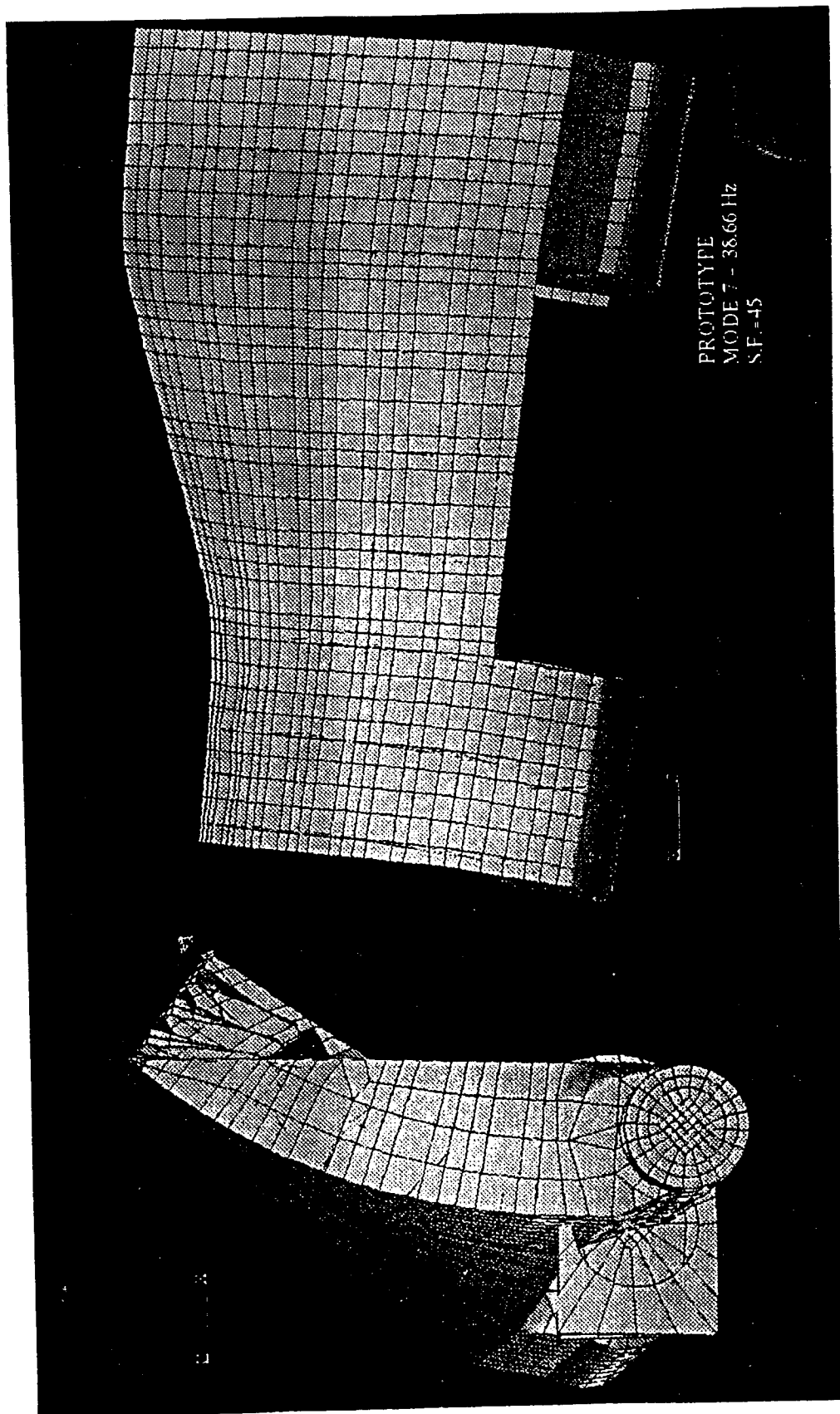


Plate 59. Finite element eigensolution for prototype. Relevant mode of vibration 7

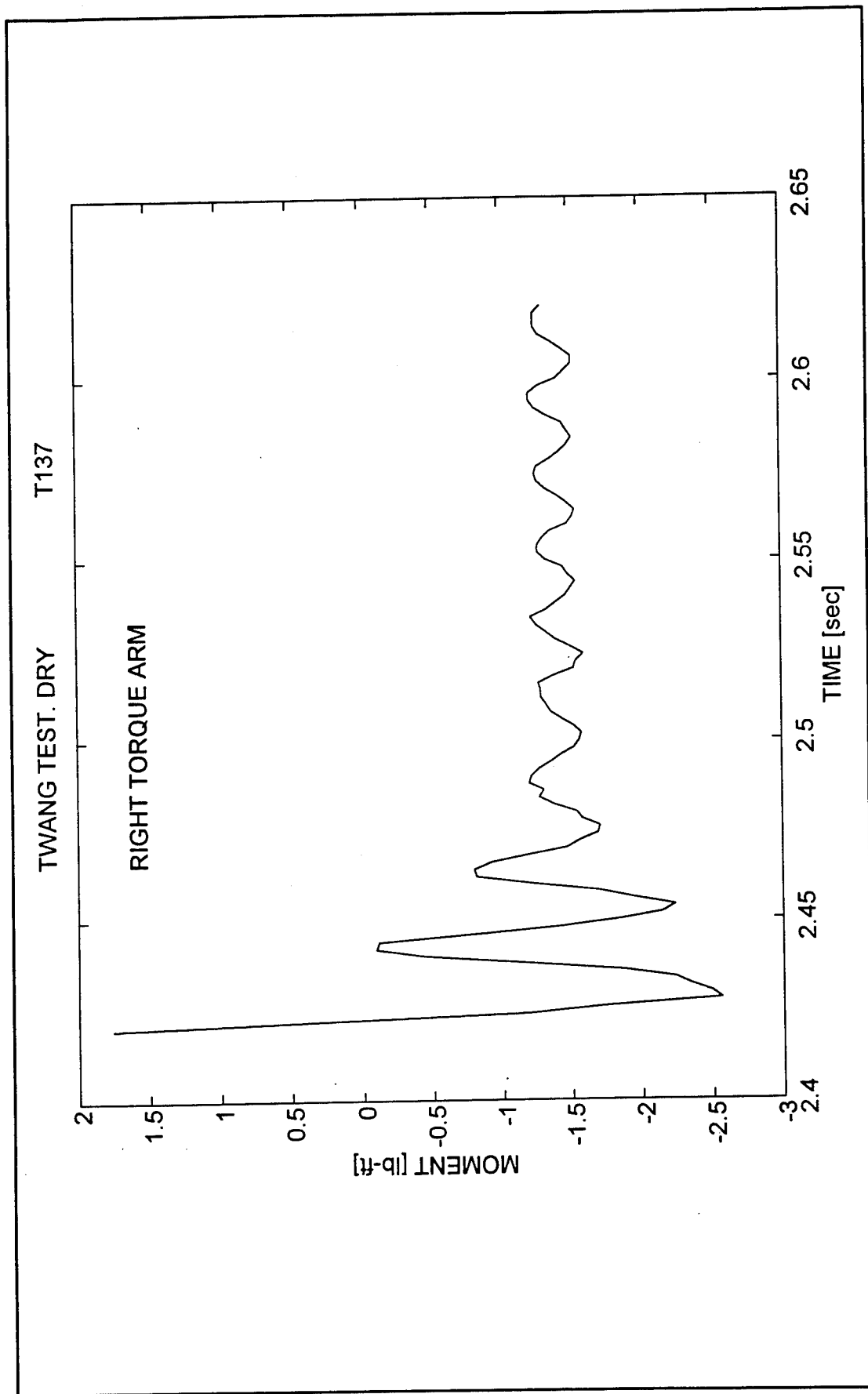


Plate 60. Dry Twang test T0137. Free-vibration decay of bending moment at the root of right operating arm

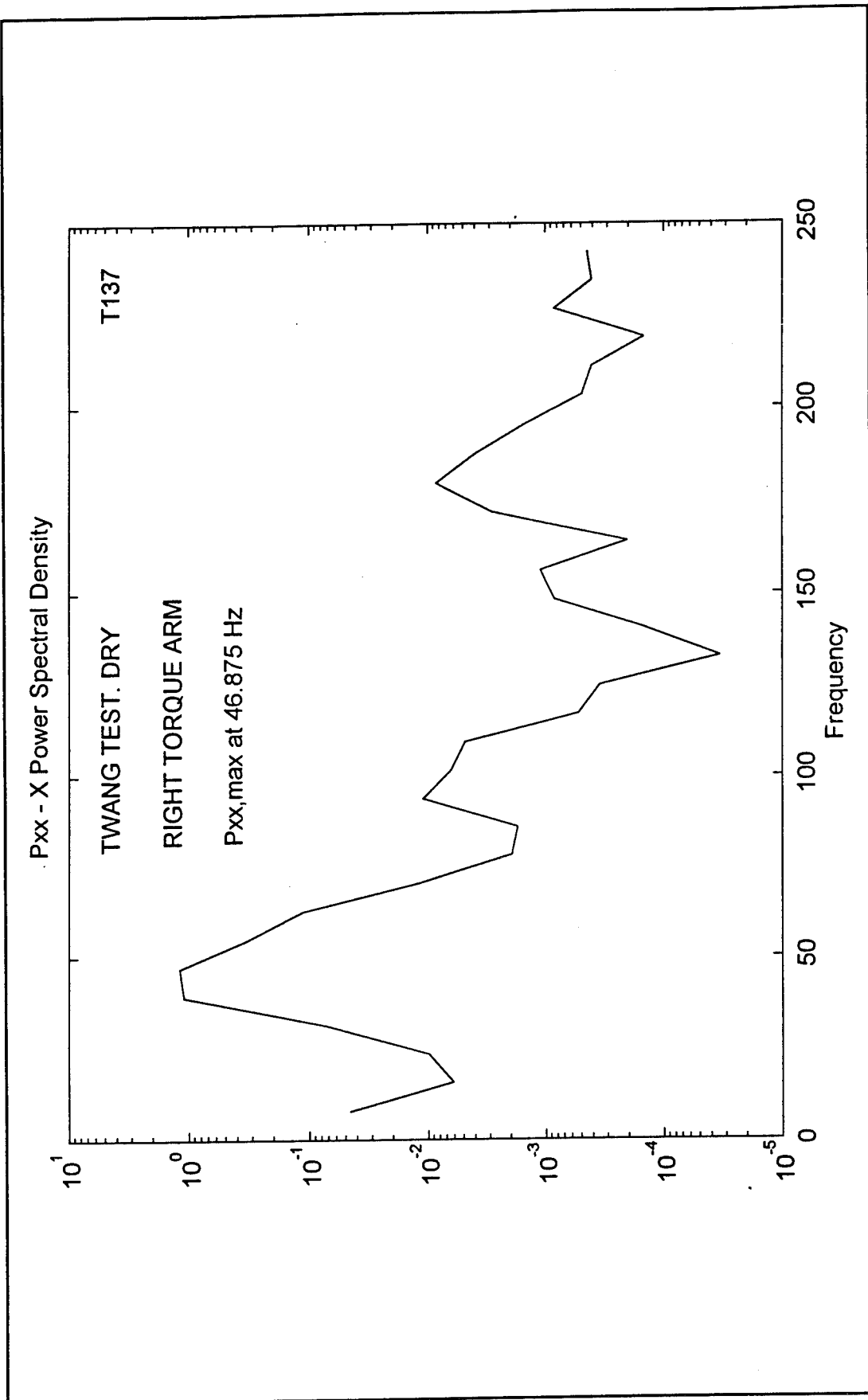


Plate 61. Spectral density function for the time-history of response in Plate 60

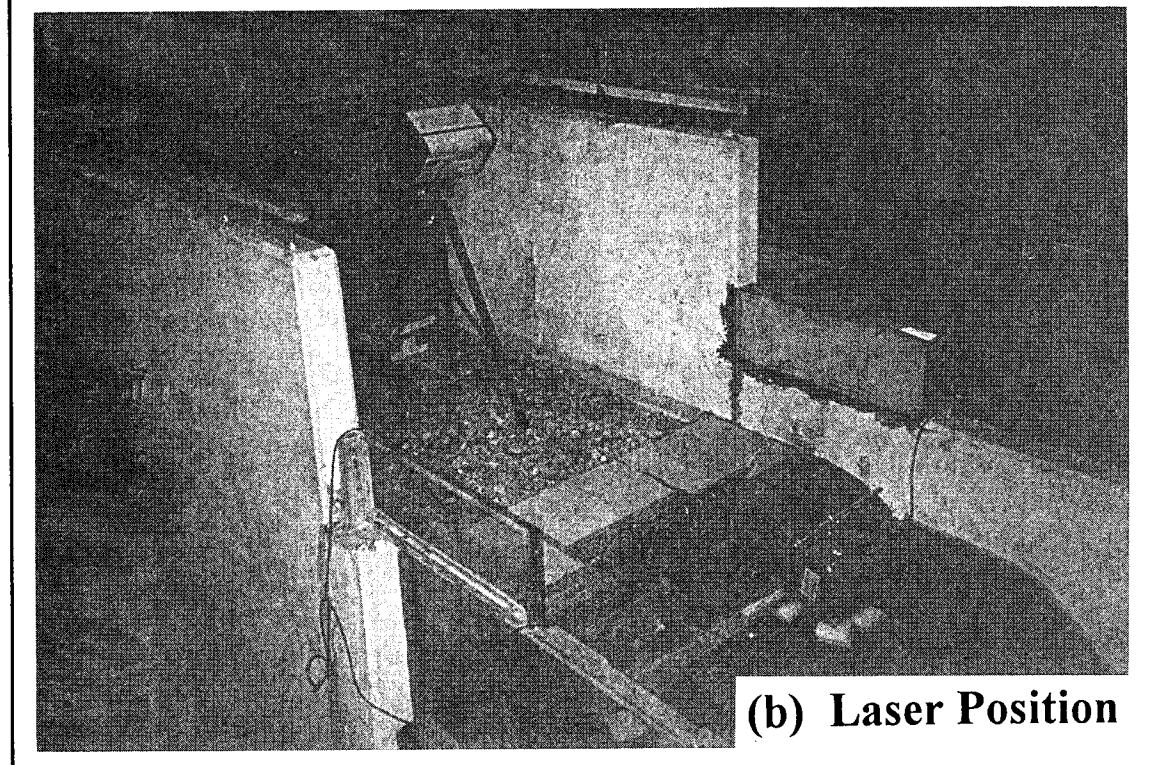
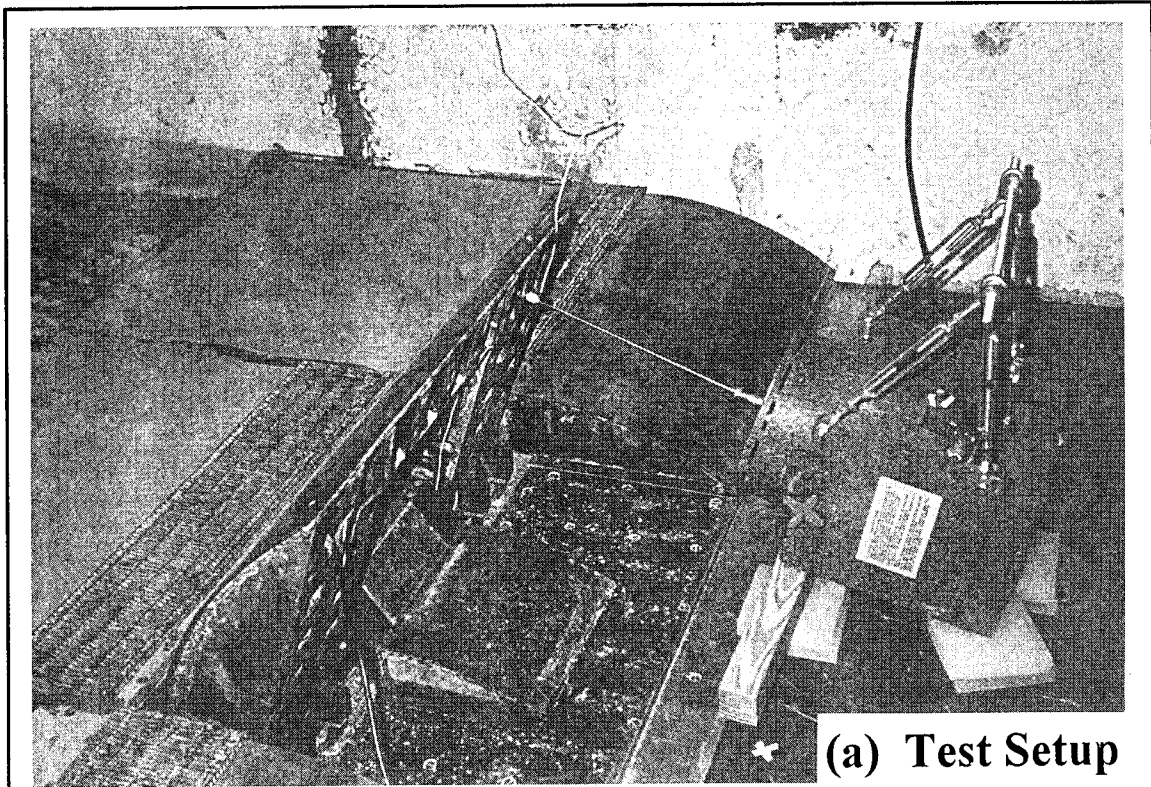


Plate 62. Scanning Laser Vibrometry System. (a) Test setup, and (b) Laser position

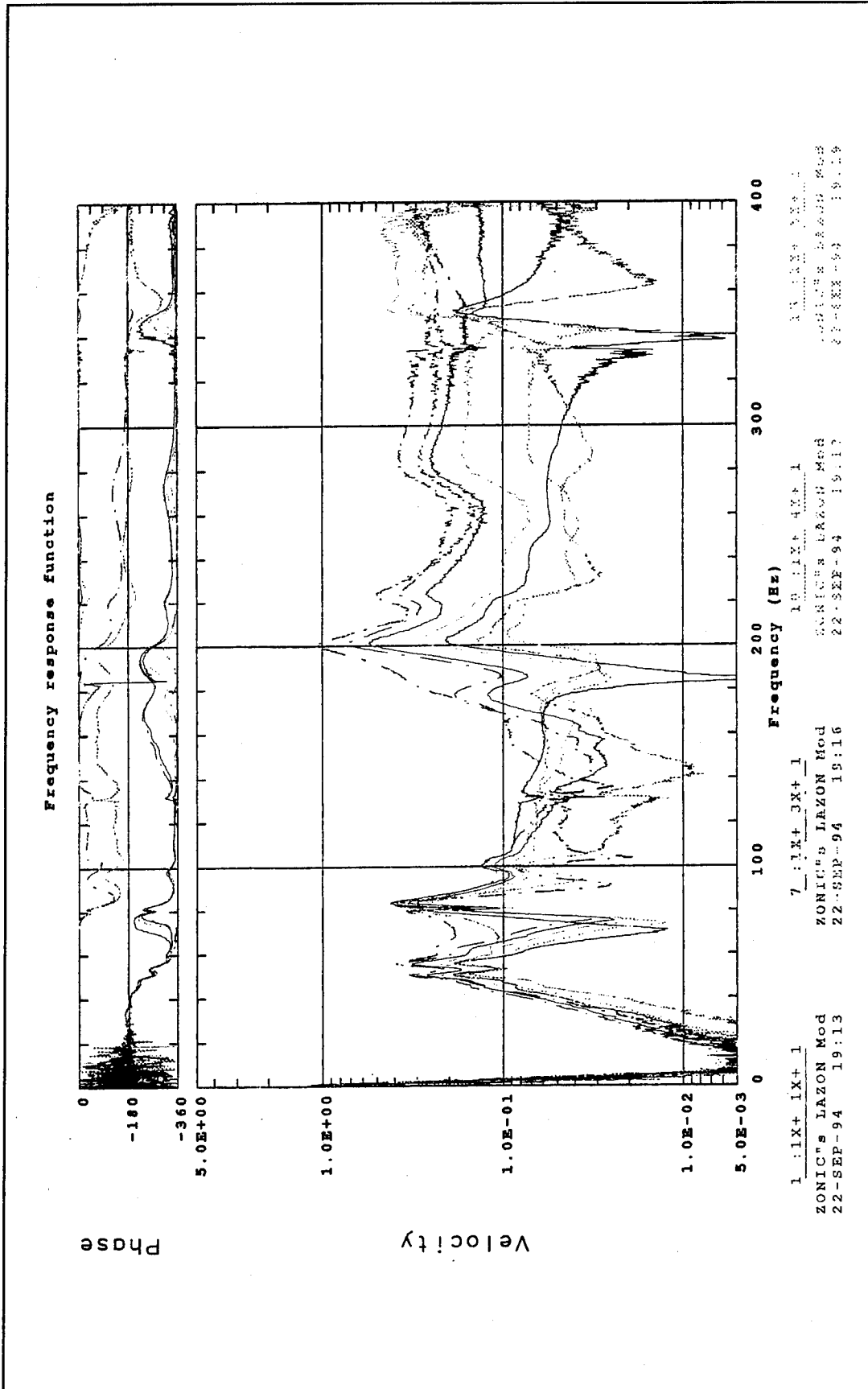


Plate 63. Scanning Laser Vibrometry System. Frequency-response function for selected nodes on the gate skin

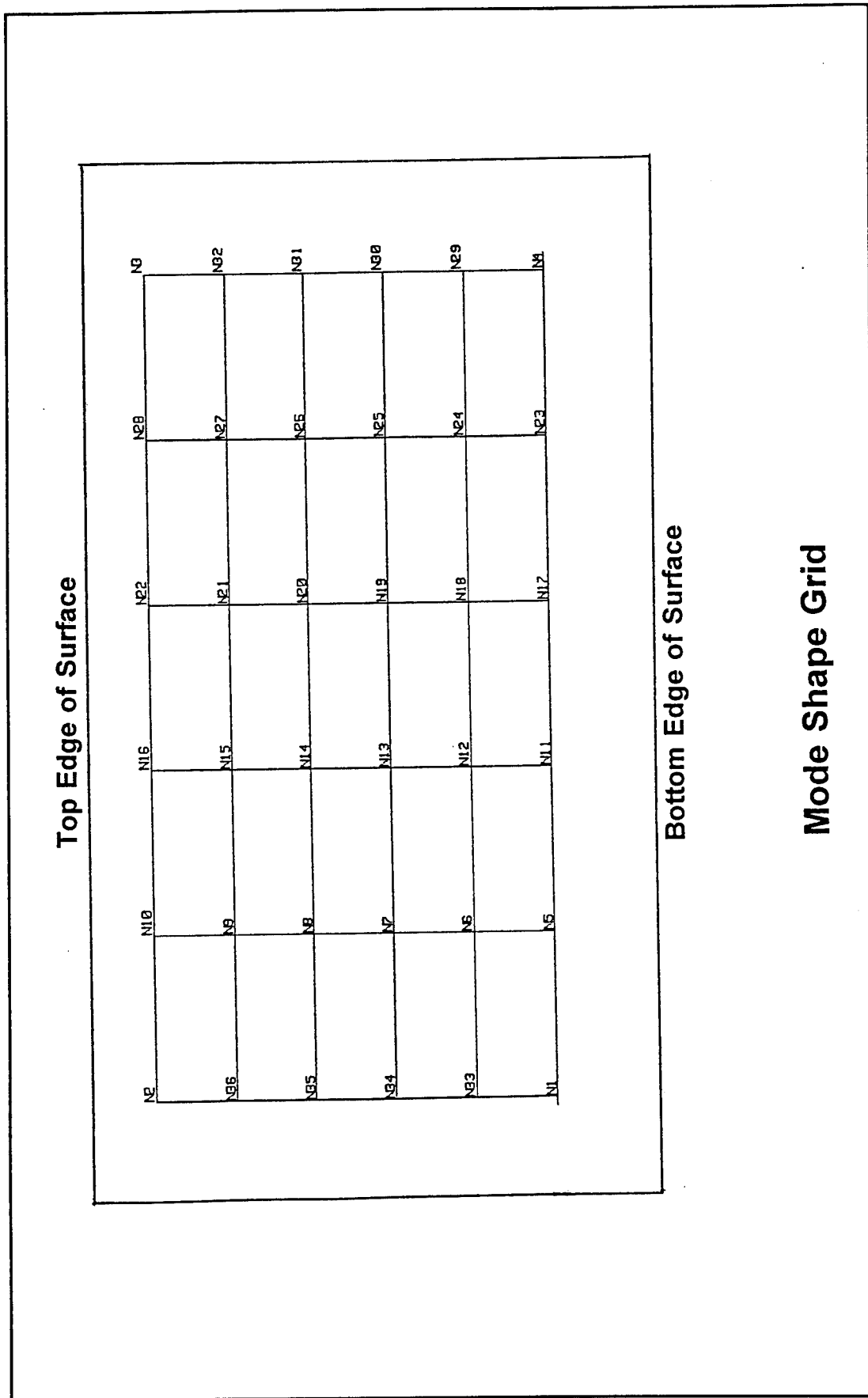


Plate 64. Scanning Laser Vibrometry System. Node definition on the gate skin

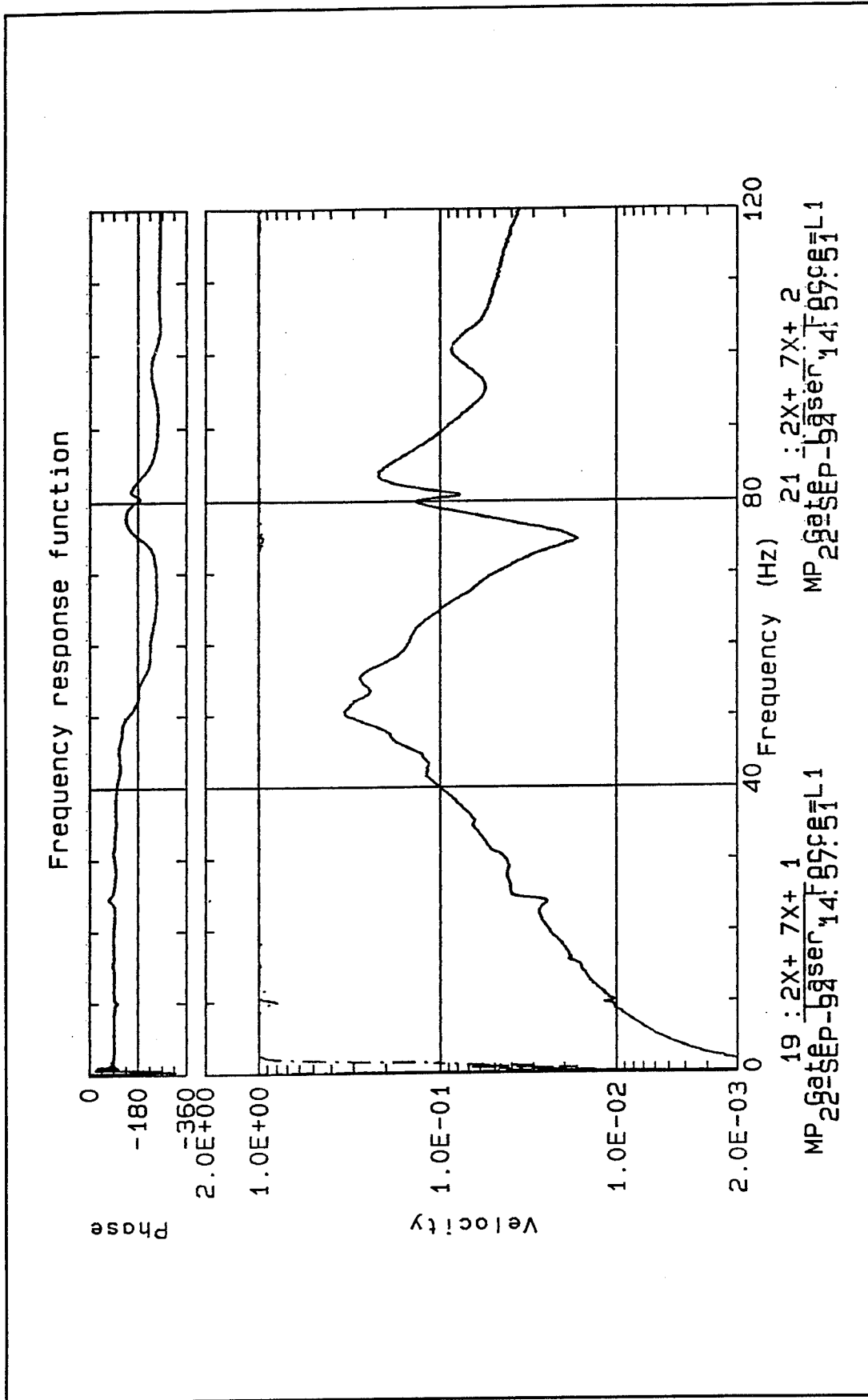


Plate 65. Scanning Laser Vibrometry System. Frequency-response function for the velocity of nodes 19 and 21 on the gate skin

RESULTS: 2-2:MP ACCEL SHAPE/56.05469
 MODE: 2 FREQ: 56.05469 DAMP: 0.0
 VELOCITY - MAG MIN: 1.45E-01 MAX: 3.80E-01
 DEFORMATION: 2-2:MP ACCEL SHAPE/56.05469
 MODE: 2 FREQ: 56.05469 DAMP: 0.0
 VELOCITY - MAG MIN: 1.45E-01 MAX: 3.80E-01
 FRAME OF REF: PART

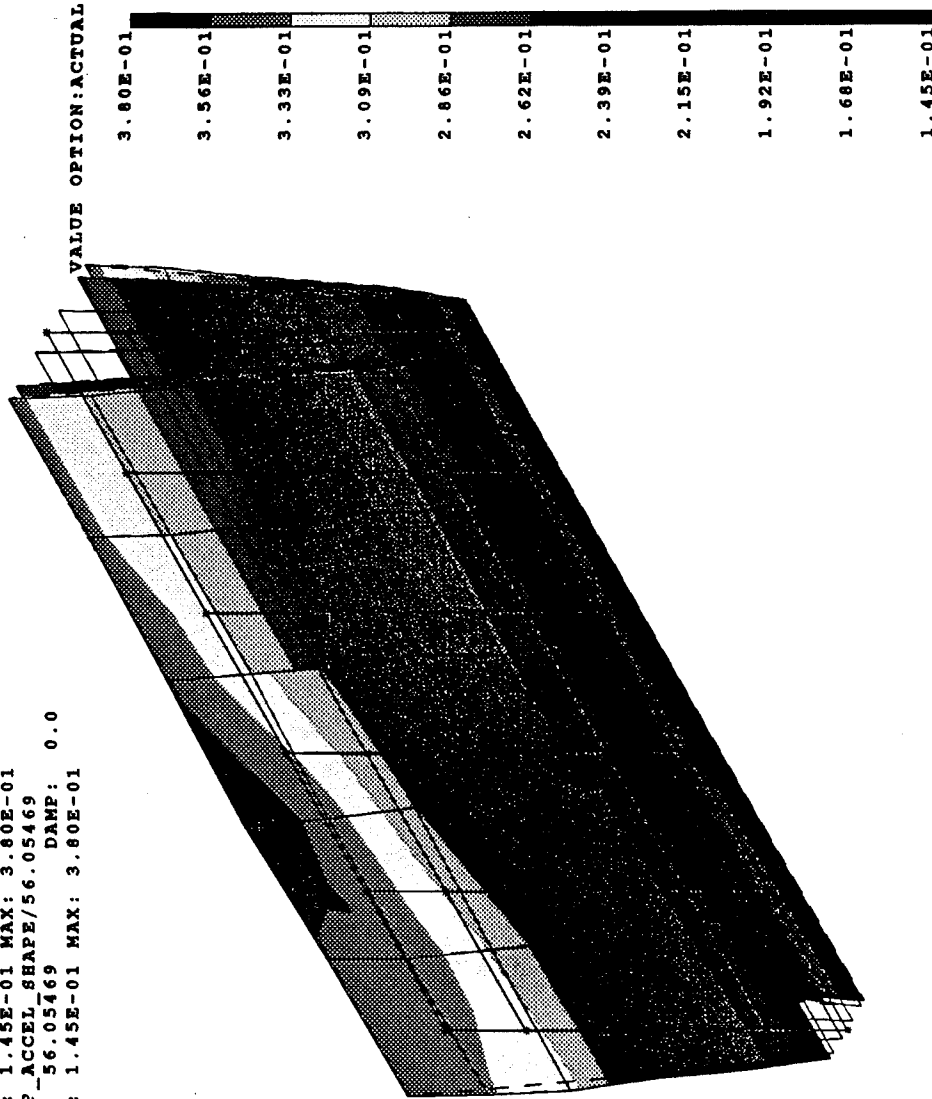


Plate 66. Scanning Laser Vibrometry System. Mode-shape 1

RESULTS: 4-4:MP ACCEL SHAPE/83.78906
 MODE: 4 FREQ: 83.78906 DAMP: 0.0
 VELOCITY - MAG MIN: 5.82E-02 MAX: 4.20E-01
 DEFORMATION: 4-4:MP ACCEL SHAPE/83.78906
 MODE: 4 FREQ: 83.78906 DAMP: 0.0
 VELOCITY - MAG MIN: 5.82E-02 MAX: 4.20E-01
 FRAME OF REF: PART

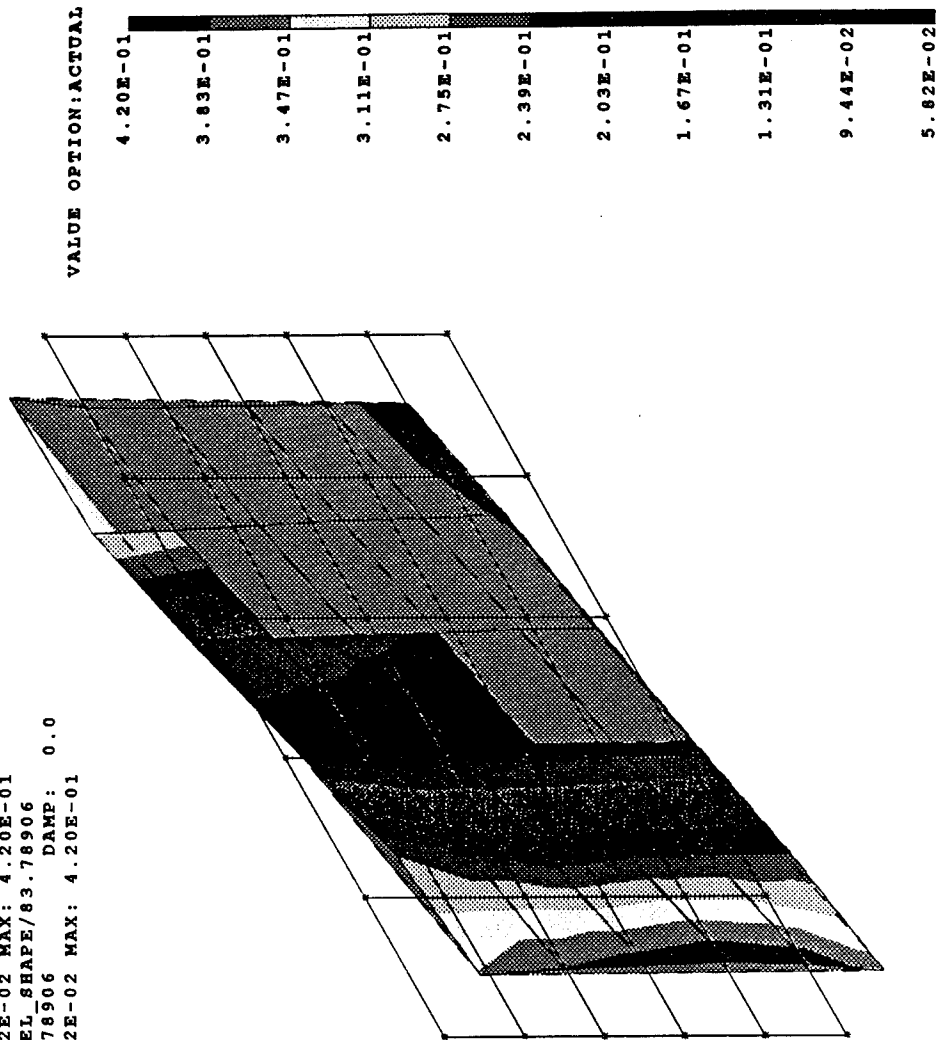


Plate 67. Scanning Laser Vibrometry System. Mode-shape 2

RESULTS: 8-8:MP ACCEL_SHAPE/200.5859
 MODE: 8 FREQ: 200.586 DAMP: 0.0
 VELOCITY - MAG MIN: 2.21E-03 MAX: 1.00E+00
 DEFORMATION: 8-8:MP ACCEL_SHAPE/200.5859
 MODE: 8 FREQ: 200.586 DAMP: 0.0
 VELOCITY - MAG MIN: 2.21E-03 MAX: 1.00E+00
 FRAME OF REF: PART

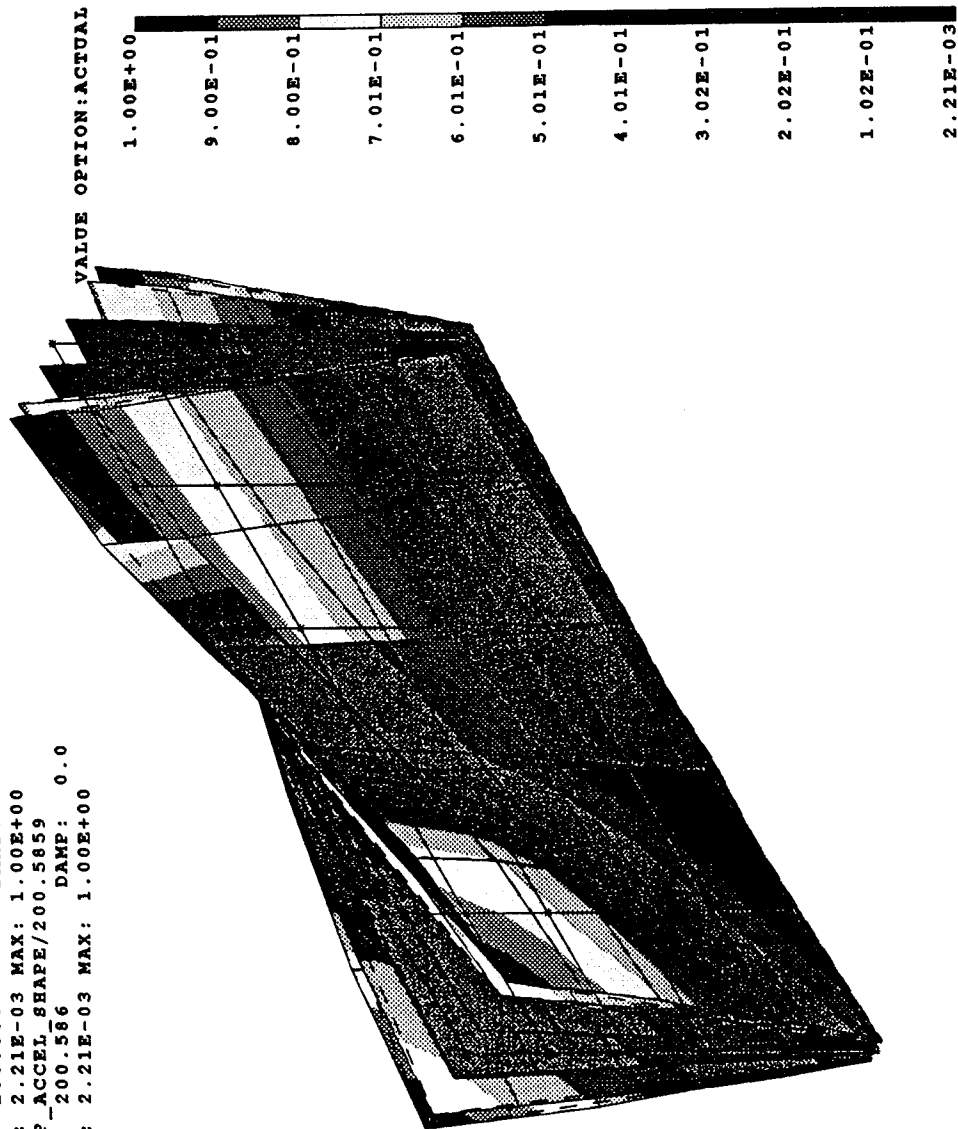


Plate 68. Scanning Laser Vibrometry System. Mode-shape 5

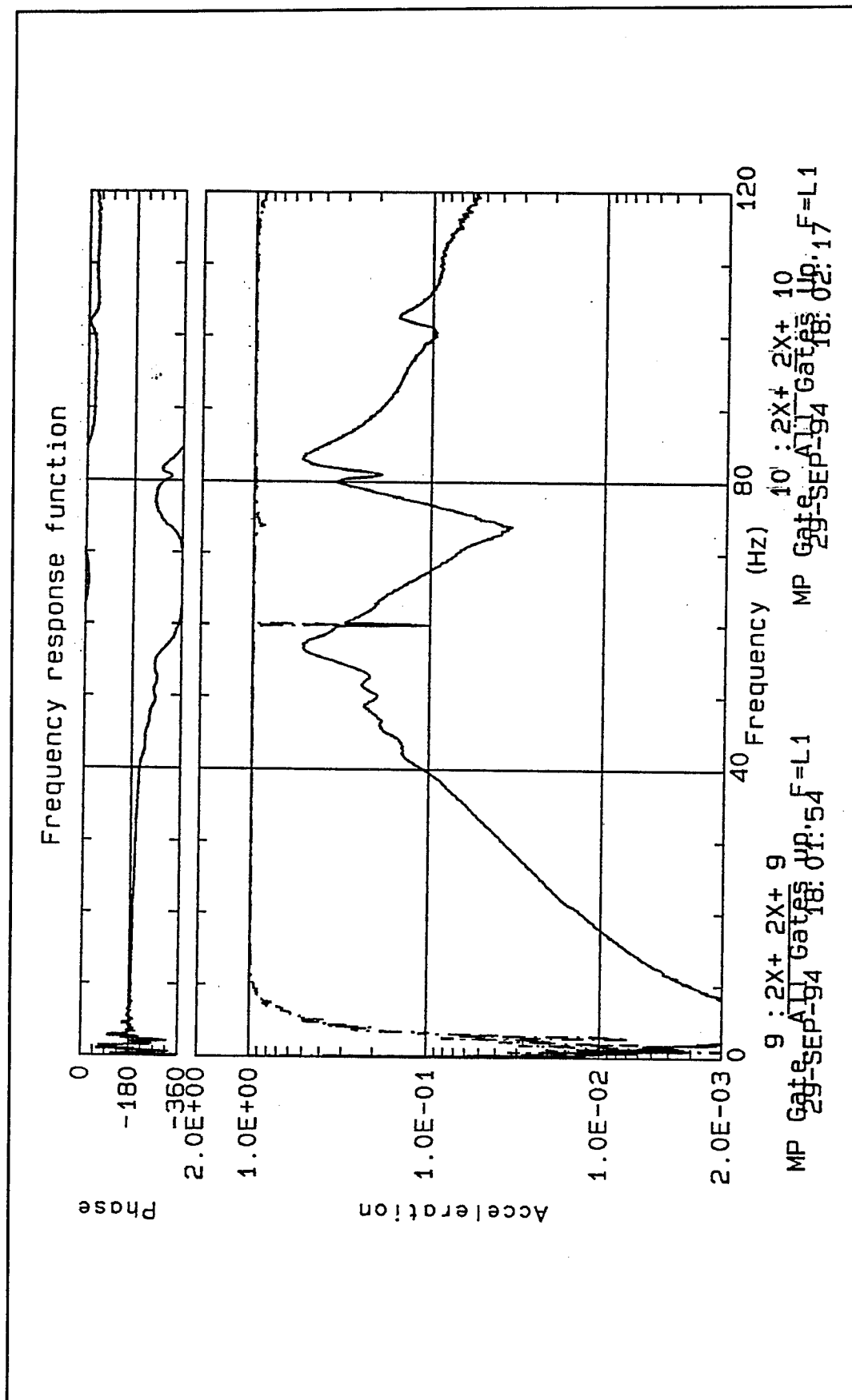


Plate 69. Scanning Laser Vibrometry System. Frequency-response function for the acceleration of nodes 9 and 10 on the gate skin when all three gates are raised

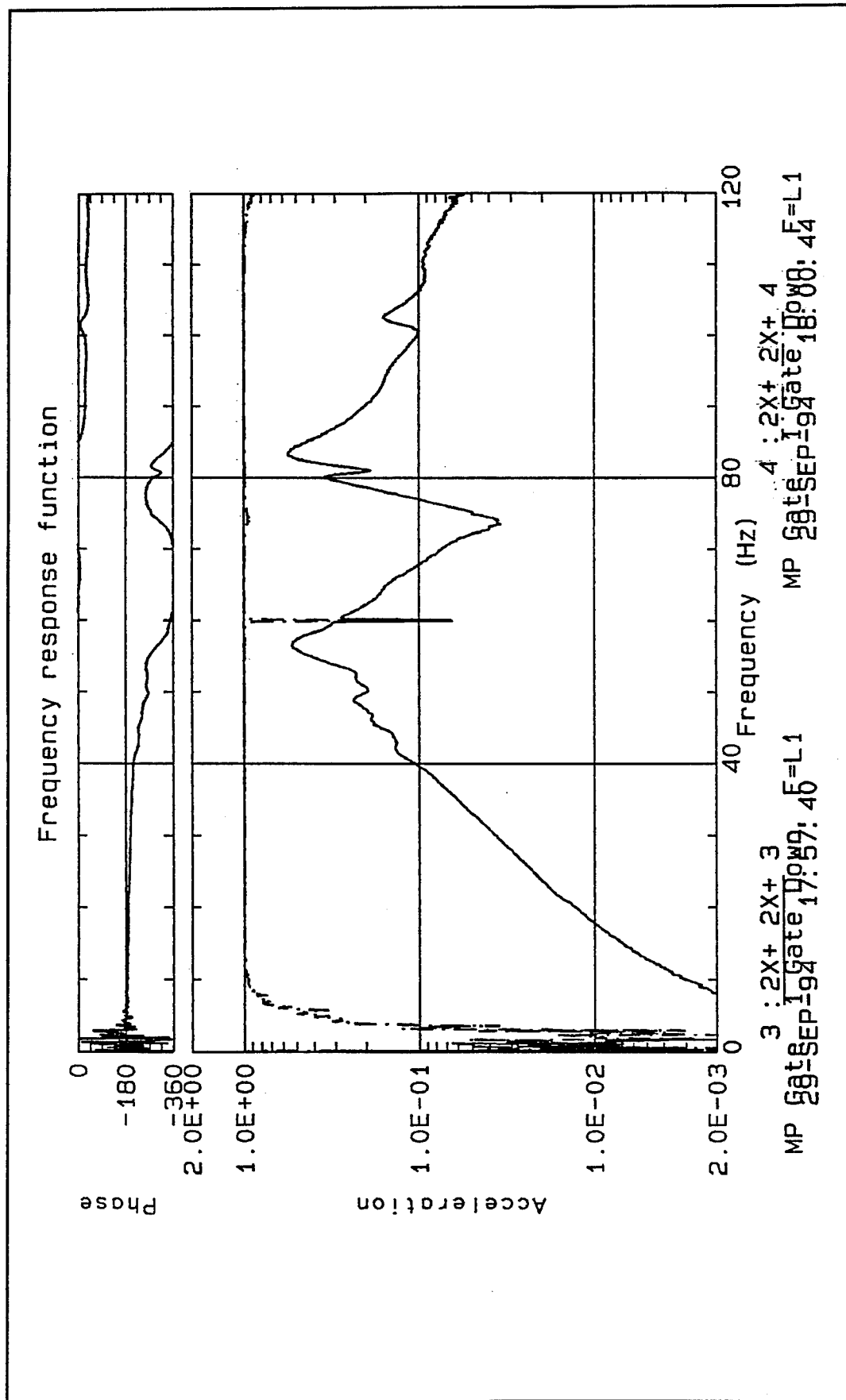


Plate 70. Scanning Laser Vibrometry System. Frequency-response function for the acceleration of nodes 3 and 4 on the gate skin when one lateral gate is down and the other two are raised

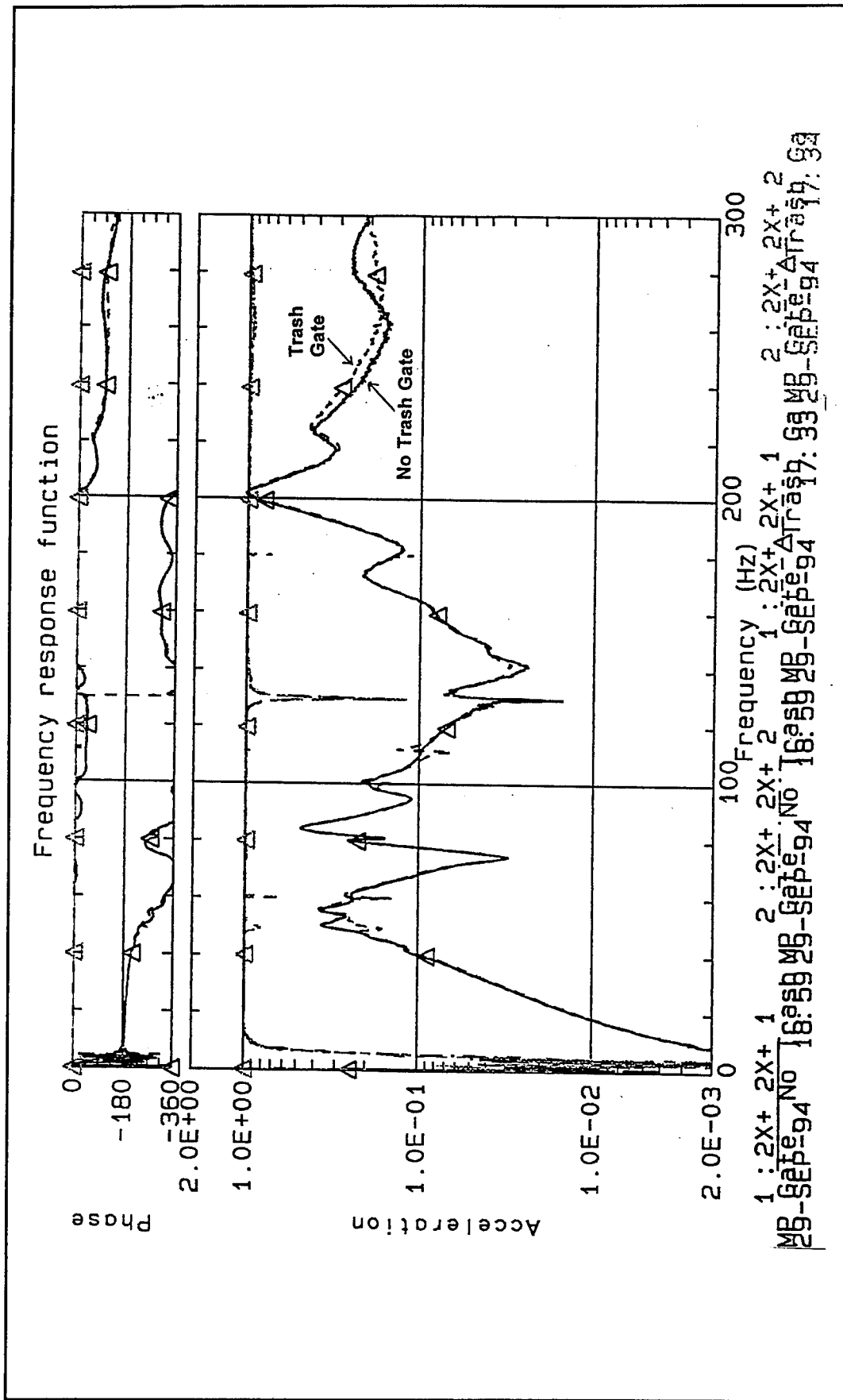


Plate 72. Scanning Laser Vibrometry System. Comparison between the frequency-response functions for the acceleration of nodes 1 and 2 on the gate skin with and without a leaning trash rack

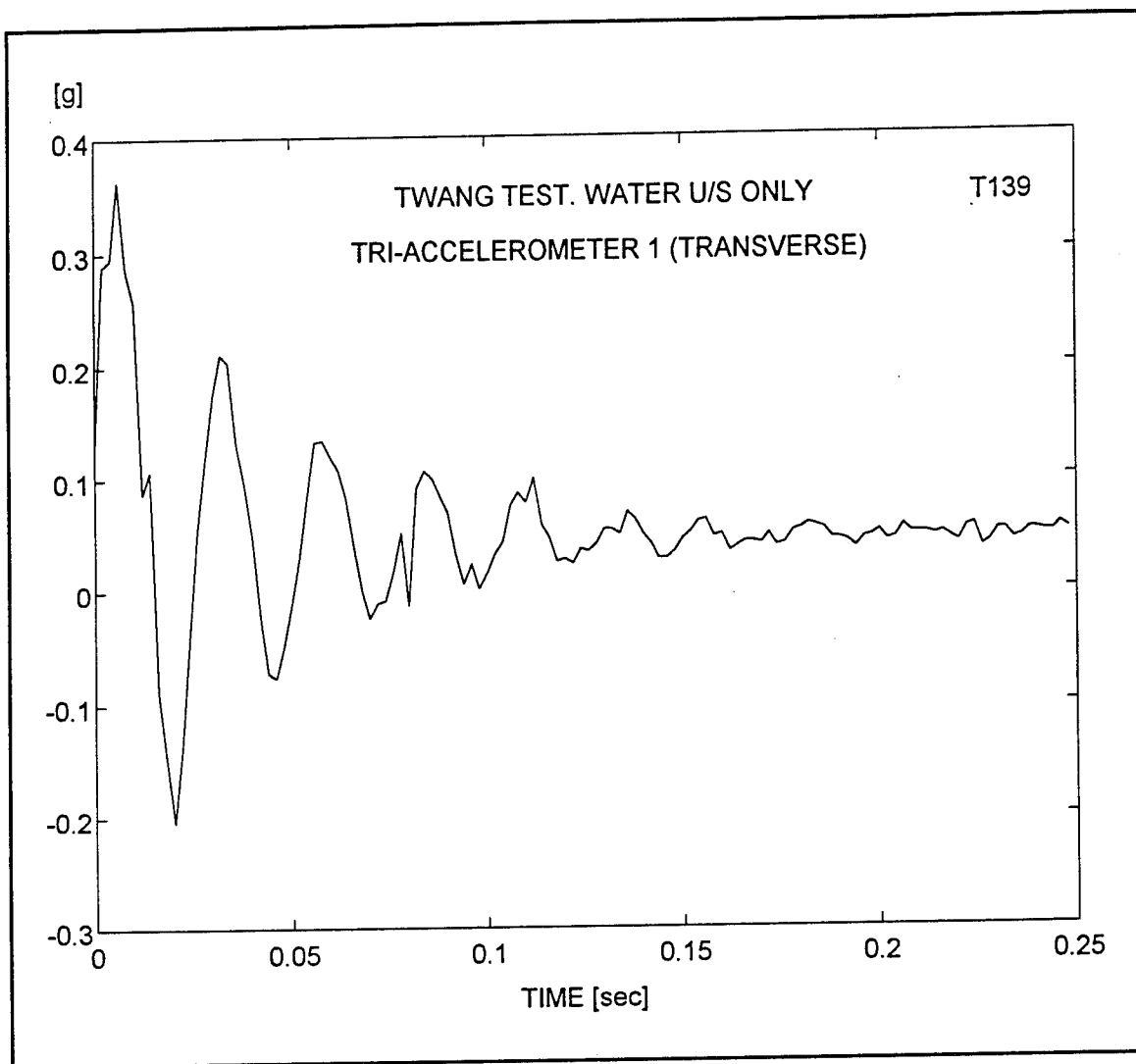


Plate 73. Free vibration of gate with upstream side submerged in water. Transverse time-history of response for triaxial accelerometer 1 (Twang test T0139)

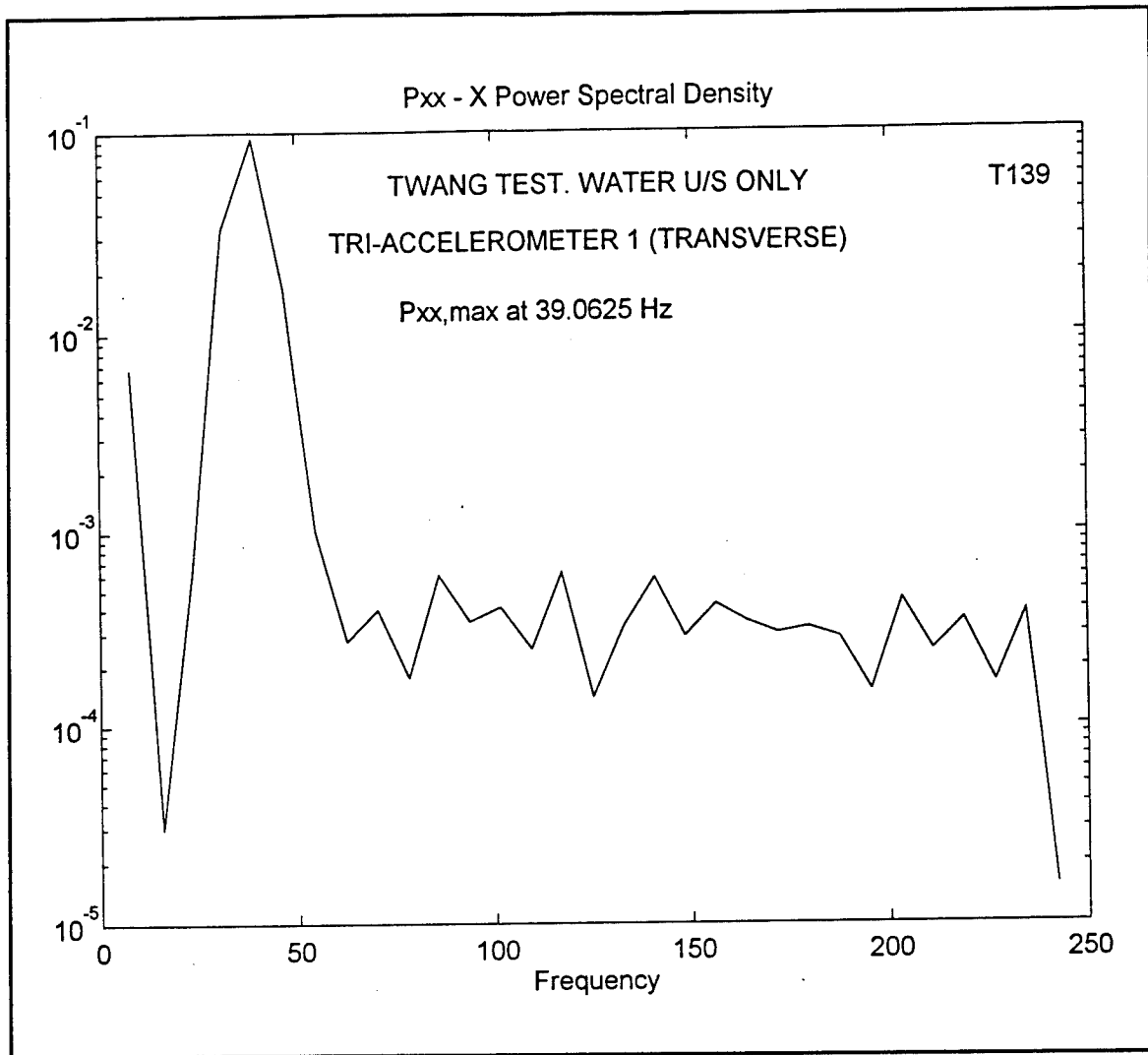


Plate 74. Free vibration of gate with upstream side submerged in water. Spectral density for transverse time-history of response for triaxial accelerometer 1 (Twang test T0139)

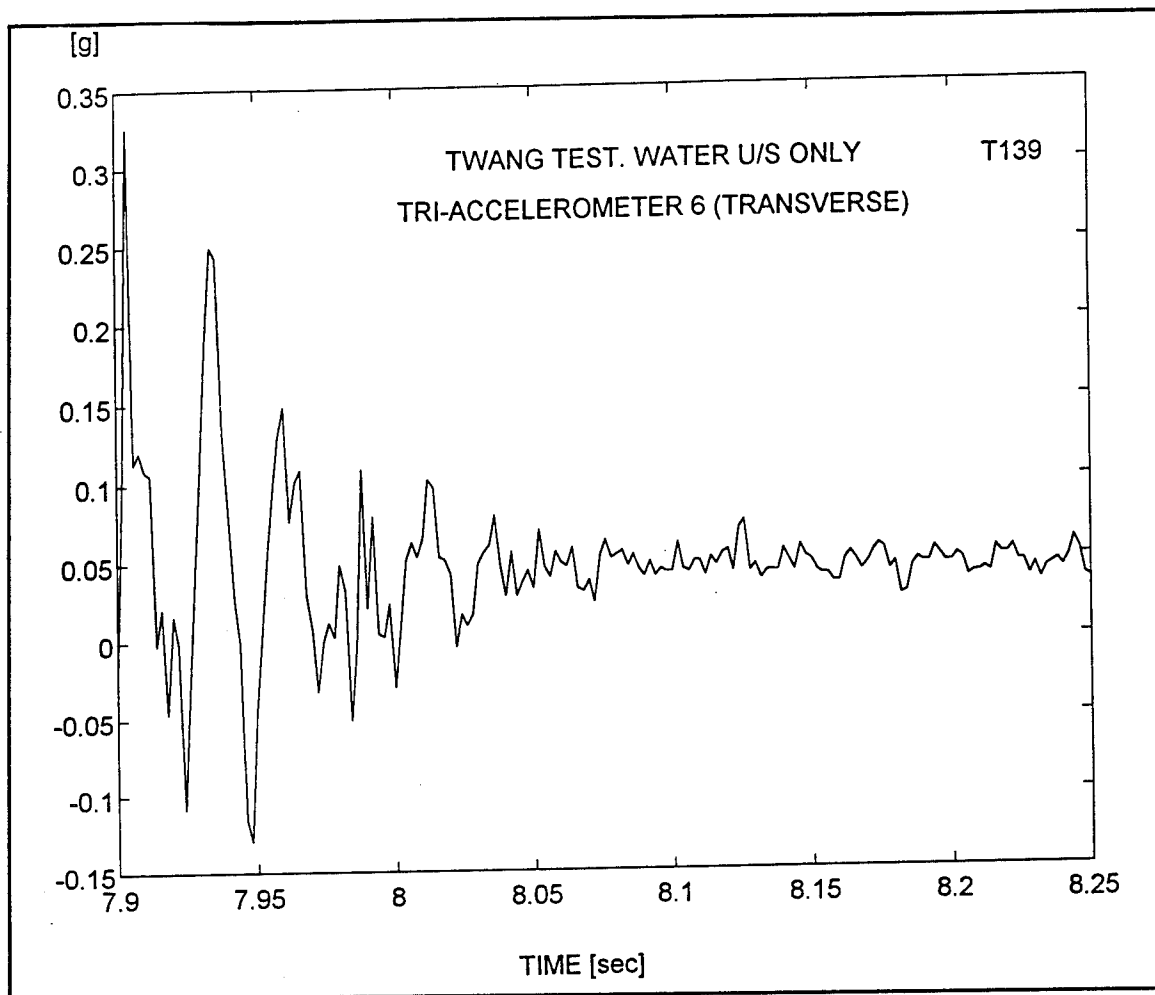


Plate 75. Free vibration of gate with upstream side submerged in water. Transverse time-history of response for triaxial accelerometer 6 (Twang test T0139)

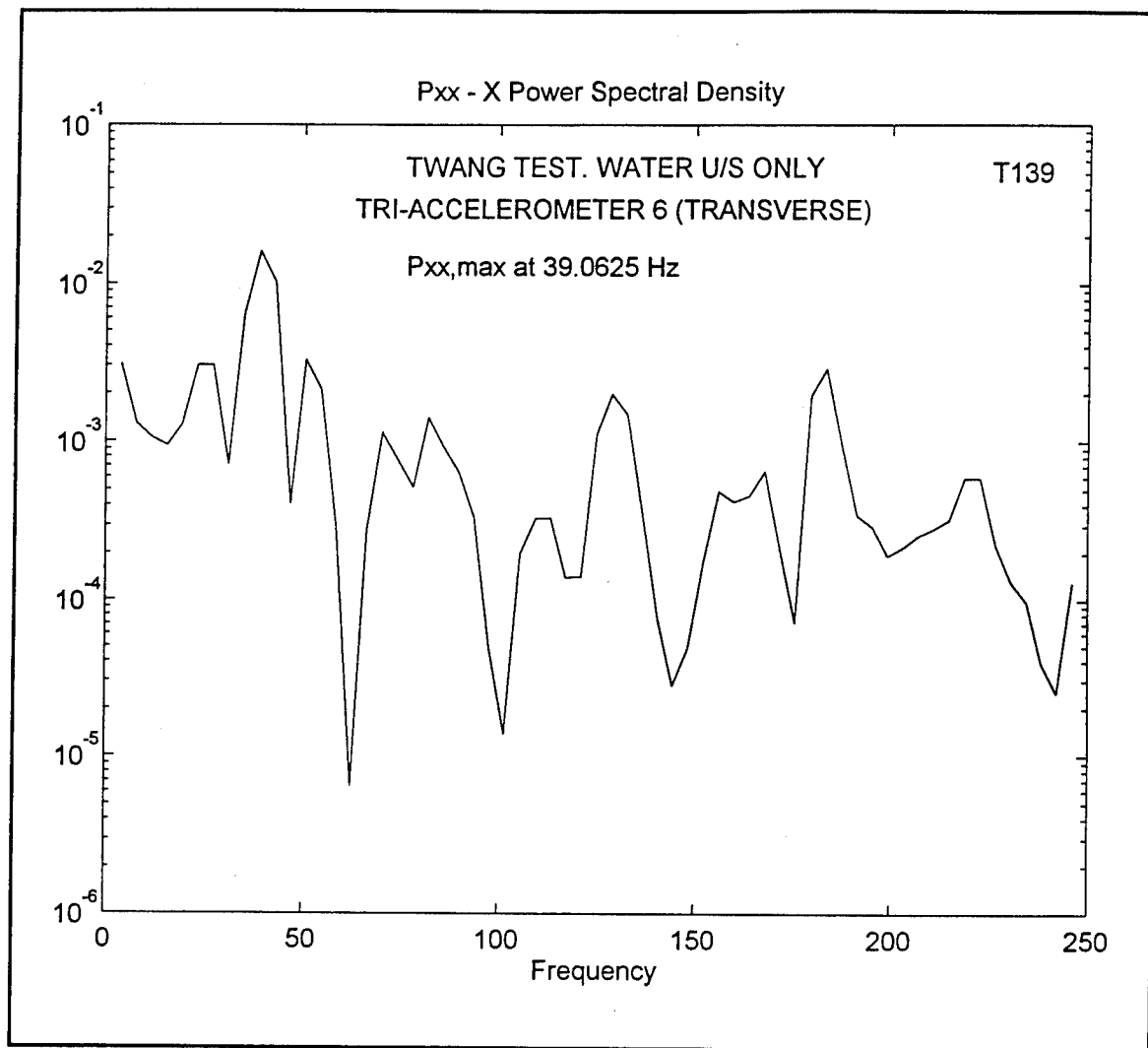


Plate 76. Free vibration of gate with upstream side submerged in water. Spectral density for transverse time-history of response for triaxial accelerometer 6 (Twang test T0139)

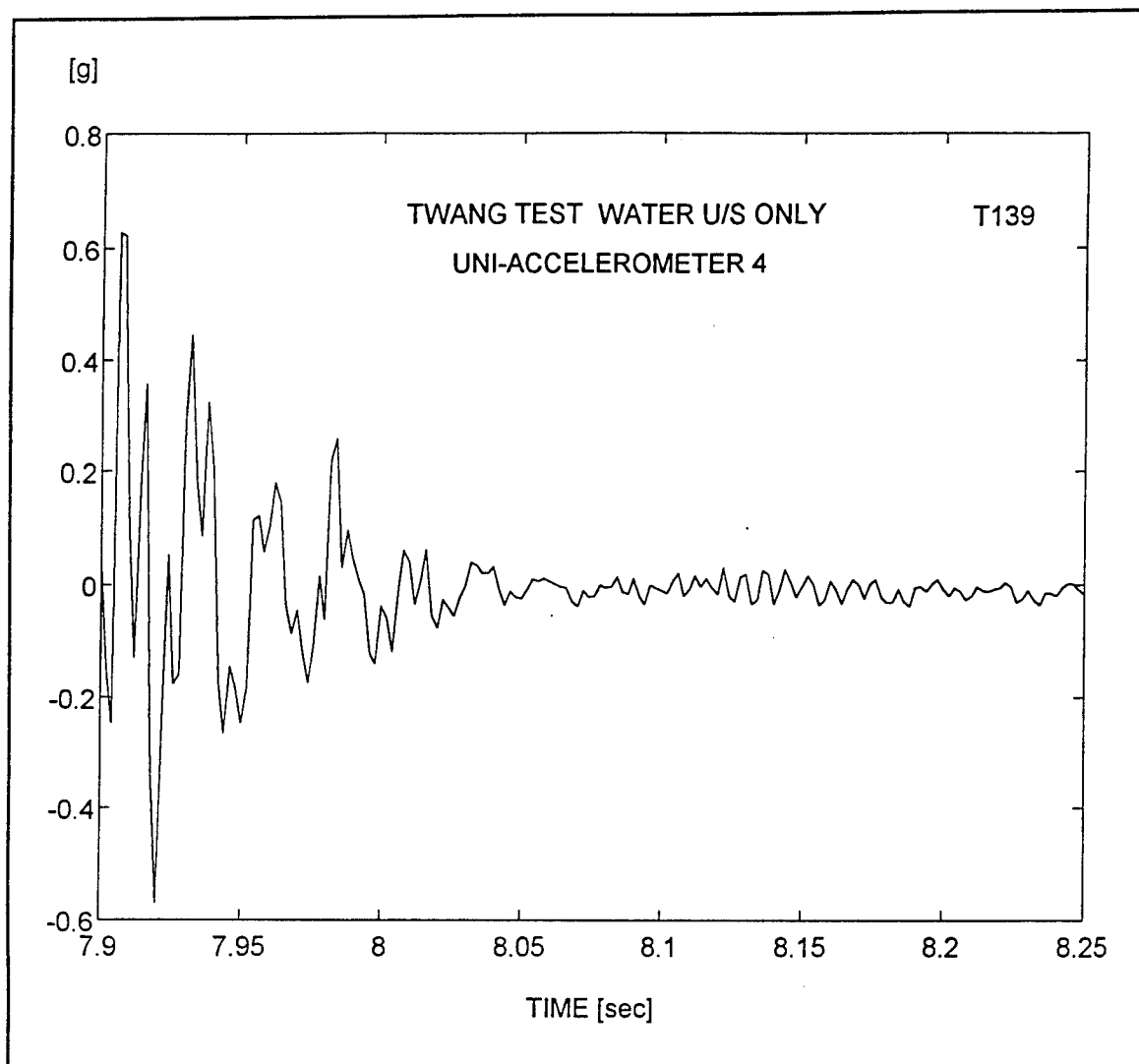


Plate 77. Free vibration of gate with upstream side submerged in water. Time-history of response for uniaxial accelerometer 4 (Twang test T0139)

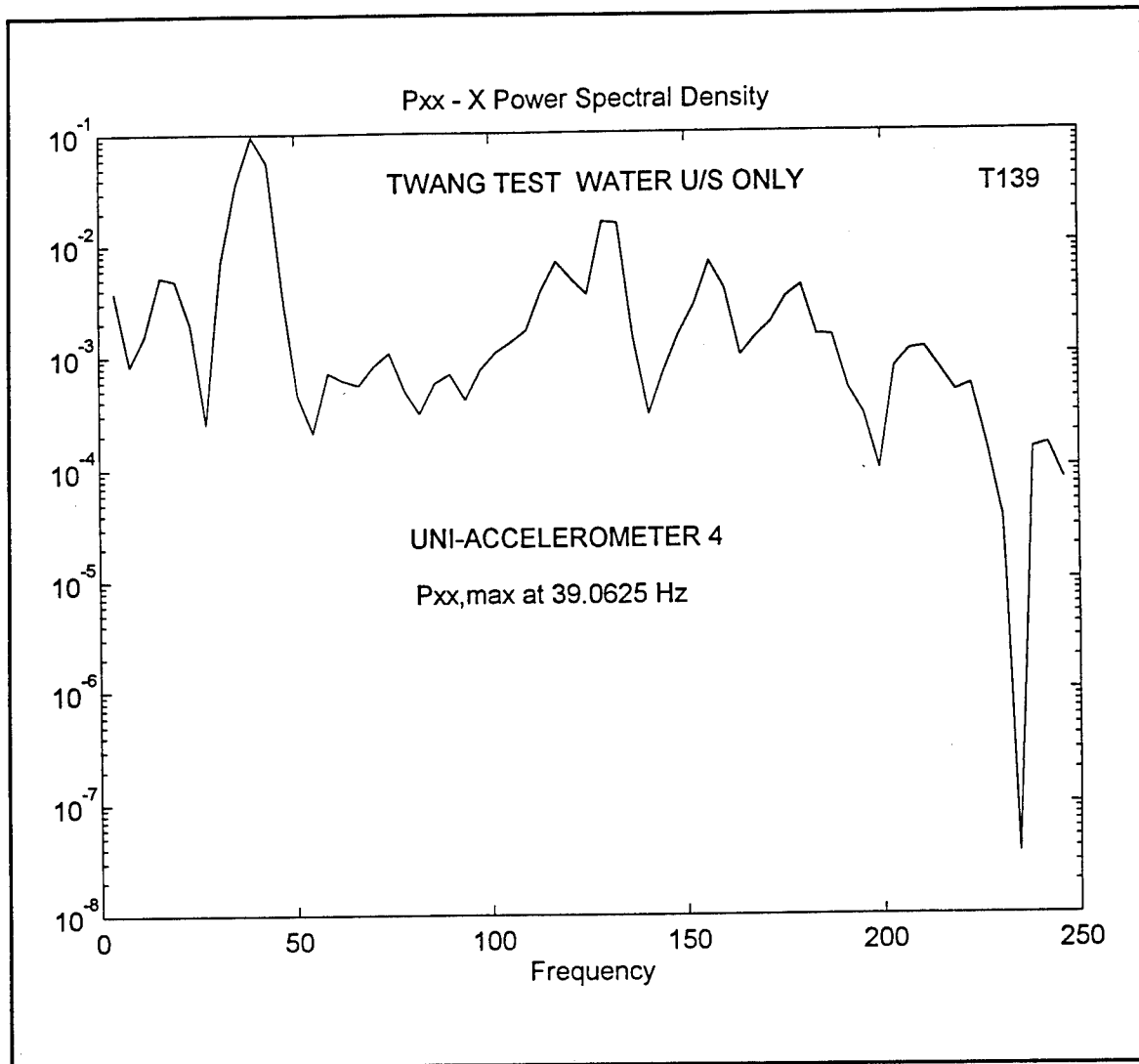


Plate 78. Free vibration of gate with upstream side submerged in water. Spectral density for time-history of response for uniaxial accelerometer 4 (Twang test T0139)

6 Engineering Model

In this chapter, an engineering model is derived to estimate the response of the gate system subjected to the upstream hydraulic pressure field. This model is based on the principles of structural dynamics applied to an idealization of the gate system conceived as a rigid-body torque-tube gate standing on simple supports and being acted upon by the hydraulic pressure field and by the visco-elastic system of resisting forces provided by the operating arms and the horizontal actuator (Clough and Penzien 1975). The model is general, but the specific numerical applications illustrating the development refer to the 1/15-scale physical model.

The first section presents the deterministic derivation of the steady-state component of the gate response—in particular, the gate rotation and the moment at the root of the operating arms. The second section presents a random vibration model for the stochastic description of the fluctuations of structural response about the steady-state component (Naudascher 1991, Yang 1986). Both models compare satisfactorily with the corresponding experimental verifications.

Deterministic Mathematical Model

Consider the rigid-body gate in closed position (angle $2\alpha = 70^\circ$) shown in Plate 79, standing on Teflon bearings and being excited by an external dynamic pressure field p and by its own weight W (mass $M = W/g$). The overturning moment of the external forces about the center of the torque tube is resisted by the eccentric force exerted by the horizontal actuator with stiffness K and equivalent viscous damping C , acting at the far end of the operating arms with flexural rigidity EI and length L . The analytical model in Plate 80 is then proposed. The gate is idealized as a rigid circular arc (radius a) spanning from an elevation $\theta_o = 20^\circ$ at O to an elevation $\theta_f = 72.75^\circ$ at D, and its mass is lumped at the centroidal point. The torque tube reduces to point O, representing the rigid connection of the operating arms to the base of the gate.

The displacements are discretized in this model by the three coordinates shown in Plate 81, i.e., rotations θ_1 and θ_2 at nodes O and B, respectively,

and the linear displacement Δ of the end B of the operating arms (Rubinstein 1966, Zienkiewicz 1977). Only the strain energy associated with bending deformations of the operating arms is considered (Boresi and Sidebottom 1985, Rubinstein 1966).

The stiffness matrix of the system may be formulated as (Przemienieki 1985, Rubenstein 1966)

$$[K] = \frac{2EI}{L} \begin{bmatrix} 2 & 1 & \frac{3}{L} \\ 1 & 2 & \frac{3}{L} \\ \frac{3}{L} & \frac{3}{L} & \left(\frac{6}{L^2} + \frac{KL \cos^2 \alpha}{2EI} \right) \end{bmatrix} \quad (33)$$

Elimination of coordinates θ_2 and Δ from the corresponding stiffness formulation by static condensation (Clough and Penzien 1975, Przemienieki 1985) produces the generalized stiffness coefficient for the degree-of-freedom θ_1 only as

$$K^* = \frac{1}{\frac{L}{3EI} + \frac{1}{KL^2 \cos^2 \alpha}} \quad (34)$$

A similar procedure applied to the viscous damping matrix renders the generalized viscous damping coefficient associated with the degree-of-freedom θ_1 only as

$$C^* = CL^2 \cos^2 \alpha \quad (35)$$

Plate 82 shows the generalized single degree-of-freedom system ($\phi \triangleq \theta_1$) vibrating under the action of the vertical and horizontal components of the resultant hydraulic force on the gate (R_1 and R_2 , respectively), the gate own weight (W), and the resisting elastic, viscous, and inertial moments (M_s , M_c , and M_i , respectively) at the gate base. Notice in the plate the viscous damper C_D representing the drag force on the gate, opposing its velocity through water. The degree of freedom ϕ is defined as the rotation of the gate with respect to its static weight-deflected configuration (Clough and Penzien 1975).

The dynamic equilibrium of the rigid-body gate is formulated by applying the virtual work principle on the structural system subjected to the virtual displacement $\delta\phi$ (a small variation from the instantaneous position of equilibrium determined by ϕ) (Mura and Koya 1992). Table 9 lists the forces on the gate, the corresponding virtual displacements, and their virtual work contributions to the energy equation $\Sigma (\delta \text{ Work}) = 0$, i.e.,

$$I_o \ddot{\phi} + (CL^2 \cos^2 \alpha + C_D') \dot{\phi} + \left(\frac{1}{\frac{L}{3EI} + \frac{1}{KL^2 \cos^2 \alpha}} - R_1 r_2 + R_2 r_1 - Ww \right) \phi = R_1 r_1 + R_2 r_2, \quad (36a)$$

where

I_o = mass moment of inertia of the gate about the torque-tube axis

r_1 and r_2 = lever arms of forces R_1 and R_2 about the same axis, respectively

Table 9 Dynamic Equilibrium, Formulation of the Principle of Virtual Displacements		
Action	Virtual Displacement	Virtual Work
$M_i = I_o \cdot \ddot{\phi}$	$\delta\phi$	$-I_o \cdot \ddot{\phi} \cdot \delta\phi$
$M_c = C^* \cdot \dot{\phi}$	$\delta\phi$	$-C L^2 \cos^2 \alpha \cdot \dot{\phi} \cdot \delta\phi$
$M_D = C_D^* \cdot \dot{\phi}$	$\delta\phi$	$-C_D^* \cdot \dot{\phi} \cdot \delta\phi$
$M_s = K^* \cdot \phi + W \cdot v$	$\delta\phi$	$-\frac{1}{\frac{L}{3EI} + \frac{1}{KL^2 \cos^2 \alpha}} \cdot \phi \cdot \delta\phi - Wv\delta\phi$
R_1	$(r_1 + r_2 \phi) \cdot \delta\phi$	$R_1 (r_1 + r_2 \phi) \cdot \delta\phi$
R_2	$(r_2 - r_1 \phi) \cdot \delta\phi$	$R_2 (r_2 - r_1 \phi) \cdot \delta\phi$
W	$(v + w \cdot \phi) \cdot \delta\phi$	$W (v + w \cdot \phi) \cdot \delta\phi$

Recognizing that the second-order terms within the parenthesis in Equation 36,

$$-R_1 r_2 + R_2 r_1 - Ww ,$$

contribute to its numerical value with a negligible amount, and that the fraction

$$\frac{1}{KL^2 \cos^2 \alpha}$$

is also negligibly small, the equation of motion may be reduced in this case to

$$\ddot{\phi} + 2 \xi \omega \dot{\phi} + \omega^2 \phi = \frac{R_1 r_1 + R_2 r_2}{I_o} , \quad (36b)$$

where

$$\omega^2 = \frac{3EI}{I_o L} \quad (36c)$$

is the square of the natural circular frequency of vibration, and

$$\xi = \frac{CL^2 \cos^2 \alpha + C_D^*}{I_o} \quad (36d)$$

is the overall equivalent viscous damping ratio.

Plate 83 shows a relevant portion of the free-vibration decay of the gate during the Twang test T0137 in dry air and the application of the logarithmic decrement method for the approximate determination of the equivalent viscous damping ratio ($\xi = 12.0$ percent, on the average). Likewise, Plate 84 shows a relevant portion of the free-vibration decay of the gate during the Twang test T0139, with water on its upstream side only, and the application of the logarithmic decrement method for the approximate determination of the equivalent viscous damping ratio ($\xi = 9.5$ percent, on the average) (Clough and Penzien 1975).

The computation of I_o was effected with the assistance of the preprocessor PATRAN-3 (PDA Engineering 1993). Plate 85 shows a schematic representation of the gate in horizontal position. With reference to the right-handed set of axes XYZ, the coordinates of the centroidal point of the torque tube are

given by CT (-2.8917, +15.6000, +11.9333), and the coordinates of the centroidal point for the gate-torque-tube system are given by CG(-1.0390, +15.200, +11.9333). The total mass of the gate-torque-tube system is given by $M = 0.178 \text{ lb-sec}^2/\text{in.}$, whereas the tensor of inertia is given by (Boresi and Sidebottom 1985)

$$[I] = \begin{bmatrix} 76.7 & -2.27 & -2.20 \\ -2.27 & 38.3 & 32.2 \\ -2.20 & 32.3 & 45.1 \end{bmatrix} \text{ lb-in.-sec}^2 .$$

Applying twice the parallel-axis theorem to transform I_{zz} (45.1 lb-in.-sec²) into $I_{z'z'}$, one obtains (Boresi and Sidebottom 1985)

$$\begin{aligned} I_{z'z'} &= I_{zz} + M(-228.53 \text{ in.}^2) \\ &= 4.42 \text{ lb-in.-sec}^2 \\ &= I_o \end{aligned}$$

as the mass moment of inertia of the gate-torque-tube system about the torque-tube axis, Z' .

If Young's modulus of elasticity for brass is taken as $E = 15,500 \text{ ksi}$ (Flinn and Trojan 1990), and the moment of inertia of both operating arms about their neutral axis in bending is calculated as

$$I = 2 \cdot \frac{1}{12} \left(\frac{4}{3} \right) (1)^3 = \frac{2}{9} \text{ in.}^4 ,$$

recognizing that $L = 9.3 \text{ in.}$, Equation 36c provides an estimation of the fundamental frequency of vibration of the system as

$$\begin{aligned} \omega^2 &= 251,380 \text{ sec}^{-2} \\ \therefore \omega &= 501.4 \text{ sec}^{-1} \\ \text{or } f &= 79.8 \text{ Hz} , \end{aligned}$$

which compares well with the finite element calculation for the first mode of vibration of the physical model for the gate system with a rigid torque tube, standing on three twist-hinges on a rigid foundation (see Plate 86: $f = 76.3$ Hz). This structural parameter is expected to reflect a more rigid system than the actual physical model standing on Teflon bearings and load-cell foundations (for this, $f \approx 47$ Hz. See Plate 83b).

When the system is subjected to the steady-state component of the hydraulic force on the upstream side of the gate, the general solution of Equation 36b is the summation of the complementary and the particular solutions (Naudascher 1991, Clough and Penzien 1975), i.e.,

$$\phi(t) = e^{-\xi_w \omega t} (A \sin \omega_D t + B \cos \omega_D t) + \frac{\bar{M}}{\omega^2 I_o} , \quad (37a)$$

where

$$\bar{M} = R_1 r_1 + R_2 r_2 , \quad (37b)$$

and

$$\omega_D = \omega \sqrt{1 - \xi_w^2} \quad (37c)$$

is the damped natural circular frequency of the system, and A and B are constants of integration to be determined from the initial conditions.

Assuming initial conditions for rest, the steady-state response of the gate system is given by (Clough and Penzien 1975)

$$\phi(t) = \frac{\bar{M}}{\omega^2 I_o} (1 - e^{-\xi_w \omega t} \cos \omega_D t) . \quad (37d)$$

Evidently, after some time, the steady-state response tends asymptotically to

$$\phi \rightarrow \frac{\bar{M}}{\omega^2 I_o} . \quad (37e)$$

Inserting the experimental values for R_1 and R_2 obtained in tests T1087 and T1109, properly scaled for the physical model ($\lambda_L^{-3} = 15^{-3}$), and the values

of r_1 and r_2 given by Equations 26a and 26b, properly scaled for the physical model ($\lambda_L = 15^{-1}$), Equation 37d gives

$$\phi \rightarrow 5.5 \cdot 10^{-4} \text{ rad} = 3.5^\circ, \quad (37f)$$

which is essentially in agreement with the experimentally observed value, if this is taken as the mean between the maximum and minimum readings during the test.

Random Vibration Model for Fluctuations

The finite element solution of the eigenproblem for the elastic gate system standing on flexible bearings on load-cell foundations yields for the first frequency of free vibration a value $f_1 = 46.91$ Hz, which compares extremely well with the identified value from the Twang test T0137 on the physical model in dry air: $f_1 = 46.875$ Hz (Plate 83b). The value of $f_1 = 46.9$ Hz is taken as the true value of the natural frequency of vibration of the instrumented gate system in dry air.

Letting

$$f_1 = \beta_f \cdot f_1^{(0)}, \quad (38a)$$

where

$f_1^{(0)}$ = natural frequency of vibration of the rigid torque-tube gate system

β_f = constant to be determined experimentally, i.e.,

$$\beta_f = \frac{46.9}{79.8} \approx \frac{6\sqrt{6}}{25}, \quad (38b)$$

one has

$$f_1 = \frac{\beta_f}{2\pi} \cdot \sqrt{\frac{3EI}{I_o L}}. \quad (38c)$$

Now when the gate with water on its upstream side is allowed to vibrate freely, an effective added mass of water increases the gate rotational inertia

about the torque-tube axis. In other words, the natural frequency of vibration for the upstream-wet gate may be expressed as

$$f_1' = \frac{\beta_f}{2\pi} \sqrt{\frac{3EI}{I_o' L}} \quad (38d)$$

where

$$I_o' = \beta_{I_o}^2 \cdot I_o \quad (38e)$$

and β_{I_o} is a constant to be determined experimentally.

Using the experimental value $f_1' = 39.0625$ Hz obtained in test T0139 (Plate 84b), the value of β_{I_o} is identified from Equation 38c as

$$\beta_{I_o} = \frac{6}{5} \quad (38f)$$

Denoting by p_i the pressure acting at the i^{th} pressure cell location on the upstream side of the gate ($i = 1, 2, \dots, 9$), assumed as uniformly distributed over its tributary area (A_i), and denoting by d_i the distance from the line of action of the force associated with p_i to the torque-tube axis, the governing equation of motion for the gate subjected to the hydraulic pressure field on the upstream side of the gate is obtained as (Clough and Penzien 1975)

$$\ddot{v}_1 + 2 \xi_w (2 \pi f_1') \dot{v}_1 + (2 \pi f_1')^2 v_1 = \left(\frac{d_1^2}{I_o'} \right) \cdot \sum_{i=1}^9 (A_i \gamma_i) p_i(t) \quad (39a)$$

where

$$v_1 = d_1 \cdot \phi \quad \text{and} \quad \gamma_i = \frac{d_i}{d_1} \quad (39b)$$

Consider the contribution of p_i only to Equation 39a, and, in particular, when $p_i = \delta(t)$, i.e., a Dirac delta function applied at the starting time (Bendat and Piersol 1993, Yang 1986):

$$\ddot{v}_{1i} + 2 \xi_w (2 \pi f'_1) \dot{v}_{1i} + (2 \pi f'_1)^2 v_{1i} = \left(\frac{d_1^2}{I_o'} \right) \cdot (A_i \gamma_i) \delta(t) \quad (39c)$$

By Fourier transforming Equation 39c, one obtains the complex frequency-response function between the pressure p_i and displacement v_1 of pressure cell 1 in the direction locally normal to the gate skin:

$$H_{1i}(f) = \frac{\frac{d_1^2}{K'} (A_i \gamma_i)}{1 - \left(\frac{f}{f'_1} \right)^2 + i(2 \xi_w) \left(\frac{f}{f'_1} \right)} \quad (40)$$

Therefore, the Fourier transform of v_1 is given by (Bendat and Piersol 1993, Crandall and Mark 1963, Yang 1986)

$$V_{1i}(f) = H_{1i}(f) \cdot P_i(f) \quad (41)$$

where $P_i(f)$ is the Fourier transform of $p_i(t)$.

The Fourier transform of the total response $v_1(t)$ is conveniently obtained by superposition in the frequency domain as

$$V_1(f) = \sum_{i=1}^9 H_{1i}(f) \cdot P_i(f) \quad (42)$$

By taking the inverse Fourier transform of Equation 42, the total response $v_1(t)$ in the time domain is obtained as

$$v_1(t) = \sum_{i=1}^9 \frac{d_1^2}{K'} (A_i \gamma_i) \int_{-\infty}^{+\infty} \frac{P_i(f) e^{i2\pi ft} df}{1 - \left(\frac{f}{f'_1} \right)^2 + i(2 \xi_w) \left(\frac{f}{f'_1} \right)} \quad (43)$$

The total elastic resisting moment at the root of the operating arms is given by

$$M_R(t) = \frac{3 EI}{L} \phi(t) = K \phi(t) \quad (44a)$$

or

$$M_R(t) = \frac{d_1}{\beta_f^2} \sum_{i=1}^9 (A_i \gamma_i) \int_{-\infty}^{+\infty} \frac{P_i(f) e^{i2\pi f t} df}{1 - \left(\frac{f}{f_1'}\right)^2 + i(2 \xi_w) \left(\frac{f}{f_1'}\right)} \quad (44b)$$

If the pressure p_i is assumed a zero-mean stationary process (by extracting the time-average of the record), then the response v_{1i} and its contribution to the elastic resisting moment $M_{R,i}$ will also be zero-mean stationary processes, and consequently, the following relations among their corresponding spectral density functions hold (Newland 1984, Crandall and Mark 1963, Bendat and Piersol 1993, Hurty and Rubinstein 1964):

$$\begin{aligned} S_{M_{R,i}}(f) &= \left(\frac{K}{d_1}\right)^2 \cdot S_{v_{1i}}(f) = \left(\frac{K}{d_1}\right)^2 \cdot |H_{1i}(f)|^2 \cdot S_{p_i}(f) \\ &= \left(\frac{K}{d_1}\right)^2 \cdot \left[\frac{d_1^2}{K'} (A_i \gamma_i)\right]^2 \cdot \frac{S_{p_i}(f)}{\left[1 - \left(\frac{f}{f_1'}\right)^2\right]^2 + \left[(2 \xi_w) \left(\frac{f}{f_1'}\right)\right]^2} \end{aligned} \quad (45)$$

By adding the contribution of all p_i 's to the total power, one obtains for the mean square of the elastic resisting moment

$$\overline{M_R^2} = \left(\frac{d_1}{\beta_f^2}\right)^2 \cdot \sum_{i=1}^9 (A_i \gamma_i)^2 \cdot \int_{-\infty}^{+\infty} \frac{S_{p_i}(f) df}{\left[1 - \left(\frac{f}{f_1'}\right)^2\right]^2 + \left[(2 \xi_w) \left(\frac{f}{f_1'}\right)\right]^2} \quad (46a)$$

or

$$\overline{M_R^2} = \left(\frac{d_1}{\beta_f^2}\right)^2 \cdot \sum_{i=1}^9 (A_i \gamma_i)^2 \cdot \int_0^{+\infty} \frac{G_{p_i}(f) df}{\left[1 - \left(\frac{f}{f_1'}\right)^2\right]^2 + \left[(2 \xi_w) \left(\frac{f}{f_1'}\right)\right]^2}, \quad (46b)$$

in terms of the half-range spectral density function $G_{p_i}(f)$ (Bendat and Piersol 1993).

A program was developed to run under MATLAB (MATHWORKS 1993) for the numerical evaluation of Equation 46b. In the particular case of test T1080, the value of the power adds up to

$$\overline{M_R^2} = 2,204 \text{ (lb-ft)}^2$$

which should be compared with the directly measured experimental value, i.e.,

$$\begin{aligned}\overline{M_R^2} &= \sigma_{M_R}^2 + \mu_{M_R}^2 \\ &= 90 + 51^2 = 2,691 \text{ (lb-ft)}^2 \quad ,\end{aligned}\tag{47}$$

where

$\sigma_{M_R}^2$ = variance of the random process M_R , given by the area under the corresponding spectral density function (Plate 87).

μ_{M_R} = mean of the process, given by Equation 37b.

The mean square of the directly measured process M_R differs from its value derived from the hydraulic pressure field because the directly measured process is really the bending moment at the root of the operating arms, which is different from the hydraulic moment about the torque-tube axis; however, results compare generally well (8-percent error).

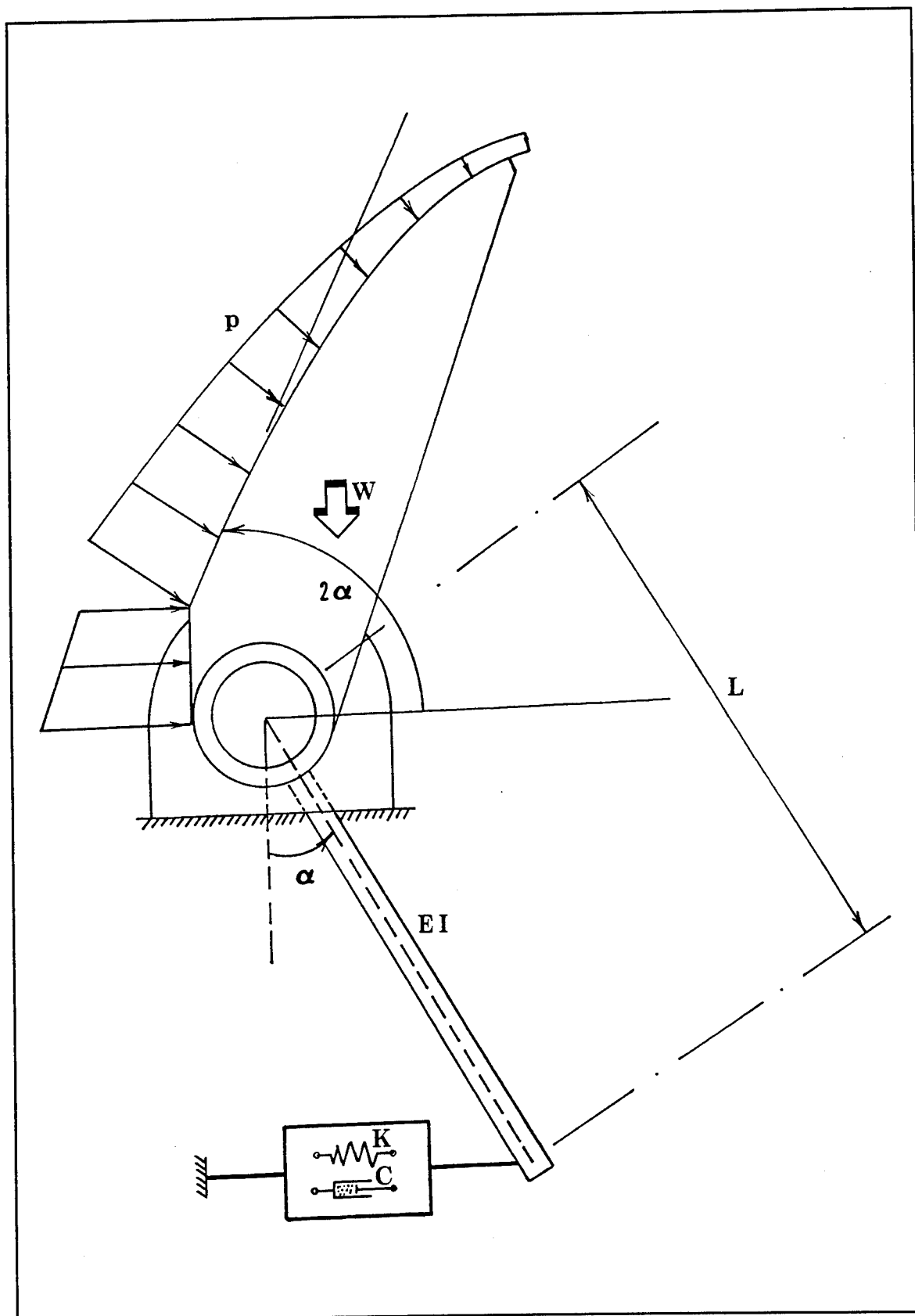


Plate 79. Lateral view of gate components, properties, and external forces

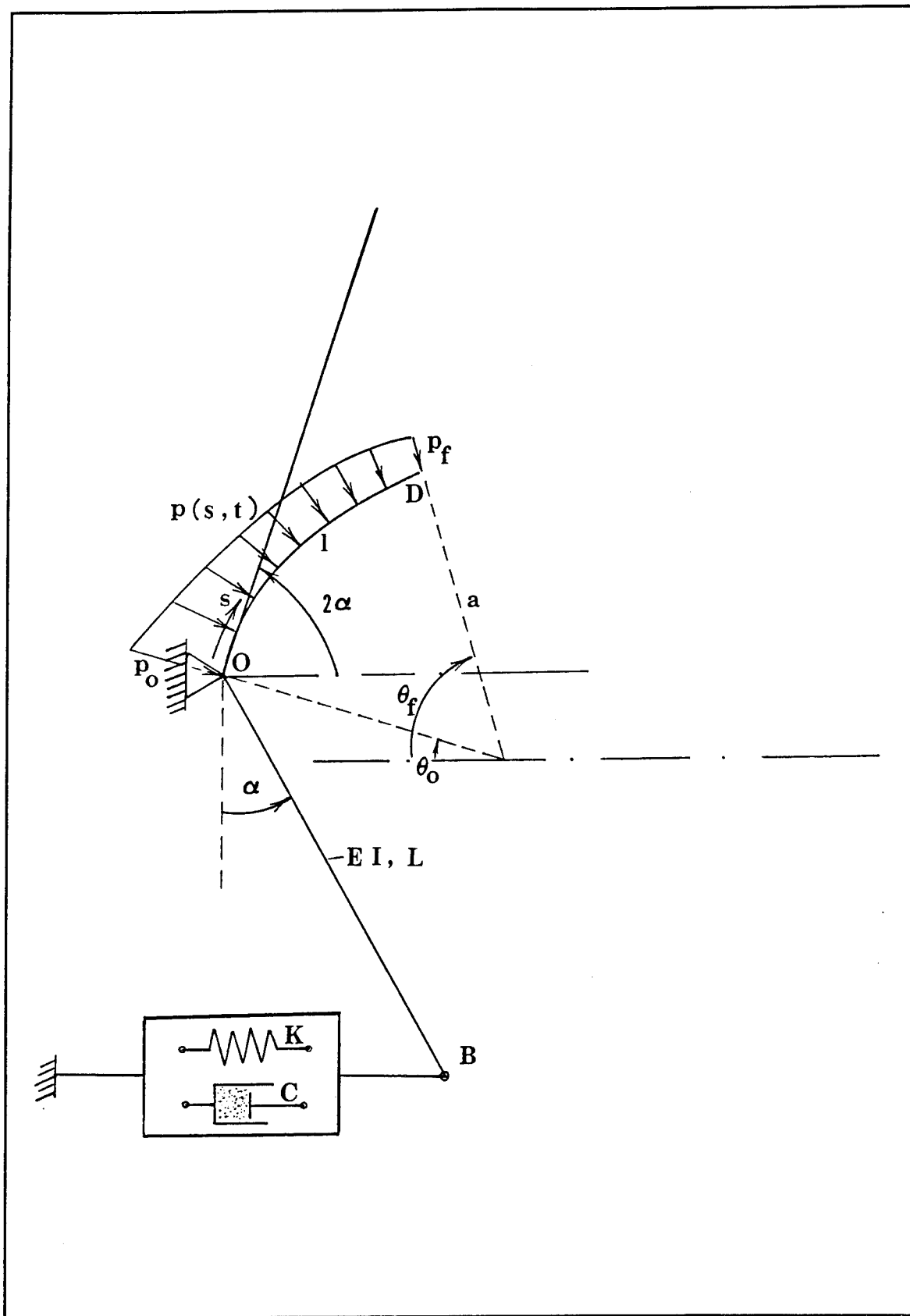


Plate 80. Analytical model. Gate components idealized as lines

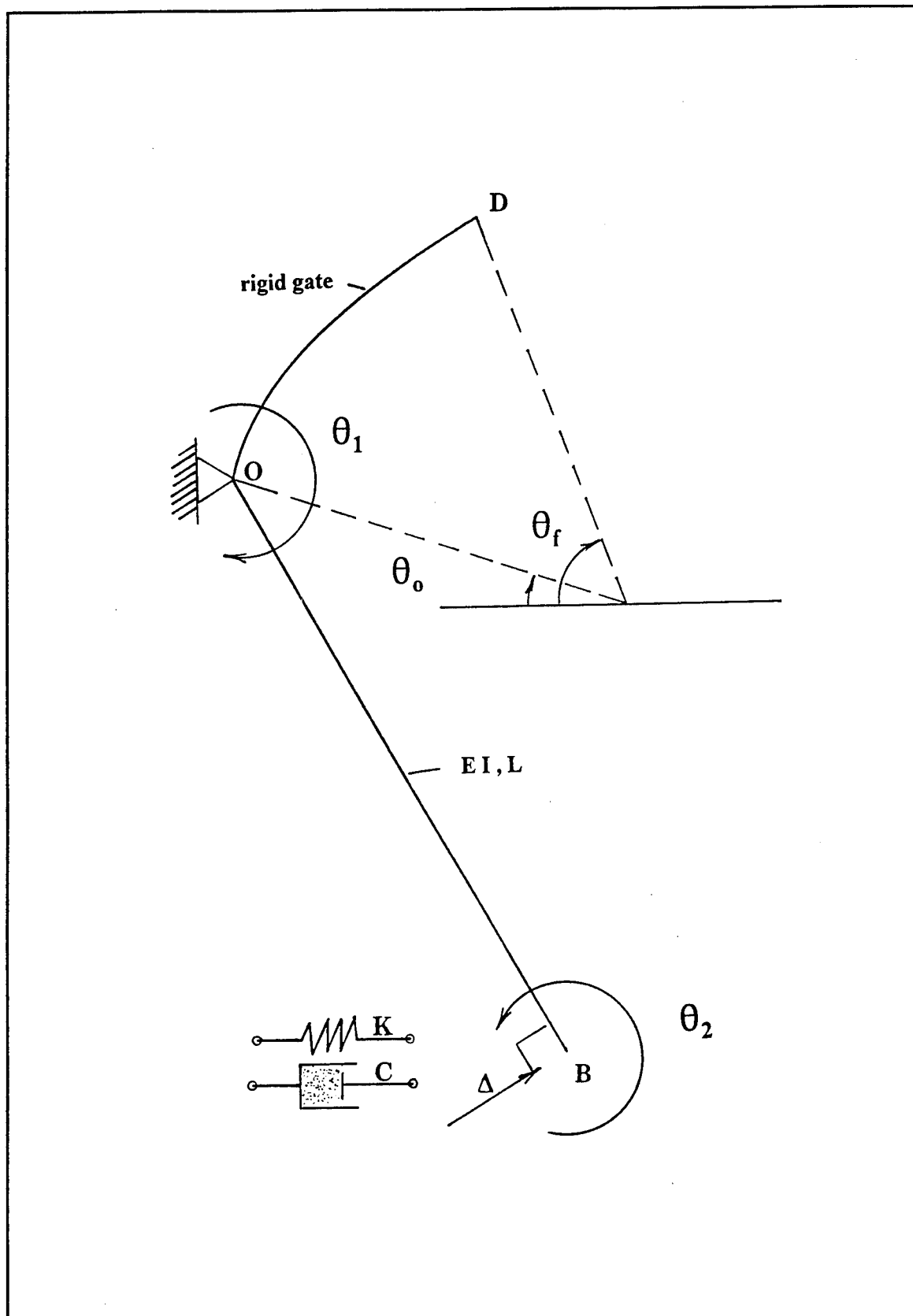


Plate 81. Mathematical model. Structural coordinates and single degree of freedom Δ

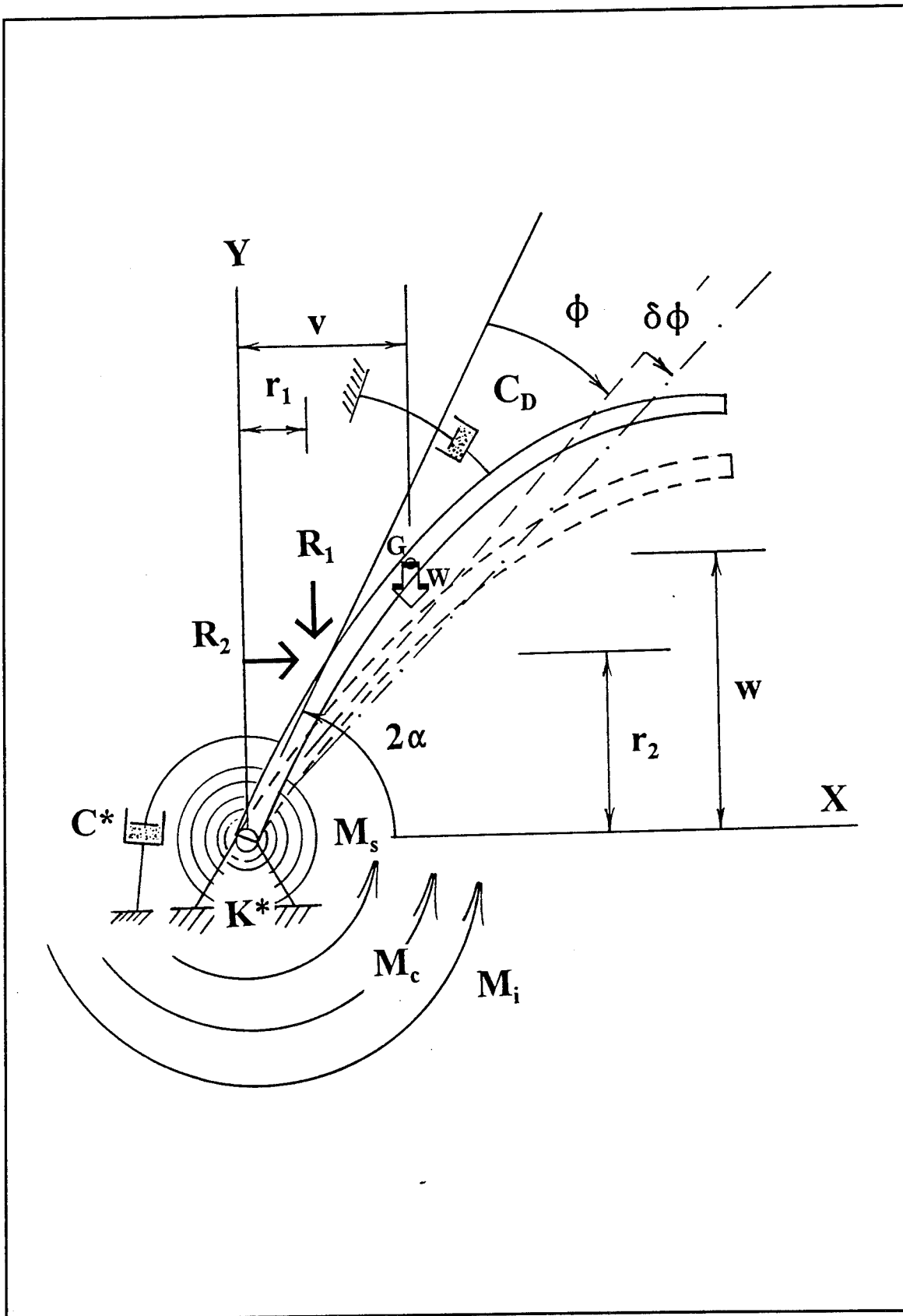


Plate 82. Dynamic equilibrium of 1-DOF rigid-body gate system. Virtual displacement

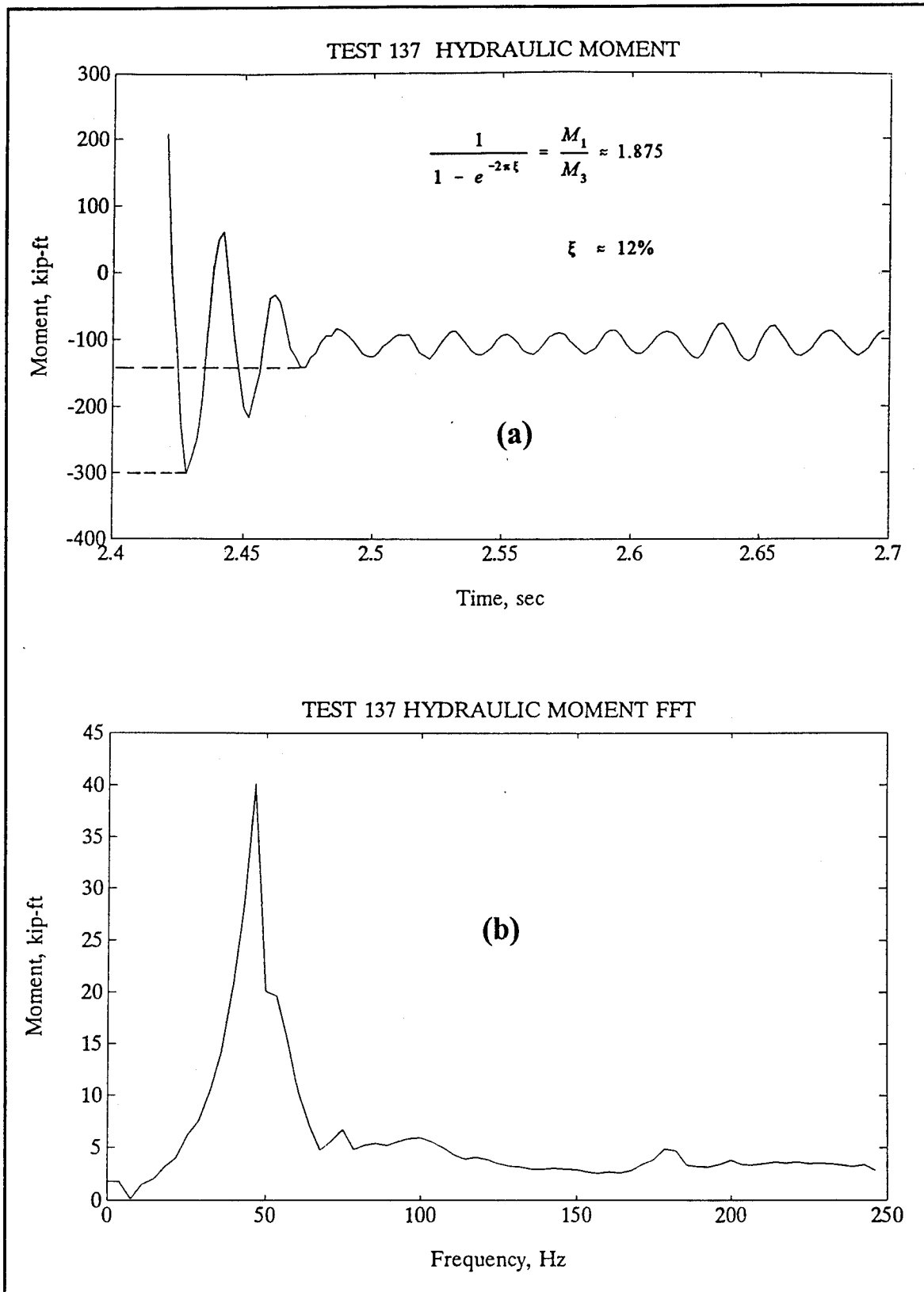


Plate 83. Identification of equivalent viscous damping ratio for dry gate. Logarithmic decrement

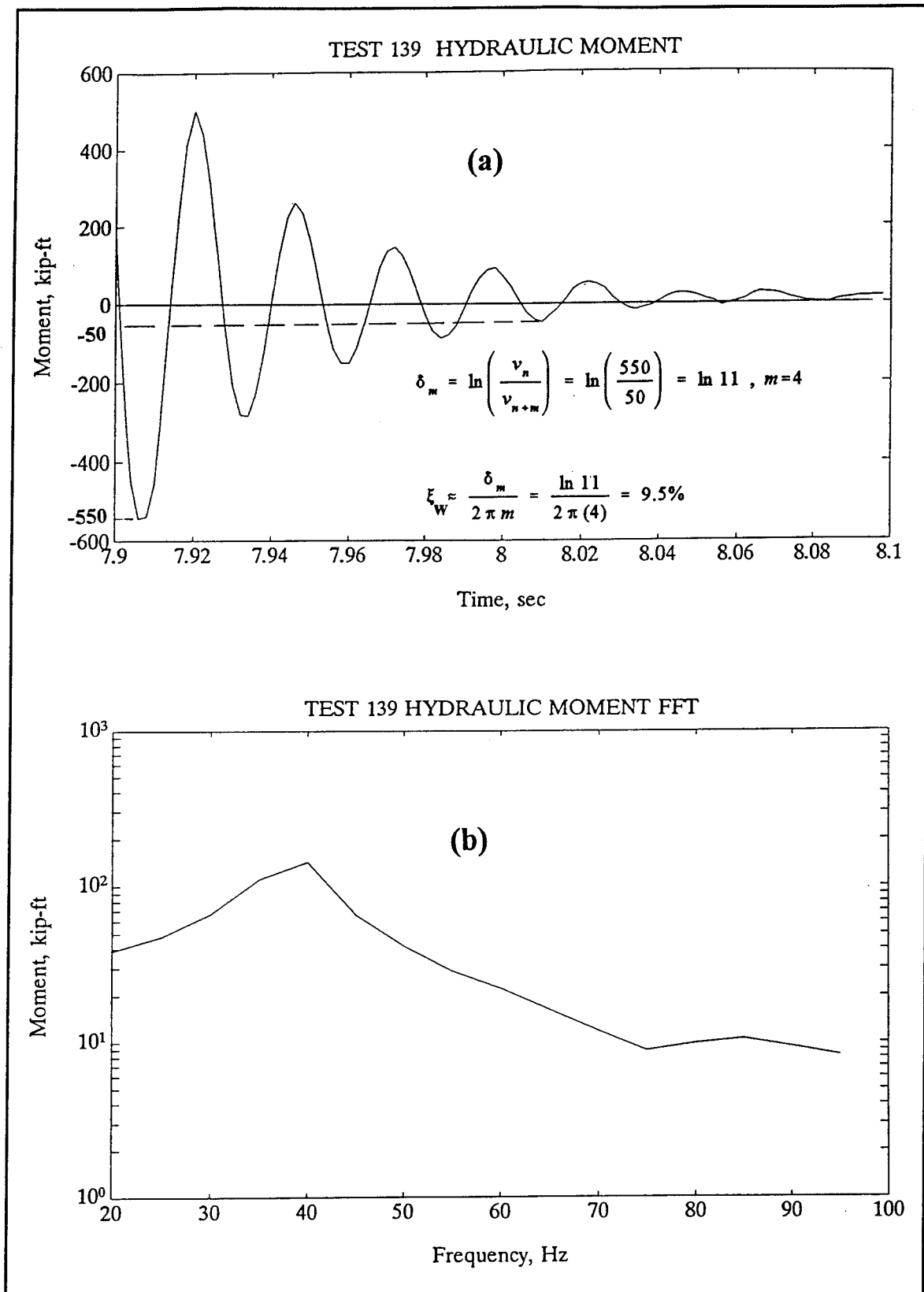


Plate 84. Identification of equivalent viscous damping ratio of gate with upstream side submerged in water

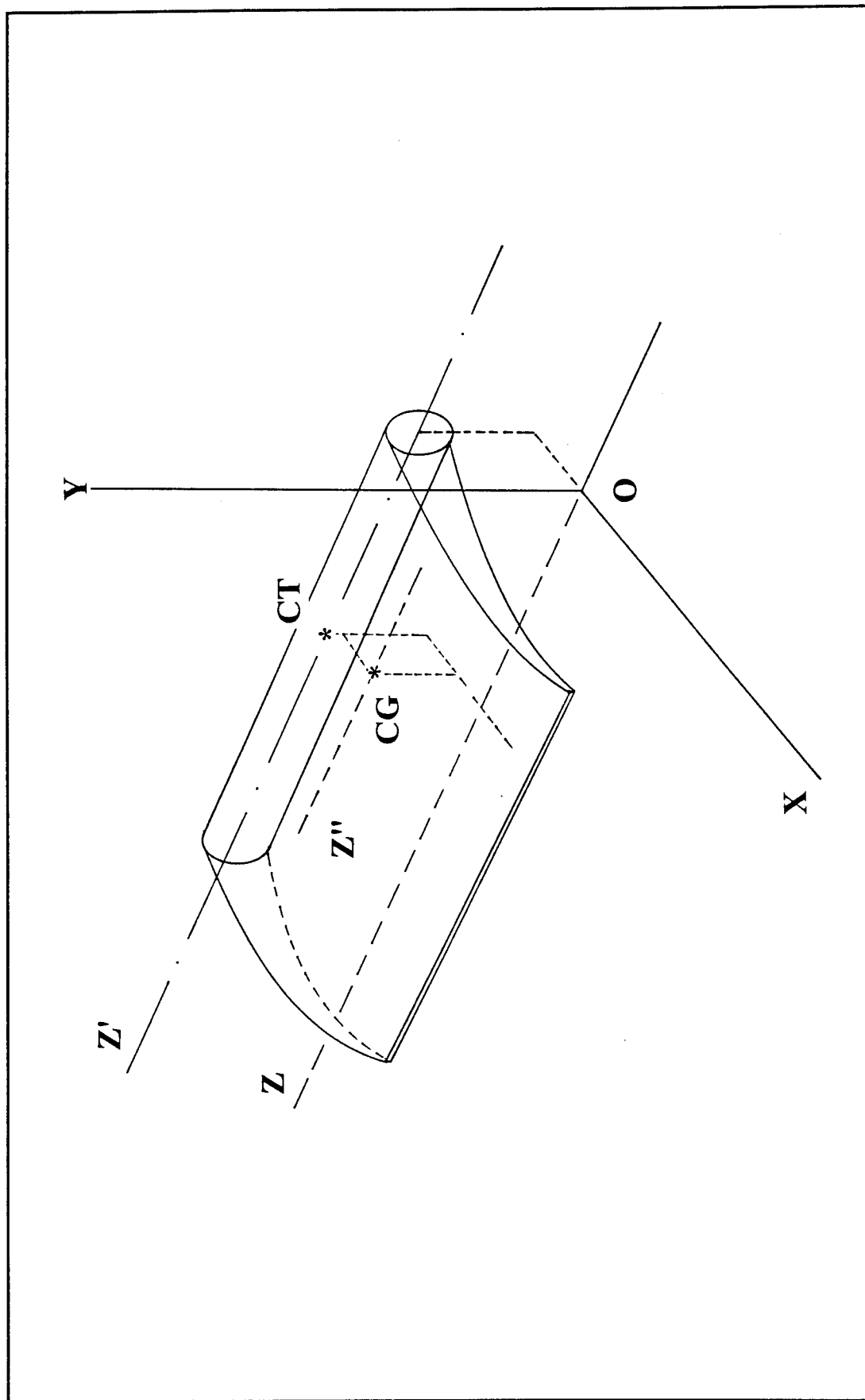


Plate 85. Rigid-body torque-tube system in horizontal position

Deformed_plot: ABAQUS-18-Aug-94 15:0

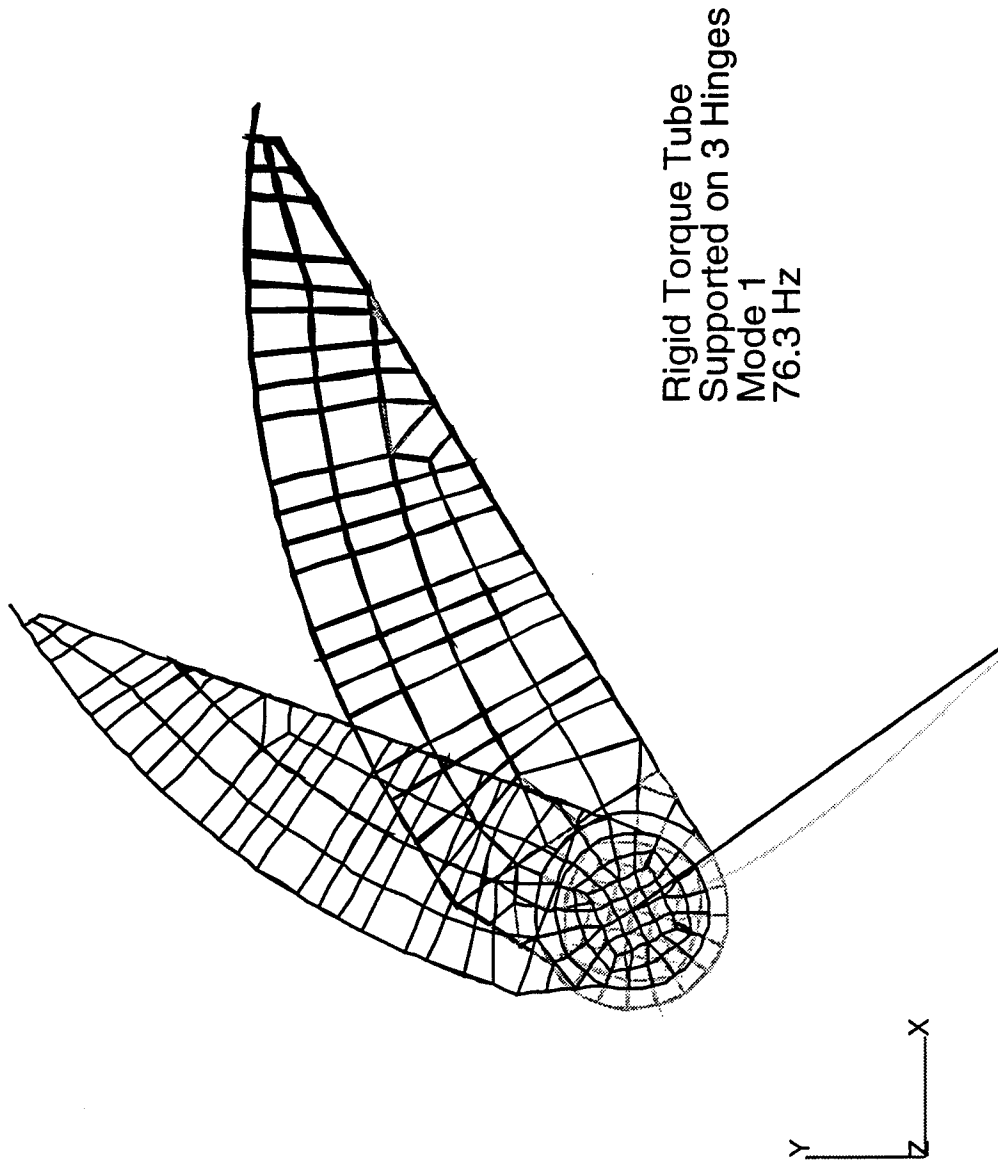


Plate 86. Finite element eigensolution for fundamental mode of vibration of the rigid-body torque-tube system

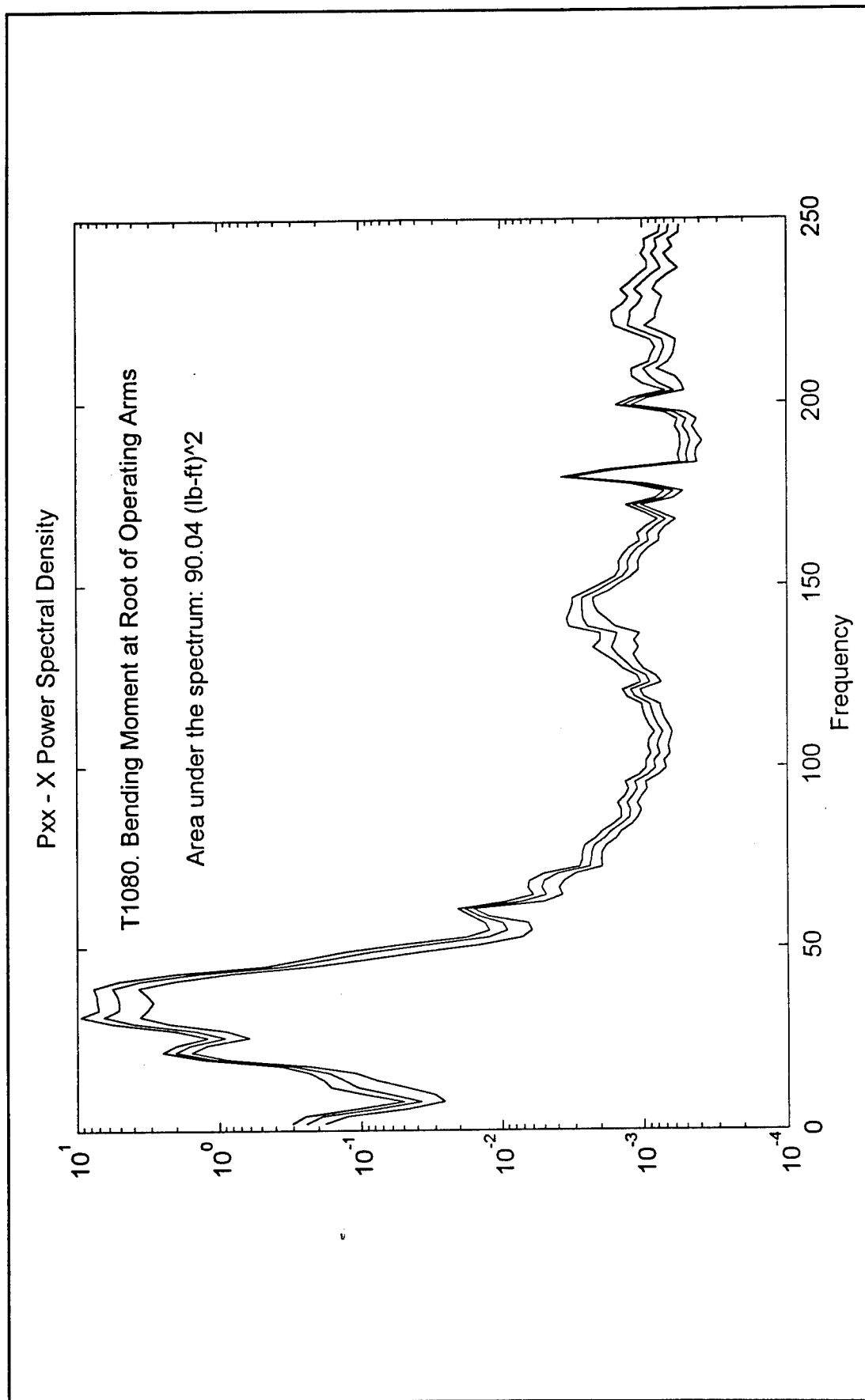


Plate 87. Spectral density of moment at root of operating arms

7 Conclusions and Recommendations

A mathematical model to evaluate the total hydraulic pressure field acting on the upstream face of a typical Montgomery Point torque-tube gate physical model was developed and experimentally verified. This semiempirical model successfully predicts the upstream pressure field acting on most of the gate skin, except over deep locations, where the estimation is slightly unconservative.

A subsequent experimental program on a 1/15-scale physical model led to a recommended design pressure line embracing both the theoretical prediction and all test results involving the regular operating conditions of the gate. This design pressure line was used as input to conduct finite element analyses on two separate structural idealizations: one for the physical model (made out of brass and standing on three supports) and another for the corresponding extrapolation for the prototype (made out of structural steel and standing on five supports). The resulting reactions at the base of the torque-tube gate and the corresponding force in the actuator cylinder were reported at the time (First Data Report) for the design of support bearings and the actuator, respectively.

Preserving the natural nappe on the gate in service increases the effective hydraulic pressure on the upper skin surface but probably not sufficiently so as to justify the implementation of an externally attached device to ventilate the nappe permanently.

Two separate mathematical models were derived to provide the designer with information as to the extreme-value pressure field on the gate that can be expected to occur during its useful life with various degrees of uncertainty, based on the information collected from typical experiments with a fixed unit discharge of approximately 50 cfs/ft (Phase 1 of the experimental project). Subsequently, further tests in Phase 2 of the experimental project (allowing variable unit discharges and generally different pool conditions from those in Phase 1, and sometimes involving improper operating conditions) provided even more unfavorable pressures, thus giving the controlling forces for design.

The results of the two phases of the experimental project were in agreement to confirm that the tests controlling the gate design generally involve the condition that all gates are simultaneously fully raised at some instant during the experiment. In general, the dynamic fluctuations of structural response about the steady-state mean value were only negligible to small in magnitude during the experiments.

The gate eigenproperties were identified by separate experimental techniques, giving results in close agreement with each other and with the finite element eigensolution. Knowledge of the gate eigenproperties is important in order to use correct parameters in future modal analyses of the gate, to compare these parameters in relation to the actual prototype gate as it is constructed, and to keep track of structural deterioration over the life of the gate in service, due to weathering, corrosion, local fatigue of component elements, or simply due to normal wear (safety assessment).

An engineering model based on fundamental principles of structural dynamics was derived to estimate the response of the gate system subjected to the upstream hydraulic pressure field. The model involves two separate facets. The first part presents the deterministic derivation of the steady-state component of the gate response. The second part presents a random vibration model for the stochastic description of the fluctuations of structural response about the steady-state component. Both methods compare satisfactorily with the corresponding experimental verification.

In an elemental spectral analysis of the test records, the study evaluated the safety of a typical torque-tube gate in service against fatigue failure from flow-induced vibrations over the long run. These initial studies indicate no significant flow-induced vibration problems in the model, since the observed flow conditions produced no outstanding oscillation energy. Therefore, no evidence was detected pointing to flow-induced vibrations of intensity such as to produce fatigue in components of the prototype; however, this does not ensure categoric safety against fatigue in the prototype.

References

- Aluminum Association. (1981). *Engineering data for aluminum structures*. 5th ed., Washington, DC.
- _____. (1982). "Specifications for aluminum structures." *Aluminum construction manual, Section 1*. 5th ed., Washington, DC.
- American Institute of Steel Construction. (1986). "Load and resistance factor design." *Manual of steel construction*, New York.
- Benjamin, J. R., and Cornell, C. A. (1970). *Probability, statistics, and decision for civil engineers*. McGraw-Hill, New York.
- Bendat, J. S., and Piersol, A. G. (1993). *Engineering applications of correlation and spectral analysis*. 2nd ed., Wiley, New York.
- Boresi, A. P., and Sidebottom, O. M. (1985). *Advanced mechanics of materials*. 4th ed., Wiley, New York.
- Cartwright, D. E., and Longuet-Higgins, M. S. (1956). "Statistical distribution of the maxima of a random function." *Proceedings of the Royal Society, Series A* (237). London, England, 212-232.
- Clough, R. W., and Penzien, J. (1975). *Dynamics of structures*. McGraw-Hill, New York.
- Crandall, S. H., and Mark, W. D. (1963). *Random vibration in mechanical systems*. Academic Press, New York.
- Davenport, A. G. (1963). "Note on the distribution of the largest value of a random function with application to gust loading." *Proceedings of the Institution of Civil Engineers*, 24(6739), London, England, 187-196.
- Fletcher, B. P., and de Bejar, L. A. (1995). "Montgomery Point Lock and Dam study; Report 1, hydraulic forces and characteristics acting on spillway gates," Technical Report SL-95-14, U.S. Army Engineer Waterways Experiment Station, Vicksburg, MS.

- Flinn, R. A., and Trojan, P. K. (1990). *Engineering materials and their applications*. 4th ed., Houghton Mifflin Co., Boston, MA.
- Hibbitt, Karlsson, and Sorensen, Inc. (1993). *ABAQUS Vers. 5.3*. Pawtucket, RI.
- Hurty, W. C., and Rubinstein, M. F. (1964). *Dynamics of structures*. Prentice-Hall, Englewood Cliffs, NJ.
- Kreyszig, E. (1988). *Advanced engineering mathematics*. 6th ed., Wiley, New York.
- March, P. A., and Elder, R. A. (1992). "Review of the 1:25 scale hydraulic model Olmsted Wicket Dam," USAE Division, Ohio River, Cincinnati, OH.
- MATHSOFT Inc. (1994). *MATHCAD + for windows Vers. 5.0*. Cambridge, MA.
- MATHWORKS Inc. (1993). *MATLAB Vers. 4.0, high-performance numeric computation and visualization software. User's guide*. Natick, MA.
- Mura, T., and Koya, T. (1992). *Variational methods in mechanics*. Oxford University Press, New York.
- Naudascher, E. (1991). *Hydrodynamic forces*. A. A. Balkema, Rotterdam, Netherlands.
- Newland, D. E. (1984). *An introduction to random vibrations and spectral analysis*. 2nd ed., Longman, New York.
- Novak, P., and Cabelka, J. (1981). *Models in hydraulic engineering: Physical principles and design applications*. Pitman Advanced Publishing Program, Boston, MA.
- Olson, R. M. (1961). *Essentials of engineering fluid mechanics*. International Textbook Company, Scranton, PA.
- PDA Engineering. (1993). *Introduction to P3/PATRAN (PAT301)*. Dayton, OH.
- Prandtl, L., and Tietjens, O. J. (1957a). *Fundamentals of hydro- and aeromechanics*. Dover Publications, New York.
- _____. (1957b). *Applied hydro- and aeromechanics*. Dover Publications, New York.
- Przemieniecki, J. S. (1985). *Theory of matrix structural analysis*. Dover Publications, New York.

- Rubinstein, M. F. (1966). *Matrix computer analysis of structures*. Prentice-Hall, Englewood Cliffs, NJ.
- Shames, I. H. (1962). *Mechanics of fluids*. McGraw-Hill, New York.
- Simiu, E., and Scanlan, R. H. (1986). *Wind effects on structures. An introduction to wind engineering*. 2nd ed., Wiley-Interscience, New York.
- U.S. Army Engineer District, Little Rock. (1993). "Montgomery Point Lock and Dam, McClellan-Kerr Arkansas River Navigation System: Design memoranda 1-5." Little Rock, AR.
- U.S. Army Engineer Waterways Experiment Station. (1994a). "First data report on reaction analysis for hydraulic model study of Montgomery Point Spillway Rigid Gate Model," Memorandum CEWES-SS-A (70/1), Vicksburg, MS.
- _____. (1994b). "Second data report on recommended design total pressure field for hydraulic model study of Montgomery Point Spillway Rigid Gate Model, Phase 2," Memorandum CEWES-SS-A (70/2.1), Vicksburg, MS.
- _____. (1994c). "Second data report on recommended design total pressure field for hydraulic model study of Montgomery Point Spillway Rigid Gate Model, Phase 2 (Amendment)," Memorandum CEWES-SS-A (70/2.2), Vicksburg, MS.
- Vennard, J. K., and Street, R. L. (1975). *Elementary fluid mechanics*. 5th ed., Wiley, New York.
- Yang, C. Y. (1986). *Random vibration of structures*. Wiley, New York.
- Zienkiewicz, O. C. (1977). *The finite element method*. 3rd ed., McGraw-Hill, London, England.
- ZONIC + AND. (1993). *LAZON User Manual*. ZONIC Co., Milford, OH.

Appendix A

Spectral Analysis

In this appendix, the outstanding issues resulting from the spectral analysis of the pressure field data are discussed. Naturally, only selected spectra for the controlling experimental pressure records are actually exhibited. Directions for future studies to assess the fatigue performance of the gate system in the long term are identified, but a thorough study of this important aspect of the gate safety deserves a separate research project in itself.

Tests T1080 and T1085, conducted at a sampling rate of 500 sps, differ only in the duration. Test T1080 lasts 100 s whereas test T1085 lasts twice as long. Plate A1 shows the pressure-cell locations for the selected pressure-record spectra actually exhibited in Plates A2 through A7. These plates show the spectral densities for the upstream, downstream, and net pressure records in sequence, at each location and for both tests. Each power spectral density function appears within the 95-percent confidence spectral band for the frequency domain $0 < f \leq 250$ Hz. The plates indicate that the test duration has very little effect on the spectral characteristics of the data.

Observing the upstream and the net pressure-record spectra, one notices that the most important amounts of energy appear concentrated in the region $10 < f \leq 50$ Hz (with the main peak at around 40 Hz) and in a secondary energy pocket in a region around 60 Hz. These frequencies correspond approximately to the first two natural frequencies of the physical model with upstream water only (see Plate 83b for the exact location of the fundamental frequency of free vibration). In fact, the frequency content of the flow exhibits peaks at 20, 30, 40, and 60 Hz (Plates A8 and A9, for test T1087), and therefore, clearly tends to excite the first (rigid-plate rotation about the torque-tube axis) and second (rigid-plate twist) modes of vibration (A similar phenomenon has previously been reported in the literature (March and Elder 1992)).¹ The energy (area under the spectrum) associated with these peaks is generally small-to-moderate and, for the major part, the flow spectrum tends to be white noise in character, at low energy levels (notice also that the pressure-cell records are influenced by the vibration of the gate itself, since they

¹ A list of references follows main text.

are attached to the gate skin); nevertheless, attention should be paid to this trend in a more complete fatigue analysis of the gate system.

Notice that there are also energy pockets in the frequency regions around 0 Hz and 150 Hz. The first pocket corresponds to the so-called DC-component of the input signal associated with the mean value of the hydraulic pressure (Bendat and Piersol 1993). The second pocket (~ 150 Hz) tends to excite higher modes of vibration and is considered inconsequential, because the amount of energy associated with the pocket is very small.

Tests T1086 and T1087 were both conducted at a sampling rate of 100 sps for 500 s. However, test T1086 involves an integral nappe, whereas in test T1087 the nappe is ventilated. Plate A8 shows the pressure-cell locations for the selected pressure-record spectra actually exhibited in Plates A9 through A14. The same phenomena discussed above appear in these plates. However, the ventilation of the nappe in test T1087 substantially dissipates the tendency toward resonance in the first two modes of vibration in test T1086, where large energy pockets in the region around 20, 30, and 40 Hz are reinforced by similar frequency contents in the downstream pressure field. These energy concentrations at periodic bands in the frequency domain are believed to be caused by a cyclic interaction among the nappe, the suctioning air entrapped by the nappe and a turbulent downstream water pool. These observations are confirmed by tests T1108 (integral nappe) and T1109 (ventilated nappe), running both at a sampling rate of 500 sps during 200 s and exhibited in Plates A15 through A19.

Plates A20 through A23 illustrate the coherence among selected pressure-cell records in test T1080, as an example. The coherence is clearly perfect ($\gamma^2 = 1$) in the frequency range around the first mode of vibration of the gate (40 Hz) among the pressure records for cells 1, 4, and 7 and tends to pick up in the frequency bands around the second and higher modes, indicating high signal-to-noise ratios and that these records are a response to the same excitation (Bendat and Piersol 1993). This effect is more clear among the pressure records for cells 7, 8, and 9 and is consistent with the magnitude and phase diagrams for the corresponding cross spectra.

This initial study indicates no significant flow-induced vibration problems in the model, since the observed flow conditions produced no outstanding oscillation energy. Therefore, no evidence was detected pointing to flow-induced vibrations of intensity such as to produce fatigue in components of the prototype; however, this does not ensure categorical safety against fatigue in the prototype.

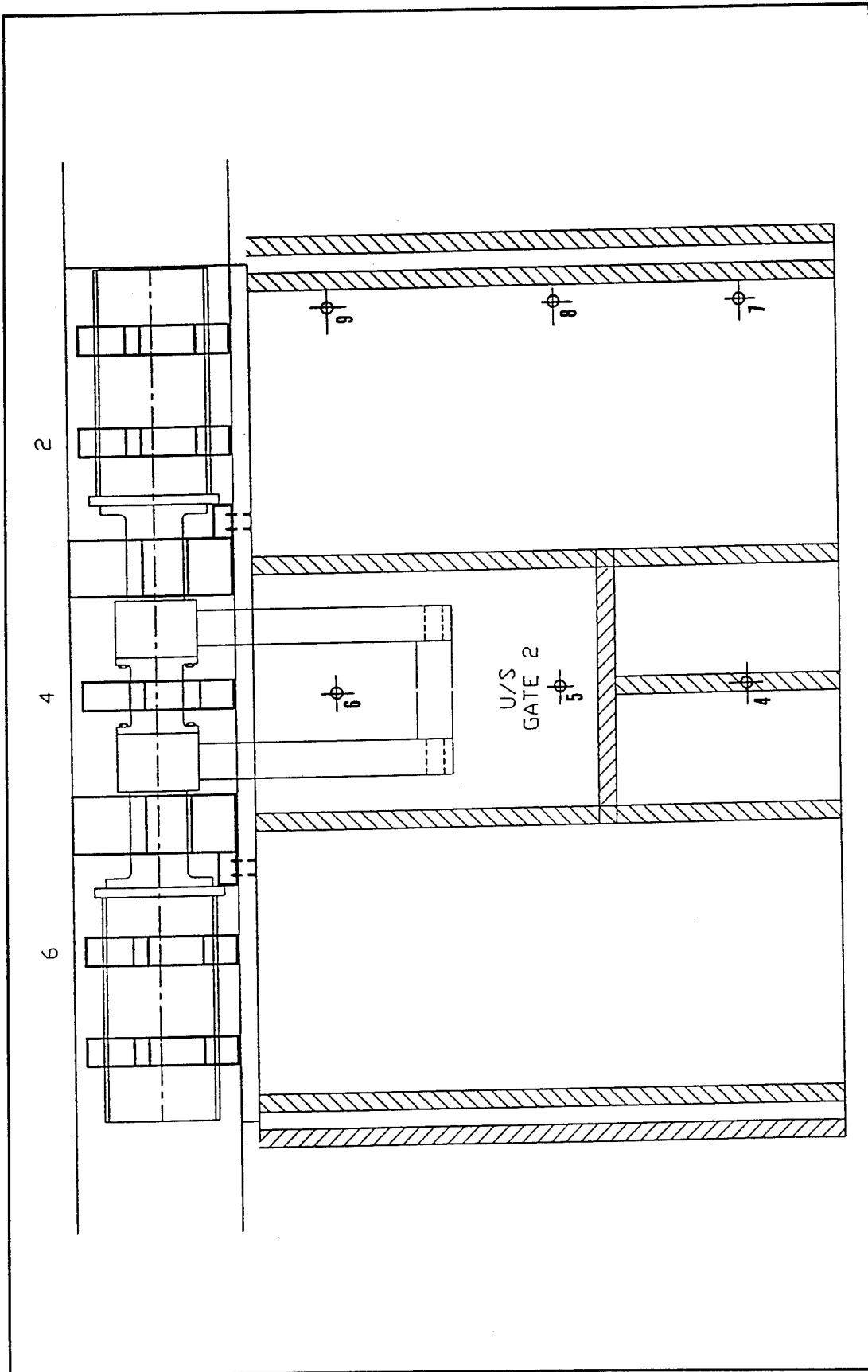


Plate A1. Pressure cells in spectral analysis of tests T1080 and T1085

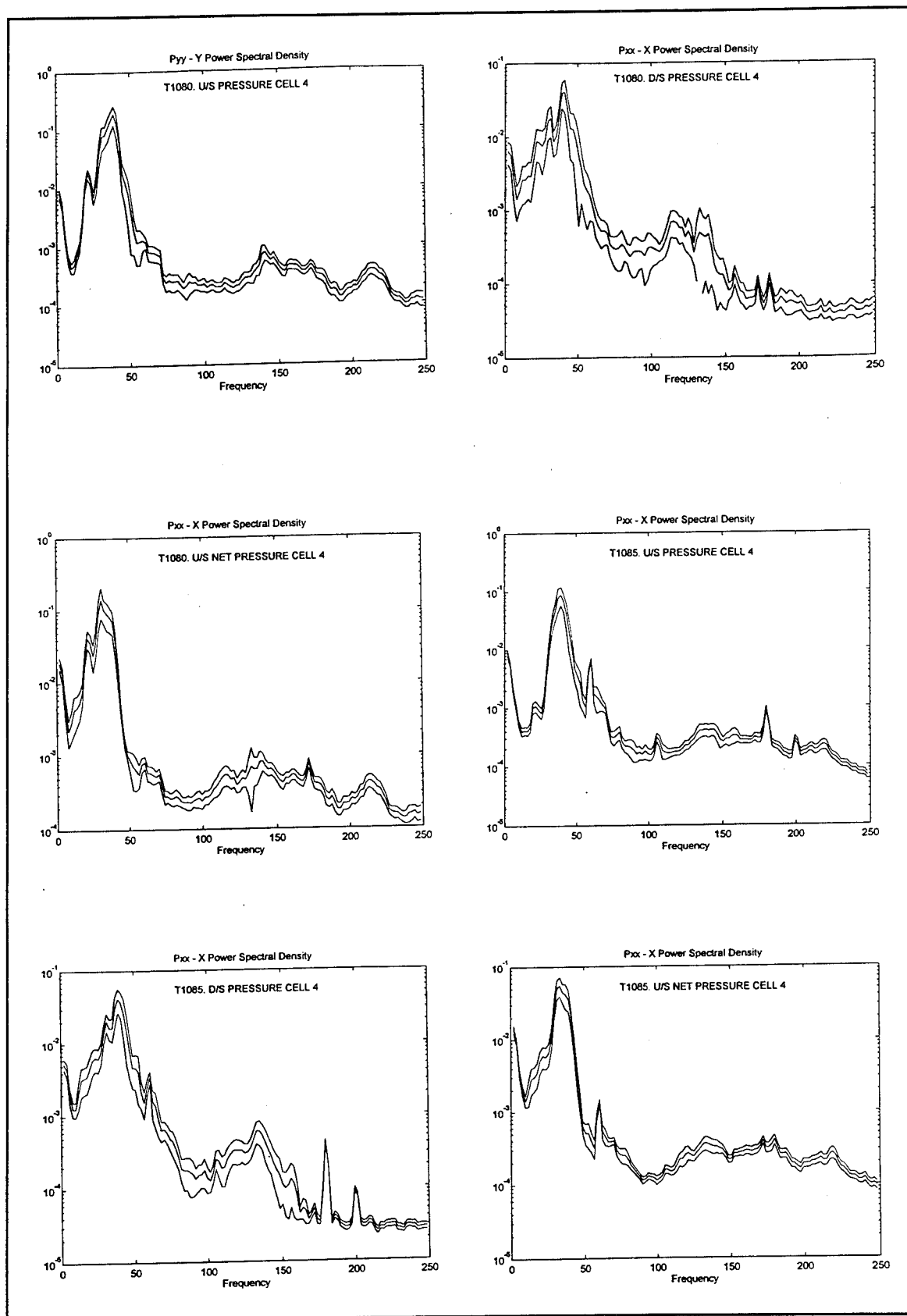


Plate A2. Spectral densities for the records of pressure cell 4 in tests T1080 and T1085

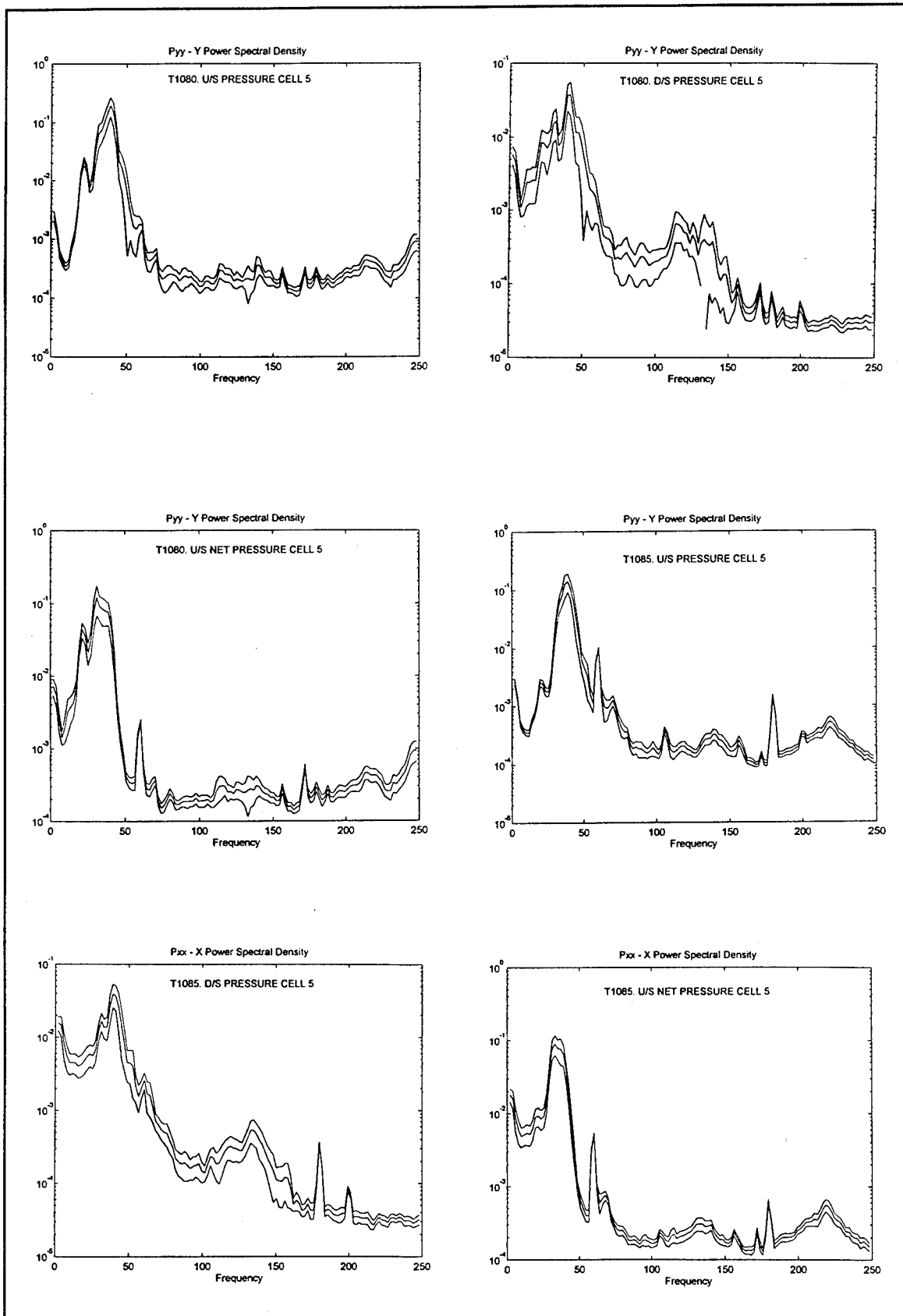


Plate A3. Spectral densities for the records of pressure cell 5 in tests T1080 and T1085

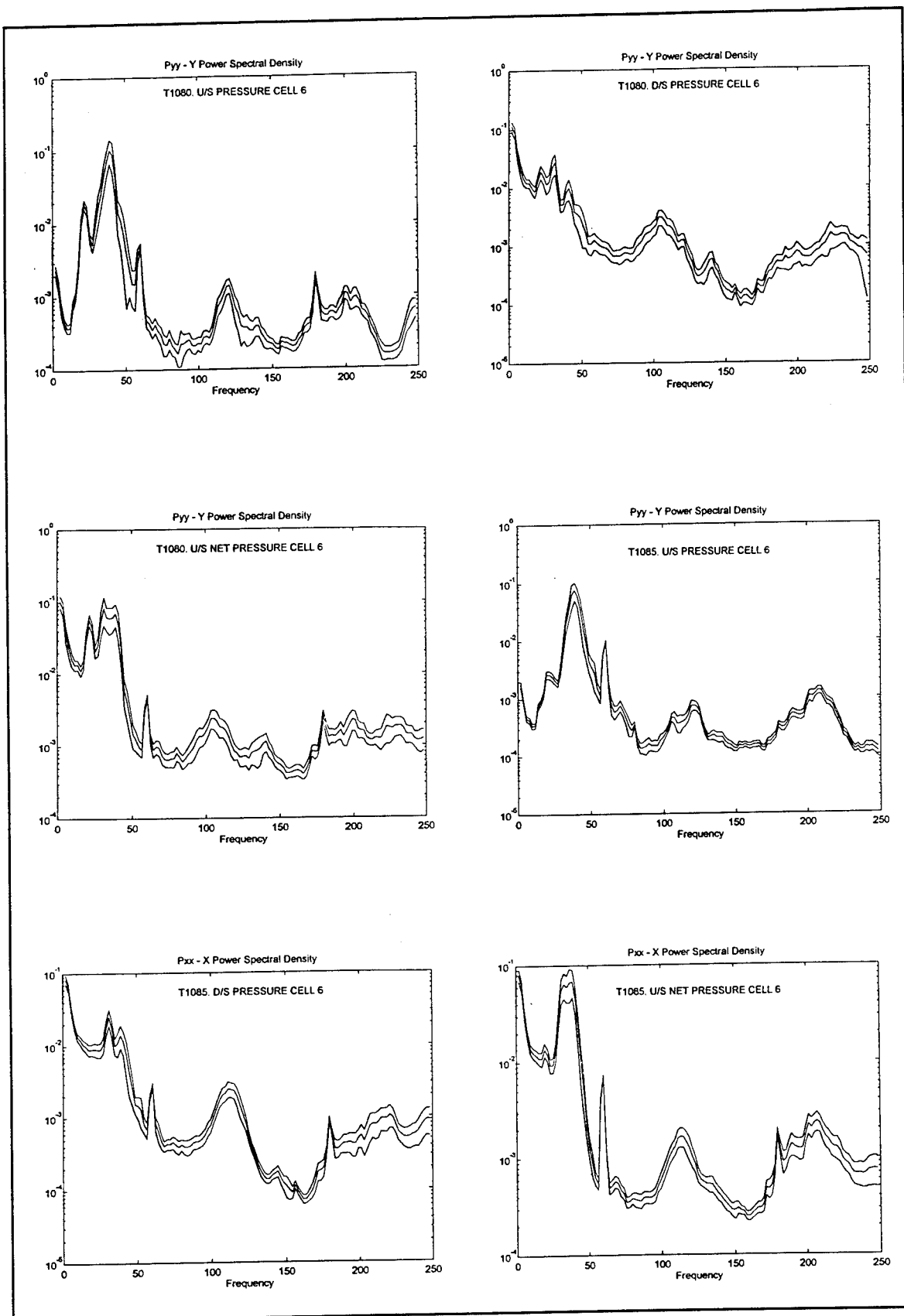


Plate A4. Spectral densities for the records of pressure cell 6 in tests T1080 and T1085

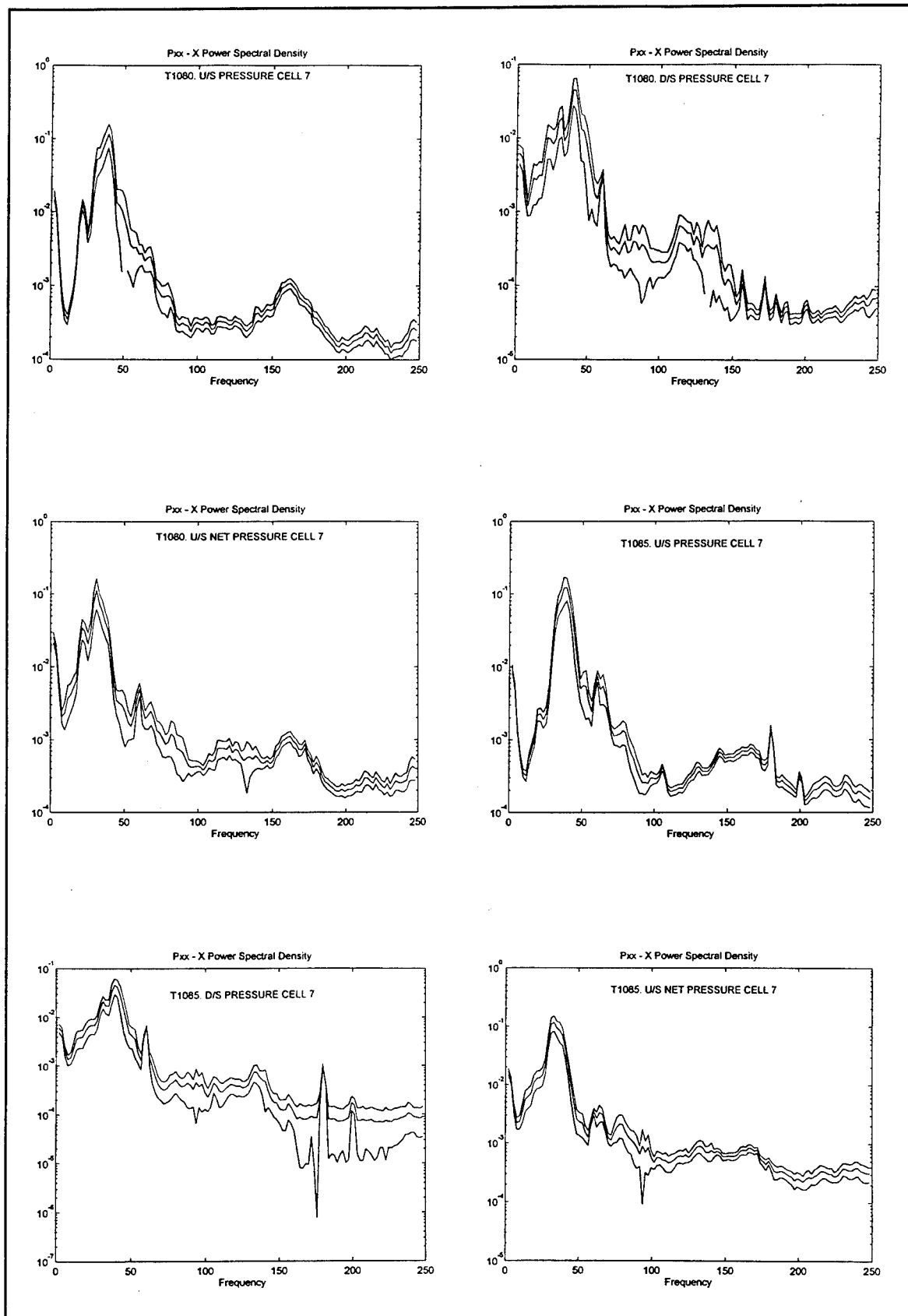


Plate A5. Spectral densities for the records of pressure cell 7 in tests T1080 and T1085

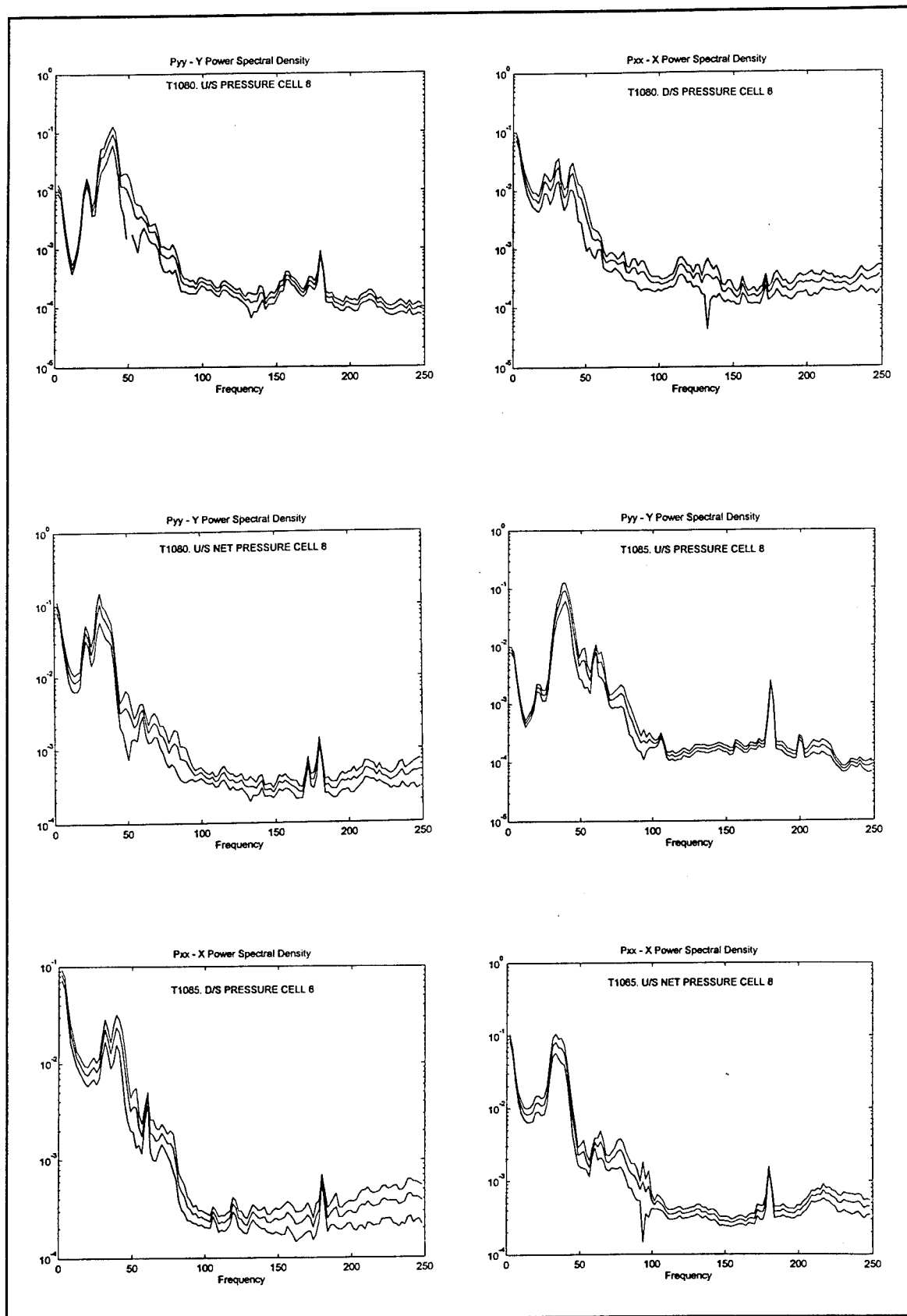


Plate A6. Spectral densities for the records of pressure cell 8 in tests T1080 and T1085

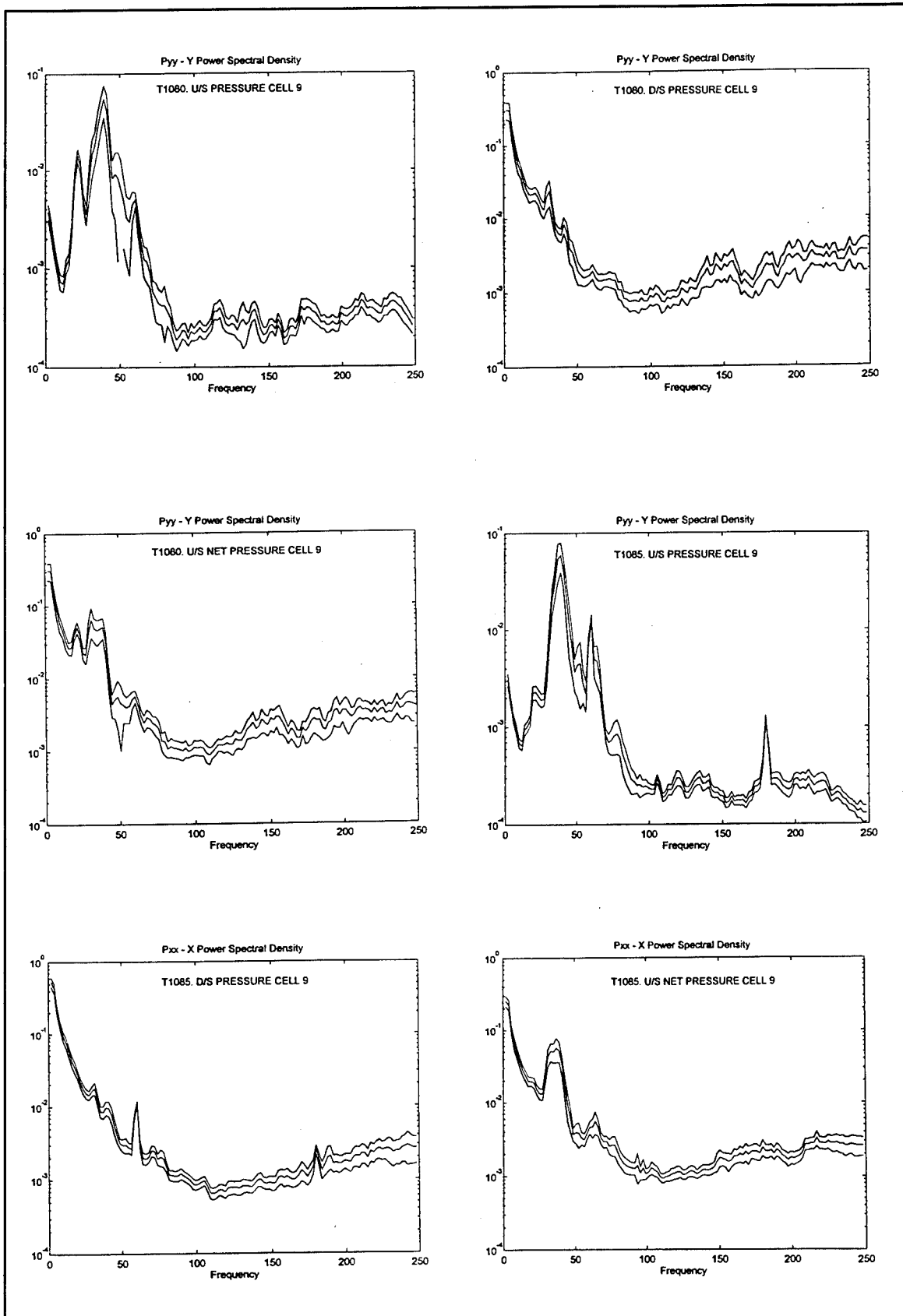


Plate A7. Spectral densities for the records of pressure cell 9 in tests T1080 and T1085

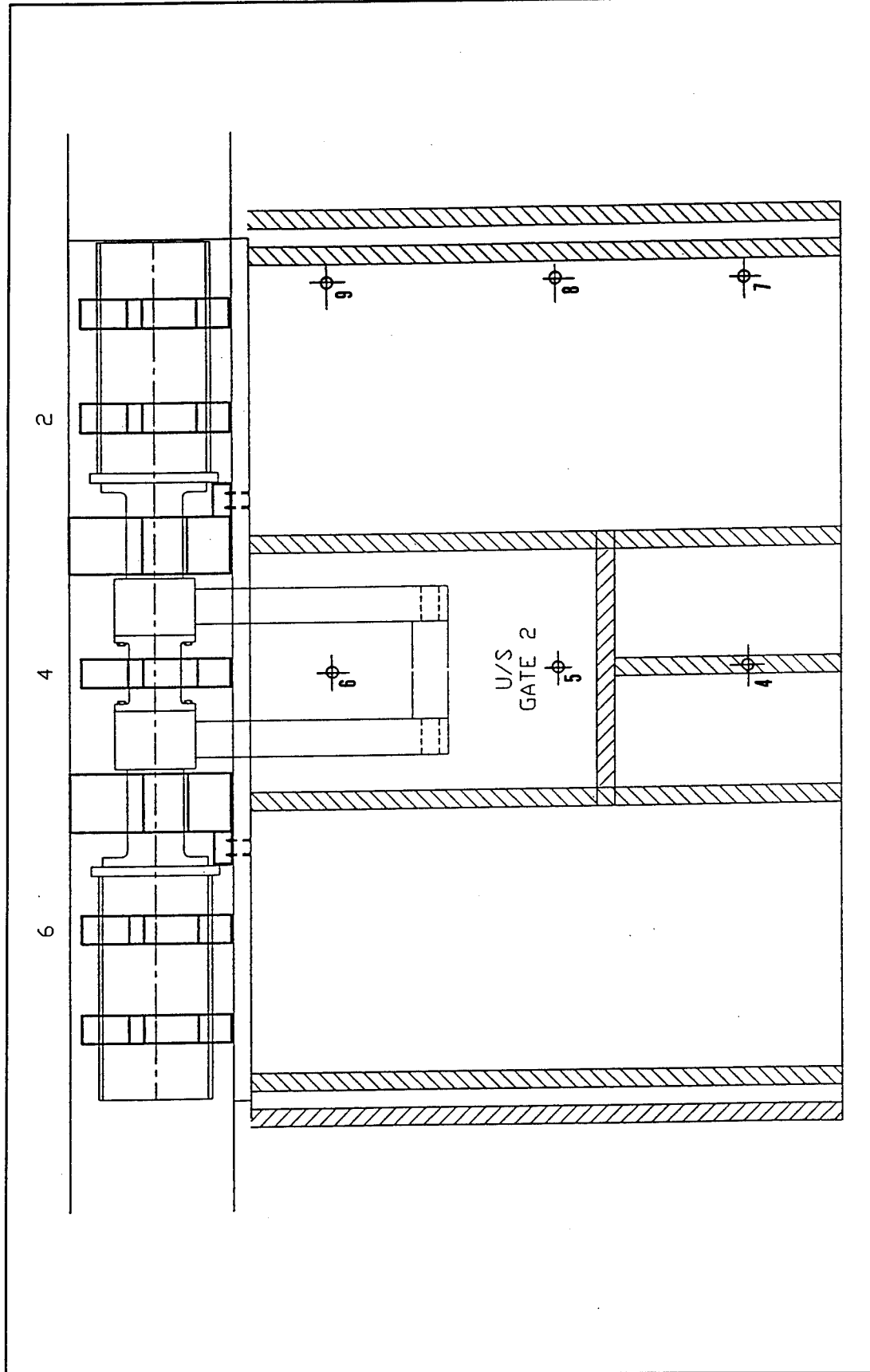


Plate A8. Pressure cells in spectral analysis of tests T1086 and T1087

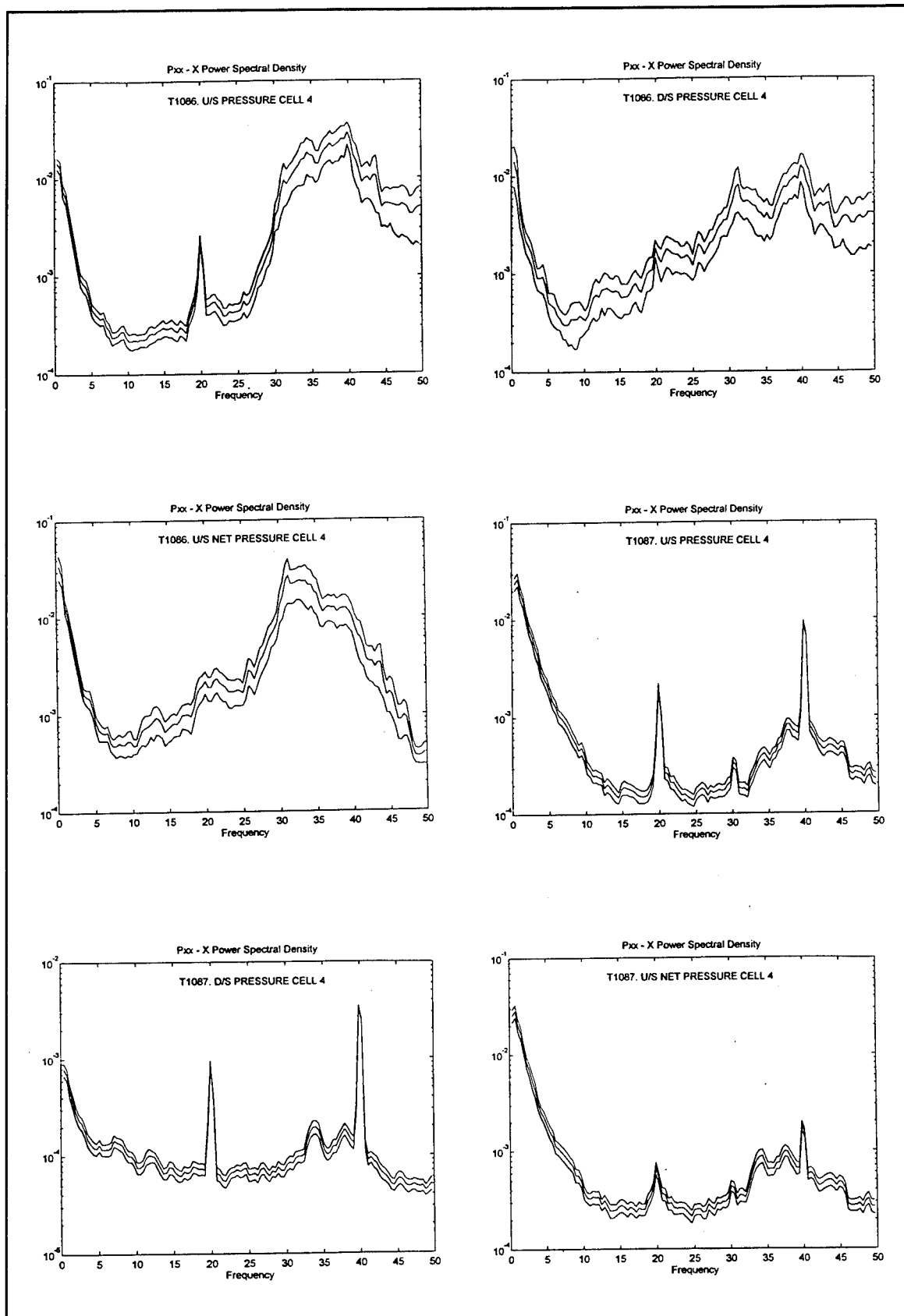


Plate A9. Spectral densities for the records of pressure cell 4 in tests T1086 and T1087

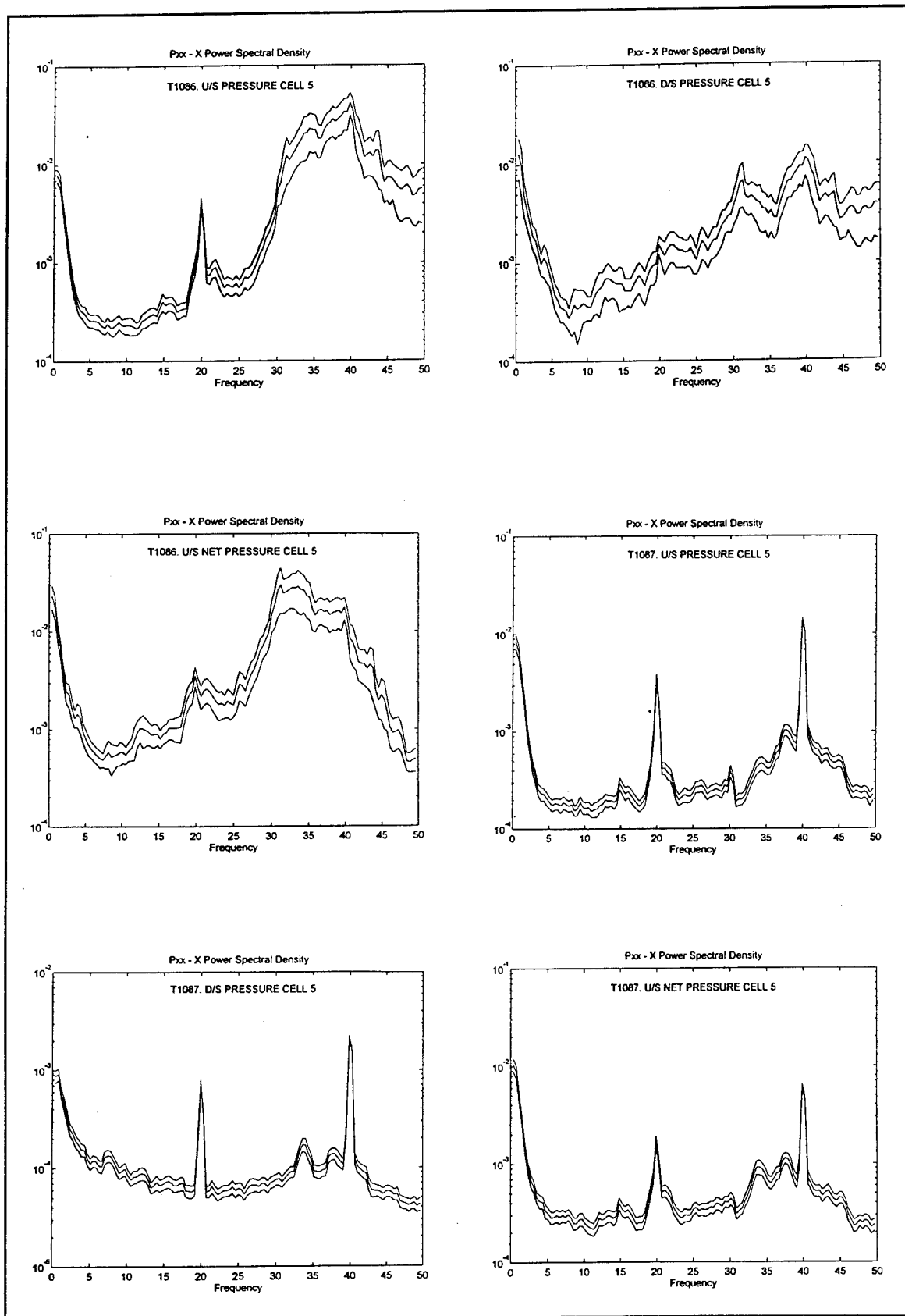


Plate A10. Spectral densities for the records of pressure cell 5 in tests T1086 and T1087

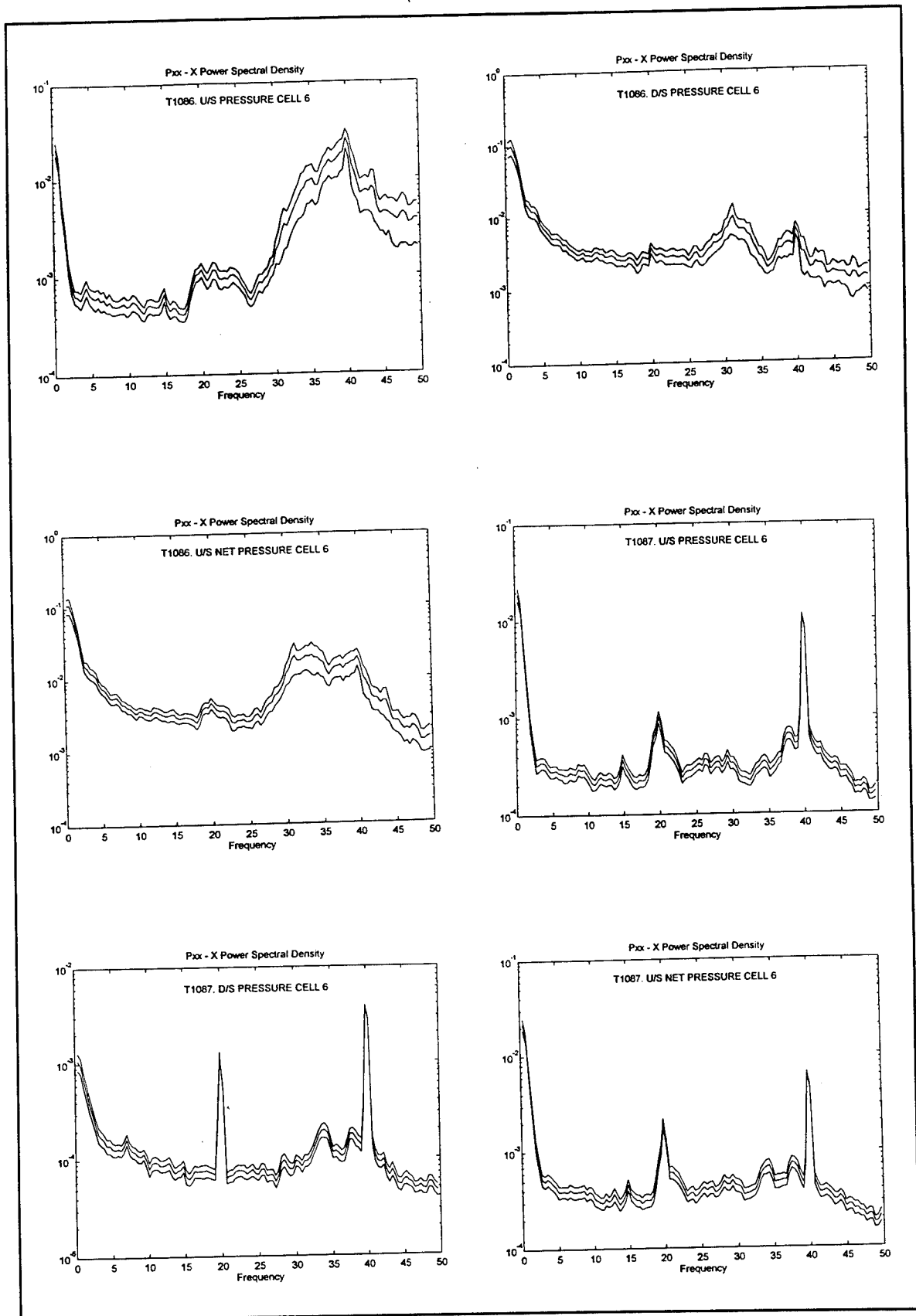


Plate A11. Spectral densities for the records of pressure cell 6 in tests T1086 and T1087

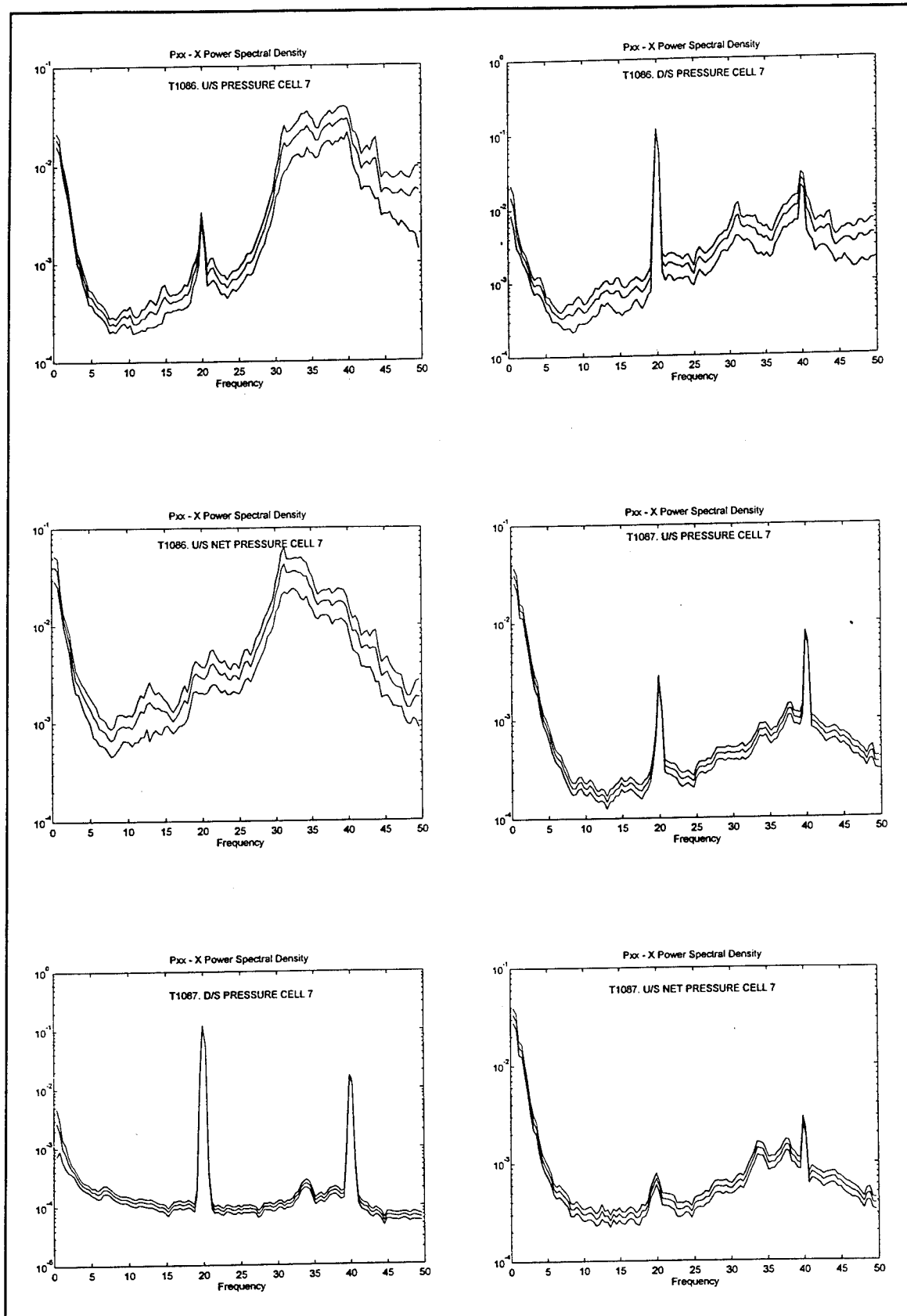


Plate A12. Spectral densities for the records of pressure cell 7 in tests T1086 and T1087

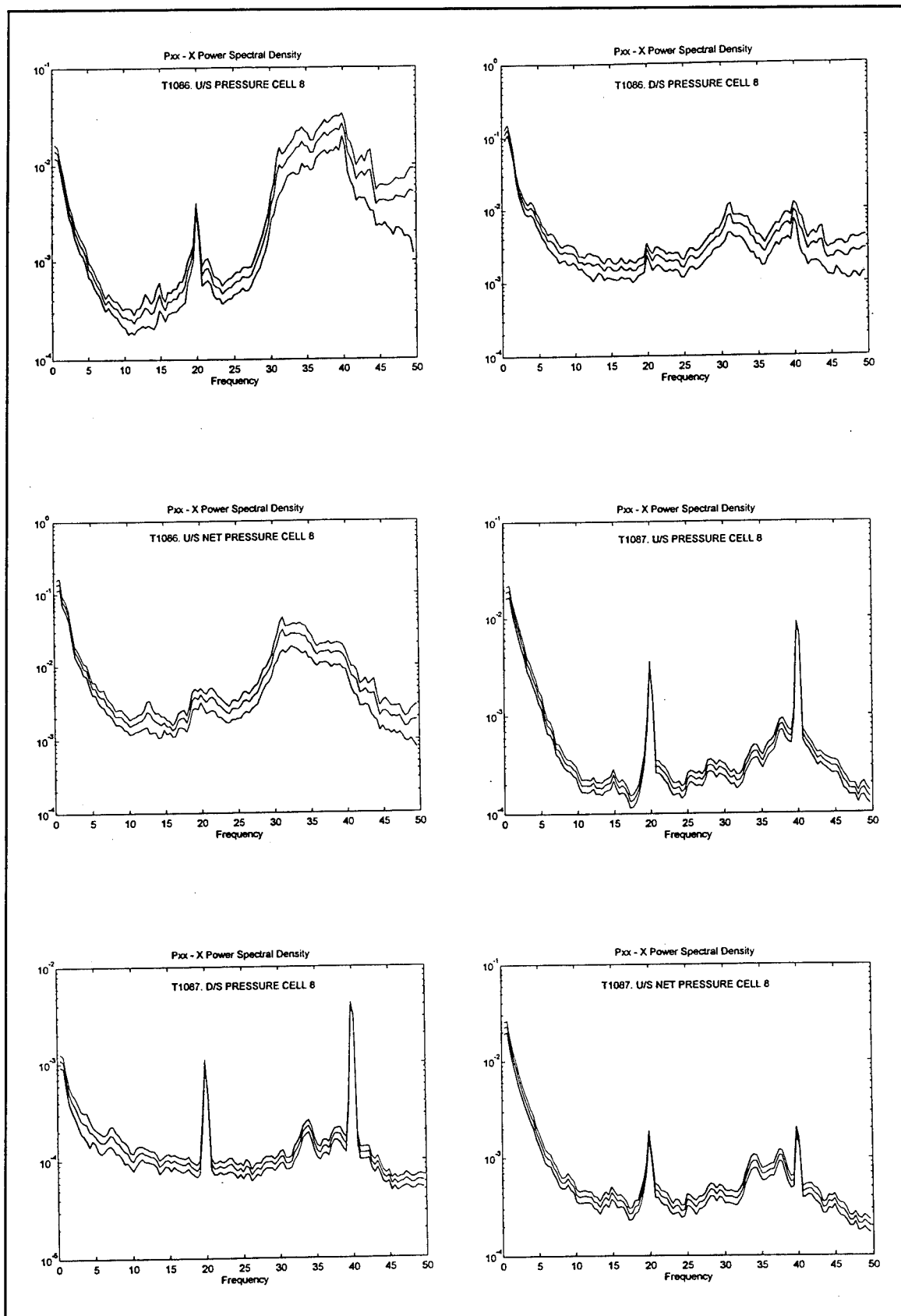


Plate A13. Spectral densities for the records of pressure cell 8 in tests T1086 and T1087

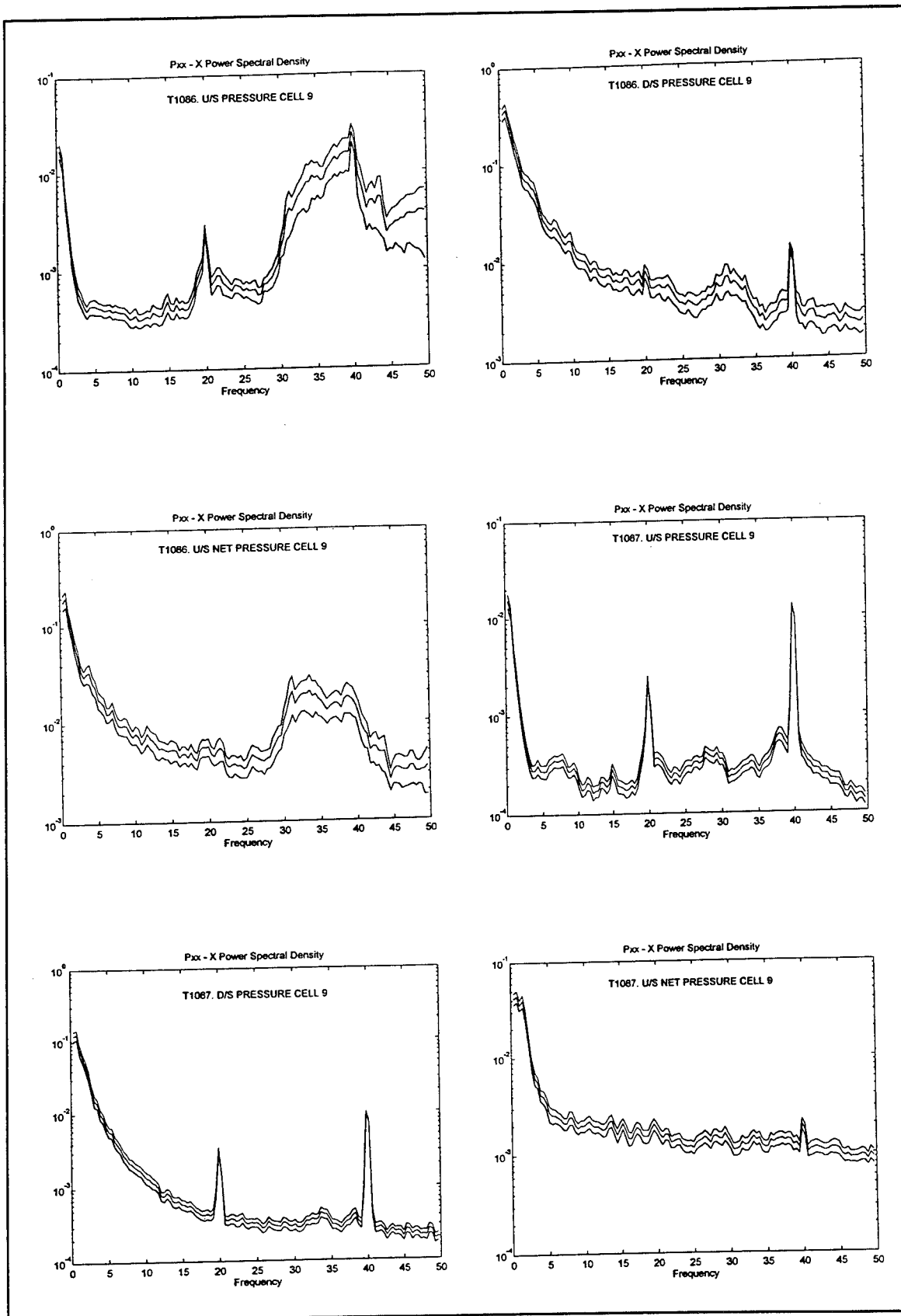


Plate A14. Spectral densities for the records of pressure cell 9 in tests T1086 and T1087

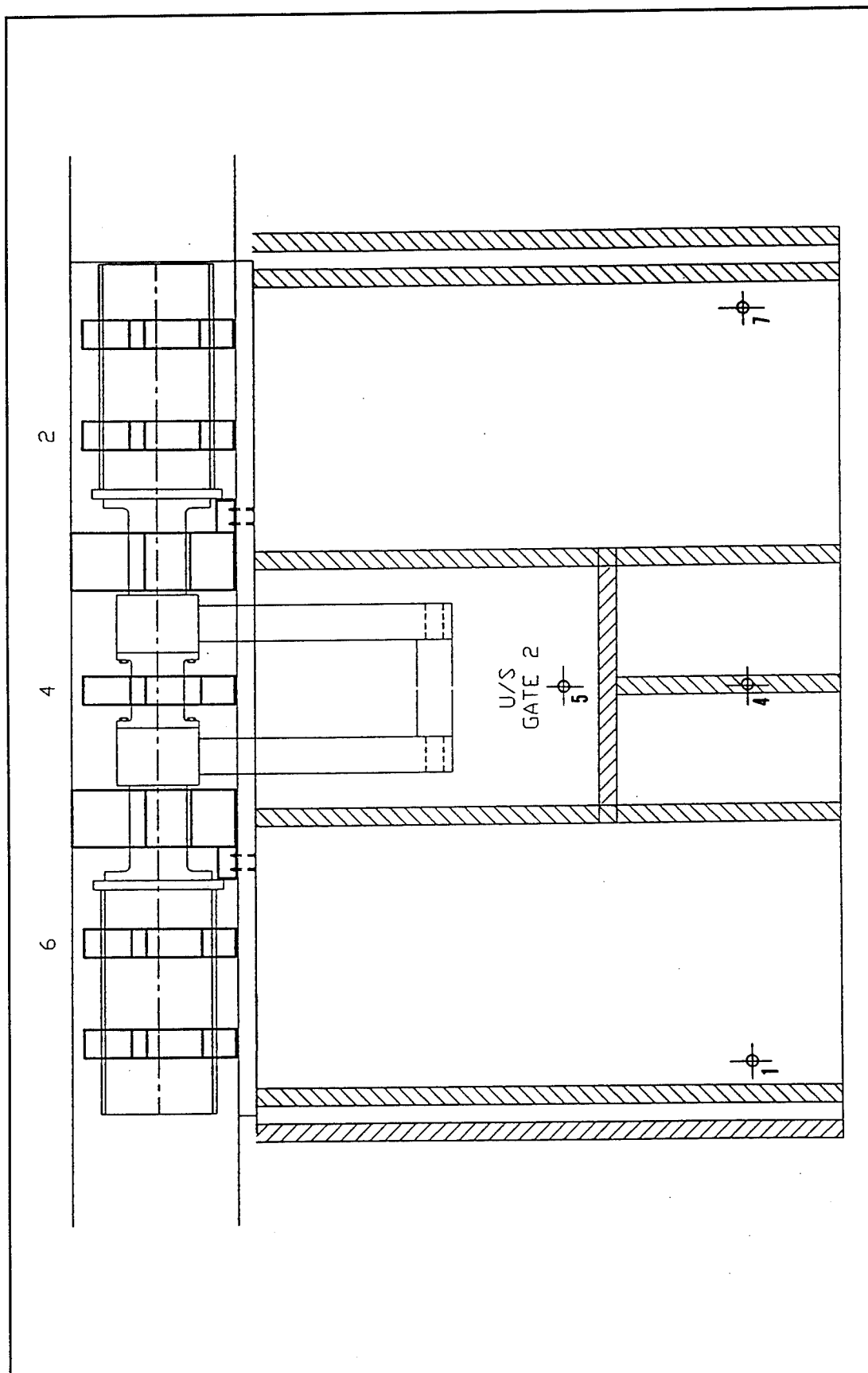


Plate A15. Pressure cells in spectral analysis of tests T1108 and T1109

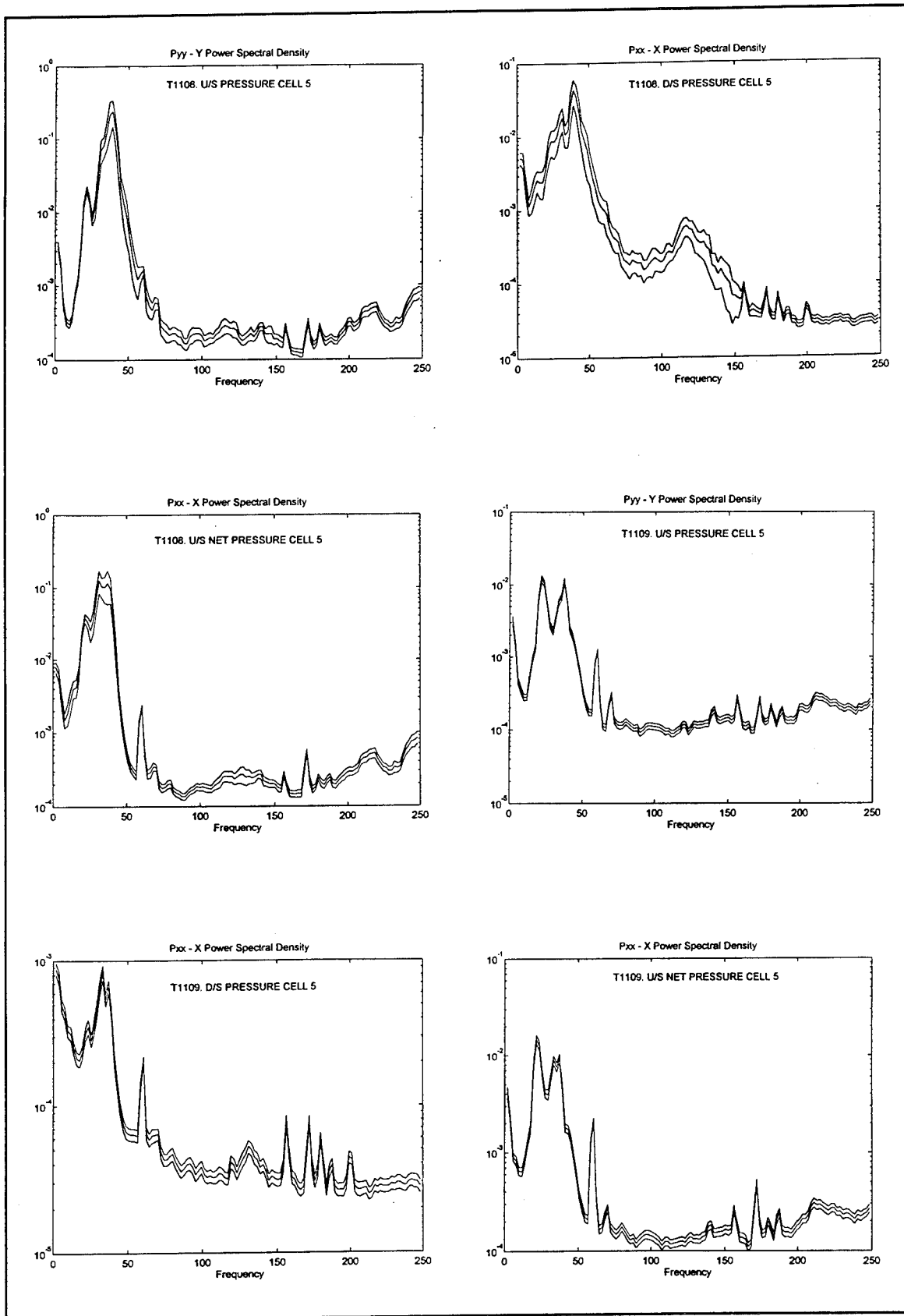


Plate A16. Spectral densities for the records of pressure cell 5 in tests T1108 and T1109

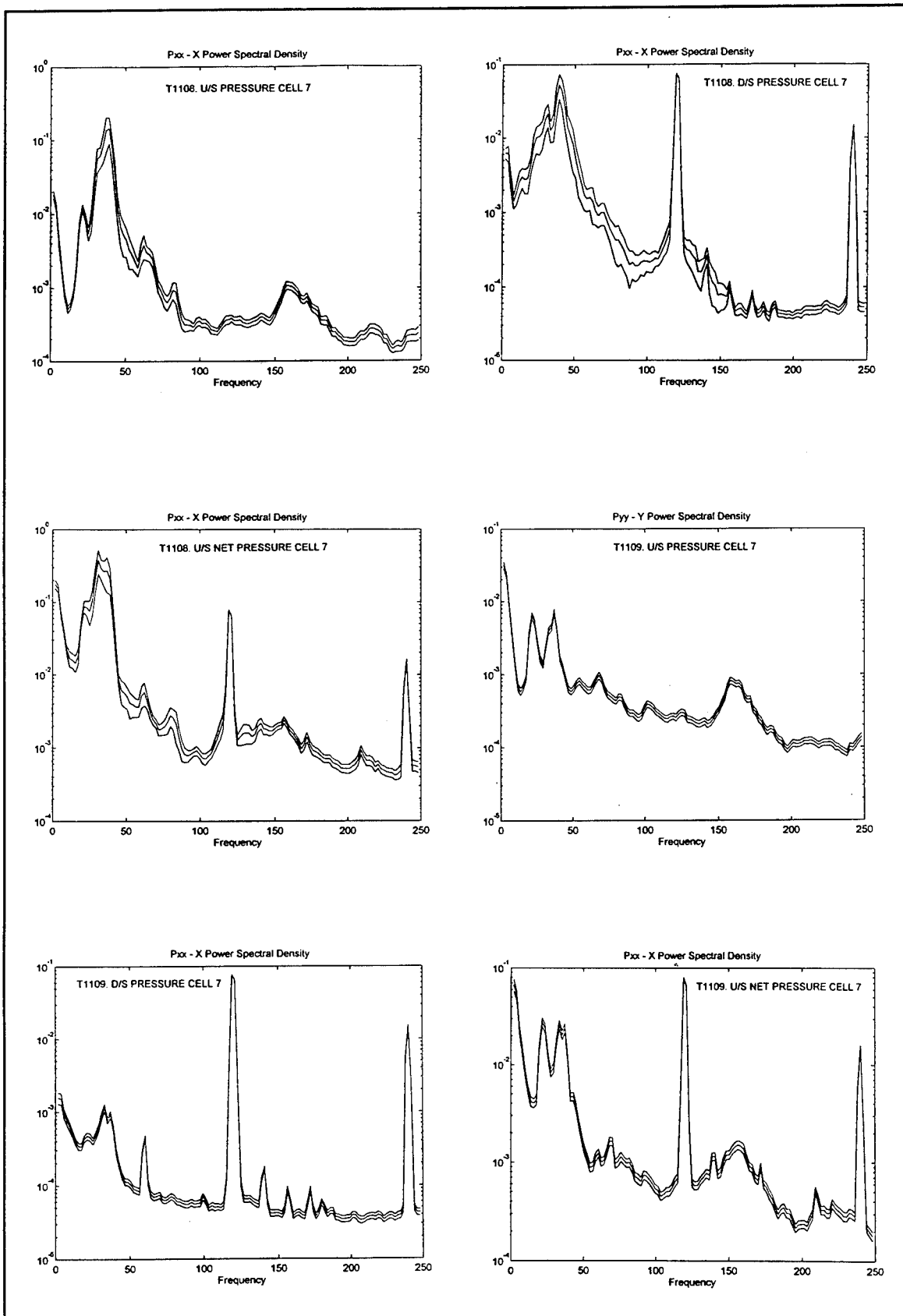


Plate A17. Spectral densities for the records of pressure cell 7 in tests T1108 and T1109

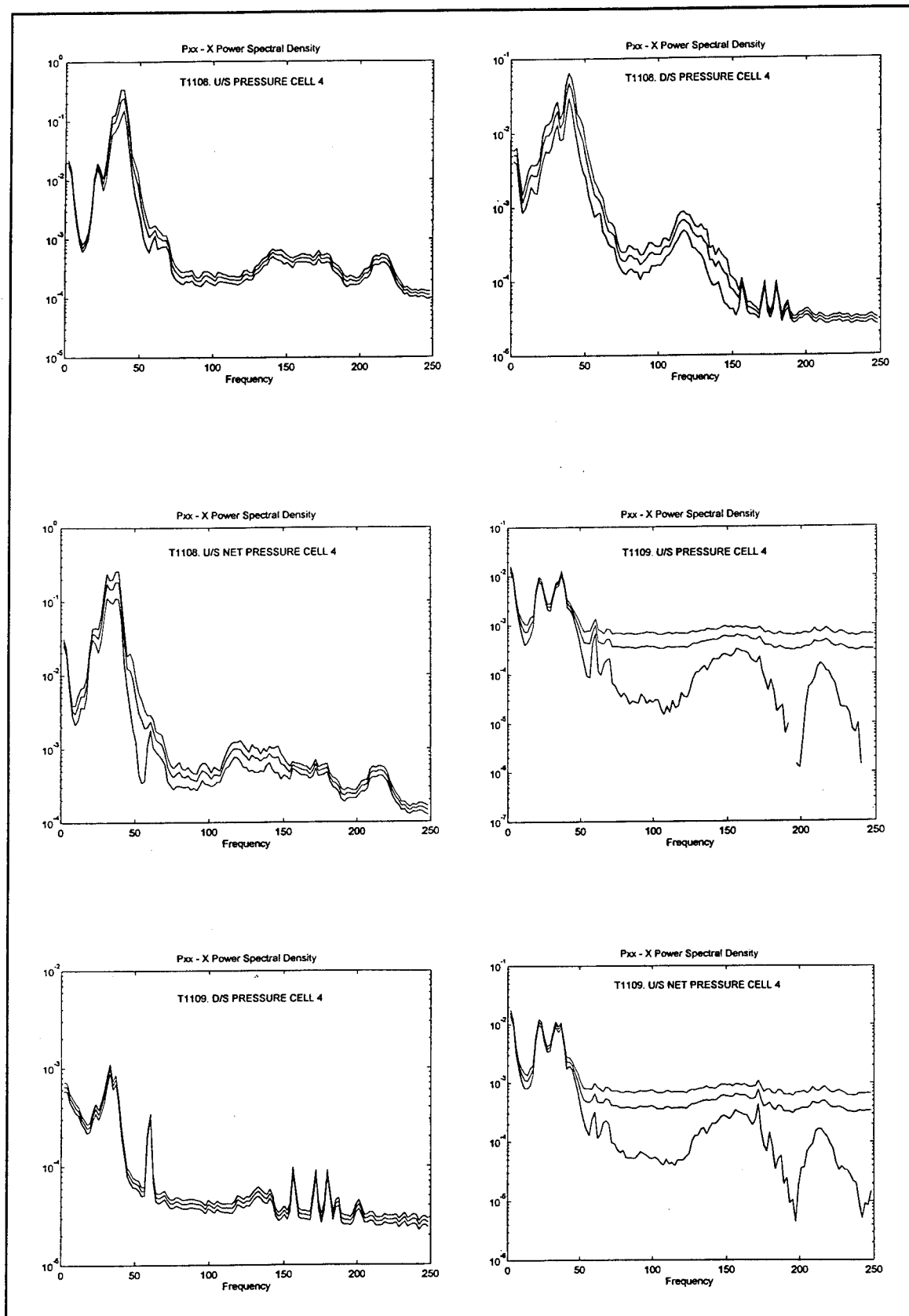


Plate A18. Spectral densities for the records of pressure cell 4 in tests T1108 and T1109

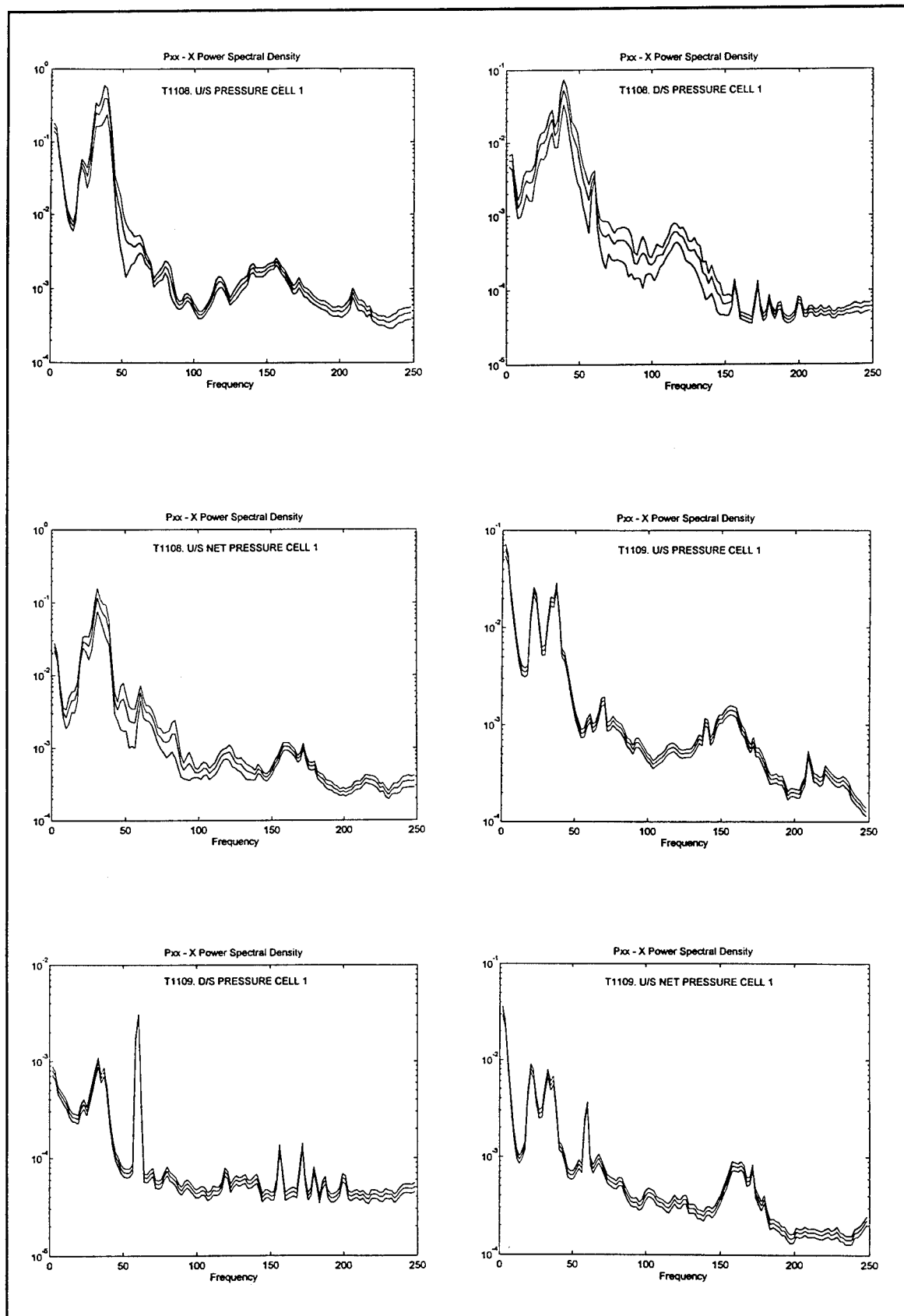


Plate A19. Spectral densities for the records of pressure cell 1 in tests T1108 and T1109

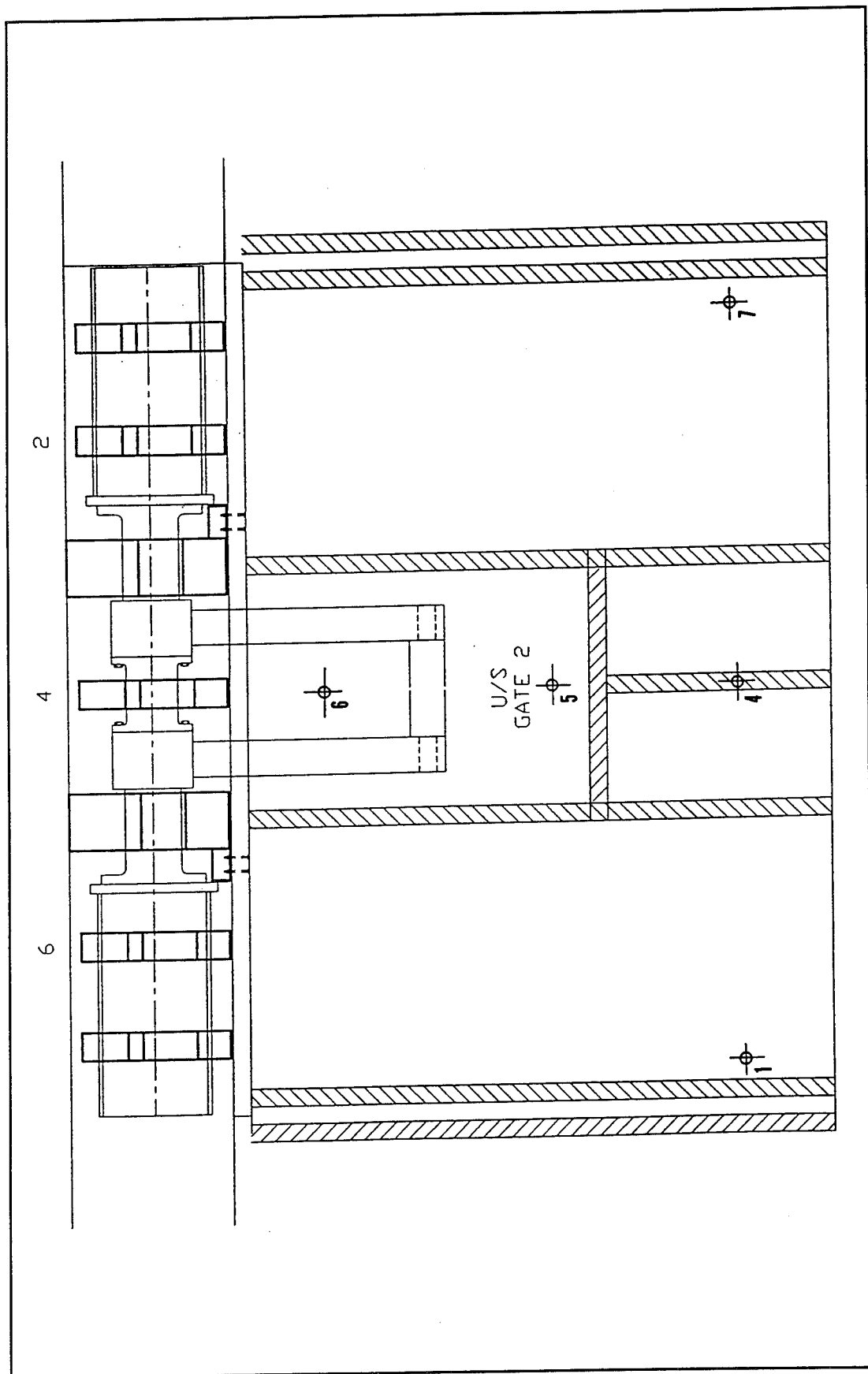


Plate A20. Pressure cells in coherence analysis of test T1080

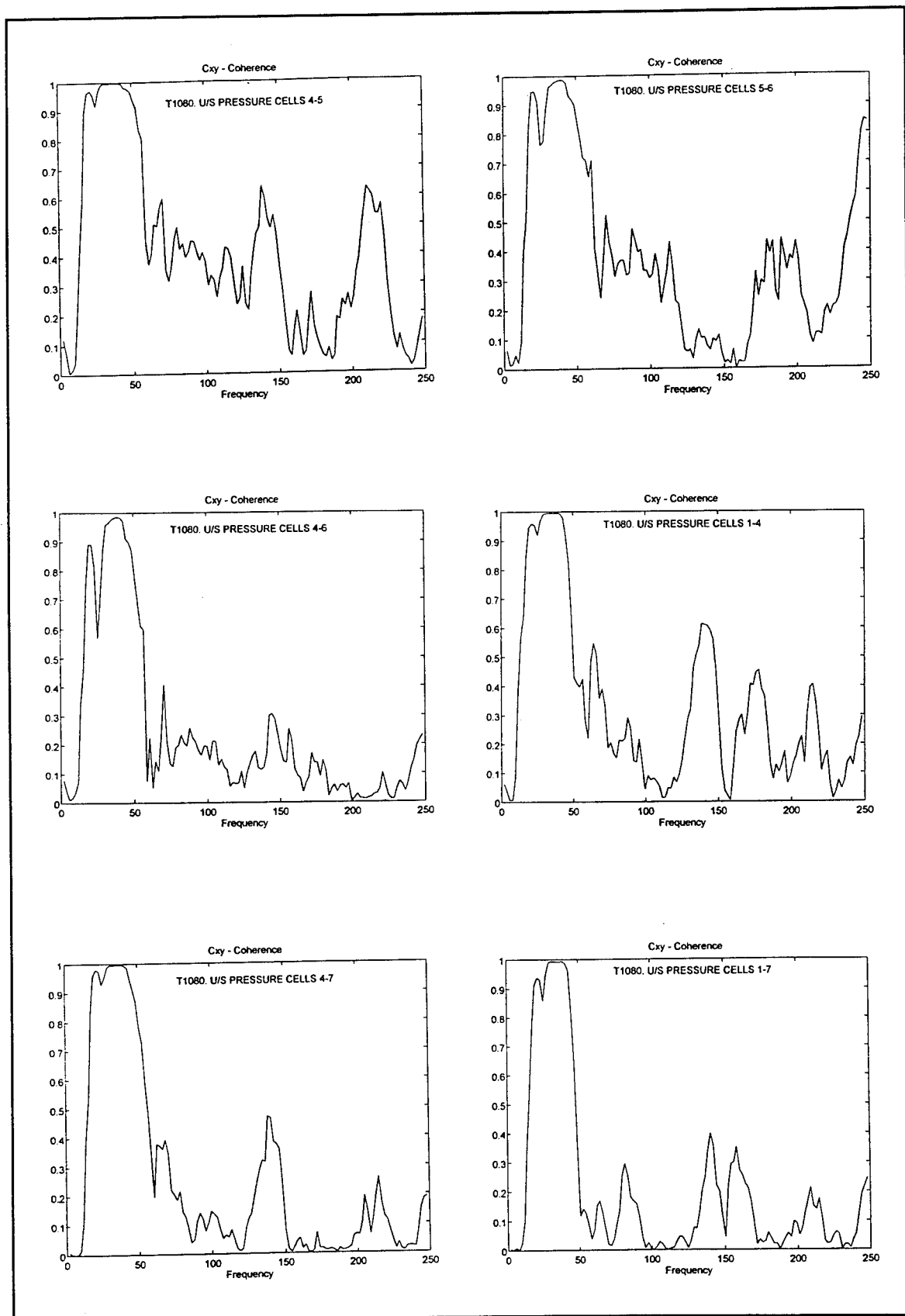


Plate A21. Coherence between upstream pressure-cell records in test T1080

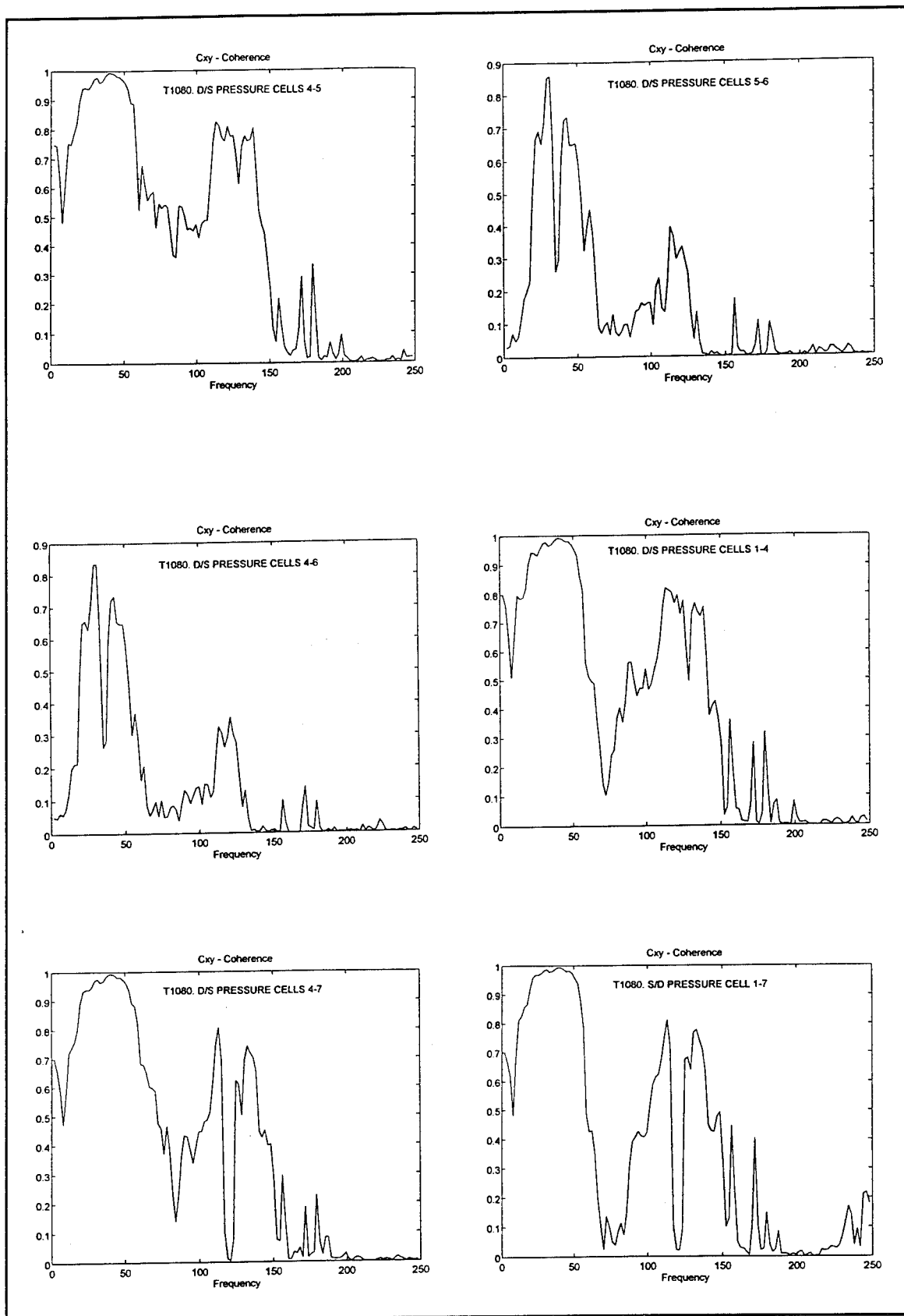


Plate A22. Coherence between downstream pressure-cell records in test T1080

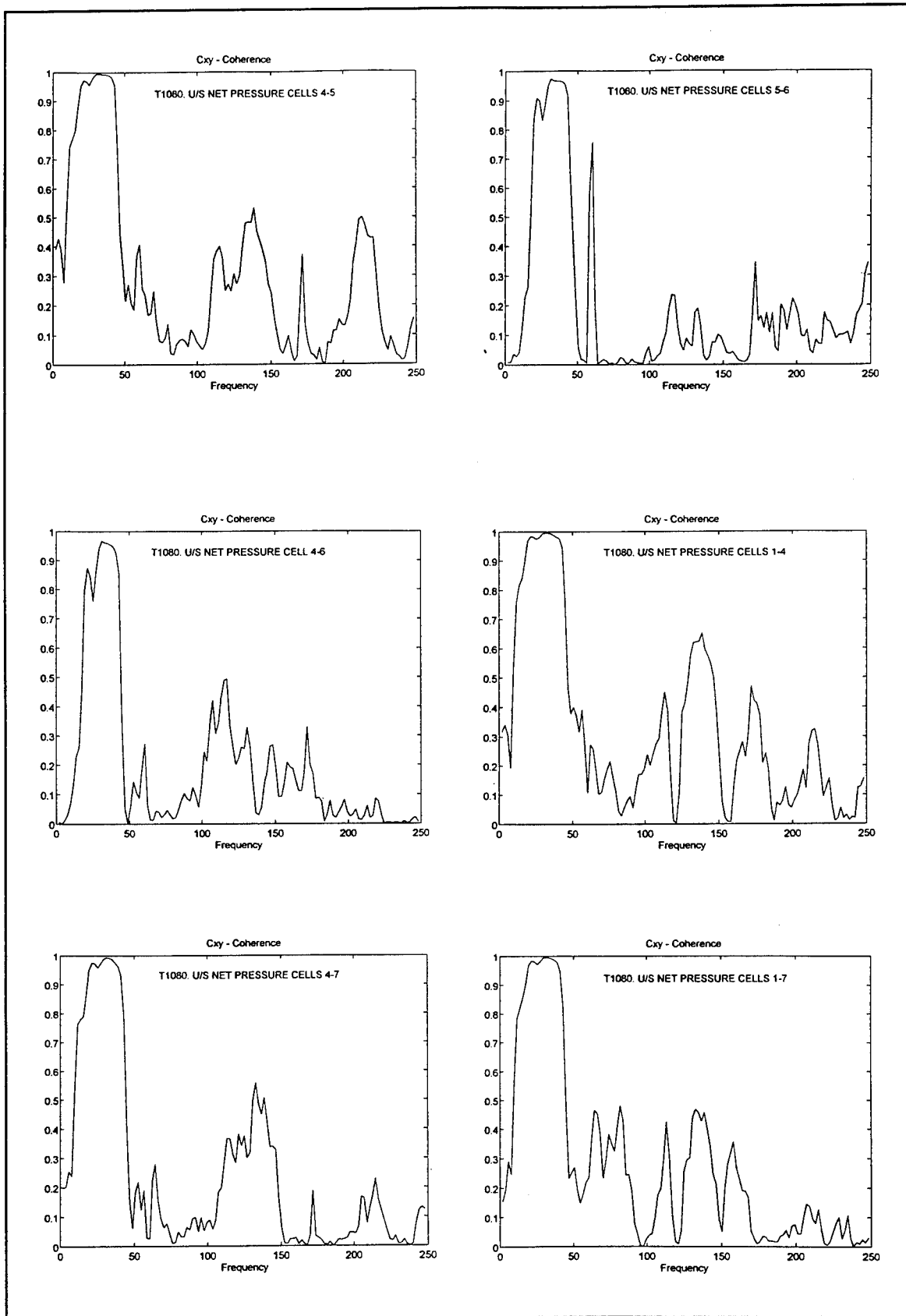


Plate A23. Coherence between net pressure-cell records in test T1080

REPORT DOCUMENTATION PAGE			Form Approved OMB No. 0704-0188	
<small>Public reporting burden for this collection of information is estimated to average 1 hour per response, including the time for reviewing instructions, searching existing data sources, gathering and maintaining the data needed, and completing and reviewing the collection of information. Send comments regarding this burden estimate or any other aspect of this collection of information, including suggestions for reducing this burden, to Washington Headquarters Services, Directorate for Information Operations and Reports, 1215 Jefferson Davis Highway, Suite 1204, Arlington, VA 22202-4302, and to the Office of Management and Budget, Paperwork Reduction Project (0704-0188), Washington, DC 20503.</small>				
1. AGENCY USE ONLY (Leave blank)	2. REPORT DATE November 1995	3. REPORT TYPE AND DATES COVERED Report 2 of a series		
4. TITLE AND SUBTITLE Montgomery Point Lock and Dam Gate Study, Report 2: Montgomery Point Torque-Tube Gate, A Structural Model Study		5. FUNDING NUMBERS		
6. AUTHOR(S) Luis A. de Bejar				
7. PERFORMING ORGANIZATION NAME(S) AND ADDRESS(ES) U.S. Army Engineer Waterways Experiment Station 3909 Halls Ferry Road, Vicksburg, MS 39180-6199		8. PERFORMING ORGANIZATION REPORT NUMBER Technical Report HL-95-14		
9. SPONSORING/MONITORING AGENCY NAME(S) AND ADDRESS(ES) U.S. Army Corps of Engineers, Washington, DC 20314-1000		10. SPONSORING/MONITORING AGENCY REPORT NUMBER		
11. SUPPLEMENTARY NOTES Available from National Technical Information Service, 5285 Port Royal Road, Springfield, VA 22161.				
12a. DISTRIBUTION/AVAILABILITY STATEMENT Approved for public release; distribution is unlimited.		12b. DISTRIBUTION CODE		
13. ABSTRACT (Maximum 200 words) Report 2 of the final report for model studies of the torque-tube gate system at Montgomery Point Lock and Dam deals with the structural aspects of the project. Analytical models for the theoretical prediction of the hydraulic forces on the gate are developed. The results of this formulations and multiple corresponding experiments on the physical model are synthesized into mathematical expressions for hydraulic pressure fields and support bearing reactions for design. Extreme-value analyses of the data in the controlling tests and additional experiments predict hydraulic pressures on the gate under unusual and improper operation conditions. The dynamic properties of the gate (natural frequencies of free vibration, modal shapes, and equivalent viscous damping ratios) are determined for evaluation of structural safety. Simplified engineering models to predict the gate's structural response from both deterministic and stochastic points of view are developed. The study concludes with a basic spectral analysis of the data collected to investigate the safety of the gate against fatigue in the long term.				
14. SUBJECT TERMS See reverse.		15. NUMBER OF PAGES 186		
		16. PRICE CODE		
17. SECURITY CLASSIFICATION OF REPORT UNCLASSIFIED	18. SECURITY CLASSIFICATION OF THIS PAGE UNCLASSIFIED	19. SECURITY CLASSIFICATION OF ABSTRACT	20. LIMITATION OF ABSTRACT	

14. (Concluded).

Engineering modeling

Experimental modeling

Extreme-value analysis

Hydraulic forces

Hydraulic pressure fields

Hydraulic structures

Mathematical modeling

Montgomery Point Lock and Dam

Physical models

Spectral analysis

Structural dynamic properties

Torque-tube gates